

**The Search for Higgs Boson Production in Association
with a Top-Quark Pair in pp Collisions at $\sqrt{s} = 8$ TeV in
the Lepton Plus Jets Final State**

John Garland Wood
Charlottesville, VA

B.S., The University of California, Berkeley, 2008

A Dissertation presented to the Graduate Faculty
of the University of Virginia in Candidacy for the Degree of
Doctor of Philosophy

Department of Physics

University of Virginia
May, 2015

Abstract

The most important goal of the Large Hadron Collider (LHC) is to elucidate the mechanism of electroweak symmetry breaking. The Standard Model (SM) Higgs boson is thought to be a prime candidate for this. The newly discovered boson announced on July 4th, 2012, with a mass of ~ 125 GeV/c 2 , has so far been shown to be consistent with a SM Higgs. However, the final confirmation of this new particle as the SM Higgs depends on subsequent measurements of all of its properties. The observation of this new particle in association with top-quark pairs would allow the couplings of this particle to top and bottom quarks to be directly measured. $t\bar{t}H$, with Higgs decaying to $b\bar{b}$ is an excellent channel to explore due to the dominant branching ratio of Higgs to $b\bar{b}$ and the kinematic handle the $t\bar{t}$ system offers on the event. However, it presents a plethora of difficult challenges due to a low signal to background ratio and uncertainties on kinematically similar SM backgrounds. This work discusses the search for Higgs boson production in association with a top-quark pair in pp collisions at $\sqrt{s} = 8$ TeV, collected by the Compact Muon Solenoid (CMS) experiment at the LHC. The search has been performed and published in two stages. The first analysis used the first 5.1 fb $^{-1}$, and was followed up by the second analysis with the full 2012 dataset, using a total integrated luminosity of 19.5 fb $^{-1}$

We approve the dissertation of John Garland Wood.

Date of Signature

Supervisor: Dr. Christopher Neu

Committee Chair: Dr. Bradley Cox

Committee Member: Dr. Hank Thacker

PhD Committee Chair: Dr. Astronomy Person

Contents

Contents	iv
List of Figures	vii
List of Tables	xv
1 Introduction	1
2 Theoretical Background	4
2.1 An Overview of Quantum Field Theory	4
2.2 Abelian Gauge Theories of Particle Interactions	7
2.3 Non-Abelian Gauge Theories of Particle Interactions	9
2.4 The Higgs Mechanism in an Abelian Theory	12
2.5 The Higgs Mechanism in a non-Abelian Theory	14
2.6 Glashow Weinberg Salam Theory	16
2.7 The Standard Model of Particle Physics	22
2.8 Higgs Production in pp Collisions at the LHC	24
2.9 $t\bar{t}H$ Production in pp Collisions at the LHC	26
2.10 Background Processes to $t\bar{t}H$	27
2.11 Potential BSM Effects on $t\bar{t}H$ production	30
3 The Large Hadron Collider	32
3.1 The LHC Accelerator Complex	34
3.2 LHC Magnets	42
3.3 LHC RF Technology	48
3.4 The LHC Cryogen System	51
3.5 The LHC Vacuum System	52
4 The Compact Muon Solenoid	54
4.1 The Tracker	56

4.1.1	The Silicon Pixel Detector	58
4.1.2	The Silicon Strip Detector	60
4.2	The Electromagnetic Calorimeter	63
4.2.1	Vacuum Photo-Triodes	67
4.2.2	Test Rig at UVa	68
4.2.3	Results of UVa Tests	69
4.3	The Hadronic Calorimeter	72
4.4	Muon Chambers	77
4.5	Data Collection Overview	81
5	Particle Reconstruction at CMS	85
5.1	Iterative Tracking	85
5.2	Calorimeter Clustering	86
5.3	Calorimeter Energy Calibration	87
5.4	Linking	89
5.5	Physics Object Reconstruction	90
5.5.1	Muon Reconstruction	90
5.5.2	Electron Reconstruction	91
5.5.3	Charged Hadron Reconstruction	92
5.5.4	Photon and Neutral Hadron Reconstruction	92
5.5.5	Jet Reconstruction	93
5.5.6	Missing Transverse Energy Reconstruction	95
6	Analysis I: The first 5 fb^{-1} of 8 TeV data	97
6.1	Data and Simulated Samples	99
6.1.1	Data Samples	100
6.1.2	Signal Samples	101
6.1.3	Background Samples	101
6.1.4	MC pileup reweighting	102
6.1.5	Additional Pileup Corrections	103
6.2	Event Selection	105
6.2.1	Event cleaning	105
6.2.2	Trigger	106
6.2.3	Muon Selection	106
6.2.4	Electron Selection	107
6.2.5	Lepton selection and trigger efficiencies	108

6.2.6	Jet selection	109
6.2.7	<i>b</i> -tagging selection	111
6.2.8	Lepton + Jets Selection	113
6.3	Multivariate Analysis	114
6.3.1	Artificial Neural Network Overview	115
6.3.2	MVA Input Variables, Data to Monte Carlo Comparisons	119
6.3.3	MVA Output, Data to Monte Carlo Comparisons	138
6.4	Systematic Uncertainties	140
6.5	Statistical Methods	146
6.6	Results and Conclusions	148
	Bibliography	150
	List of Acronyms	158

List of Figures

1.1	The CMS experiment has observed a new boson at $m \sim 125 \text{ GeV}/c^2$	1
1.2	A Feynman diagram of the $t\bar{t}H$ process, with Higgs $\rightarrow b\bar{b}$, and the $t\bar{t}$ -system decaying semi-leptonically	3
2.1	Leading and Next to Leading Order Feynman diagrams for the coulomb scattering process	6
2.2	The global average of α_s , the QCD coupling constant.	7
2.3	A visual representation of the Higgs potential	12
2.4	Experimental milestones of the Standard Model	23
2.5	Higgs production cross-sections at the LHC, for 7-14 TeV pp collisions	24
2.6	Feynman diagrams for the three largest Higgs production modes at the LHC	25
2.7	Feynman diagram for $t\bar{t}H$ production	26
2.8	Feynman diagrams for the semileptonic $t\bar{t}H$ process and its irreducible background, $t\bar{t} + b\bar{b}$	27
2.9	Feynman diagrams for the $t\bar{t}W$ and $t\bar{t}Z$ background processes	28
2.10	Feynman diagrams for the single t s,t, and tW background processes	28
2.11	Feynman diagrams for the W, Z plus jets, and diBoson (WW, WZ, ZZ) production.	29
2.12	Measurements of $t\bar{t}H$ backgrounds at CMS	29
2.13	The cancellation of the divergent Higgs mass from a loop of top-quarks is cancelled by a loop of supersymmetric top-quarks, stop-quarks,	31
3.1	Aerial view of the LHC complex, spanning the French-Swiss border [1]	32
3.2	Integrated Luminosity delived to the CMS experiment from 2010-12	34
3.3	The LHC accelerator complex, taking protons from a bottle of Hydrogen at the Linac2, all the way to the LHC ring	35
3.4	Features of the Linac2, the first stage of acceleration in the LHC injection chain	36
3.5	Features of the PS booster, the second stage of the LHC injection chain	37
3.6	Features of the PS, the third stage of the LHC injection chain	40

3.7	Features of the SPS, the fourth and final stage of the LHC injection chain	41
3.8	The LHC ring is divided into eight octants	43
3.9	The single turn injection scheme. A septum magnet makes the initial alignment. The kicker magnet times the injection and makes the final alignment. Bumper magnets align the LHC beam with the injected beam.	44
3.10	Layout of Interaction Region 8, where one proton beam is injected into the LHC ring. A transfer line from the SPS bring a proton in from the right. In green, a septum magnet aligns the beam horizontally with the LHC. In blue, a kicker magnet makes the final vertical alignment into the LHC, and is timed to fill one of the 400 MHz buckets of the RF capture system	44
3.11	The initial filling of 6 batches of protons from the PSB to the PS, leaves 12 empty buckets in the PS bunch structure. The rise time of the SPS magnet creates an additonal gap in the SPS bunch structure. Additional gaps emerge due to the rise time of the LHC injection and dumping kicker magnets	45
3.12	Features of the dipole magnets used in the LHC	46
3.13	Features of the dipole magnets used in the LHC	47
3.14	Features of the 400 MHz superconducting RF system used in the LHC	48
3.15	A klystron uses a weak RF signal coupled to a resonace cavity to bunch an electron beam, which in turn creates an amplified RF signal as it passes through a second resonance cavity tuned to the same frequency.	49
3.16	One of sixteen 300 kW, 400 MHz klystrons that power the superconducting RF cavities that accelerate the proton beam.	50
3.17	Layout of the five cryogenic islands, which are home to the eight facilities that provide liquid helium to the LHC	51
3.18	Features of the 4.5 K refridgeration system	51
3.19	Cross section schematic of the cryogenic distribution system in the LHC tunnel .	52
3.20	Beam screen for the LHC, with slits to allow for easy pumping of residual gas molecules in the beampipe.	53
4.1	A cutaway diagram of the CMS detector. Two humans are present at the bottom of the image to provide scale.	54
4.2	A slice of the CMS detector showing how various particles interact and deposit energy. The trajectory of charged particles is measured in the tracker; electrons and photons deposit most of their energy in the ECAL; charged and neutral hadrons deposit most of their energy in the HCAL; the muon chambers measures the trajectory of muons or long-lived charged particles	55

4.3 A side view of the tracker. The pixel detector is the innermost sub-system, with three concentric rings of detectors in the barrel, and two in the endcap. The tracker inner barrel (TIB) is a silicon strip detector, with four concentric rings. The tracker inner disks (TID) are three layers deep. The tracker outer barrel (TOB) is six concentric rings and the tracker end caps (TEC) are nine layers deep.	57
4.4 A head-on view of the beamline and barrel components of the tracker.	57
4.5 The three barrel and two disk layers of the silicon pixel tracker provide coverage of $ \eta < 2.5$	58
4.6 The readout electronics chain for the pixel detector	59
4.7 In 2012 pp collisions at $\sqrt{s} = 8$ TeV, the pixel detector performed with a resolution of $11.8 \mu\text{m}$. The above is a plot of the residual difference between a pixel and the results of a fit to a particle track.	60
4.8 A silicon strip module, with two $500 \mu\text{m}$ thick sensors.	61
4.9 Schematic of the readout sequence of the silicon strip detector.	62
4.10 Measurements of the performance of the silicon strip track using pp collisions from 2011 at $\sqrt{s} = 7$ TeV	62
4.11 Layout of the ECAL sub-detector	63
4.12 Typical Lead Tungstate crystal, with APD attached to the rear face in the left frame, and a VPT attached in the right frame.	63
4.13 A simulation of the evolution of an electromagnetic shower being initiated by an electron entering the center of the front face.	64
4.14 A module of 500 crystals (25 crystals wide by 20 crystal tall).	65
4.15 Schematic of the On-Detector Readout for the ECAL	66
4.16 A section of the ECAL end-cap, a Dee. Two Dees form a disk with an inner bore for the beam-line to pass through. 5x5 modules, or supercrystals, are mounted in preparation for installation at CMS	67
4.17 Vacuum Photo-Triode devices used in the ECAL end-caps (EE)	67
4.18 Features of the UVa VPT test stand	70
4.19 3 runs of 5 VPTs, exposed to blue LED light, and fit to a sum of two exponentials.	71
4.20 3 runs of 5 VPTs, exposed to orange LED light, and fit to a sum of two exponentials.	72
4.21 Longitudinal cross-section of the HCAL with the four sub-systems labeled	73

4.22 Closeup of the HCAL barrel section. The center section of each of the 18 wedges are labeled, optical cables lay accross the joint of the center and staggered edge sections of each wedge. The blue lines show the apporximate azimuthal division of the wedge.	74
4.23 Over 1 million Russian shells of military artillery were re-processed in the construction of the HCAL	75
4.24 Optical readout chain of the HCAL scintillator tiles	75
4.25 HCAL endcap, 18 azimuthal divisions of alternating layers of brass and plastic scintillator.	76
4.26 Longitudinal cross-section of the HCAL forward calorimetry, the HF	76
4.27 Longitudinal cross-section of one of the 5 wheels of the muon system. Drift tubes are placed in 4 concentric layers, with 2 being placed inside the return yoke of the magnet, and 12 azimuthal divisions.	78
4.28 A cross-section view of a drift cell. The anode wire is held at 3600 V, creating a potential difference with the walls. Electric field lines are shown in blue.	79
4.29 RPC layout for the barrel and endcaps	79
4.30 Exploded diagram of an RPC	80
4.31 Cross-section of one quarter of the muon endcap system, with the 4 disks of CSC systems shown in red	80
4.32 A CSC station with 7 layers, making 6 gas chambers. Cathode strips are shown in yellow, perpendicular to the vertical anode wires in orange.	81
4.33 A block diagram of the L1 trigger	82
4.34 A schematic of the e/γ trigger algorithm	82
4.35 Layout of the CMS DAQ	83
 5.1 Results of the uncertainty on the ECAL intercalibration coefficients for the barrel (left) and endcaps (right)	88
5.2 Instantaneous luminosity response to the crystals as measured by the laser and LED system. Additional crystal calibration constants are derived to normalize the crystal reponse over the range of collected data	89
5.3 Results of using a χ^2 minimization procedure to estimate the neutral hadron energy contribution in the HCAL using simulated events	90
5.4 Muon validation plots for the particle-flow reconstruction	91
5.5 Electron validation plots for the particle-flow reconstruction	92
5.6 The anti-kt jet clustering algorithm with distance parameter R=1.0	93

5.7	Commissioning of the particle-flow algorithm on jets, involved comparing the energy measured from charged hadron tracks, to energy measured in calorimeter clusters linked to the tracks	94
5.8	A b -meson will travel a distance L_{xy} before decaying and creating a secondary vertex. The impact parameter, d_0 measures the longitudinal displacement of the two vertices	95
6.1	This figure shows the breakdown of jet-to-parton assignments for the two jets with the minimum ΔR separation in the event for events with greater or equal 4 b -tagged jets.	98
6.2	Comparison of number of reconstructed vertices for data (black) and the $t\bar{t}$ MC sample before (blue) and after (red) pileup reweighting. After pileup reweighting, the MC matches the data well.	103
6.3	H_T distribution for 8 TeV lepton plus jet events with ≥ 4 jets and ≥ 2 tags shown for different amounts of pileup. The left-hand plot shows low pileup, the middle plot shows medium pileup, and the right-hand plot shows high pileup.	104
6.4	H_T distribution for 8 TeV lepton plus jet events with ≥ 4 jets and ≥ 2 tags. The left-hand plot shows the distribution before correction. The right-hand plot shows the distribution after correction. Note that the ratio in the right-hand plot is flatter than the left-hand plot.	105
6.5	Muon and electron ID, isolation selection and trigger efficiency scale factors in bins of p_T and η	109
6.6	Number of jets (left) and number of b -tagged jets (right) in data and simulation for events with ≥ 4 jets + ≥ 2 b -tags in the lepton+jets channel at 8 TeV. The background is normalized to the SM expectation; the uncertainty band (shown as a hatched band in the stack plot and a green band in the ratio plot) includes statistical and systematic uncertainties that affect both the rate and shape of the background distributions. The $t\bar{t}H$ signal ($m_H = 125 \text{ GeV}/c^2$) is normalized to $30 \times$ SM expectation.	114
6.7	A simple example of a MLP type ANN, with one layer of input neurons that make connections to a hidden layer, which is connected to the output layer	115
6.8	The CFMlpANN architechture used in this analysis features two hidden layers, and 10 input variables for each jet/tag category (11 variables for the ≥ 6 jets, ≥ 4 b -tags category)	116
6.9	Comparisons of the testing and training samples used to optimize the CFMlpANN weights for each jet/tag category	118

6.10 Lepton + jets data/MC comparison for the ≥ 6 jets + 2 tag category. The uncertainty band includes statistical and systematic uncertainties that affect both the rate and shape of the background distributions.	125
6.11 Lepton + jets data/MC comparison for the ≥ 6 jets + 2 tag category. The uncertainty band includes statistical and systematic uncertainties that affect both the rate and shape of the background distributions.	126
6.12 Lepton + jets data/MC comparison for the 4 jets + 3 tag category. The uncertainty band includes statistical and systematic uncertainties that affect both the rate and shape of the background distributions.	127
6.13 Lepton + jets data/MC comparison for the 4 jets + 3 tag category. The uncertainty band includes statistical and systematic uncertainties that affect both the rate and shape of the background distributions.	128
6.14 Distributions of the five ANN input variables with rankings 1 through 5, in terms of separation, for the 5 jets + 3 b-tags category of the lepton+jets channel at 8 TeV. Definitions of the variables are given in the text. The background is normalized to the SM expectation; the uncertainty band (shown as a hatched band in the stack plot and a green band in the ratio plot) includes statistical and systematic uncertainties that affect both the rate and shape of the background distributions. The $t\bar{t}H$ signal ($m_H = 125 \text{ GeV}/c^2$) is normalized to the total background yield, for easier comparison of the shapes.	129
6.15 Distributions of the five ANN input variables with rankings 6 through 10, in terms of separation, for the 5 jets + 3 b-tags category of the lepton+jets channel at 8 TeV. Definitions of the variables are given in the text. The background is normalized to the SM expectation; the uncertainty band (shown as a hatched band in the stack plot and a green band in the ratio plot) includes statistical and systematic uncertainties that affect both the rate and shape of the background distributions. The $t\bar{t}H$ signal ($m_H = 125 \text{ GeV}/c^2$) is normalized to the total background yield, for easier comparison of the shapes.	130
6.16 Lepton + jets data/MC comparison for the ≥ 6 jets + 3 tag category. The uncertainty band includes statistical and systematic uncertainties that affect both the rate and shape of the background distributions.	131
6.17 Lepton + jets data/MC comparison for the ≥ 6 jets + 3 tag category. The uncertainty band includes statistical and systematic uncertainties that affect both the rate and shape of the background distributions.	132

6.18 Lepton + jets data/MC comparison for the 4 jets + 4 tag category. The uncertainty band includes statistical and systematic uncertainties that affect both the rate and shape of the background distributions.	133
6.19 Lepton + jets data/MC comparison for the 4 jets + 4 tag category. The uncertainty band includes statistical and systematic uncertainties that affect both the rate and shape of the background distributions.	134
6.20 Lepton + jets data/MC comparison for the 5 jets + 4 tag category. The uncertainty band includes statistical and systematic uncertainties that affect both the rate and shape of the background distributions.	135
6.21 Lepton + jets data/MC comparison for the 5 jets + 4 tag category. The uncertainty band includes statistical and systematic uncertainties that affect both the rate and shape of the background distributions.	136
6.22 Lepton + jets data/MC comparison for the ≥ 6 jets + 4 tag category. The uncertainty band includes statistical and systematic uncertainties that affect both the rate and shape of the background distributions.	137
6.23 Lepton + jets data/MC comparison for the ≥ 6 jets + 4 tag category. The uncertainty band includes statistical and systematic uncertainties that affect both the rate and shape of the background distributions.	138
6.24 The distributions of the CFMlpANN output for lepton+jets events at 8 TeV in the various analysis categories. Background-like events have a low CFMlpANN output value. Signal-like events have a high CFMlpANN output value. The background is normalized to the SM expectation; the uncertainty (shown as a hatched band in the stack plot and a green band in the ratio plot) includes statistical and systematic uncertainties that affect both the rate and shape of the background distributions. The $t\bar{t}H$ signal ($m_H = 125 \text{ GeV}/c^2$) is normalized to $30 \times \text{SM}$ expectation.	139
6.25 Comparison of the MVA discriminator for JES shift upwards (red) and downwards (blue) relative to the nominal (black) shape for the $t\bar{t}H(120)$ signal (left) and the main background sample $t\bar{t} +$ light flavor (right). The plots shown are from the ≥ 6 jet ≥ 4 tag category in the lepton+jets channel. All plots are normalized to unit area.	141

6.26 Comparison of the MVA discriminator for b -tag scale factor shift upwards (red) and downwards (blue) relative to the nominal (black) shape for the $t\bar{t}H(120)$ signal (left) and the main background sample $t\bar{t} + \text{light flavor}$ (right). The plots are from the ≥ 6 jets + ≥ 4 tags category in the lepton+jets channel. All plots are normalized to unit area.	142
6.27 Comparison of the MVA discriminator for additional PU correction systematic upwards (red) and downwards (blue) relative to the nominal (black) shape for the $t\bar{t}H(120)$ signal (left) and the main background sample $t\bar{t} + \text{light flavor}$ (right). The plots are from the ≥ 6 jets + ≥ 4 tags category in the lepton+jets channel. All plots are normalized to unit area.	143
6.28 The rate and shape variations for selected categories due to the Q^2 uncertainty. . .	145
6.29 A dedicated CFMlpANN trained to isolate $t\bar{t} + b\bar{b}$ from $t\bar{t} + \text{jets}$. The left plot shows is for the case of nominal $t\bar{t} + b\bar{b}$ cross-section, the right plot shows the case for $x2 t\bar{t} + b\bar{b}$ cross-section. The left-most region of both plots is the most sensitivite to the $t\bar{t} + b\bar{b}$ normalization, and shows no significant improment in data to MC agreement, justifying the reasoning that an uncertainty larger than 50% is needed.	146
6.30 The expected and observed 95% CL upper limits on the signal strength parameter $\mu = \sigma/\sigma_{SM}$ for the lepton+jets channel using the 2012 dataset. These limits were extracted using the asymptotic method.	149

List of Tables

2.1	The quantum numbers Isospin and Hypercharge are assigned for each of the $SU(2)$ and $U(1)$ symmetries respectively	20
4.1	Fit Results for VPT Conditioning Studies at U.Va. and Brunel, Blue Reference LED	71
4.2	Fit Results for VPT Conditioning Studies at U.Va., Orange LED	72
6.1	The datasets analyzed for this analysis.	101
6.2	List of signal MC datasets and cross sections used to determine the SM expectation.	101
6.3	List of background MC datasets and cross sections used for normalization.	102
6.4	List of lepton+jets triggers	106
6.5	Tight and loose muon definition	108
6.6	Tight and loose muon definition	108
6.7	Jet definition	110
6.8	Jet Energy Resolution (JER) scale factors	110
6.9	Expected event yields in 5 fb^{-1} for signal and backgrounds in the $\mu+\text{jets}$ channel.	123
6.10	Expected event yields in 5 fb^{-1} for signal and backgrounds in the $e+\text{jets}$ channel.	123
6.11	The ANN inputs for the nine jet-tag categories in the $8 \text{ TeV } t\bar{t}\text{H}$ analysis in the lepton+jets and dilepton channels. The choice of inputs is optimized for each category. Definitions of the variables are given in the text. The best input variable for each jet-tag category is denoted by \star	124
6.12	Summary of the systematic uncertainties considered on the inputs to the limit calculation. Except where noted, each row in this table will be treated as a single, independent nuisance parameter.	140
6.13	Relative yield change due to JES shift up/down for the ≥ 6 jets + ≥ 4 tags category in the lepton+jets channel.	141
6.14	Relative yield change due to b -tag scale factor shift up/down for the ≥ 6 jets + ≥ 4 tags category in the lepton+jets channel.	142

6.15 Cross section uncertainties used for the limit settings. Each column in the table is an independent source of uncertainty, except for the last column which represents uncertainties uncorrelated with any others. Uncertainties in the same column for two different processes (different rows) are completely correlated.	144
6.16 Expected and observed upper limits for SM Higgs for lepton + jets channel using the first 5.1 fb^{-1} of the 2012 dataset. These limits were extracted using the asymptotic method.	148

¹ Chapter 1

² Introduction

³ On July 4th, 2012, the Compact Muon Solenoid (CMS) and A Toroidal LHC Apparatus (ATLAS)
⁴ experiments announced the discovery of a new boson of mass $\sim 125 \text{ GeV}/c^2$ [2] [3]. The particle
⁵ has been shown to be increasingly consistent with the description of the boson predicted by the
⁶ Higgs mechanism of the SM, as measurements on its mass, width, and quantum numbers are
⁷ completed. However, there are several properties of this new boson, which remain to be tested.
⁸ Figure 1.1 shows a consistent mass peak between the $H \rightarrow ZZ$ and $H \rightarrow \gamma\gamma$ channels at the
⁹ CMS experiment.

¹⁰ The Yukawa coupling of the Higgs boson to the top-quark in the SM is the largest coupling
¹¹ among the fundamental particles and is well predicted - thus offering an excellent test of the
¹² nature of the coupling of the Higgs to fermions, as well as a potential probe into physics Beyond
¹³ the Standard Model (BSM) that would alter this value from the SM prediction. The production
¹⁴ of the Higgs boson in association with top-quark pairs is the best production mode at the LHC
¹⁵ that offers direct access to the top-Higgs coupling. The dominant production mode of Higgs
¹⁶ at the LHC, gluon-gluon fusion, involves a triangle loop of strongly-coupled fermions, which

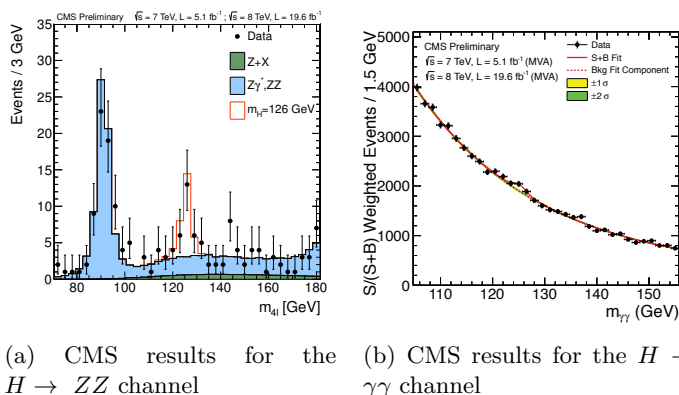


Figure 1.1: The CMS experiment has observed a new boson at $m \sim 125 \text{ GeV}/c^2$

¹⁷ includes all of the other quarks, as well as the potential for BSM particles.

¹⁸ $t\bar{t}H$ production also has the ability to constrain some extensions of the SM that would not
¹⁹ modify the Higgs branching fractions enough to be seen within current experimental precision.
²⁰ Such models include Little Higgs models, models with extra dimensions, top-color models, and
²¹ composite Higgs models that introduce a vector-like top partner, a t' , that can decay to tH ,
²² bW , or tZ states. Both $t't'$ and $t't$ production would produce a $t\bar{t}H$ final state, or one that is
²³ indistinguishable from it ($tHbW$). Upper limits on $t\bar{t}H$ production would also provide limits on
²⁴ the previously described models, which would be complementary to existing direct searches for
²⁵ t' particles, which attempt to reconstruct the t' resonance.

²⁶ The $t\bar{t}H$ channel has a rich set of possible final states. Each top-quark will decay to a b -
²⁷ quark and a W boson. The W boson will subsequently decay to two quarks, or a lepton and a
²⁸ neutrino. These decays are classified as either hadronic, semi-leptonic, or di-leptonic for zero,
²⁹ one, or both t quarks decaying leptonically respectively. The Higgs may decay to b -quark, W ,
³⁰ Z , τ , or γ pairs. In fact, this is one of the only production modes at the LHC which has access
³¹ to every Higgs decay mode, as other production mechanisms are swamped by large backgrounds
³² preventing measurements of all Higgs decay types.

³³ The search is performed with the CMS experiment, a modern, general purpose particle
³⁴ detector capable of reconstructing and identifying hadronic jets, photons, electrons, muons,
³⁵ and tau leptons. The hermetic design, and its high precision and efficiency in reconstructing
³⁶ and tracking every particle in a pp collision, also makes it suitable for reconstructing missing
³⁷ transverse energy from the calculated momentum imbalance of all of the measured particles in
³⁸ the event. This missing transverse energy is often the signature of a neutrino, which is the
³⁹ only SM particle capable of escaping detection. The detector uses a 3.8 T axial magnetic field,
⁴⁰ produced by the solenoid it is named after, to bend charged particles as they travel through
⁴¹ the detector. The measured curvature of their tracks allows the momentum of the particles to
⁴² be calculated with to a high precision. Tracks are formed and particles are reconstructed by a
⁴³ combination of sub-detector systems which work together to form the final reconstructed
⁴⁴ image of each particle in the collision.

⁴⁵ This thesis will focus on a semi-leptonic decay of the top-quarks, with the Higgs decaying to
⁴⁶ a b -quark pair. Figure 1.2 is Feynman diagram of the $t\bar{t}H$ process. The largest background to
⁴⁷ this process is top-quark pair production with extra jets originating from Initial State Radiation
⁴⁸ (ISR) or Final State Radiation (FSR) radiation, $t\bar{t} + jets$. The irreducible background is formed
⁴⁹ by top-quark pairs, where a gluon is radiated and decays to b -quark pairs, $t\bar{t} + b\bar{b}$. In addition
⁵⁰ to the large backgrounds, the high jet multiplicity in the $t\bar{t}H$ final state gives rise to a combina-
⁵¹ torics problem in associating each jet with its role in the $t\bar{t}H$ system. This inevitably leads to

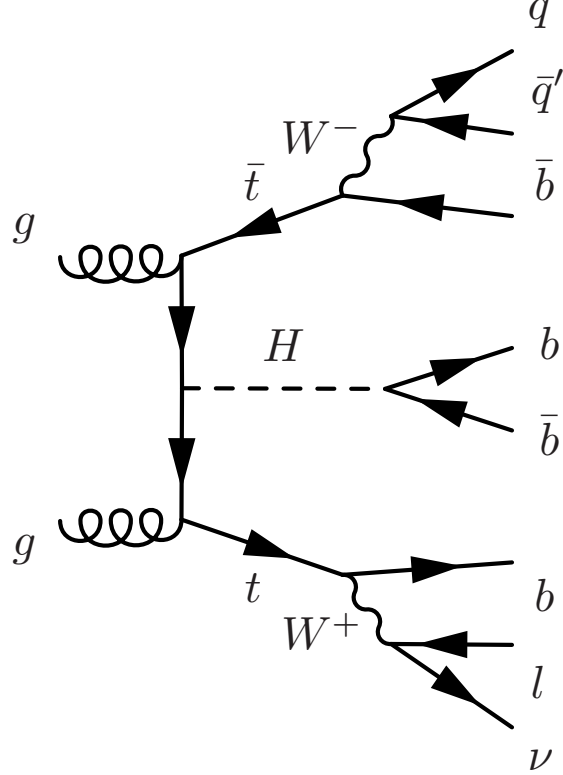


Figure 1.2: A Feynman diagram of the $t\bar{t}H$ process, with $H \rightarrow b\bar{b}$, and the $t\bar{t}$ -system decaying semi-leptonically

misidentifying which jets are the decay product of the Higgs, and thus additionally smears out the resolution on the mass of the Higgs. Due to the similarity of the $t\bar{t} + b\bar{b}$ background and the combinatorics issue, no single variable is suitable for signal extraction. A Multi-Variate Analysis (MVA) technique is used in an attempt to isolate the $t\bar{t}H$ signal from the $t\bar{t} + jets$ background. The MVA provides a one-dimensional discriminant based on several input variables related to the kinematics of the event. This discriminant is then used to perform signal extraction and set upper-limits on $t\bar{t}H$ production. The results of two searches will be presented. The first result used the first 5.1 fb^{-1} of the 2012 dataset, with center of mass energy of 8 TeV, and was published in the Journal of High Energy Physics (JHEP), May 2013. The second result was update with the full 19.4 fb^{-1} 8 TeV dataset, and was published in JHEP, Spetember 2014.

⁶² Chapter 2

⁶³ Theoretical Background

⁶⁴ The Standard Model (SM) of particle physics represents the sum of knowledge of the fundamen-
⁶⁵ tal particles and their interactions with each other. It is a Quantum Field Theory (QFT) that
⁶⁶ represents the interactions of each of the fundamental forces through the symmetry of a mathe-
⁶⁷ matical object known as a Lie group. It is the theory that dictates the rate that the $t\bar{t}H$ process
⁶⁸ is produced, as well as the kinematics of every particle involved. As such, its predictions are
⁶⁹ critical for modeling the characteristic signature of the $t\bar{t}H$ signal in the CMS detector, as well as
⁷⁰ the background processes, like $t\bar{t} + b\bar{b}$ which leave a kinematically similar final state signature.

⁷¹ 2.1 An Overview of Quantum Field Theory

⁷² Quantum Field Theory (QFT) was developed out of the need for a relativistic description of
⁷³ quantum mechanics. Since the Einstein relation $E = mc^2$ allows for the creation of particle-
⁷⁴ antiparticle pairs, the single-particle description used in non-relativistic quantum mechanics,
⁷⁵ fails describe this phenomenon [4]. This additionally fails when considering that Heisenberg's
⁷⁶ uncertainty relation, $\Delta E \cdot \Delta t = \hbar$, allows for an arbitrary number of intermediate, virtual
⁷⁷ particles to be created. By quantizing a field representing a certain type of particle, multiparticle
⁷⁸ states are naturally described as discrete excitations of that field.

⁷⁹ Lorentz invariance, and the need to preserve causality, also define a fundamental relationship
⁸⁰ between matter and antimatter. The propagation of a particle across a space-like interval is
⁸¹ treated equivalently to the an anti-particle propagating in the opposite direction [4]. This is
⁸² done so that the net probability amplitude for the particles to have an effect on a measurement
⁸³ occurring across a space-like interval cancel each other, thus preserving causality. This cancel-
⁸⁴ lation requirement additionally implies that the particle and anti-particle have the same mass,
⁸⁵ with opposite quantum numbers such as spin or electric charge.

86 The Lorentz transformations for a scalar field are different than for a field with internal de-
 87 grees of freedom, such as spin. A rotation on a vector field, will affect both its location, as well
 88 as it's orientation [4]. This means the Lorentz invariant equation of motion describring a scalar
 89 field will have a different form than equations of motion for a field with spin. The most relevant
 90 equations describe the particles of SM, which contain spins of 0, 1/2, and 1. They are described
 91 by the Klein-Gordan, Dirac, and Proca equations respectively.

92

Klein-Gordon equation, for scalar (spin 0) fields

$$(\partial^2 + m^2)\phi = 0 \quad (2.1)$$

Dirac equation, for spinor (spin 1/2) fields

$$(i\gamma^\mu \partial_\mu - m)\psi = 0 \quad (2.2)$$

Proca equation, for vector (spin 1) fields

$$\partial_\mu(\partial^\mu A^\nu - \partial^\nu A^\mu) + m^2 A^\nu = 0 \quad (2.3)$$

93 With these equations, one can build a theory of free particles. The Lagrangian formulation is
 94 the most appropriate since all expressions are explicitly Lorentz invariant [4]. The Lagrangians
 95 for the Klein-Gordon, Dirac, and Proca equations are given as:

96

Klein-Gordon Lagrangian, for real and complex scalar fields

$$\begin{aligned} \mathcal{L} &= \partial_\mu \partial^\mu \phi^2 - \frac{1}{2} m^2 \phi^2 \\ \mathcal{L} &= (\partial_\mu \phi)^*(\partial^\mu \phi) - m^2 (\phi)^*(\phi) \end{aligned} \quad (2.4)$$

Dirac Lagrangian, for spinor fields

$$\mathcal{L} = i\bar{\psi} \gamma^\mu \partial_\mu \psi - m\bar{\psi} \psi \quad (2.5)$$

Proca Lagrangian, for vector fields

$$\mathcal{L} = -\frac{1}{4} F_{\mu\nu} F^{\mu\nu} + m^2 A^\nu A_\nu \quad (2.6)$$

97 where $F_{\mu\nu}$, is the field strength tensor, defined as $F_{\mu\nu} = \partial_\mu A_\nu - \partial_\nu A_\mu$

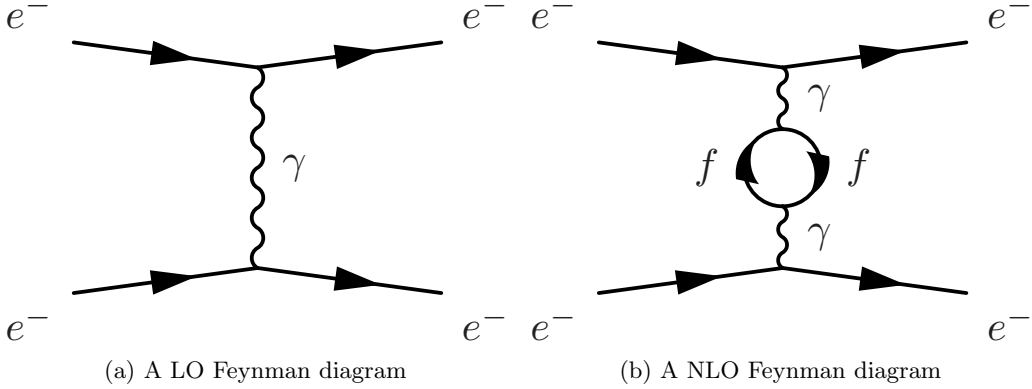


Figure 2.1: Leading and Next to Leading Order Feynman diagrams for the coulomb scattering process

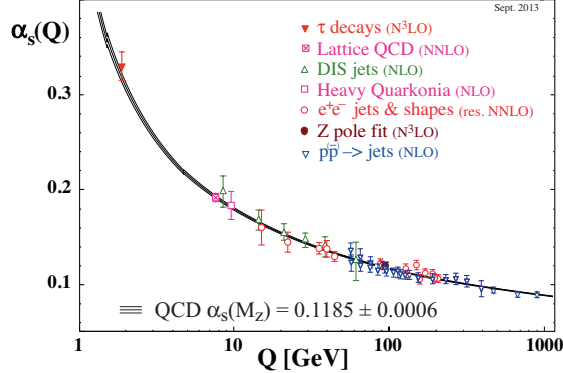
98 Interactions are generated by coupling multiple fields together in a single term, such as
 99 $i e A_\mu \bar{\psi} \psi$ and treating it as a perturbation to the free field theory. This implies every interaction
 100 between particles is carried out by a virtual mediating particle. When two electrons scatter off
 101 one another, they are really exchanging a virtual photon, the mediator of the electromagnetic
 102 force. The W^\pm and Z bosons mediate the weak force, while the *gluons* mediate the strong force.

$$\mathcal{L} = \mathcal{L}_{Free} + \mathcal{L}_{Interacting} \quad (2.7)$$

103 In order to calculate the probability and dynamics of two particles interacting with one
 104 another, an integral, constrained by energy and momentum conservation, over the phase space
 105 of outgoing particles and the scattering amplitude, \mathcal{M} , is evaluated. The scattering amplitude is
 106 calculated by using the propagator (Green's function of the free particle theory) for the incoming,
 107 mediating, and outgoing particles, with an appropriate weighting function, or vertex factor,
 108 for each point the particles interact in the scattering process, and then integrating over the
 109 momentum of the mediating particle. Richard Feynmann developed a set of rules for the writing
 110 down the propagators and vertex factors directly from the Lagrangian, and easily computing the
 111 scattering amplitude. He also introduced an elegant pictographic notation useful for visualizing
 112 particle interactions, known as Feynmann diagrams.

113 With these tools, one can calculate the probability amplitudes of a given process occurring
 114 to Leading Order (LO) without any difficulties. However, when calculations in Next to Leading
 115 Order (NLO) are performed, and loop diagrams of virtual particles are considered, the probability
 116 amplitudes associated with a given process diverge to infinity. This occurs when one integrates
 117 over all of the possible momentum allowed by intermediate, loops of virtual particles, which due
 118 to Heisenberg's uncertainty principle, are allowed to take on any value of momentum. Figure
 119 2.1 shows an example of a LO and NLO process.

120 The systematic removal of divergences from a theory is called renormalization. The di-

Figure 2.2: The global average of α_s , the QCD coupling constant.

vergences are absorbed into the definitions of the free parameters of the theory, making the parameters a function of the energy scale the process occurs at, instead of a constant. This allows for the calculations of fundamental processes to completed, as long as the energy scale of the interaction is known. A modern interpretation of renormalization was provided by Kenneth Wilson [5] [6]. Instead of seeing the effects of high momentum calculations after moving to NLO in perturbation theory, one uses an effective Lagrangian, computed by integrating out shells of momentum beginning at the energy cutoff of the theory, where the NLO effects begin the dominate. The dimensions of integration are then rescaled and the result of evaluating the integral over the momentum shell is absorbed into the definition of free parameters. The processes is iterated until the energy scale of the interaction is reached. The functional dependence of the parameters is then directly present in the resulting effective Lagrangian, instead of appearing suddenly when accounting for the one-loop contributions at NLO. Regardless of how strange this procedure seem, the running of the coupling constant as a function of interaction engergy has been validated experimentally time and time and again, as shown in Figure 2.2 [7].

2.2 Abelian Gauge Theories of Particle Interactions

In 1930, Herman Weyl introduced the idea that the interactions between fields can be generated by requiring them to be invariant under guage tansformations of a local symmetry [8]. For electromagnetism, the local symmetry is that of the Lie group, $U(1)$. It is an abelian group, which has the property that the generators of the group symmetry commutes with themselves. The $U(1)$ symmetry is invariant under phase rotations. By requiring local guage invariance, the Lagrangian must be unchanged under the

$$\psi(x) \rightarrow e^{i\alpha(x)}\psi(x). \quad (2.8)$$

¹⁴² Consider the Lagrangian for a free spin 1/2 particle:

$$\mathcal{L} = \bar{\psi}(i\gamma^\mu \partial_\mu - m)\psi \quad (2.9)$$

¹⁴³ The first term in the Lagrangian, involving the derivative, acts on $\alpha(x)$, creating a new term in
¹⁴⁴ the Lagrangian, breaking its invariance under the local phase transformation.

$$\mathcal{L} \rightarrow \mathcal{L} - (\partial_\mu \alpha) \bar{\psi} \gamma^\mu \psi \quad (2.10)$$

¹⁴⁵ Thus, a new term must be added to the original Lagrangian to cancel out the term arising from
¹⁴⁶ the local phase transformation. This is achieved by defining the covariant derivative:

$$D_\mu = \partial_\mu + ieA_\mu \quad (2.11)$$

¹⁴⁷ where A_μ is a new vector field that transforms as follows:

$$A_\mu(x) \rightarrow A_\mu(x) - \frac{1}{e}\partial_\mu \alpha(x) \quad (2.12)$$

¹⁴⁸ The covariant derivative thus transforms like

$$\begin{aligned} D_\mu \psi(x) &\rightarrow [\partial_\mu + ie(A_\mu - \frac{1}{e}\partial_\mu \alpha)] e^{i\alpha(x)} D_\mu \psi(x) \\ &= e^{i\alpha(x)} [\partial_\mu + ie(A_\mu - \frac{1}{e}\partial_\mu \alpha + \frac{1}{e}\partial_\mu \alpha)] D_\mu \psi(x) \\ &= e^{i\alpha(x)} (\partial_\mu + ieA_\mu) \psi(x) \\ &= e^{i\alpha(x)} D_\mu \psi(x) \end{aligned} \quad (2.13)$$

¹⁴⁹ This covariant derivative transforms in the same way that $\psi(x)$ does, and the new locally gauge
¹⁵⁰ invariant Lagrangian becomes

$$\begin{aligned} \mathcal{L} &= \bar{\psi}(i\gamma^\mu D_\mu - m)\psi - \frac{1}{4}F^{\mu\nu}F_{\mu\nu} \\ &= i\bar{\psi}\gamma^\mu \partial_\mu \psi - \bar{\psi}\gamma^\mu \psi A_{\mu\nu} - m\bar{\psi}\psi - \frac{1}{4}F^{\mu\nu}F_{\mu\nu} \end{aligned} \quad (2.14)$$

¹⁵¹ where

$$F^{\mu\nu} = (\partial^\mu A^\nu - \partial^\nu A^\mu) \quad (2.15)$$

¹⁵² and $\frac{1}{4}F^{\mu\nu}F_{\mu\nu}$ is the kinetic energy term of the Proca equation for the new vector field.

¹⁵³ This new Lagrangian is identical to the QED Lagrangian, except it was derived beginning
¹⁵⁴ with a free Dirac theory and requiring the field to be locally gauge invariant under $U(1)$ transfor-
¹⁵⁵ mations. This necessitated the introduction of a new vector field, A_μ , as well as an interaction

¹⁵⁶ term with it. This implies that the electromagnetic force can be represented by the requirement
¹⁵⁷ of local $U(1)$ symmetry on a free Dirac particle.

¹⁵⁸ It should be noted, that if the photon had mass, an additional term from the Proca equation
¹⁵⁹ would have to be added to the Lagrangian, $m^2 A_\mu A^\mu$. This term complicates the picture since
¹⁶⁰ it is not invariant under local phase transformations, and cannot be compensated for through a
¹⁶¹ different choice of A_μ . This implies that the bosons of a gauge theory must be massless in order
¹⁶² to preserve local gauge invariance.

¹⁶³ 2.3 Non-Abelian Gauge Theories of Particle Interactions

¹⁶⁴ In 1954, Yang and Mills worked to extend this idea to symmetries of different gauge groups [9].
¹⁶⁵ Their most important accomplishment was developing this procedure for non-abelian groups.
¹⁶⁶ These are groups, where the transformation does not involve a simple variable $\alpha(x)$, but rather an
¹⁶⁷ entire matrix of dimension $n > 2$. These matrices do not commute with each other, and their work
¹⁶⁸ developed the procedure for applying local gauge invariance described above to the more complex,
¹⁶⁹ higher dimensional symmetries, such as $SU(2)$ and $SU(3)$. Consider the case of $SU(2)$ symmetry.
¹⁷⁰ The theory is appropriate for describing the dynamics of two fermion fields, represented as a
¹⁷¹ doublet:

$$\psi = \begin{pmatrix} \psi_1(x) \\ \psi_2(x) \end{pmatrix} \quad (2.16)$$

¹⁷² this will transform under the $SU(2)$ transformation as a two-component spinor:

$$\psi \rightarrow \exp\left(i\alpha^i \frac{\sigma_i}{2}\right) \psi \quad (2.17)$$

¹⁷³ where σ^i are the Pauli matrices:

$$\sigma^1 = \begin{pmatrix} 0 & 1 \\ 1 & 0 \end{pmatrix}, \sigma^2 = \begin{pmatrix} 0 & -i \\ i & 0 \end{pmatrix}, \sigma^3 = \begin{pmatrix} 1 & 0 \\ 0 & -1 \end{pmatrix} \quad (2.18)$$

¹⁷⁴ and have the commutation relation defined by:

$$\left[\frac{\sigma^i}{2}, \frac{\sigma^j}{2} \right] = i\epsilon^{ijk} \frac{\sigma^k}{2} \quad (2.19)$$

¹⁷⁵ Similar to the case of the $U(1)$ Abelian symmetry, in order to form a lagrangian that is locally
¹⁷⁶ gauge invariant, three vector fields, A_μ^i , $i = 1, 2, 3$, are introduced, and coupled to ψ through the
¹⁷⁷ covariant derivative:

$$D_\mu = (\partial_\mu - igA_\mu^i \frac{\sigma^i}{2}) \quad (2.20)$$

¹⁷⁸ to ensure that the derivative covaries with the transformation, the fields, A_μ^i will transform like:

$$A_\mu^i \frac{\sigma^i}{2} \rightarrow A_\mu^i \frac{\sigma^i}{2} + \frac{1}{g}(\partial_\mu \alpha^i) \frac{\sigma^i}{2} + i \left[\frac{\alpha^i \sigma^i}{2}, A_\mu^i \frac{\sigma^i}{2} \right] \quad (2.21)$$

¹⁷⁹ The third term, which was absent from the abelian form of the transformation, is necessary to
¹⁸⁰ account for the non-commutation of the pauli matrices. This non-communtation also changes
¹⁸¹ the form of the field strength tensor, $F_{\mu\nu}^i$:

$$F_{\mu\nu}^i = \partial_\mu A_\nu^i - \partial_\nu A_\mu^i + g\epsilon^{ijk} A_\mu^j A_\nu^k \quad (2.22)$$

¹⁸² The entire $SU(2)$ invariant Lagrangian can then be written as:

$$\begin{aligned} \mathcal{L}_{Yang-Mills} &= -\frac{1}{4}F_{\mu\nu}^i F^{i\mu\nu} + \bar{\psi}(i\gamma^\mu D_\mu)\psi \\ &= -\frac{1}{4}F_{\mu\nu}^i F^{i\mu\nu} + \bar{\psi}(i\gamma^\mu \partial_\mu - igA_\mu^i \frac{\sigma^i}{2})\psi \end{aligned} \quad (2.23)$$

¹⁸³ This procedure generalizes to any continuous group of symmetries. The basic steps involve
¹⁸⁴ idenitifying the generators of the transformation:

$$\psi(x) \rightarrow e^{i\alpha^a t^a} \psi \quad (2.24)$$

¹⁸⁵ where t^a are a set of matrices with the commutation relationship:

$$[t^a, t^b] = if^{abc}t^c \quad (2.25)$$

¹⁸⁶ where f^{abc} is the structure constant for the goup. The covariant derivative is then defined as:

$$D_\mu = \partial_\mu - igA_\mu^a t^a \quad (2.26)$$

¹⁸⁷ where the fields, A_μ^a , transform like:

$$A_\mu^a \rightarrow A_\mu^a + \frac{1}{g}\partial_\mu \alpha^a + f^{abc}A_\mu^b \alpha^c \quad (2.27)$$

¹⁸⁸ the field strength tensor is then formed as:

$$F_{\mu\nu}^a = \partial_\mu A_\nu^a - \partial_\nu A_\mu^a + f^{abc} A_\mu^b A_\nu^c \quad (2.28)$$

¹⁸⁹ and finally, the locally, gauge invariant Lagrangian will have the form:

$$\begin{aligned}\mathcal{L}_{\text{General, non-Abelian}} &= -\frac{1}{4}F_{\mu\nu}^a F^{a\mu\nu} + \bar{\psi}(i\gamma^\mu D_\mu)\psi \\ &= -\frac{1}{4}F_{\mu\nu}^a F^{a\mu\nu} + \bar{\psi}(i\gamma^\mu \partial_\mu - igA_\mu^a t^a)\psi\end{aligned}\quad (2.29)$$

190 In 1964, Murray Gell-Mann and Zweig independently developed a model of hadron interactions,
 191 that described the spectrum of baryons and mesons in terms of combinations of fundamental
 192 particles, which Gell-Mann named quarks [10] [11] [12]. In their model, three quarks: u, d, s
 193 formed an $SU(3)$ flavor symmetry. However, this did not explain the appearance of only two and
 194 three quark combinations, the mesons and baryons. It also could not explain the spin statistics
 195 of the baryons. The Δ^{++} , Δ^- , and Ω^- , particles all have uuu , ddd , sss quark combinations,
 196 respectively, with their spins aligned. That is to say, these baryons seem to violate the Pauli-
 197 exclusion principle since all three quarks seem to occupy the same quantum state simultaneously.

198 In 1964, O.W. Greenberg solved this problem by proposing that quarks also have an additional
 199 quantum number, *color*, that come in three types: red, green, blue [13]. The requirement that
 200 all stable hadrons be color neutral: either possessing equal amounts of all three colors in qqq
 201 combinations, or a $q\bar{q}$ pair sharing the same color, also explained the observation of only 2 and
 202 3 quark combinations in experiments. These three colors form an $SU(3)$ symmetry, and is the
 203 gauge symmetry describing the interactions of quarks and leptons. This theory is known as
 204 Quantum Chromodynamics (QCD). Its derivation follows from the procedure outlined above.
 205 This group has eight generators, known as the Gell-Mann matrices, and are defined as:

$$\begin{aligned}t^1 &= \frac{1}{2} \begin{pmatrix} 0 & 1 & 0 \\ 1 & 0 & 0 \\ 0 & 0 & 0 \end{pmatrix}, \quad t^2 = \frac{1}{2} \begin{pmatrix} 0 & -i & 0 \\ i & 0 & 0 \\ 0 & 0 & 0 \end{pmatrix}, \quad t^3 = \frac{1}{2} \begin{pmatrix} 1 & 0 & 0 \\ 0 & -1 & 0 \\ 0 & 0 & 0 \end{pmatrix} \\ t^4 &= \frac{1}{2} \begin{pmatrix} 0 & 0 & 1 \\ 0 & 0 & 0 \\ 1 & 0 & 0 \end{pmatrix}, \quad t^5 = \frac{1}{2} \begin{pmatrix} 0 & 0 & -i \\ 0 & 0 & 0 \\ i & 0 & 0 \end{pmatrix} \\ , \quad t^6 &= \frac{1}{2} \begin{pmatrix} 0 & 0 & 0 \\ 0 & 0 & 1 \\ 0 & 1 & 0 \end{pmatrix}, \quad t^7 = \frac{1}{2} \begin{pmatrix} 0 & 0 & 0 \\ 0 & 0 & -i \\ 0 & -i & 0 \end{pmatrix}, \quad t^8 = \frac{1}{2\sqrt{3}} \begin{pmatrix} 1 & 0 & 0 \\ 0 & 1 & 0 \\ 0 & 0 & -2 \end{pmatrix}\end{aligned}\quad (2.30)$$

206 and a Lagrangian defined as:

$$\begin{aligned}\mathcal{L}_{QCD} &= -\frac{1}{4}G_{\mu\nu}^a G^{a\mu\nu} + \bar{\psi}(i\gamma^\mu D_\mu)\psi \\ &= -\frac{1}{4}G_{\mu\nu}^a G^{a\mu\nu} + \bar{\psi}(i\gamma^\mu \partial_\mu - igA_\mu^a t^a)\psi\end{aligned}\quad (2.31)$$

207 where t^a are the Gell-Mann matrices defined in equation 2.30 and the fields A_μ^a are the eight
 208 mediators of the QCD force, the *gluons*.

209 Like all non-abelian guage theories, it is asymptotically free. Thus, the strength of the cou-
 210 pling constant, α_s , decreases as the momentum-transfer, Q in interaction increases. This allows
 211 the use of perturbation theory for high-momentum calculations, therefore allowing calculations
 212 of hadronic-processes for experimental evaluation.

The idea of local gauge invariance was successful in describing the dynamics of QED and QCD, which only contain massless gauge bosons. Theorists had long postulated that the weak force was so weak because it was being facilitated by massive bosons, but adding a mass term for a boson breaks the local gauge invariance. So, a tool was needed to reconcile the concept of local gauge invariance, which works so well for the other forces, with the prospect of the weak force being facilitated by massive gauge bosons.

2.4 The Higgs Mechanism in an Abelian Theory

In 1964 Peter Higgs introduced the idea that the gauge bosons can acquire their mass through the breaking of an underlying symmetry [14]. In other words, the natural symmetry of the Lagrangian describing a particular interaction could be different than the symmetry we observe in nature. Consider an abelian example of complex scalar field theory, coupled to itself and to an electromagnetic field [4].

$$\mathcal{L} = -\frac{1}{4}(F_{\mu\nu})^2 + |D_\mu\phi|^2 - V(\phi) \quad (2.32)$$

where $D_\mu = \partial_\mu + ieA_\mu$, is the familiar covariant derivative, and the Lagrangian is invariant under the $U(1)$ transformation as described earlier. The potential term, $V(\phi)$ has the form

$$V(\phi) = -\mu^2\phi^*\phi + \frac{\lambda}{2}(\phi^*\phi)^2 \quad (2.33)$$

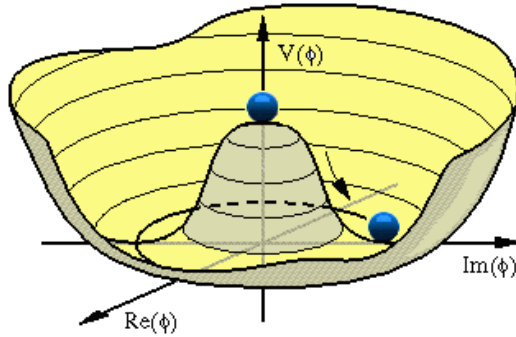


Figure 2.3: A visual representation of the Higgs potential

if $\mu^2 > 0$ the shape of the potential no longer has a minimum at $\langle\phi\rangle = 0$. Figure 2.3 shows a plot of the potential energy of ϕ in terms of each of its components. The new minimum potential energy occurs at:

$$\langle\phi\rangle = \phi_0 = \left(\frac{\mu^2}{\lambda}\right)^{1/2} \quad (2.34)$$

and while the field has a ground state at the zero potential point it is in an unstable equilibrium. Any quantum fluctuation about this point will take the field into the lower energy configuration with a ground state about the new minimum. When the Langrangian is expanded about 2.34, the field, ϕ is rewritten as:

$$\phi(x) = \phi_0 + \frac{1}{\sqrt{2}}(\phi_1(x) + i\phi_2(x)) \quad (2.35)$$

the potential term, $V(x)$, then becomes:

$$V(x) = -\frac{1}{2\lambda}\mu^4 + \frac{1}{2} \cdot 2\mu^2\phi_1^2 + \mathcal{O}(\phi_i^3) \quad (2.36)$$

where we can notice that ϕ_1 has acquired a mass term with, $m = \sqrt{2}\mu$, while the scalar field ϕ_2 remains massless, and is known as the Goldstone boson. The covariant derivative is also transformed as:

$$|D_\mu\phi|^2 = \frac{1}{2}(\partial_\mu\phi_1)^2 + \frac{1}{2}(\partial_\mu\phi_2)^2 + \sqrt{2}e\phi_0 \cdot A_\mu\partial^\mu\phi_2 + e^2\phi_0^2A_\mu A^\mu + \dots \quad (2.37)$$

where cubic and quartic terms of A_μ , ϕ_1 , and ϕ_2 have been dropped. The important term is the last one, which can be interpreted as a mass term of the vector field, A_μ

$$\Delta\mathcal{L}_M = \frac{1}{2}m_A A_\mu A^\mu = e^2\phi_0^2 A_\mu A^\mu \quad (2.38)$$

where $m_A = 2e^2\phi_0^2$, has arisen from consequences of a non-zero vacuum expectation value of the ϕ field. The remaining, massless Godlstone boson, ϕ_2 is not a physical particle, but rather a consequence of the choice of guage. This is illustrated when we can use the $U(1)$ guage symmetry to rotate the field $\phi(x)$ such that the field disappears.

$$\begin{aligned} \phi &\rightarrow \phi' = e^{i\alpha}(\phi_1 + \phi_2) \\ &= (\cos\alpha + i\sin\alpha)(\phi_1 + \phi_2) \\ &= (\phi_1 \cos\alpha - \phi_2 \sin\alpha) + i(\phi_1 \sin\alpha + \phi_2 \cos\alpha) \\ &= (\phi_1 - \phi_2 \tan\alpha) + i(\phi_1 \tan\alpha + \phi_2) \end{aligned} \quad (2.39)$$

Choosing $\alpha = -\tan\phi_2/\phi_1$ will make ϕ' a real quantity and elminate it's imaginary component, ϕ'_2 . The lagrangian can then be rewritten in terms of the rotated field ϕ' and see that massless boson is indeed removed from the theory.

$$\begin{aligned}\mathcal{L} = & \frac{1}{2}(\partial_\mu\phi'_1)(\partial^\mu\phi'_1) - \frac{1}{2} \cdot 2\mu^2\phi'_1\phi'_1 \\ & - \frac{1}{4}(F^{\mu\nu}F_{\mu\nu}) + \frac{1}{2} \cdot e^2\phi_0^2A_\mu A^\nu \\ & + \phi_0e^2\phi'_1A_\mu A^\mu + \frac{1}{2}e^2\phi'^2A_\mu A^\mu + \mathcal{O}(\phi'^3)\dots\end{aligned}\quad (2.40)$$

247 The degree of freedom that ϕ_2 represents, is absorbed as a longitudinal polarization of the
248 A_{mu} field, a forbidden for massless gauge bosons, but necessary for massive bosons.

249 For this case of an abelian symmetry $U(1)$, it was shown that if a complex scalar field, which
250 interacts with itself and another vector field, can gain a non-zero vacuum expectation value.
251 The Lagrangian can be expanded about this new minimum, generating a mass term for the
252 vector field. One of the degrees of freedom of the original complex scalar field is then absorbed
253 as a longitudinal polarization state of the massive vector field.

254 2.5 The Higgs Mechanism in a non-Abelian Theory

255 Before describing the electroweak gauge theory of $SU(2) \otimes U(1)$, it will be helpful to see the effects
256 of the Higgs mechanism for the non-Abelian group, $SU(2)$ by itself. Consider an example
257 of an $SU(2)$ gauge field coupled to a scalar field that transforms like a real-valued vector under
258 $SU(2)$ transformations [4]. The field ϕ will have the form:

$$\phi = \begin{pmatrix} \phi_1 \\ \phi_2 \\ \phi_3 \end{pmatrix} \quad (2.41)$$

259 where the components, ϕ_i are real-valued fields. The $SU(2)$ transformation for this scalar field
260 will also look like:

$$\phi \rightarrow e^{i\alpha^i T^i} \phi \quad (2.42)$$

261 where the matrices, T^i are defined as:

$$iT^1 = \begin{pmatrix} 0 & 0 & 0 \\ 0 & 0 & 1 \\ 0 & -1 & 0 \end{pmatrix}, \quad T^2 = \begin{pmatrix} 0 & 0 & -1 \\ 0 & 0 & 0 \\ 1 & 0 & 0 \end{pmatrix}, \quad T^3 = \begin{pmatrix} 0 & 1 & 0 \\ -1 & 0 & 0 \\ 0 & 0 & 0 \end{pmatrix} \quad (2.43)$$

262 The Lagrangian for this field will feature a Higgs potential term along with the previously
263 mentioned $SU(2)$ gauge fields, A_μ^a coupled to the scalar field, ϕ , and is given by:

$$\mathcal{L} = -\frac{1}{4}F_{\mu\nu}^a F^{a\mu\nu} + |D_\mu\phi|^2 + \mu^2\phi^*\phi - \frac{\lambda}{4}(\phi^*\phi)^2 \quad (2.44)$$

264 where $F_{\mu\nu}^a$, the field strength tensor is defined as:

$$F_{\mu\nu}^a = (\partial_\mu A_\nu^a - \partial_\nu A_\mu^a) + g\epsilon^{abc} A_\mu^b A_\nu^c \quad (2.45)$$

265 and the covariant derivative is defined as:

$$D_\mu = (\partial_\mu + igA_\mu^a T^a)\phi \quad (2.46)$$

266 Similarly to the Abelian case, the Higgs potential will induce a spontaneous symmetry breaking,
267 and one of the components of the field ϕ will gain a vacuum expectation value. After this
268 breaking and expanding around the ground state potential, the field ϕ will have the form:

$$\phi = \frac{1}{\sqrt{2}} \begin{pmatrix} 0 \\ 0 \\ v+h \end{pmatrix} \quad (2.47)$$

269 There has been no loss in generality in assuming this form since, similarly to the abelian case,
270 we can use the gauge symmetry of $SU(2)$ to rotate the field into this configuration. Goldstone's
271 theorem tells us that we should expect two massive gague bosons corresponding to the T^1 , and
272 T^2 generators, while the T^3 generator will correspond to a massless gauge boson, since ϕ is still
273 invariant under T^3 transformations.

274 As in the Abelian case, the mass terms for the gauge bosons are generated from the covariant
275 derivative term, $|D_\mu\phi|^2$

$$\begin{aligned} D_\mu\phi &= \frac{1}{\sqrt{2}} \left(\partial_\mu + gA_\mu^1 \begin{pmatrix} 0 & 0 & 0 \\ 0 & 0 & 1 \\ 0 & -1 & 0 \end{pmatrix} + gA_\mu^2 \begin{pmatrix} 0 & 0 & -1 \\ 0 & 0 & 0 \\ 1 & 0 & 0 \end{pmatrix} + gA_\mu^3 \begin{pmatrix} 0 & 1 & 0 \\ -1 & 0 & 0 \\ 0 & 0 & 0 \end{pmatrix} \right) \begin{pmatrix} 0 \\ 0 \\ v+h \end{pmatrix} \\ &= \frac{1}{\sqrt{2}} \begin{pmatrix} 0 \\ 0 \\ \partial_\mu \end{pmatrix} + \frac{gA_\mu^1}{\sqrt{2}} \begin{pmatrix} 0 \\ v+h \\ 0 \end{pmatrix} - \frac{gA_\mu^2}{\sqrt{2}} \begin{pmatrix} v+h \\ 0 \\ 0 \end{pmatrix} \\ &= \frac{1}{\sqrt{2}} \begin{pmatrix} g(v+h)A_\mu^1 \\ g(v+h)A_\mu^2 \\ \partial_\mu h \end{pmatrix} \end{aligned} \quad (2.48)$$

276 Therefore

$$|D_\mu \phi|^2 = \frac{1}{2} \partial_\mu h \partial^\mu h + \frac{g^2 v^2}{2} ((A_\mu^1)^2 + (A_\mu^2)^2) + \frac{g^2}{2} (h^2 + 2hv) ((A_\mu^1)^2 + (A_\mu^2)^2) \quad (2.49)$$

This theory produces two massive bosons, A_μ^1 and A_μ^2 , both with mass, $m_A = gv$. These fields have h , and h^2 couplings to the Higgs boson. The third gauge field, A_μ^3 , remains massless and is not coupled to the Higgs field. This model is beginning to resemble a description of electroweak physics, however, a third massive boson is necessary, as is a new gauge symmetry in order to generate it. That is the subject of the next section.

2.6 Glashow Weinberg Salam Theory

Glashow, Weinberg, and Salam published their theory unifying electromagnetic and weak forces in the 1960s [15] [16] [17]. It begins with the requirement of a $SU(2)_L \otimes U(1)$ symmetry and incorporates the Higgs mechanism to give mass to the gauge bosons of the weak force. As described earlier, the $U(1)$ symmetry requires introducing a vector field, which will be labeled B_μ , and an interaction term, which is absorbed into the covariant derivative, D_μ . The transformation will also be parameterized with a with a quantum number, Y , known as hypercharge. The $SU(2)$ symmetry requires the introduction of three new vector fields, which will be labeled $W_\mu^i, i = 1, 2, 3$. The quantum number associated with this gauge group is known as isospin, and is determined by the T^3 operator, acting on an $SU(2)$ doublet on the third generator of the group. The $SU(2) \otimes U(1)$ transformation, $U(x)$, will then be given by:

$$U(x) = e^{i\alpha^a(x)\tau^a} e^{iY\alpha(x)} \quad (2.50)$$

where $\tau^a = \sigma^a/2$, the Pauli matrices, 2.18. These gauge fields will be coupled, via the covariant derivative, to a doublet of complex scalar fields ϕ , with hypercharge $Y = +1/2$. A Higgs potential will be added to generate the spontaneous symmetry breaking that will give mass to three of the gauge fields, and leave one massless. In order to preserve the $SU(2)_L \otimes U(1)$ symmetry, the new covariant derivative will take the form:

$$D_\mu = (\partial_\mu - igW_\mu^a \tau^a - \frac{i}{2}g'B_\mu) \quad (2.51)$$

The subscript L on $SU(2)_L$ refers to the experimental results that the weak force violates parity maximally, by only interacting with the left-handed chiral component of a field. Right versus left chirality is determined by whether the spin of a particle is aligned or anti-aligned with its direction of motion, and in general a particle is represented by a linear combination

of its right and left handed components. This idea was first proposed by Chen Ning Yang and Tsung-Dao Lee, in the 1950s. Their ideas were validated by the experimental discovery of parity violation in 1957, through the beta decays of Cobalt 60 atoms by C.S Wu. That same year, Yang and Lee were awarded the nobel prize for their insight [18]. In this model, then, the left-handed components of the particles participate in the weak interaction and are formed into doublets, while the right handed components are singlets, and will only interact with the electromagnetic field, B_μ . The quantum numbers of the doublet will be given by +1/2 for the upper component of the $SU(2)$ doublet, and -1/2 for the lower component. The fermion content of this theory is then given by:

$$\begin{pmatrix} \nu_L \\ e_L \end{pmatrix}, e_R \quad \begin{pmatrix} u_L \\ d_L \end{pmatrix}, u_R, d_R \quad (2.52)$$

where the right handed neutrino, ν_R has been omitted, since it has zero charge, and isospin, and therefore does not participate in any of the interactions of this theory. The complete Lagrangian is given by a sum of free particle terms for massless bosons, fermions, and Higgs scalar fields; the Higgs potential; and a Yukawa coupling term between the fermions and the Higgs, which generates their masses.

$$\mathcal{L}_{GWS} = \mathcal{L}_{BosonKE} + \mathcal{L}_{Higgs} + \mathcal{L}_{FermionKE} + \mathcal{L}_{Yukawa} \quad (2.53)$$

The Higgs potential will have the form:

$$\mathcal{L}_{Higgs} = (D_\mu \phi)^\dagger (D^\mu \phi) + \mu^2 \phi^\dagger \phi - \lambda (\phi^\dagger \phi)^2 \quad (2.54)$$

The Higgs potential will break the symmetry of the Lagrangian when one of the four degrees of freedom in the complex scalar doublet, ϕ , spontaneously acquires a vacuum expectation value. In this case, it will generate three massive gauge bosons, one massless gauge boson, and a massive scalar field. After gaining a vacuum expectation value, and expanding about this value, the scalar fields will have the form:

$$\langle \phi \rangle = \frac{1}{\sqrt{2}} \begin{pmatrix} 0 \\ v + h \end{pmatrix} \quad (2.55)$$

where no loss of generality has occurred since we are always able to rotate into this form through the appropriate gauge transformations, similar to what was described in the Abelian case. It should also be noted that this form is not invariant to any of the individual generators t^a , however ϕ will be invariant to a combination of $T^3 + Y$ generators. Per Goldstone's theorem, we

should expect this linear combination of fields to be the massless vector boson after symmetry breaking. The massless eigenstate will be the electromagnetic field, $A_\mu \sim A_\mu^3 + B_\mu$. The electric charge quantum number, Q , is then defined as

$$Q = T^3 + Y \quad (2.56)$$

³²¹ As before, the generation of the masses for the gauge bosons are generated by the interaction
³²² of their fields with the Higgs field via the covariant derivative.

$$\begin{aligned} D_\mu \phi &= \frac{1}{\sqrt{2}} \left(\partial_\mu - \frac{ig}{2} A_\mu^1 \begin{pmatrix} 0 & 1 \\ 1 & 0 \end{pmatrix} - \frac{ig}{2} A_\mu^2 \begin{pmatrix} 0 & -i \\ i & 0 \end{pmatrix} - \frac{ig}{2} A_\mu^3 \begin{pmatrix} 1 & 0 \\ 0 & -1 \end{pmatrix} \right) \begin{pmatrix} 0 \\ v+h \end{pmatrix} \\ &= \frac{1}{\sqrt{2}} \left(\partial_\mu + i(\frac{1}{2}(v+h)(gA_\mu^3 - g'B_\mu)) \right) \end{aligned} \quad (2.57)$$

³²³ Taking the dot product of this with its hermitian conjugate gives the $|D_\mu \phi|^2$ term:

$$\begin{aligned} |D_\mu \phi|^2 &= \frac{1}{2} \partial_\mu h \partial^\mu h + \frac{1}{2} \frac{g^2 v^2}{4} ((A_\mu^1)^2 + (A_\mu^2)^2) + \frac{v^2}{4} (gA_\mu^3 - g'B_\mu)^2 \\ &\quad + \frac{1}{2} g^2 4(h^2 + 2vh)((A_\mu^1)^2 + (A_\mu^2)^2) + \frac{1}{2} \frac{1}{4}(h^2 + 2vh)(gA_\mu^3 - g'B_\mu) \end{aligned} \quad (2.58)$$

³²⁴ From equation 2.58 we can identify three massive and one massless gauge bosons, corresponding
³²⁵ to the charged and neutral weak currents, and the electromagnetic current.

$$\begin{aligned} W_\mu^\pm &= \frac{1}{\sqrt{2}} (A_\mu^1 \mp iA_\mu^2) && \text{with mass } m_W = g \frac{v}{2}; \\ Z_\mu^0 &= \frac{1}{\sqrt{g^2 + g'^2}} (gW_\mu^3 - g'B_\mu) && \text{with mass } m_Z = \frac{v}{2} \sqrt{g^2 + g'^2}; \\ A_\mu &= \frac{1}{\sqrt{g^2 + g'^2}} (gW_\mu^3 + g'B_\mu) && \text{with mass } m_A = 0; \end{aligned} \quad (2.59)$$

³²⁶ where the last field, A_μ is absent from the covariant derivative term, but already identified as
³²⁷ the massless gauge boson of the theory due to its gauge invariance under a $T^3 + Y$ rotation.
³²⁸ Using these definitions the covariant derivative has the following form:

$$\begin{aligned} D_\mu &= \partial_\mu - \frac{ig}{\sqrt{2}} (W^+ T^+ + W^- T^-) \\ &\quad - \frac{i}{\sqrt{g^2 + g'^2}} Z_\mu^0 (gT^3 - g'Y) - \frac{gg'}{\sqrt{g^2 + g'^2}} A_\mu (T^3 + Y) \end{aligned} \quad (2.60)$$

³²⁹ where $T^\pm = \frac{1}{2}(\sigma^1 \pm \sigma^2)$. From this form, we can identify the fundamental electric charge, e , as

$$e = \frac{gg'}{\sqrt{g^2 + g'^2}} \quad (2.61)$$

³³⁰ The similarity in the forms between Z_μ^0 and A_μ suggest that their relationship can be ex-
³³¹ pressed in a simpler form, as the rotation of underlying guage fields A_μ^3 and B_μ through the
³³² weak mixing angle, θ_W

$$\begin{pmatrix} Z_\mu^0 \\ A_\mu \end{pmatrix} = \begin{pmatrix} \cos \theta_W & -\sin \theta_W \\ \sin \theta_W & \cos \theta_W \end{pmatrix} \begin{pmatrix} A_\mu^3 \\ B_\mu \end{pmatrix} \quad (2.62)$$

³³³ where $\tan \theta_W = \frac{g'}{g}$. Expanding 2.62, we have the definitions of the Z_μ^0 and A_μ fields in terms of
³³⁴ θ_W

$$\begin{aligned} Z_\mu^0 &= A_\mu^3 \cos \theta_W - B_\mu \sin \theta_W \\ A_\mu &= A_\mu^3 \sin \theta_W + B_\mu \cos \theta_W \end{aligned} \quad (2.63)$$

³³⁵ The weak mixing angle, θ_W , also provides a simple relationship between the W_μ^\pm and Z_μ^0 fields:

$$m_W = m_Z \cos \theta_W \quad (2.64)$$

³³⁶ The covariant derivative, D_μ is also rewritten in terms of the mass eingenstates of the gauge
³³⁷ fields

$$D_\mu = (\partial_\mu - \frac{ig}{\sqrt{2}}(W_\mu^+ + W_\mu^- T^-) - \frac{ig}{\cos \theta_W} Z_\mu^0(T_3 - \sin^2 \theta_W Q) - ieA_\mu Q) \quad (2.65)$$

³³⁸ where $g = e/\cos \theta_W$. The square of the covariant derivative is then written as

$$\begin{aligned} |D_\mu|^2 &= \frac{1}{2}\partial_\mu h \partial^\mu h + \frac{1}{2}m_W^2 W_\mu^+ W^{\mu+} + \frac{1}{2}m_W^2 W_\mu^- W^{\mu-} + \frac{1}{2}m_Z^2 Z_\mu^0 Z^{\mu 0} \\ &\quad + \left(\frac{h^2}{v^2} + \frac{h}{v}\right)\left[\frac{1}{2}m_W^2(W_\mu^+ W^{\mu+} + W_\mu^- W^{\mu-}) + \frac{1}{2}m_Z^2 Z_\mu^0 Z^{\mu 0}\right] \end{aligned} \quad (2.66)$$

³³⁹

³⁴⁰

³⁴¹ With the form of the covariant derivative in place, the fermionic kinematic term of the
³⁴² Lagrangian can be described. As mentioned earlier, the masses of the fermions in the model
³⁴³ will be generated by the Yukawa interaction term with the Higgs, so this term only involves the
³⁴⁴ covariant derivatives acting on the left-handed doublet and right-handed singlet states of this
³⁴⁵ model.

³⁴⁶ The quantum number assignments for the leptons, which are chosen in order to reproduce the
³⁴⁷ known values of their electric charges, are shown in table 2.1. The values of these quantum

	ν_L	e_L	e_R	u_L	d_L	u_R	d_R
Isospin	+1/2	-1/2	0	+1/2	-1/2	0	0
Hypercharge	-1/2	-1/2	-1	+1/6	1/3	2/3	-1/3
Electric Charge	0	-1	-1	2/3	-1/3	2/3	-1/3

Table 2.1: The quantum numbers Isospin and Hypercharge are assigned for each of the $SU(2)$ and $U(1)$ symmetries respectively

numbers enter into the covariant derivative via the Z_μ^0 term of equation 2.65. The fermionic kinetic energy term of the Lagrangian is given by:

$$\begin{aligned} \mathcal{L}_{Fermion} = & \bar{E}_L(i\gamma^\mu D_\mu)E_L + \bar{e}_R(i\gamma^\mu D_\mu)e_R \\ & \bar{Q}_L(i\gamma^\mu D_\mu)Q_L + \bar{u}_R(i\gamma^\mu D_\mu)u_R + \bar{d}_R(i\gamma^\mu D_\mu)d_R \end{aligned} \quad (2.67)$$

Expanding the covariant term for the left-handed electron shows its explicit coupling to the gauge boson fields.

$$\begin{aligned} \mathcal{L}_{E_L} = & \begin{pmatrix} \bar{\nu}_L & \bar{e}_L \end{pmatrix} \left((i\gamma^\mu(\partial_\mu - \frac{ig}{\sqrt{2}}(W_\mu^+T^+ + W_\mu^-T^-) - \frac{ig}{\cos\theta_W}Z_\mu^0(T^3 - \sin^2\theta_W Q) - ieA_\mu Q)) \right) \begin{pmatrix} \nu_L \\ e_L \end{pmatrix} \\ = & \bar{\nu}_L i\gamma^\mu \partial_\mu \nu_L + \bar{e}_L i\gamma^\mu \partial_\mu e_L + \frac{ig}{\sqrt{2}} W_\mu^+ \bar{\nu}_L \gamma^\mu e + \frac{ig}{\sqrt{2}} W_\mu^- \bar{e}_L \gamma^\mu \nu_L \\ & + \frac{ig}{\cos\theta_W} \bar{\nu}_L (1/2) \gamma^\mu \nu_L + \frac{ig}{\cos\theta_W} \bar{e}_L \gamma^\mu (-1/2 + \sin^2\theta_W (+1)) e_L + (ie) \bar{e}_L \gamma^\mu A_\mu (-1) \end{aligned} \quad (2.68)$$

All of the terms will be combined with the final, spontaneously broken GWS Lagranian at the end of this section.

The final term to discuss in the theory, before combing all of the results, is the Yukawa interaction term between the fermion fields and the Higgs. For the electron, this term takes the form:

$$\begin{aligned} \mathcal{L}_{Yukawa} = & -\lambda_e \bar{E}_L \cdot \phi e_R - \lambda_e E_L \cdot \phi \bar{e}_R \\ = & -\frac{\lambda_e}{\sqrt{2}} (v+h)(\bar{e}_L e_R + e_L \bar{e}_R) \\ = & -\frac{\lambda_e v}{\sqrt{2}} (\bar{e}_L e_R + e_L \bar{e}_R) - \frac{\lambda_e}{\sqrt{2}} (\bar{e}_L e_R + e_L \bar{e}_R) h \end{aligned} \quad (2.69)$$

where the mass of the electron is identified as $m_e = \frac{\lambda_e v}{\sqrt{2}}$. In order to generate the masses of the particles, each fermion has its own unique λ value. So while the Higgs mechanism is able to generate the masses in a way that preserves the underlying $SU(2) \otimes U(1)$ symmetry, it does not explain the heirarchy of masses since each λ value is unique to each lepton. The second term in last equation of 2.69 is the coupling of the Higgs particle, h , to the fermions. The coupling is proportional to the mass of the particle. The largest of these is to the top quark,

³⁶³ with $m_t = 73.21 \pm 0.51 \pm 0.71 \text{ GeV}$.

³⁶⁴ The Yukawa coupling for the quarks is necessarily modified when additional quarks besides
³⁶⁵ the u and d are added to the theory. This is because there can be additional coupling terms
³⁶⁶ that mix generations. This occurs when the mass eigenstate of the quarks is not the same as the
³⁶⁷ interaction eigenstate. The modification requires the expansion of the u_L and d_L components
³⁶⁸ into a vector of left handed quarks. If we let

$$u_L^i = (u_L, c_L, t_L), \quad d_L^i = (d_L, s_L, b_L) \quad (2.70)$$

³⁶⁹ represent the up and down-type quarks in the original weak interaction basis, then the vectors,
³⁷⁰ u_L^i and d_L^i , can be defined as the diagonalized basis for the Higgs coupling. They are related
³⁷¹ through a unitary transformation.

$$u_L^i = U_u^{ij} u_L^{j'}, \quad d_L^i = U_d^{ij} d_L^{j'} \quad (2.71)$$

³⁷² The interaction terms with the charged gauge boson currents must then be rewritten as

$$J_W^{\mu+} = \frac{1}{\sqrt{2}} \bar{u}_L^i \gamma^\mu d_L^i = \frac{1}{\sqrt{2}} \bar{u}_L^{i'} \gamma^\mu (U_u^\dagger U_d) d_L^{j'} = \frac{1}{\sqrt{2}} \bar{u}_L^{i'} \gamma^\mu V_{ij} d_L^{j'} \quad (2.72)$$

³⁷³ where V_{ij} is the 3x3 Cabibbo-Kobayashi-Maskawa (CKM) matrix describing the mixing among
³⁷⁴ six quarks [19] [20]. It is an extension of the Glashow-Iliopoulos-Maiani mechanism, which
³⁷⁵ was a 2x2 matrix that predicted the existence of a fourth quark, the charm quark. The GIM
³⁷⁶ mechanism was an attempt to suppress flavor-changing-neutral currents, which occur at LO in
³⁷⁷ a three-quark model, but not in a four-quark model. The CKM matrix, however, was motivated
³⁷⁸ by an attempt to explain CP violation in the weak interaction. At the time of its publication,
³⁷⁹ the bottom and top quarks were not predicted. After these were discovered, they were awarded
³⁸⁰ the nobel prize in physics in 2008.

³⁸¹ At this point, all the pieces are ready to write down the GWS Lagrangian, after the
³⁸² Higgs mechanism has spontaneously broken the $SU(2) \otimes U(1)$ symmetry.

$$\begin{aligned} \mathcal{L}_{Unbroken} = & -\frac{1}{4} A_{\mu\nu}^a A^{\mu\nu a} - \frac{1}{4} F_{\mu\nu} F^{\mu\nu} \\ & + |D_\mu \phi|^2 + \mu^2 (\phi^\dagger \phi) - \lambda (\phi^\dagger \phi)^2 \\ & + \bar{E}_L (i\gamma^\mu D_\mu) E_L + \text{similar terms for } e_R, U_L, u_R, d_R \\ & - \lambda_e \bar{E}_L \cdot \phi e_R + h.c. + \text{similar terms for } e_R, U_L, u_R, d_R \end{aligned} \quad (2.73)$$

$$\begin{aligned}
\mathcal{L}_{GWS} = & -\frac{1}{4}(Z_{\mu\nu}^0)^2 - \frac{1}{2}(W_{\mu\nu}^+ W_{\mu\nu}^-) - \frac{1}{4}(F_{\mu\nu})^2 \\
& + ig \cos \theta_W ((W_\mu^- W_\nu^+ - W_\nu^- W_\mu^+) \partial^\mu Z^{0\nu} + W_{\mu\nu}^+ W^{-\mu} Z^{0\nu} + W_{\mu\nu}^- W^{+\mu} Z^{0\nu}) \\
& + ie ((W_\mu^- W_\nu^+ - W_\nu^- W_\mu^+) \partial^\mu A^\nu + W_{\mu\nu}^+ W^{-\mu} A^\nu - W_{\mu\nu}^- W^{+\mu} A^\nu) \\
& + g^2 \cos^2 \theta_W (W_\mu^+ W_\nu^- Z^{0\mu} Z^{0\nu} - W_\mu^+ W^{-\mu} Z_\nu^0 Z^{0\nu}) \\
& + g^2 (W_\mu^+ W_\mu^- A^\mu A^\nu - W_\mu^+ W^{-\mu} A_\nu A^\nu) \\
& + ge \cos \theta_W (W_\mu^+ W_\nu^- (Z^{0\mu} A_\nu + Z^{0\nu} A^\mu) - 2W_\mu^+ W^{-\mu} A^\nu) \\
& + \frac{1}{2}g^2 (W_\mu^+ W_\nu^-) (W^{+\mu} W^{-\nu} - W^{+\nu} W^{-\mu}) \\
& + \frac{1}{2}\partial_\mu h \partial^\nu h - v^2 \lambda h^2 + \frac{1}{2}m_W^2 W_\mu^+ W^{+\mu} + \frac{1}{2}m_W^2 W_\mu^- W^{-\mu} + \frac{1}{2}m_Z^2 Z_\mu^0 Z^{0\mu} \\
& + \left(\frac{h^2}{v^2} + \frac{h}{v}\right) \left(\frac{1}{2}m_W^2 (W_\mu^+ W^{+\mu} + W_\mu^- W^{-\mu}) + \frac{1}{2}m_Z^2 Z_\mu^0 Z^{0\mu}\right) - \lambda v h^3 - \frac{1}{4}\lambda h^4 \\
& + \bar{E}_L (i\gamma^\mu \partial_\mu) E_L + e_R^- (i\gamma^\mu \partial_\mu) e_R + \bar{Q}_L (i\gamma^\mu \partial_\mu) Q_L + u_R^- (i\gamma^\mu \partial_\mu) u_R + \bar{d}_R (i\gamma^\mu \partial_\mu) d_R \\
& + g(W_\mu^+ J_W^{\mu+} + W_\mu^- J_W^{\mu-} + Z_\mu^0 J_Z^\mu) + e A_\mu J_{EM}^\mu \\
& - \frac{\lambda_e v}{\sqrt{2}} (\bar{e}_L e_R + \bar{e}_R e_L) - \frac{\lambda_e h}{\sqrt{2}} (\bar{e}_L e_R + \bar{e}_R e_L) \\
& - \frac{\lambda_u v}{\sqrt{2}} (\bar{u}_L u_R + \bar{u}_R u_L) - \frac{\lambda_u h}{\sqrt{2}} (\bar{u}_L u_R + \bar{u}_R u_L) \\
& - \frac{\lambda_d v}{\sqrt{2}} (\bar{d}_L d_R + \bar{d}_R d_L) - \frac{\lambda_d h}{\sqrt{2}} (\bar{d}_L d_R + \bar{d}_R d_L)
\end{aligned} \tag{2.74}$$

where the currents of the electroweak interaction, $J_W^{\mu+}$, $J_W^{\mu-}$, J_Z^μ , J_A^μ are defined as:

$$\begin{aligned}
J_W^{\mu+} &= \frac{1}{\sqrt{2}} (\bar{\nu}_L \gamma^\mu e_L + \bar{u}_L^i \gamma^\mu V_{ij} d_L^j) \\
J_W^{\mu-} &= \frac{1}{\sqrt{2}} (\bar{e}_L \gamma^\mu \nu_L + \bar{d}_L^i \gamma^\mu V_{ij} u_L^j) \\
J_Z^\mu &= \frac{1}{\cos \theta_W} (\bar{\nu}_L \gamma^\mu (+1/2) \nu_L + \bar{e}_L \gamma^\mu (-1/2 + \sin^2 \theta_W) e_L + \bar{e}_R \gamma^\mu \sin^2 \theta_W e_R \\
&\quad + \bar{u}_L \gamma^\mu (1/2 - 2/3 \sin^2 \theta_W) u_L + \bar{u}_R \gamma^\mu (-2/3 \sin^2 \theta_W) u_R \\
&\quad + \bar{d}_L \gamma^{mu} (-1/2 + 1/3 \sin^2 \theta_W) d_L + \bar{d}_R \gamma^\mu (1/3 \sin^2 \theta_W) d_R) \\
J_{EM}^\mu &= e_{L,R}^- \gamma^\mu (-1) e_{L,R} + u_{L,R}^- \gamma^\mu (2/3) u_{L,R} + d_{L,R}^- \gamma^\mu (-2/3) d_{L,R}
\end{aligned} \tag{2.75}$$

383 2.7 The Standard Model of Particle Physics

The Standard Model of particle physics, extends the GWS model by incorporating the QCD interaction between the quarks and gluons. The symmetry of this theory is that of:

$$SU(3)_C \otimes SU(2)_L \otimes U(1)_Y \tag{2.76}$$

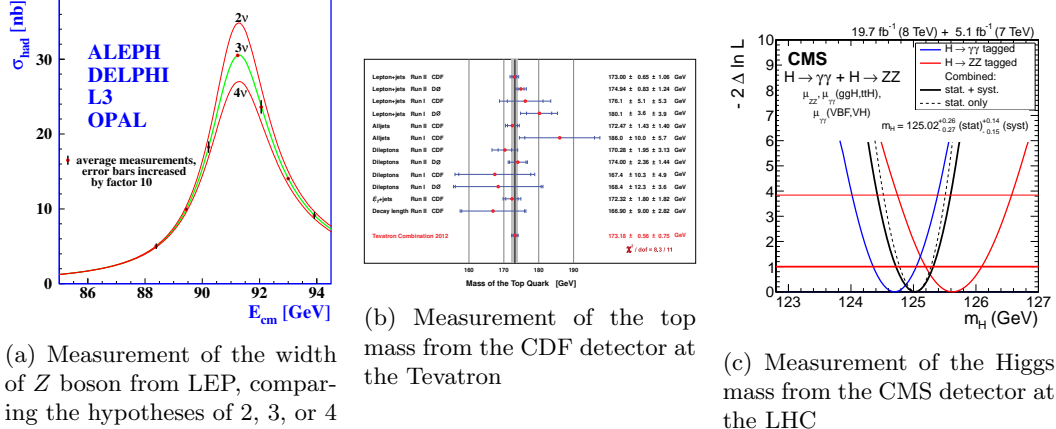


Figure 2.4: Experimental milestones of the Standard Model

³⁸⁴ The Lagrangian of the model is given by

$$\mathcal{L}_{SM} = \mathcal{L}_{GWS} - \frac{1}{4} G_{\mu\nu}^a G^{a\mu\nu} + g_S C_\mu^a J_{QCD}^{a\mu} \quad (2.77)$$

³⁸⁵ where the current for the QCD interaction, $J_{QCD}^{a\mu}$ is defined as:

$$J_{QCD}^a = \bar{u}^i \gamma^\mu t^a u^i + \bar{d}^i \gamma^\mu t^a d^i \quad (2.78)$$

³⁸⁶ where t^a are the Gell-Mann matrices defined in equation 2.30. The field strength tensor for the
³⁸⁷ eight gluon fields, $G_{\mu\nu}^a$, is defined as

$$G_{\mu\nu}^a = (\partial_\mu C_\nu^a - \partial_\nu C_\mu^a) - g_S f^{abc} C_\mu^b C_\nu^c \quad (2.79)$$

³⁸⁸ The experimental evidence in favor of the SM is compelling. It has not only been able
³⁸⁹ to describe existing phenomenon to great precision, but has also predicted the existence of
³⁹⁰ new forms of matter and interactions among fundamental particles. The UA1 [21] [22] and
³⁹¹ UA2 [23] [24] experiments at CERN, under the leadership of Carlo Rubbia, discovered the
³⁹² W and Z bosons in 1983. The experiments observed a handful of events, in $p\bar{b}$ collisions, at
³⁹³ $\sqrt{s} = 540$ GeV, and were able to measure the masses to be $M_W \sim 80$ GeV and $M_Z \sim 95$ GeV.

³⁹⁴ In the following years, from 1989-2000, the Large electron-positron (LEP) collider at CERN
³⁹⁵ conducted precision measurements of the Standard Model [25] [26]. Along with high-precision
³⁹⁶ measurements on the W, Z masses:

$$m_Z = 91.1875 \pm 0.0021 \text{ GeV} \quad (2.80)$$

$$m_W = 80.376 \pm 0.0033 \text{ GeV}$$

³⁹⁷ the experiment was also able to put stringent limits on the existence of more than three families of

398 leptons and quarks by measuring the width of the Z boson. Figure 2.4(a) shows the comparison
399 of two, three, and four family hypotheses to data.

400 Another milestone for the Standard Model occurred in 1995 when the CDF [27] and D0 experiments
401 [28] at the Tevatron announced the observation of the top quark, with $m_t \sim 176$ GeV,
402 in $p\bar{p}$ collisions at $\sqrt{s} = 1.8$ TeV. Figure 2.4(c) shows a plot from 2012, the latest top quark
403 mass measurements from CDF, which reports a $m_t = 173.18 \pm 0.56 \pm 0.75$ GeV. It was the
404 last quark predicted by the CKM matrix to be observed, and earned Makoto Kobayashi and
405 Toshihide Maskawa the nobel prize in 2008 for their work extending the quark sector to three
406 families and parameterizing their electroweak mixing.

407 Yet another milestone was reached in 2012, when the CMS and ATLAS detectors at CERN
408 announced the observation of a new boson, with characteristics strikingly similar to the elusive
409 Higgs boson of the SM. Figure 2.4(c) shows the latest measurement results on the mass from the
410 $H \rightarrow \gamma\gamma$ and $H \rightarrow ZZ$ channels, with a $m_H = 125.02 \pm 0.27 \pm 0.15$. One of the most important
411 remaining goals is to measure the couplings of this new boson to all of the other particles in
412 the Standard Model. Of particular interest is the coupling to the top-quark, since it offers the
413 largest value of the Higgs Yukawa coupling to measure. This offers a test of the nature of the
414 coupling, as well as a probe into deviations from its value.

415 2.8 Higgs Production in pp Collisions at the LHC

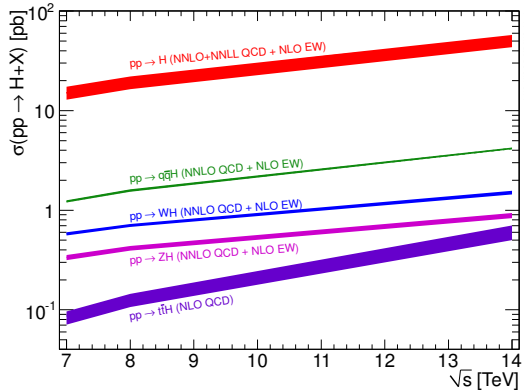


Figure 2.5: Higgs production cross-sections at the LHC, for 7–14 TeV pp collisions

416 The rest of the thesis will describe the search for Higgs boson production in proton-proton
417 collisions at the LHC, so it will be useful to understand the production mechanisms for the Higgs
418 in this scenario. At the LHC collision energies 7 – 14 TeV, there are four dominant production
419 mechanisms that produce Higgs events: gluon-gluon fusion (ggf), vector-boson fusion (vbf),
420 associated production with vector bosons (VH), and associated production with top-quark pairs
421 (tth). Figure 2.5 shows the relative cross sections for each of these mechanisms.

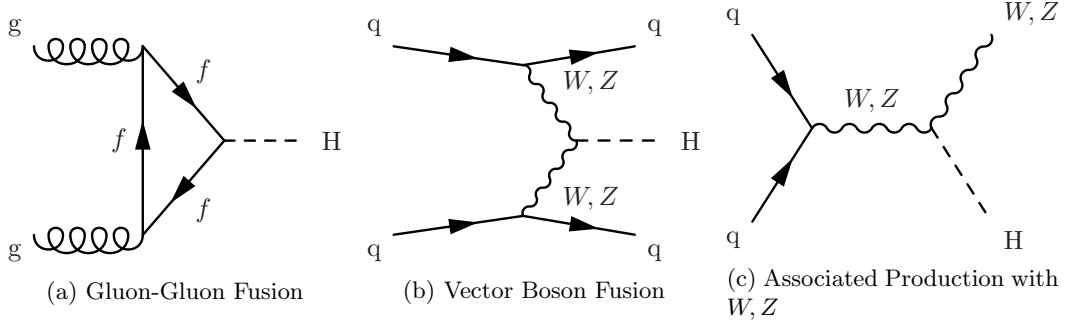


Figure 2.6: Feynman diagrams for the three largest Higgs production modes at the LHC

Gluon-gluon fusion, which proceeds via a heavy quark loop [29], is the dominant production mechanism at the LHC. The QCD radiative corrections to the total cross section have been computed at the next-to-leading order (NLO) and at the next-to-next-to-leading order (NNLO accuracy). The cross section for Higgs production at $m_H = 125$ GeV and $\sqrt{s} = 8$ TeV, the cross section is given as:

$$\sigma_{ggF} = 19.27 \pm \text{QCD Scale Unc.}^{+7.2\%}_{-7.8\%} \pm \text{PDF} + \alpha_S \text{ Unc.}^{+7.4\%}_{-6.9\%} \text{ pb}^{-1} \quad (2.81)$$

422 Figure 2.6(a) shows a Feynman diagram for this process. The triangle loop contains all strongly
423 coupled fermions, which is dominated by the top-quark since the Yukawa coupling to the Higgs
424 is the largest.

Vector boson fusion proceeds through the fusion of W^+W^- or Z^0Z^0 gauge bosons [29]. The characteristic signature of the production mode is the associated production of two quarks, typically at a low angle relative to the proton beam. This process has been calculated to NNLO for QCD and NLO for Electroweak corrections [29]. The cross section at $m_H = 125$ GeV and $\sqrt{s} = 8$ TeV is given as:

$$\sigma_{VBF} = 1.653 \pm \text{EW Unc.}^{+4.5\%}_{-4.5\%} \pm \text{QCD Scale Unc.}^{+0.2\%}_{-0.2\%} \pm \text{PDF} + \alpha_S \text{ Unc.}^{+2.6\%}_{-2.8\%} \text{ pb}^{-1} \quad (2.82)$$

425 Figure 2.6(b) shows a Feynman diagram for VBF production. The large coupling to the W, Z
426 bosons helps to make this the sub-dominant production mechanism at the LHC. However, the
427 gluon content of the proton at TeV energies is much larger than that of the valence quarks, thus
428 the relative suppression.

The third largest production mechanism for Higgs bosons at the LHC is through associated production with a W or Z boson [29]. It has been calculated to NNLO for QCD and NLO for Electroweak corrections. This process is also sometimes referred to as, Higgstrahlung, since it resembles the bremsstrahlung process of an electron radiating a photon. The higher order

electroweak corrections are similar to that of the Drell-Yan, so much of the technology to compute the cross-section can be borrowed from existing EW calculations. The cross section for $m_H = 125 \text{ GeV}$ and $\sqrt{s} = 8 \text{ TeV}$ is:

$$\begin{aligned}\sigma_{WH} &= 0.7046 \pm \text{QCD Scale Unc.}^{+1.0\%}_{-1.0\%} \pm \text{PDF} + \alpha_S \text{ Unc.}^{+2.3\%}_{-2.3\%} \text{ pb}^{-1} \\ \sigma_{ZH} &= 0.4153 \pm \text{QCD Scale Unc.}^{+3.1\%}_{-3.1\%} \pm \text{PDF} + \alpha_S \text{ Unc.}^{+2.5\%}_{-2.5\%} \text{ pb}^{-1}\end{aligned}\quad (2.83)$$

⁴²⁹ Figure 2.6(c) shows the Feynman diagram for VH production. This channel is most useful for
⁴³⁰ identifying hadronic decays of the Higgs, since the associated gauge boson can decay to leptons,
⁴³¹ giving a strong kinematic handle over backgrounds that would normally overwhelm a similar
⁴³² search in the ggF channel.

⁴³³ 2.9 $t\bar{t}H$ Production in pp Collisions at the LHC

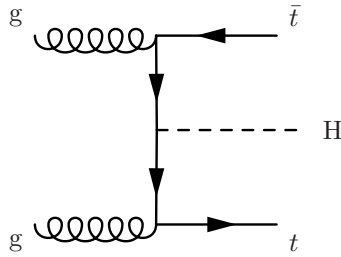


Figure 2.7: Feynman diagram for $t\bar{t}H$ production

⁴³⁴ The $t\bar{t}H$ production mode is the fourth largest production mode at the LHC [29]. This produc-
⁴³⁵ tion mode has been calculated to NLO in QCD [30] [31] and has been studied recently with the
⁴³⁶ state of the art NLO tools using the aMC@NLO [32] and POWHEG (PYTHIA+HERWIG) [33]
⁴³⁷ frameworks. Studies have also been performed interfacing NLO QCD studies [34] with the
⁴³⁸ Sherpa parton shower framework [35]. Additional studies on the effects of spin correlations with
⁴³⁹ the aMC@NLO and Madspin framework have also been performed [36].

It has been found that the addition of NLO effects increases the cross-section relative to LO by $\sim 20\%$. The largest theoretical uncertainty comes from the variation of the renormalization and factorization scale, the QCD coupling α_S , and the PDF uncertainty. The renormalization and factorization scales are set to $\mu_R = \mu_F = (1/2)(m_T + m_T + m_H)$ and are varied by a factor of 2 to determine the cross-section's dependence on these parameters. Three different PDF sets, MSTW2008, CTEQ6.6, and NNPDF2.0 were used with the appropriate corresponding values of α_S to determine the combined effect of varying PDF + α_S . The cross section for $m_H = 125 \text{ GeV}$

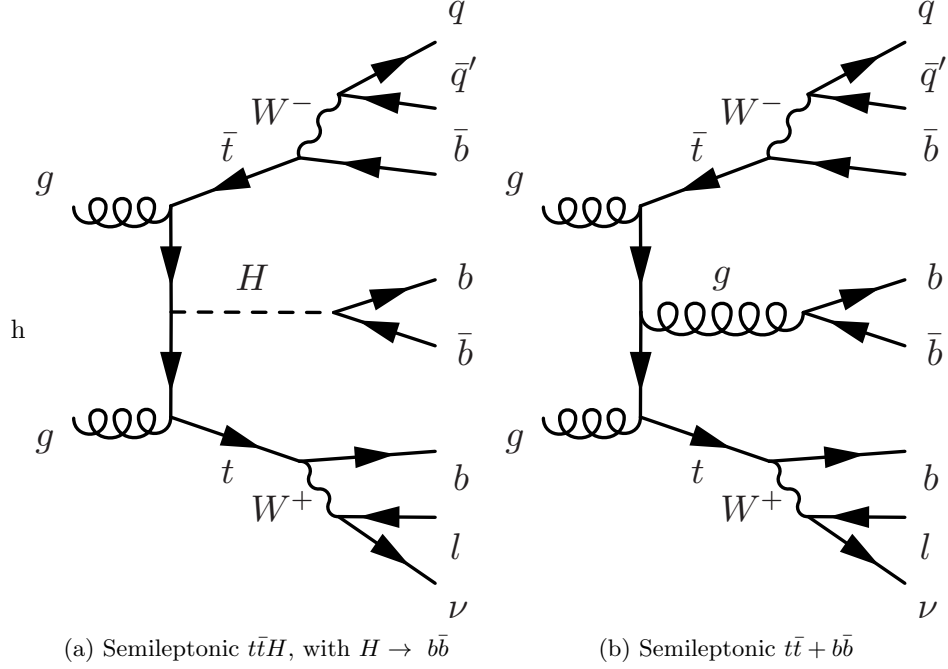


Figure 2.8: Feynman diagrams for the semileptonic $t\bar{t}H$ process and its irreducible background, $t\bar{t} + b\bar{b}$

and $\sqrt{s} = 8$ TeV is given by:

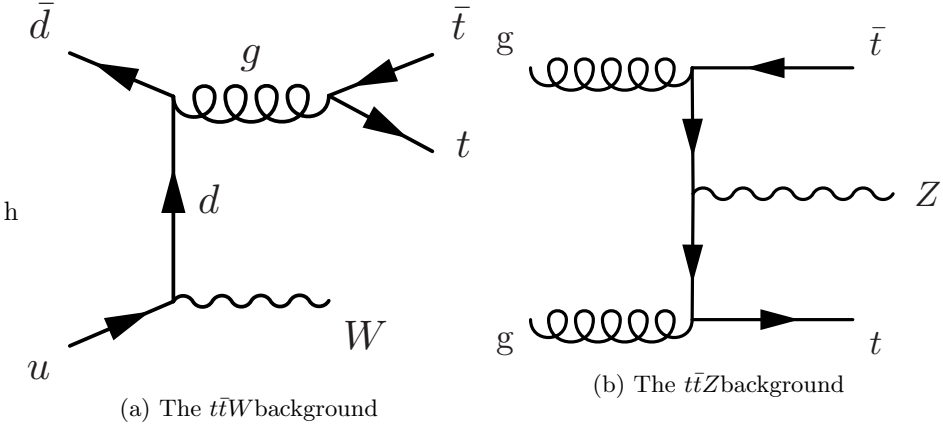
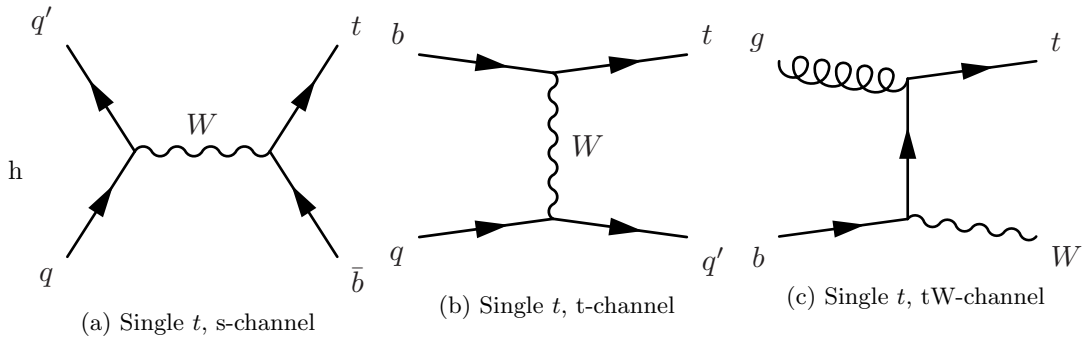
$$\sigma_{ttH} = 0.1293 \pm \text{QCD Scale Unc.}^{+3.8\%}_{-9.3\%} \pm \text{PDF} + \alpha_S \text{ Unc.}^{+8.1\%}_{-8.1\%} \text{ pb}^{-1} \quad (2.84)$$

440 A search for the Higgs in this production mode is additionally challenging due to this large
441 $\sim 10\%$ error on the theoretical cross-section. Figure 2.7 shows a Feynman diagram for this
442 process before the branching of the top-quarks or Higgs to final states.

443 When asking for the Higgs to decay to b-quark pairs, yet another complication arises when
444 trying to identify which b-quarks came from a top decay or from a Higgs decay. For example, in
445 the semileptonic decay of top quarks, there will be four b-quarks, and two light-flavor quarks in
446 the final state. This means there are 15 (six choose four) possibilities to associate quarks to the
447 top system. Although this is potentially constrained by b-tagging, and kinematic requirements
448 (such as forming the top or W masses), the number of remaining possibilites smears out the
449 resolution on peaking variables such as the invariant mass of b-quark pairs.

450 2.10 Background Processes to $t\bar{t}H$

451 The dominant background for $t\bar{t}H$ production of top-quark pairs with additional ISR/FSR jets,
452 $t\bar{t} + jets$. The irreducible component of this background is comes when the extra radiation
453 produces a final state with two additional b-quarks, $t\bar{t} + b\bar{b}$. Figure 2.8 compares the Feynman

Figure 2.9: Feynman diagrams for the $t\bar{t}W$ and $t\bar{t}Z$ background processesFigure 2.10: Feynman diagrams for the single t s,t, and tW background processes

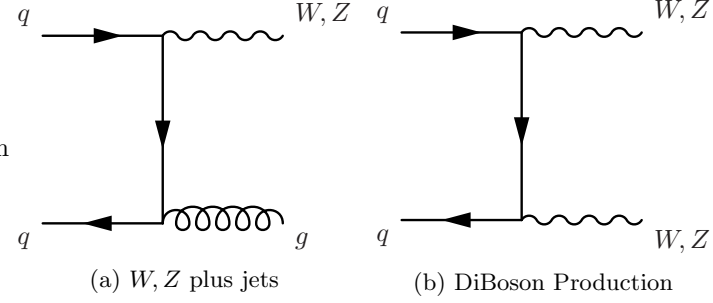
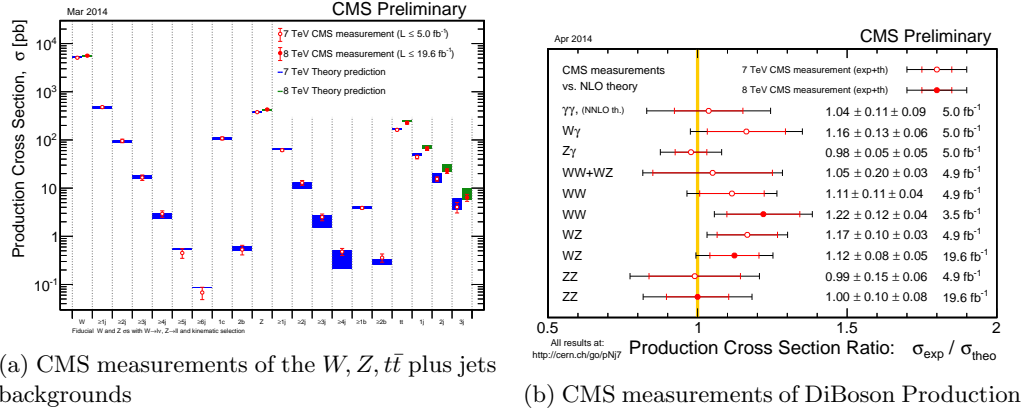
454 diagrams for the semileptonic decays of $t\bar{t}H$ and $t\bar{t} + b\bar{b}$.

455 Additional difficulties come from the theoretical uncertainty on the $t\bar{t} + b\bar{b}$ background [29].

456 The process has been calculated to NLO QCD in Sherpa [35] and OpenLoops [37] [38] [39]. It
457 has been found that depending on selection cuts, and use of NLO PDF inputs, the difference
458 between LO and NLO calculations on the cross section can be anywhere from 0.99% to 1.96%.

459 The light flavor component of the $t\bar{t} + jets$ background also enters in the selection when any
460 of the jets from the $t\bar{t}$ system or extra radiation are misidentified as b -jets. The cross-section
461 for the $t\bar{t} + jets$ process is $\sim 245 \text{ pb}^{-1}$. This is a factor of 1800, so even if a b -tagging algorithm
462 performs with a 1% mis-identification rate of light-jets, there will still be a large contribution
463 from this process that will leave a very similar signature in the detector as $t\bar{t}H$.

464 The next largest background is the production of vector bosons in association with top-
465 quark pairs, $t\bar{t}W$ and $t\bar{t}Z$. Figure 2.9 shows Feynman diagrams from these two processes. They
466 have cross-sections of $\sigma_{ttW} = 0.249 \text{ pb}^{-1}$ and $\sigma_{ttZ} = 0.208 \text{ pb}^{-1}$, which are only a factor of
467 ~ 2 greater than the $t\bar{t}H$ process. These processes can enter the semileptonic $t\bar{t}H$ selection by a
468 semileptonic $t\bar{t}$ decay, while the vector bosons decay to quarks, or through a hadronic $t\bar{t}$ decay,
469 while the vector bosons decay to quarks, and in the case of $t\bar{t}Z$, if the leptons is not identified
470 in the reconstruction.

Figure 2.11: Feynman diagrams for the W, Z plus jets, and diBoson (WW, WZ, ZZ) production.Figure 2.12: Measurements of $t\bar{t}H$ backgrounds at CMS

Single top production is also an important background to consider in a search for $t\bar{t}H$ production.

Figure 2.10 shows Feynman diagrams for this process. It does not have as large of a contribution as the other backgrounds, since it requires additional radiation in order to have a similar final state jet multiplicity as $t\bar{t}H$. However, since a top-quark is still involved in the process, the final state kinematics of its decay products will be very similar. Single t production has a cross section of $\sigma_t = 71.3 \text{ pb}^{-1}$, while Single \bar{t} production has a cross section of $\sigma_{\bar{t}} = 43.6 \text{ pb}^{-1}$, due to charge asymmetry of the valence quarks of the proton

The last backgrounds to consider are the electroweak production of W and Z bosons in association with jets, as well as WW , WZ , and ZZ pairs in association with jets. Figure ?? shows the Feynman diagrams for these processes, where the V , stands in for either W or Z bosons. For a semileptonic selection of $t\bar{t}H$ events, Z plus jets events enter from a misidentification of one of the leptons from the Z boson decay. Extra FSR/ISR radiation is also to leave a similar signature in the signal region of a $t\bar{t}H$ search, so it mainly contributes to control regions of the data.

All of these backgrounds have been measured at CMS. With the exception of a small degree of tension in the WW cross-section measurement, all backgrounds are in good agreement with Standard Model predictions. Figure 2.12(a) shows the results of CMS measurements on $V+jets$ and $t\bar{t} + jets$ backgrounds. Figure 2.12(b) shows the same, but for diBoson production.

489 2.11 Potential BSM Effects on $t\bar{t}H$ production

490 The phenomenological motivation for the existence of physics beyond the Standard Model come
 491 from the observation of phenomenon or states of matter not described by the theory. Observations
 492 of the cosmic microwave background from the Plank telescope have estimated that only
 493 $\sim 5\%$ of the observable universe is composed of ordinary matter [40]. The remaining composition
 494 is divided between Dark Matter ($\sim 27\%$, and $\sim 68\%$ respectively). Evidence for Dark Matter
 495 also comes from discrepancies between the observed rotational velocities of galaxies, and the
 496 observed mass distributions, suggesting the presence of additional form of matter which does
 497 not interact electromagnetically [41].

498 Additionally, in 1998, the Super-Kamiokande experiment proved that neutrinos oscillated
 499 between flavors, implying indirectly that they also have mass [42]. This is something not de-
 500 scribed in the Standard Model of physics. Due to their neutral charge, these particles are
 501 extremely difficult to detect, so experiments have only been able to measure differences in the
 502 mass squared between the three mass eigenstates. In 2005, the KamLAND experiment reported
 503 $|\Delta m_{12}^2 = 0.000079 eV^2|$ [43]. In 2006, the MINOS experiment reported $|\Delta m_{23} = 0.0027 eV^2|$ [44].

504 One of the largest theoretical problems with the Standard Model, comes the mechanism which
 505 made it all possible- the Higgs. In equation 2.73 there are terms that couple the Higgs boson
 506 to itself, $-\lambda vh^3$, and $-\frac{1}{4}\lambda h^4$. When computing NLO effects, these terms lead to a divergence
 507 in the Higgs mass, when considering the effect of a loop of fermions on the Higgs propagator.
 508 The corrections are of the form $\Delta m_H = -\frac{\lambda_f^2}{8\pi^2} \Lambda_{UV}$. Where Λ_{UV} is the high energy cut off for the
 509 theory, which in the limit of a perfect theory, should extend to infinity. This is known as the
 510 hierarchy problem.

511 Beyond the Standard Model physics is a term that describes extensions of the Standard
 512 Model in order to describe the observed phenomenon. For the neutrino oscillations, a solution
 513 similar to CKM matrix has been proposed, the PontecorvoMakiNakagawaSakata (PMNS) ma-
 514 trix. This proposes that the mass eigenstates of the neutrino are linear combinations of the weak
 515 eigenstates, allowing for the mixing of flavors. Current experiments now seek to measure the
 516 free parameters of this matrix.

517 Both the dark matter and hierarchy problems suffer in the fact that there is no clear model,
 518 such as the PMNS matrix, to provide a theoretical solution. Out of the plethora of theories that
 519 attempt to solve these problems, supersymmetry (SUSY) is the most popular in the theoretical
 520 and experimental community. It suggests that there is a broken symmetry between fermions
 521 and bosons, and introduces a partner to each Standard Model particle with a spin quantum
 522 number less 1/2 [45]. For the hierarchy problem, this provides a set of particles to cancel out the

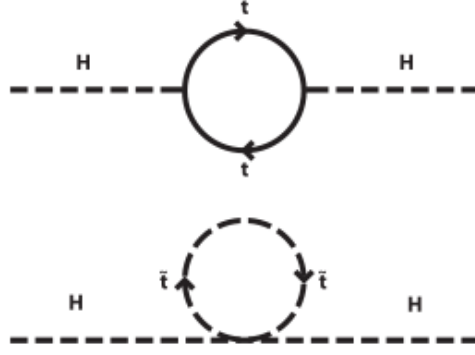


Figure 2.13: The cancellation of the divergent Higgs mass from a loop of top-quarks is cancelled by a loop of supersymmetric top-quarks, stop-quarks,

523 divergences in the NLO corrections to the Higgs mass. Figure 2.13 shows the Feynmann diagrams
 524 for a supersymmetric top-quark, or stop quark, that would cancel the divergent contribution from
 525 the Standard Model top quark. Depending on the specific form of the SUSY model, the stop
 526 quarks can potentially couple directly or indirectly to the top-quark, producing them at a higer
 527 rate during pp collisions. This would effect the number of observed events making it into the
 528 $t\bar{t}H$ selection.

529 A number of extensions to the SM also involve introducing new top-like particles into the
 530 theory. Vector-like quarks would be spin 1/2 particles that transform as triplets under the $SU(3)$
 531 color group and whose left and right-handed components have the same color and electroweak
 532 quantum numbers [46]. These objects are common to several different types of models. Little
 533 Higgs models [47] [48] [49], models with extra dimensions [50] [51], top-color models [52], and
 534 composite Higgs models [53], include a vector-like top partner, t' that decays to a top-quark and
 535 either a Higgs, W , or Z particle. Both $t't'$ pair production and $t't$ production would yield the $t\bar{t}H$
 536 final state, or at least one indistinguishable detector signature. $t\bar{t}H$ search can provide indirect
 537 limits on these models, by observing an excess or lack thereof of $t\bar{t}H$ events, without having to
 538 directly construct a t' resonance.

539 **Chapter 3**

540 **The Large Hadron Collider**



Figure 3.1: Aerial view of the LHC complex, spanning the French-Swiss border [1]

541 The Large Hadron Collider (LHC), is a superconducting, proton-proton, accelerator and
542 collider operated by the European Center for Nuclear Research (CERN) laboratory in Geneva,
543 Switzerland [54]. Figure 3.1 shows an aerial view of the LHC complex, with the main laboratory
544 campus being labeled as CERN, with four of the detector experiments being labeled as ALICE,
545 ATLAS, CMS, and LHCb. Three smaller experiments, not pictured, also use the LHC ring, and
546 are TOTEM, LHCf, and MOeDAL. It was designed to elucidate the mechanism of electroweak
547 symmetry breaking and explore TeV scale of particle physics. As such, it is required to produce
548 a large number of high center-of-mass energy events. The high center-of-mass energy allows the
549 creation of heavy particles, while a large luminosity allows for the creation of rare processes.
550 The number of events produced at a collider is a product of the luminosity of the collider and

551 the total cross-section for the objects being collided.

$$N_{events} = L\sigma_{event} \quad (3.1)$$

552 The cross-section, σ_{event} , can be estimated from the theory of the Standard Model as described
 553 in section 2.1 and validated by measurement at detectors, such as CMS, as shown in section 2.10.
 554 The luminosity is a control of the experiment, and for Gaussian distributed beams, is given by
 555 the equation:

$$L = \frac{N_b^2 n_b f_{rev} \gamma_r}{4\pi \epsilon_n \beta^*} F \quad (3.2)$$

556 The parameters of this equation and their value for the LHC is as follows:

- 557 • N_b - Number of particles per bunch, squared since there are two beams. The mechanism
 558 of achieving such high energies is based in Radio-Frequency (RF) cavity technology, which
 559 clusters the protons together into packets, which are all accelerated and collided together.
 560 For the LHC, $N_b = 1.15 \times 10^{11}$.
 - 561 • n_b - Number of bunches per beam. The maximum design for the LHC allows for $n_b = 2808$
 562 bunches, however in practice, lower number of bunches have been run with in order to
 563 create more time between bunch crossings.
 - 564 • f_{rev} - Revolution frequency of the protons in the LHC ring. This is determined by ring
 565 circumference, and for the LHC, $f_{rev} = 11.2$ kHz.
 - 566 • γ_r - This is the relativistic gamma-factor, determined by the speed, and thus the center of
 567 mass energy of the collisions.
 - 568 • ϵ_n - This is the normalized transverse emittance of the beam, which describes the RMS
 569 spread of the beam in its transverse plane. For the LHC $\epsilon_n = 3.75 \mu\text{m}$.
 - 570 • β^* - Is the minimum of the β function, which is defined as the square of the transverse
 571 beamsize divided by ϵ_n . It is minimized at interaction regions, where the beams are being
 572 squeezed into the smallest region possible, to maximize the probability of protons colliding
 573 during each bunch crossing. For the LHC, $\beta^* = 0.55$
 - 574 • F - This is the efficiency for having the two beams head-on, and is determined by the
 575 crossing angle at which the two counter-rotating beams meet each other.
- 576 The LHC is designed to deliver a maximum luminosity of $L = 10^{34} \text{ cm}^{-2}\text{s}^{-1}$ to the CMS and ATLAS
 577 experiments, with a maximum center-of-mass energy of $\sqrt{s} = 14 \text{ TeV}$.

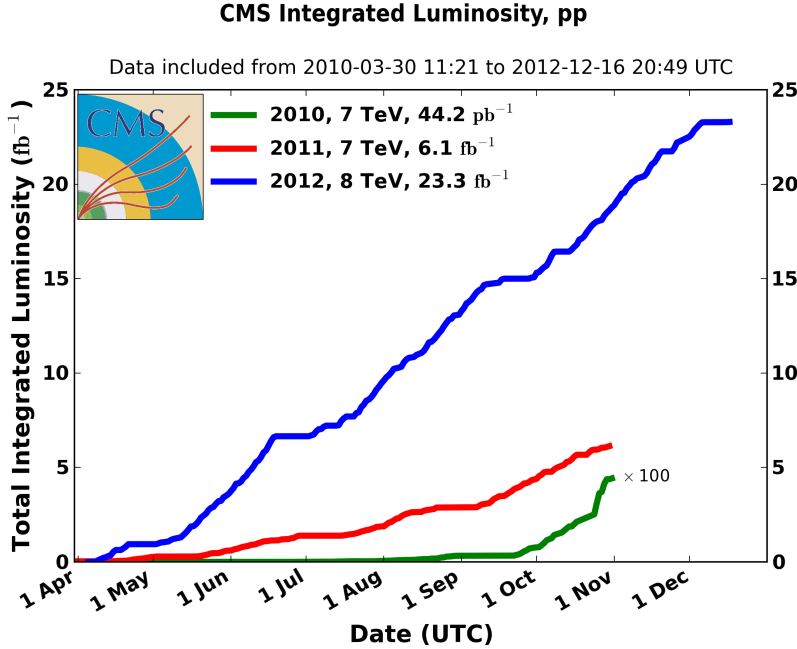


Figure 3.2: Integrated Luminosity delivered to the CMS experiment from 2010-12

578 In 2010-11, the LHC ran at center-of-mass energy, $\sqrt{s} = 7 \text{ TeV}$ and delivered $\sim 6 \text{ fb}^{-1}$ of
 579 data to the CMS experiment. In 2012, it ran at $\sqrt{s} = 8 \text{ TeV}$ and collected $\sim 23 \text{ fb}^{-1}$. Figure 3.2
 580 shows a diagram of the luminosity collected as a function of time for each year running.

581 The next sections will describe the LHC accelerator complex, the chain of events leading
 582 up to collisions of protons at the LHC, and the associated technologies that allow for the con-
 583 trol and operation of the high-energy, high-luminosity beams that allow the CMS and ATLAS
 584 experiments to search for heavy particles and rare-processes.

585 3.1 The LHC Accelerator Complex

586 The main LHC ring is a 26.7 km tunnel, that is 45 m to 170 m underneath the surface of the
 587 earth, with 1.4% slope towards Lake Leman. It extends accross the French-Swiss border, into
 588 the French coutnryside. The tunnel was originally constructed between 1984 and 1989 for the
 589 Large Electron Positron (LEP) experiment that is famous for it's precision mesaurements of
 590 several Standard Model parameters [54]. The choice to build the ring underground was driven
 591 by real estate costs, but the underground setting also provides natural radiation shielding from
 592 the beamline and greatly reduces the impact of cosmic radiation on the detectors.

593 The LHC also utilizes the existing accelerator complex from the LEP experiment, which is
 594 shown in figure 3.3. The complex is composed a series of increasingly powerful accelerators that
 595 gradually increase the energy of the protons.

596 Protons are initially accelerated by the Linac2 linear accelerator up to 50 MeV [55] [56]. A

The LHC injection complex

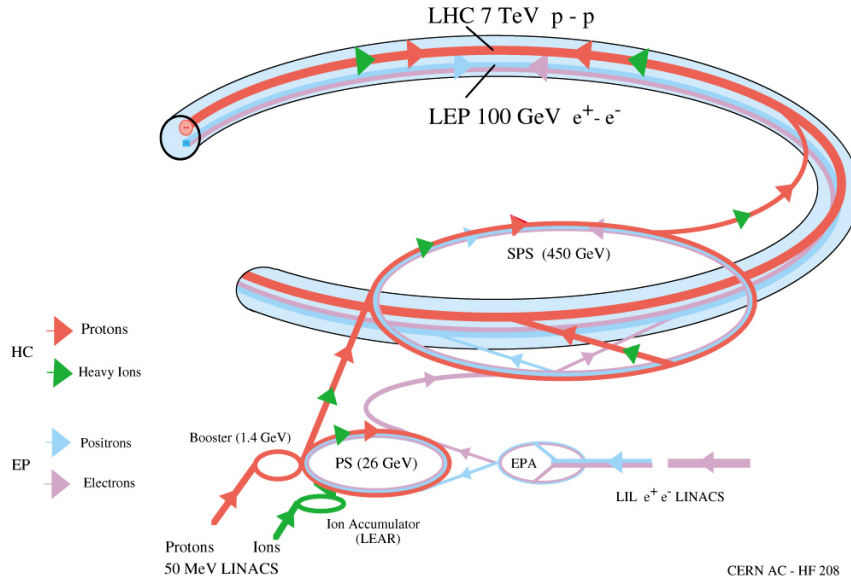


Figure 3.3: The LHC accelerator complex, taking protons from a bottle of Hydrogen at the Linac2, all the way to the LHC ring

bottle of Hydrogen is attached to a duoplasmatron source. This device ionizes the Hydrogen, and creates a 300 mA beam of protons, through a high-voltage anode, and a geometry designed to focus and collimate the beam as it leaves the device. Figure 3.4(a) shows a schematic for this device, showing the gas input on the left, and proton beam leaving to the right. Figure 3.4(b) shows the actual device used in the Linac2 at CERN. The proton beam then enters the Radio-Frequency Quadropole (RFQ) system, which accelerates and bunches the protons up to 750 keV. The RFQ is a waveguide with four flanges, which have been machined with a sinusoidal modulation in the longitudinal direction, which creates an standing electric wave in this direction, accelerating the protons. Figure 3.4(c) shows a schematic of this modulation, and figure 3.4(d) is a close-up image of this modulation in an actual RFQ. The last stage of acceleration is provided by three Alvarez tanks. Each Alvarez tank holds a series of elctrically isolated cylinders, known as drift tubes, coaxial with the main tank, with gaps in between them. An alternating electric field is present in the gaps, and space between each drift tube and the walls of the tank. Protons passing through the center of the drift tubes feel no electric field, but the gaps are located such that, a proton will always see an accelerating field in the gap, and are thus receive a boost of energy from each gap as it traverses the length of the three tanks. Figure 3.4(e) shows an image of the inside of an Alvaez tank, and figure 3.4(f) shows the tanks at the Linac2 at CERN. The final product is a 180 mA, 50 MeV proton beam, which is steered to the Proton Synchotron Booster for the next stage of acceleration.

The Proton Synchotron Booster (PS booster) complex accelerates the protons up to 1.4

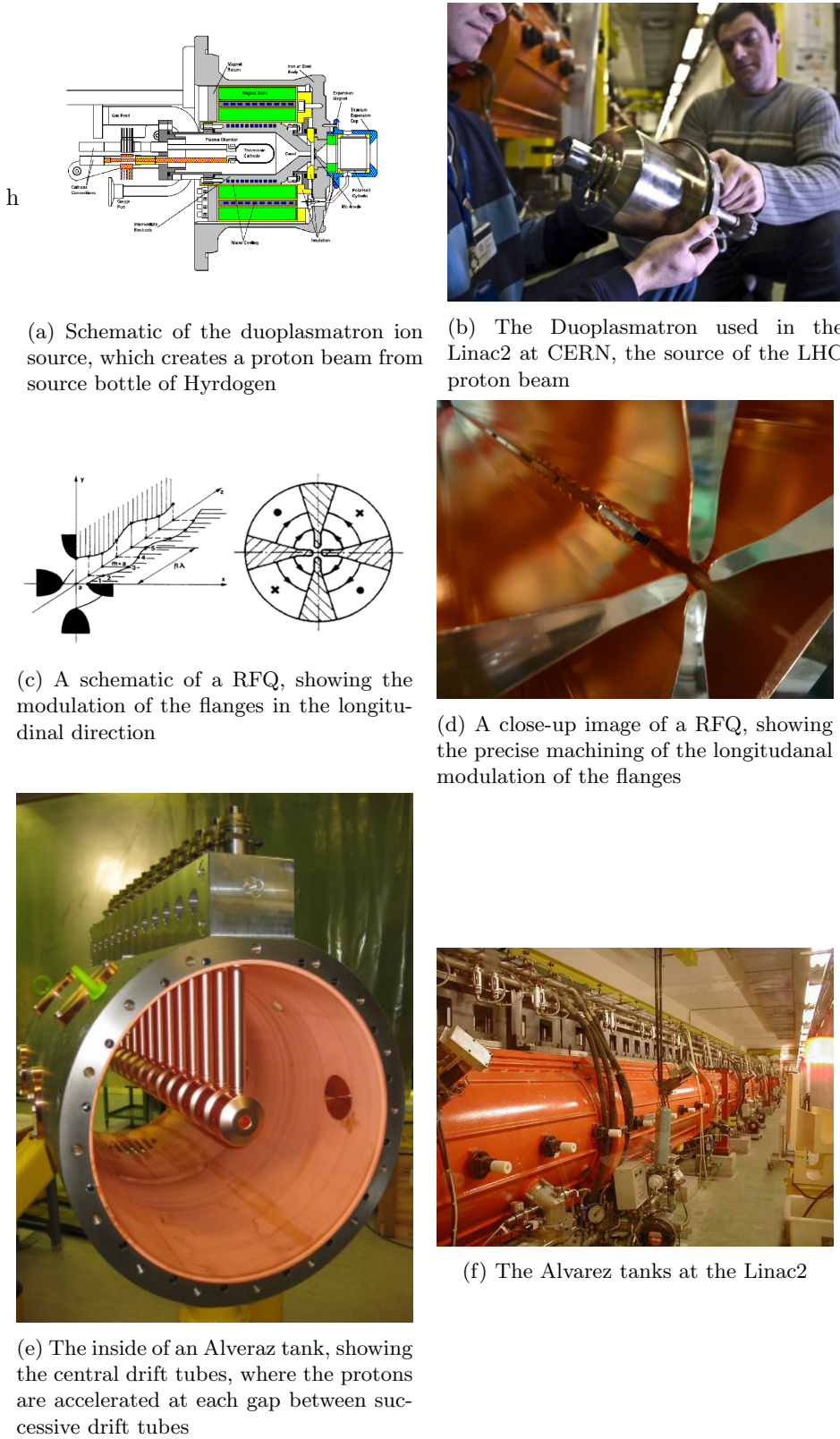


Figure 3.4: Features of the Linac2, the first stage of acceleration in the LHC injection chain

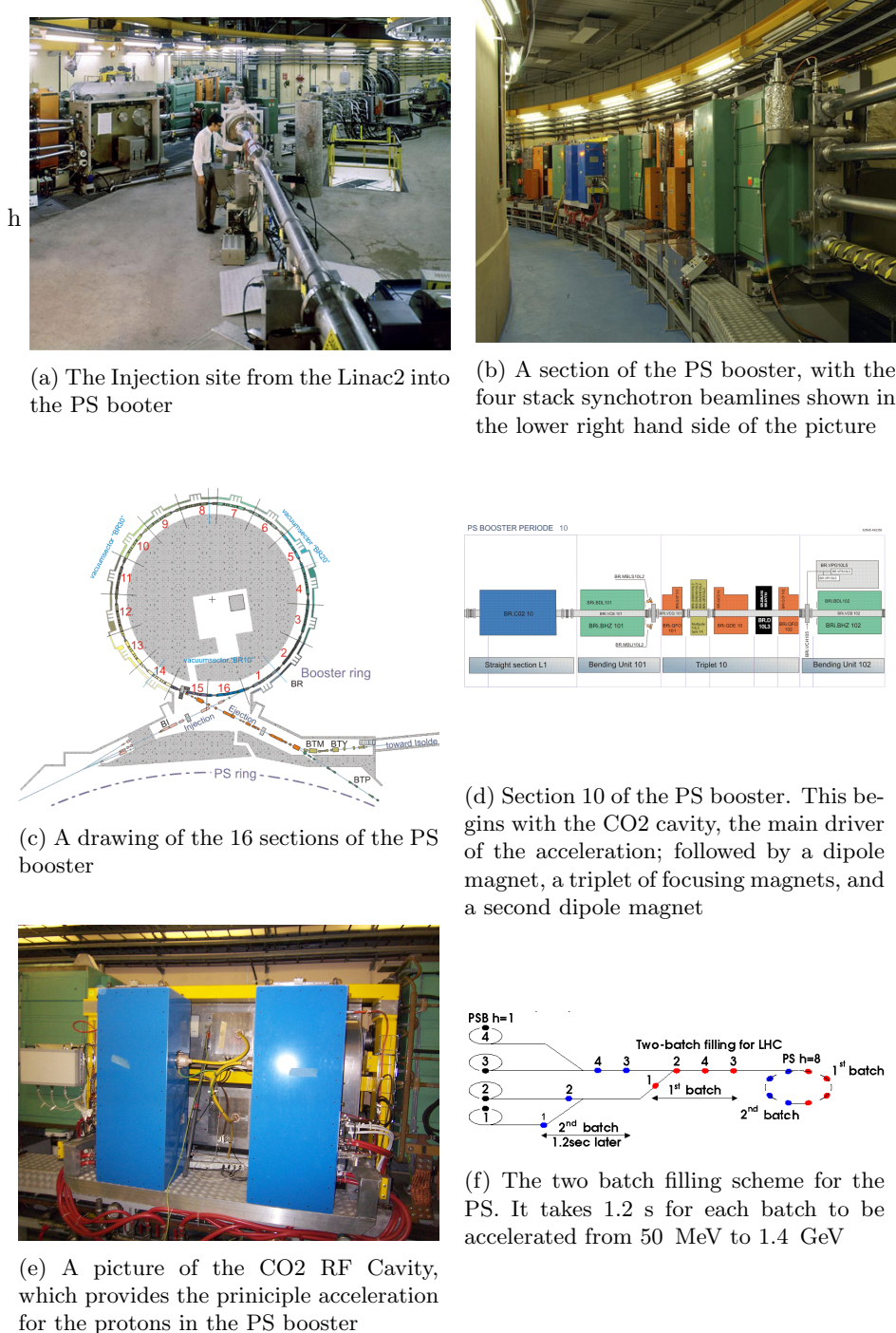


Figure 3.5: Features of the PS booster, the second stage of the LHC injection chain

617 GeV [55]. The complex takes the proton beam from the Linac2 and splits the beam into four
 618 separate, synchrotrons, stacked on top of one another. Figure 3.5(a) shows the injection site of
 619 the proton beam from the Linac2 into the PS booster. The right side of figure 3.5(b) shows the
 620 four synchotron beam pipes stacked vertically on top one another. The splitting of the beam is
 621 done in order to reduce the effect of the space charge of the proton beam, which would increase
 622 the transverse emmitance beyond a tolerable degree. The PS booster uses thirty-two 0.87 T
 623 dipole magnets to bend the beams, and fourty-eight quadrupoles to focus the beam as it makes
 624 its way around each of the 50 m diameter rings. Each magnet is composed of a vertical stack
 625 of four magnets, one for each of the synchotrons, and share a common yoke, allowing one power
 626 supply to provide the current to all of them in series [57]. The booster is divided into 16 arcs, as
 627 shown in figure 3.5(c). Each arc contains a bending dipole, 3 focusing quadrupoles, and a second
 628 bending dipole, followed by a straight section containing beam diagnostic, injection and ejection
 629 systems, and in three sections, the Radio-Frequency (RF) cavities, which is the mechanism of
 630 accelerating the beam [58]. Figure 3.5(d) shows the layout of the tenth arc, which also contains
 631 one of the RF cavities in the first section.

632 An RF cavity is a specially shaped, hollow conductor, that the beam passes through [59].
 633 The shape of the cavity determines the resonant frequency and harmonics (integer multiples of
 634 the fundamental frequency), of the standing electromagnetic fields that result when the cavity
 635 is driven by an alternating voltage source. The idea is to choose a resonant frequency such
 636 that the proton will always experience a positive electric field, and thus an acceleration, each
 637 time it passes through the RF cavity. This means that the revolution frequency of the proton
 638 must be equal to the fundamental frequency or harmonic of the RF cavity, $f_{RF} = n \times f_{rev}$, with
 639 $n = 1, 2, 3, \dots$. Eventually, the proton is accelerated up to an equilibrium speed and will enter the
 640 cavity just as the standing electric field is alternating through it's zero point. If arrives too early
 641 for this (moving too fast), then it will experience a negative electric force, a deceleration, which
 642 will eventually bring it back to the equilibrium revolution frequency, where it experiences zero
 643 net force. A diffuse beam of protons will be bunched into groups of protons through this effect
 644 as well, as the faster protons in the beams are decelerated, and the slower ones accelerated,
 645 until they all reach the same equilibrium revolution frequency. Driving the RF cavity with a
 646 harmonic, n , of the proton's revolution speed will thus create n bunches of protons. Each one of
 647 the potential n bunch positions is referred to as a bucket. In the case where a proton has to be
 648 accelerated through a wide range of energies, the frequency of the cavity must also increase to
 649 maintain synchronization with the proton revolution frequency.

650 Three types of RF cavities are used to accelerate the beam during each revolution. The first
 651 of the three types of RF cavities is the CO₂, with frequency range of 0.6 to 2.0 MHz and is used

652 to drive the $h = 1$ harmonic of the synchrotron, and is pictured in figure 3.5(e). The second
 653 type of cavity is the CO4 chamber, with a frequency range of 1.2 to 3.9 MHz, and drives the
 654 $h = 2$ mode of the synchrotron. This second mode is capable of splitting the beam and creating
 655 two separate bunch structures. However, for LHC running, only one bunch is used, and is driven
 656 primarily by the $h = 1$ mode. The $h = 2$ mode is supplemental and is used to shape the beam.
 657 A third type of RF cavity, CO16, has a frequency range of 5 to 16 MHz, and is used to control
 658 the longitudinal shape of a bunch during acceleration. The beam leaves the PS booster and enters
 659 the PS in a two-batch filling scheme, taking only 1.2 s to accelerate a second batch of protons
 660 from 50 MeV to 1.4 GeV. This second batch enters just as the first batch has traveled to the
 661 opposite side of the PS ring. A schematic of this process is shown in figure 3.5(f). To achieve
 662 the 25 ns bunch spacing design of the LHC, only 6 bunches of proton beam need to be delivered
 663 to PS. This is achieved by either using a 4+2 or 3+3 filling scheme, in terms of the number of
 664 proton bunches derived from the four possible synchotrons.

665 The next stage is the Proton Synchrotron (PS), which will boost the protons up to 25
 666 GeV [55]. The layout is shown in figure 3.6(a). The ring has a circumference of 628 m, and
 667 uses 100 dipole magnets and 177 higher-order focusing magnets, to steer the beam around the
 668 ring. Figure 3.6(b) shows a picture of one of the dipole magnets used at the PS. In addition
 669 to providing acceleration up to 25 GeV, the PS forms the basis of the bunch structure that is
 670 eventually used in the LHC. The $h = 7$ harmonic is used to capture the 6 bunches of protons
 671 delivered from the PS booster, leaving a gap in the place of a seventh bunch. The beam is then
 672 split into three, by using three different RF cavities tuned to the $h = 7, 14, 21$ modes of the PS.
 673 Figure 3.6(c) shows a simulation of a proton bunch being divided into three over the course of
 674 25 ms. The $h = 21$ mode is then used to accelerate the protons to from 1.4 to 25 GeV using the
 675 20 MHz RF cavity. Each bunch is then split twice, using the $h = 21, 42, 84$ synchroton modes,
 676 to create 72 bunches, spaced 25 ns apart, with a 320 ns gap for the 12 unused buckets of the
 677 $h = 84$ harmonic. This process is simulated in figure 3.6(d), over the course of 125 ms. The 320
 678 ns gap is created to account for the rise time of the kicker magnet, which ejects the beam out of
 679 the PS into the SPS. The entire splitting process is summarized in figure 3.6(e). For the case of
 680 50 ns bunch spacing, the final stage of splitting is not performed, and the $h = 21, 42$ modes are
 681 used to split the beam. Finally, in order to fit the bunches into the 200 MHz RF acceleration
 682 scheme of the SPS, the bunch length must be compressed from 11 ns to 4 ns. This is achieved
 683 by rotating the beam in the energy vs time phase space by sequential increases in voltage to
 684 the 40 MHz $h = 84$ mode, followed by an increase to the 80 MHz $h = 168$ mode. Figure 3.6(f)
 685 shows the result of this rotation - a distortion free ellipse with a smaller 4 ns spread, but a larger
 686 spread in the energy spectrum of the proton beam.

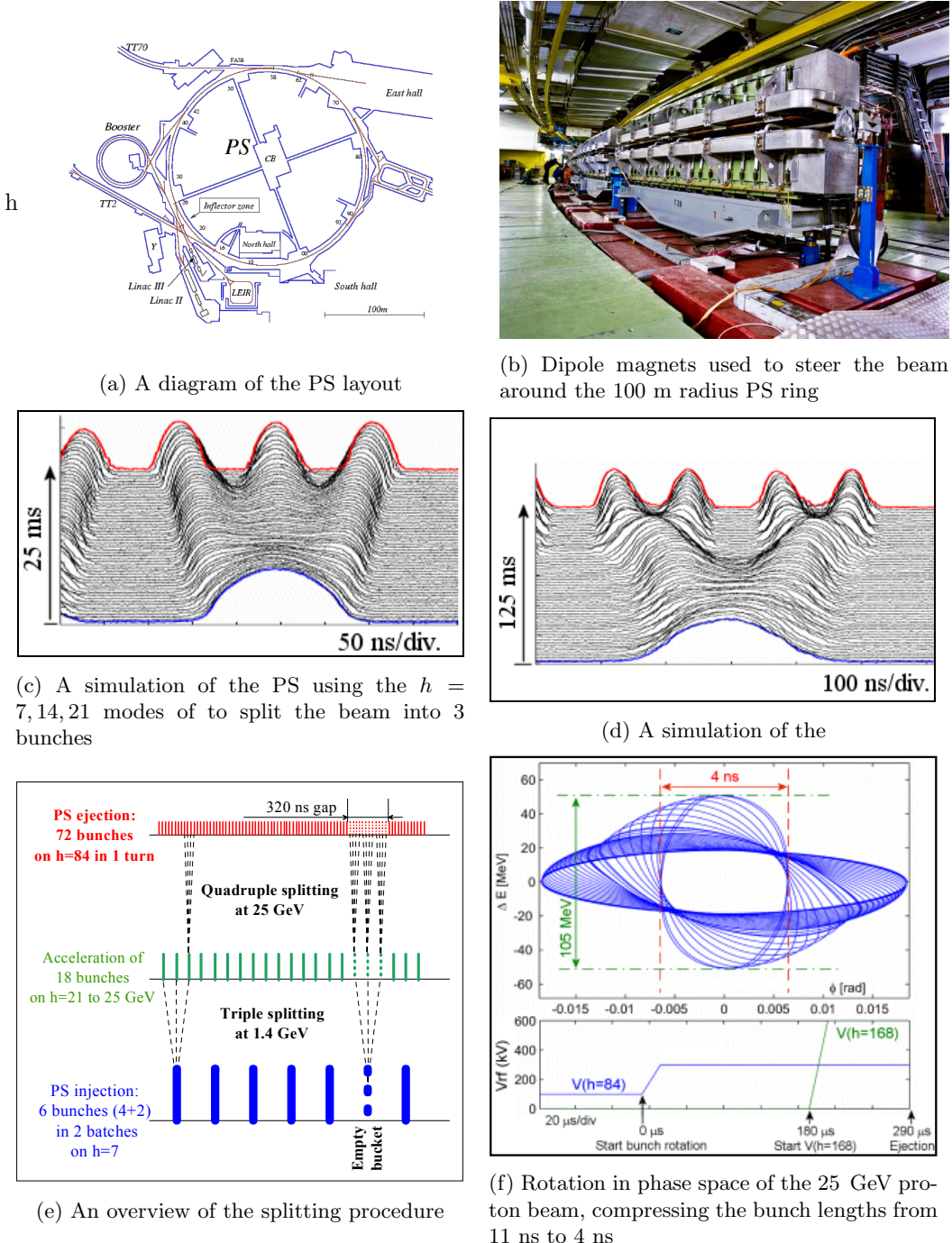


Figure 3.6: Features of the PS, the third stage of the LHC injection chain

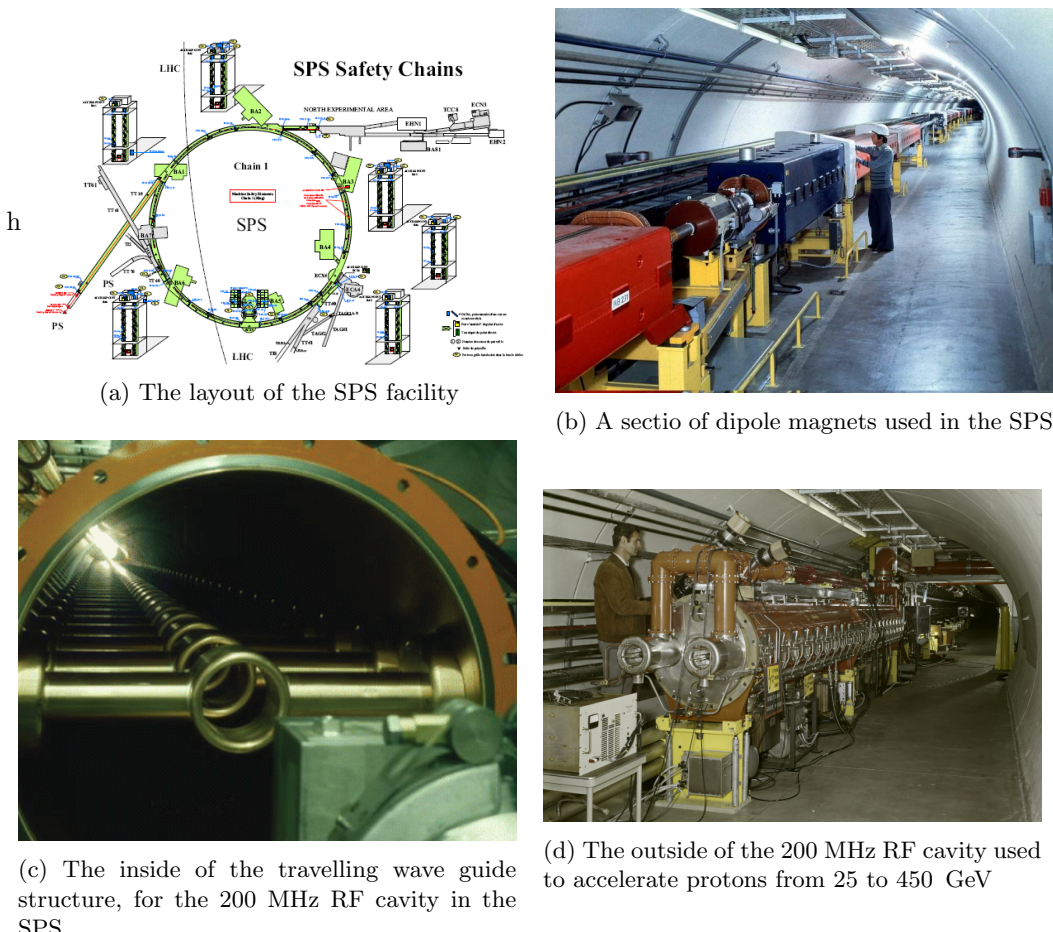


Figure 3.7: Features of the SPS, the fourth and final stage of the LHC injection chain

687 Next, the protons arrive at the Super Proton Synchotron (SPS), where they will be acceler-
 688 erated to 450 GeV. The SPS is the last stage of acceleration before the protons are injected
 689 into the LHC. The layout is show in figure 3.7(a). It has a circumference of 7 km, and steers
 690 the proton beam with 744 dipole magnets, with 573 higher-order focusing magnets [60]. Figure
 691 3.7(b) shows one of the dipole mangets in the SPS tunnel. Like all the other synchrotrons in
 692 the injection chain, the acceleration is provided by RF cavities. A 200 MHz system of RF cavi-
 693 ties capture and fill the SPS by using 2-4 batches of 72 bunch proton beams from the PS [55].
 694 Although the relative change in frequency is small, the large degree of acceleration necessitates
 695 the use of a tunable RF cavity. The 200 MHz system has 2 sections of 4 travelling wave cavities
 696 in series, and another 2 sections of 5 cavities in series. Figure 3.7(c) shows the insde of this
 697 structure, which uses drift tubes to accelerate protons in the gaps between tubes, with horzion-
 698 tally mounted bars, spaced 374 mm [61] apart, determining the periodicity of the resonant RF
 699 field that builds up inside. The outside of the structure is shown in figure 3.7(d). An additional
 700 800 MHz system is used to control the transverse emmitance. It is also used to stabalize the
 701 beam-line and prevent coupled-bunch instabilities [55].

702 Finally, protons are injected into the LHC ring in one clockwise, and another counter-
 703 clockwise rotating beams. In order to work in the limited space of the existing LEP tunnel,
 704 the two beams are contained within a single meachanical and cryostate structure, with a dual-
 705 bore design for each of the beams. Here, each proton beam is accelerated to their final energy of
 706 7 TeV, moving at 99.999991% the speed of light, before they meet head on, producing 14 TeV
 707 center-of-mass collisions.

708 The LHC ring itslef is divided into eight octants, with eight straight sections that are located
 709 in front and behind each of the eight collision points, where the beams are made to cross and
 710 collide, as shown in figure 3.8. These crossings are known as interaction regions (IRs). Four
 711 of these points are currently being used by experiments. TOTEM has detectors on either side
 712 of the CMS experiment at one interaction region, known as point 5 (P5). LHCf has detectors
 713 on either side of ATLAS at point 1 (P1). MOeDAL has detectors near LHCb at point 8 (P8)
 714 and the ALICE detector is located at point 2 (P2). The following sections will cover the RF,
 715 magnet, cryogen, and vaccuum technologies used in the LHC ring.

716 3.2 LHC Magnets

717 Several types of magnets are used in order to properly circulate and focus the proton beam as
 718 it makes its way around the 26.7 km long tunnel. A complete list of all types, can be found in
 719 the technical design report [62], as well as through CERN's outreach web resources [63]. This

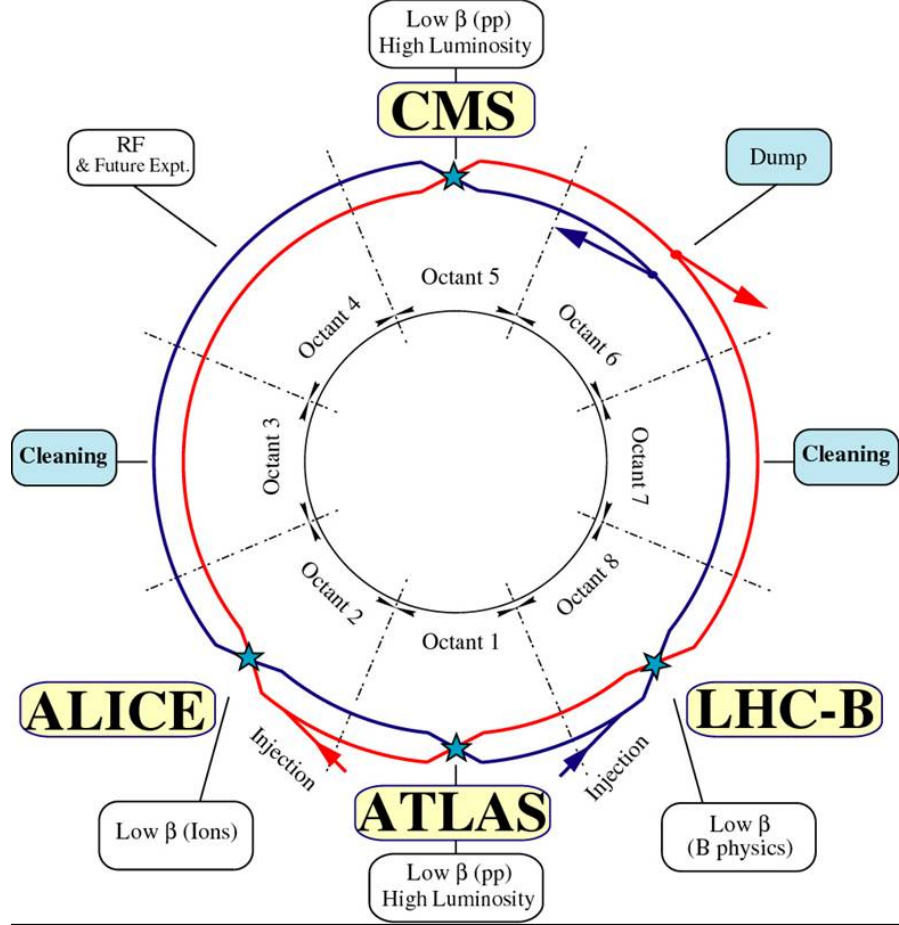


Figure 3.8: The LHC ring is divided into eight octants

section will give an overview of the a few of the critical subsystems: the septum and kicker magnets used for injection from the SPS, the dipole magnets used for bending the beam around the circumference of the ring, and the higher-order-pole magnets that are used for focusing the beam.

The injection and extraction of proton beams from one synchrotron to another involves three types of magnets, septums, kickers, and bumpers. Septum magnets contain a partition, or a septum, that provides a boundary between a high magnetic field region and a near-zero magnetic field region and are operated in DC or a slow-pulsed mode [64]. In case of injecting a beam of protons into a synchrotron, the target beampipe of the synchrotron passes through the low-field region, so the trajectory is unaffected by the high-field region, which bends the injection beam towards the synchrotron aligning it horizontally, with the target beam. The kicker magnet, is a fast-pulsed magnet and provides the timing selection in order to make a final bend vertical bend into the synchrotron orbit, and into the correct basket of the synchrotron bunch train [65]. Finally, bumper magnets make small bends to the beam and align it with the injection site. Figure 3.9 shows a schematic for this process, where a transfer line brings protons to a septum, which bends the beam to a kicker, which makes the final corrections to match the synchrotron

Single-turn injection

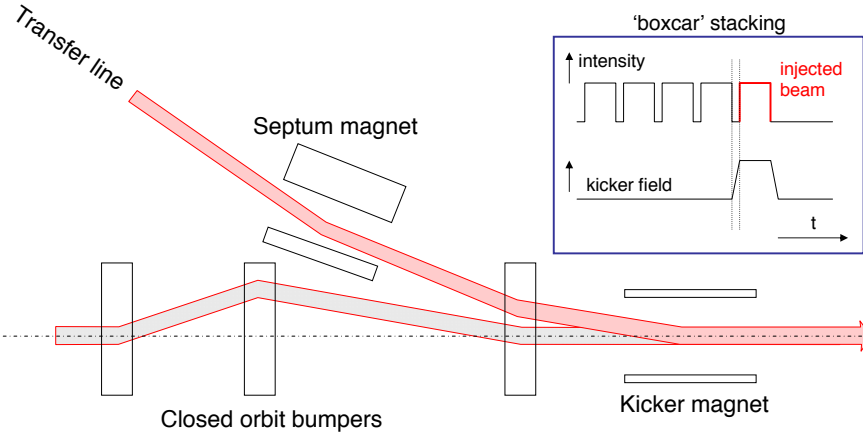


Figure 3.9: The single turn injection scheme. A septum magnet makes the initial alignment. The kicker magnet times the injection and makes the final alignment. Bumper magnets align the LHC beam with the injected beam.

736 orbit. For extraction, the kicker magnet quickly displaces a portion of the beam, which is steered
 737 away by the septum, while the original beam passes through its low-field region unaffected.

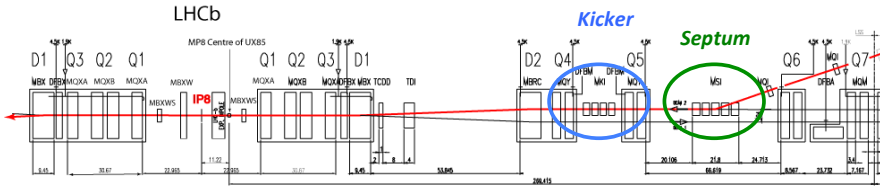


Figure 3.10: Layout of Interaction Region 8, where one proton beam is injected into the LHC ring. A transfer line from the SPS brings a proton in from the right. In green, a septum magnet aligns the beam horizontally with the LHC. In blue, a kicker magnet makes the final vertical alignment into the LHC, and is timed to fill one of the 400 MHz buckets of the RF capture system

738 At the LHC, beam is injected at Interaction Regions (IR) 2 and 8 [54]. Two transfer lines
 739 bring the beam extracted from the SPS to ~ 150 m of the LHC ring. Five Labertson-type septum
 740 magnets, of field strength ~ 1 T, are used to deflect each of the transfer line beams 12 mrad
 741 to align the transfer beam horizontally with the LHC orbit. Then, four ~ 0.12 T MKI kicker
 742 magnets quickly deflect the beam 0.85 mrad to close the orbit with the LHC ring. Figure 3.10
 743 shows the layout of the injection point at IR 8. The green circle encloses the septum structure,
 744 which provides the horizontal alignment, and the blue encloses the kicker structure, which makes
 745 the final vertical alignment and synchronizes the injection of the beam into the LHC. The rise
 746 time for the field provided by the kicker magnets in the LHC and SPS determine the final bunch
 747 structure of the LHC. Figure 3.11 extends figure 3.6(e) showing how the rise times of the kickers
 748 that inject, or eject beam create gaps in the bunch structure of the LHC. The initial filling of the
 749 PS with 6 batches of protons from the PSB, leaves one initial bucket unused in the PS. After

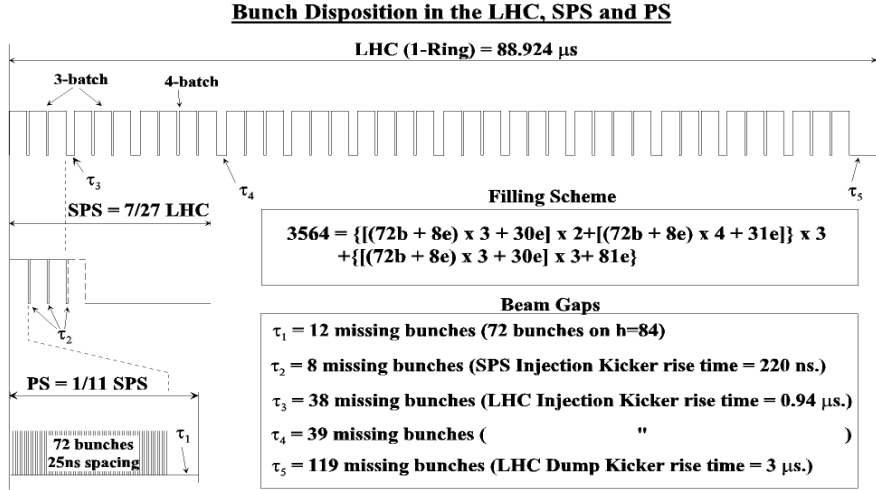


Figure 3.11: The initial filling of 6 batches of protons from the PSB to the PS, leaves 12 empty buckets in the PS bunch structure. The rise time of the SPS magnet creates an additional gap in the SPS bunch structure. Additional gaps emerge due to the rise time of the LHC injection and dumping kicker magnets

750 the splitting of the beam into the 25 ns bunches, there 12 empty buckets at the of the PS bunch
 751 train. The SPS is filled with three to four of these trains, leaving an additional 8 25 ns buckets
 752 unfilled due to the 220 ns rise time of the SPS kicker magnet. These three to four trains are
 753 then injected into the LHC, where there are 38 or 39 bunch gaps due to the LHC injector 0.94
 754 μ s rise time. At the end of a full LHC orbit, 119 buckets are left empty to allow for the rise time
 755 of the beam dumping kicker magnet, used to remove beam from the LHC.

756 Once the beam is injected, the curved path around the circumference of the LHC is main-
 757 tained via 1232 superconducting dipole magnets. The superconducting material niobium-titanium,
 758 NbTi, is cooled to 1.9 K in order to produce the 8.33 T field. Figure 3.12(a) shows a cross-section
 759 view of one of the LHC dipoles. The dual-bore design of the beam-pipe is enclosed by an iron
 760 yoke, that serves as the cold mass to maintain the superconducting temperature, and provides
 761 a 195 mm gap between each beam. A close up picture of the non-magnetic collar and supercon-
 762 ducting coils are shown in figure 3.12(b). A simulation of the magnet in figure 3.12(c) shows the
 763 homogenous, vertical magnetic field produced in the center of the coil. Diagram 3.12(d) shows
 764 an exaggerated view of the 2812 m radius curvature of each dipole. However, since each dipole
 765 is only ~ 14 m in length, this curvature is hardly noticeable, as shown in a photo of an actual
 766 dipole magnet in a staging area at CERN, awaiting installation in figure ??(e).

767 Quadrupole, septupole, octupole, and other multipole magnets are used to focus a single
 768 beam, as well as squeeze the two beams together. There are 392 quadrupole magnets on the
 769 LHC ring, each controlling the height and width of the beam. Figure 3.13(a) shows a schematic
 770 of a dual-bore quadrupole magnet, and figure 3.13(b) shows an actual quadrupole in a staging
 771 area before installation. Quadrupole magnets use four sets of coils to create a magnetic field that

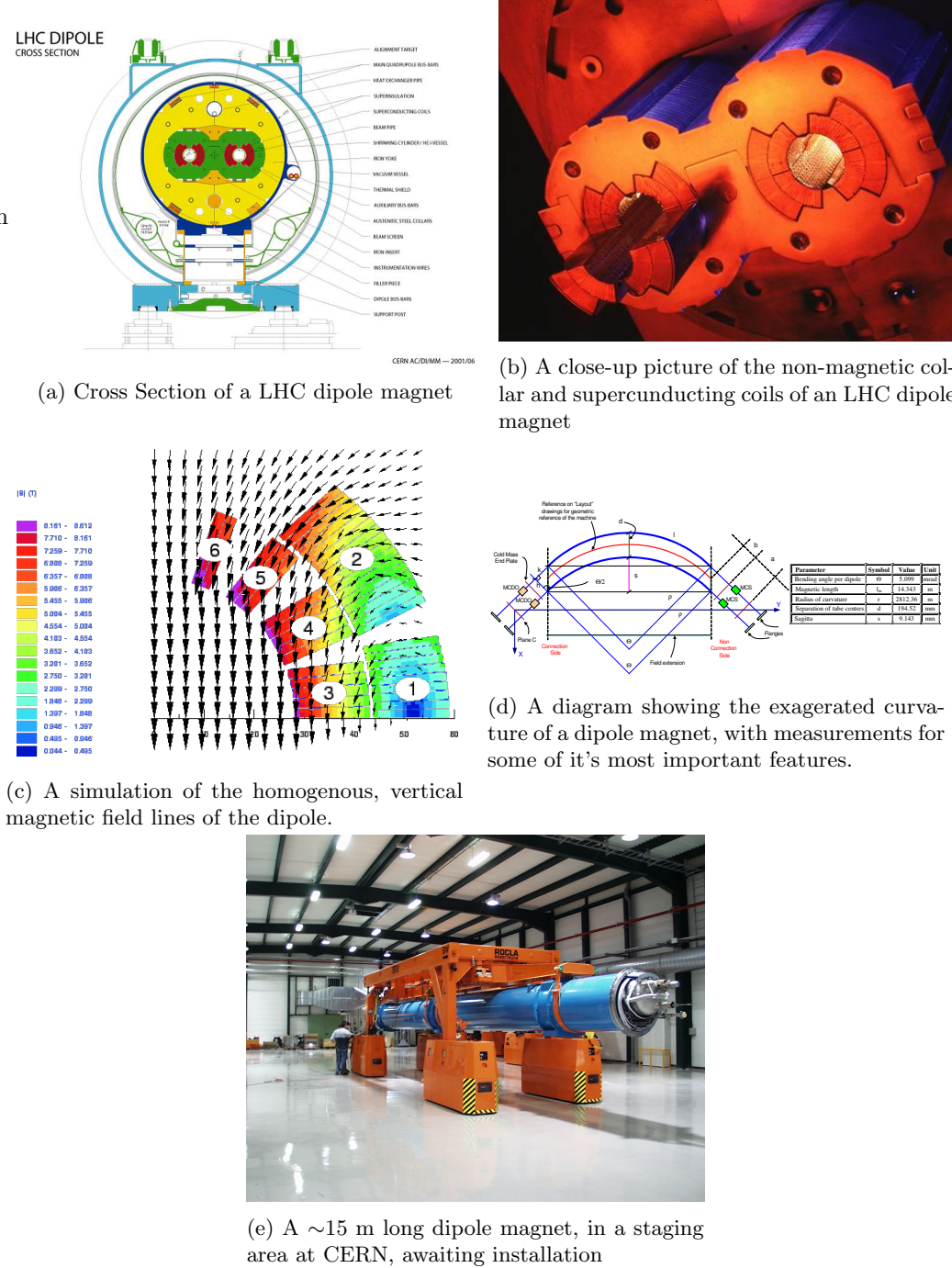
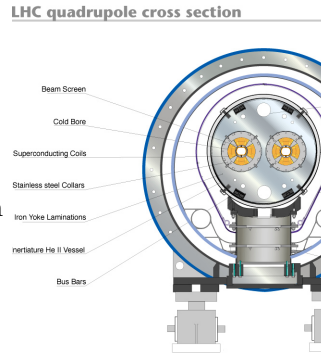


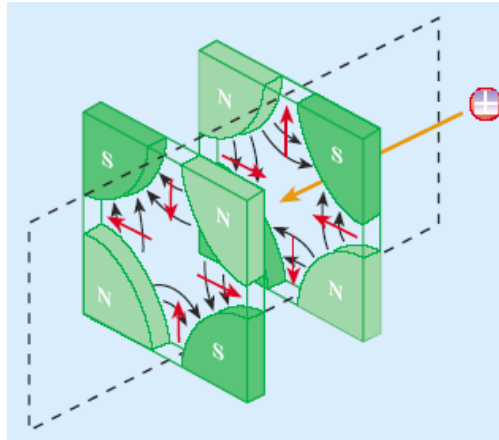
Figure 3.12: Features of the dipole magnets used in the LHC



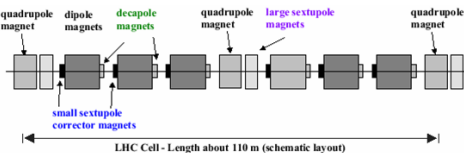
(a) Cross Section of a LHC quadrupole magnet



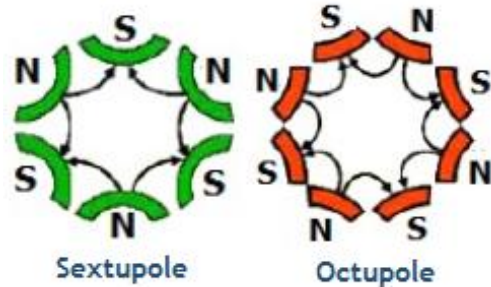
(b) A dual-bore quadrupole magnet, in a staging area prior to installation



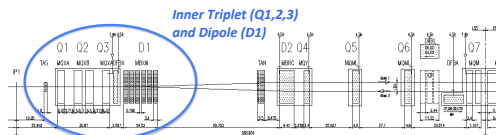
(c) A quadrupole magnet can provide focusing either in the horizontal or vertical direction



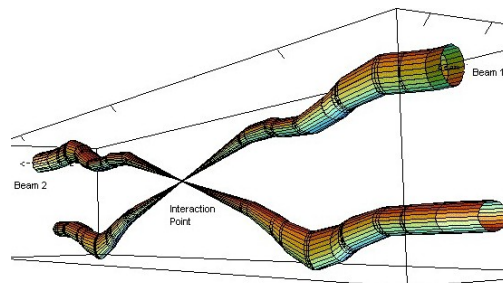
(e) A typical 110m long magnetic cell at the LHC featuring several types of multipole magnets



(d) Multipole fields from a sextupole and an octupole magnet



(f) Schematic of the Inner triplet structure that brings the two separate beams together in the interaction region



(g) A simulation of two beams being squeezed together by the inner triplet.

Figure 3.13: Features of the dipole magnets used in the LHC

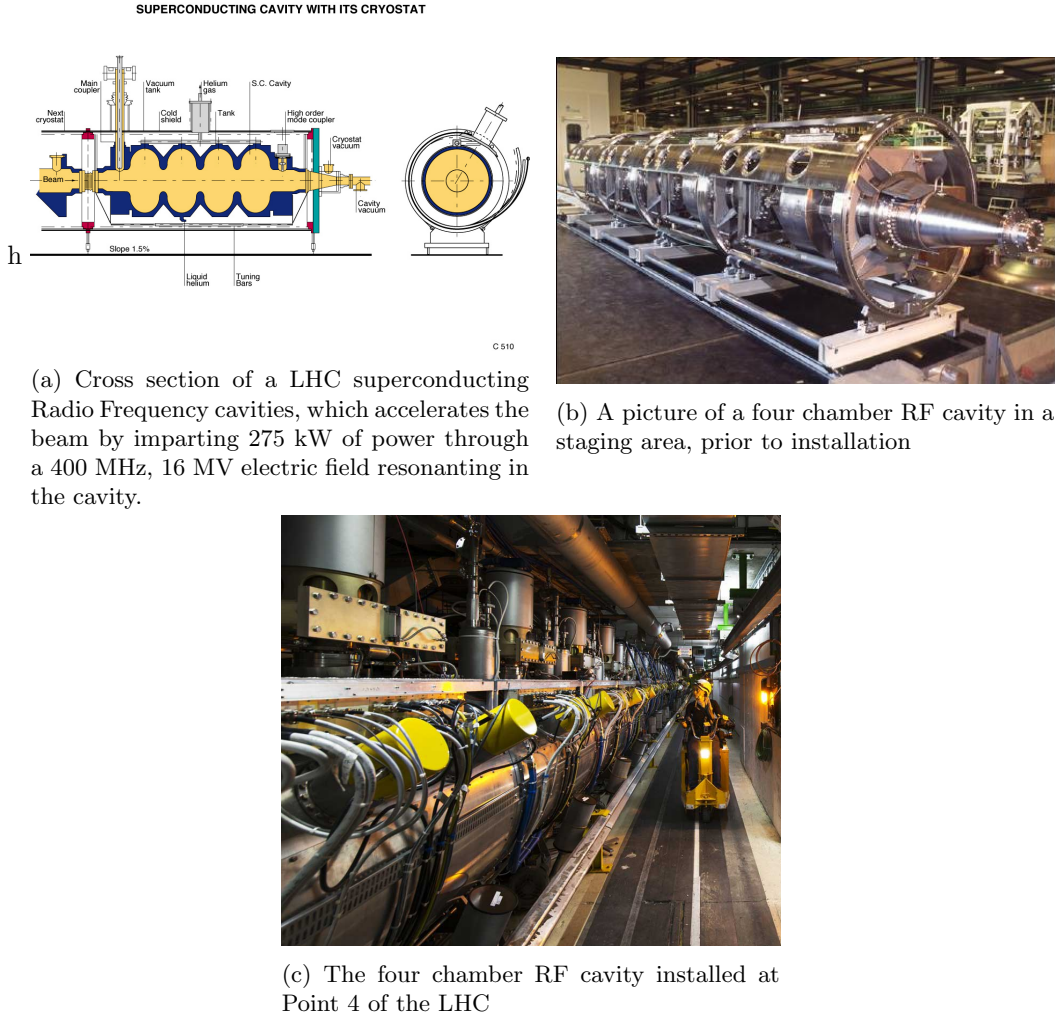


Figure 3.14: Features of the 400 MHz superconducting RF system used in the LHC

either squeezes the beam horizontally or vertically, as shown in figure 3.13(c). Finer corrections to the beam shape are made with the multipole magnets, since they are able to compress the beam from more than two axes. Figure 3.13(d) shows the fields lines of a sextupole and octupole magnet. A typical cell of magnets, 110 m long, in the LHC beamline is shown in a diagram in figure 3.13(e), where the dipole, quadrupole and higher order magnet work in series to confine the protons to the LHC ring. Finally, a set of single bore magnets, known as an inner triplet, bring the two beams together into an interaction region. Figure 3.13(f) shows the arrangement of magnets that squeeze the beam together, while figure 3.13(g) shows a simulation of the beams being brought together to collide in the interaction region.

3.3 LHC RF Technology

The LHC uses a 400 MHz superconducting RF cavity system to capture and accelerate the beam from 450 GeV to 7 TeV [54]. Two independent system are used to provide 8 MV of RF voltage

at injection at 16 MV during equilibrium at 7 TeV and deliver 275 kW of power to each beam. This is provided by 16 niobium sputtered cavities, housed in 4.5 K refrigeration units, known as cryomodules, at Point 4 of the LHC octant. The superconducting material covering the inside of the cavity has near-zero resistivity, which dissipates much less power and has a much narrower resonance width, or Q-factor, than a cavity made from normally conducting material. Figure 3.14(a) shows a schematic of a four cavity cryomodule. The beam pipe passes through the center of each chamber and longitudinal (left to right in the diagram) electric fields accelerate the protons each time they circulate the LHC ring. Figure 3.14(b) shows an actual four cavity module in a staging area prior to installation. In this picture, the resonance cavities are concealed underneath the cylindrical housing of the vacuum tank and cryostat. Figure 3.14(??) is a picture of the module installed at Point 4. The thin cylindrical structures extending off the top is the LHe intake valve and quench system. The thicker cylindrical structures are the waveguides that couple the cavities to the source of the electric field, the klystrons.

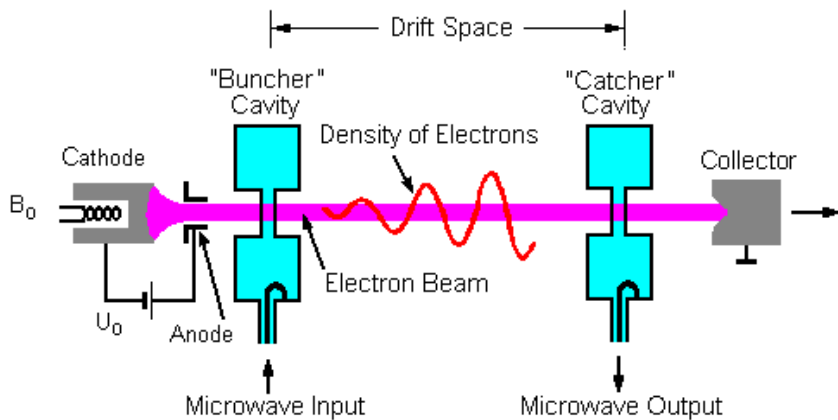


Figure 3.15: A klystron uses a weak RF signal coupled to a resonance cavity to bunch an electron beam, which in turn creates an amplified RF signal as it passes through a second resonance cavity tuned to the same frequency.

A Klystron is the source of RF power that builds up as a resonance in the cavities that accelerate the protons. Figure 3.15 shows a diagram of the basic operating principle. The device uses an anode to accelerate the thermionic emission of electrons off of a cathode material into one or more bunching cavities tuned to the frequency the device is designed to produce. This cavity is driven with a weak RF source, that groups electrons into bunches. Just as discussed for protons earlier, when electrons arrive at the entrance of the cavity at just the right time, it will experience the zero-point of the oscillation of the resonating electric field. If it arrives early or late, it is accelerated or decelerated and thus bringing it closer to its neighbors, and increasing the density of the beam. After passing through multiple chambers, the tightly bunched electrons enter a catcher cavity tuned to the same resonance frequency. As the electrons pass through at

807 this resonance frequency, standing electric waves are excited and quickly build up in the catcher
 808 cavity. The electron beam is thus used to amplify the original RF signal in the catcher cavity,
 809 which is then transported via waveguide to power the RF cavity used to accelerate the proton
 810 beamline.

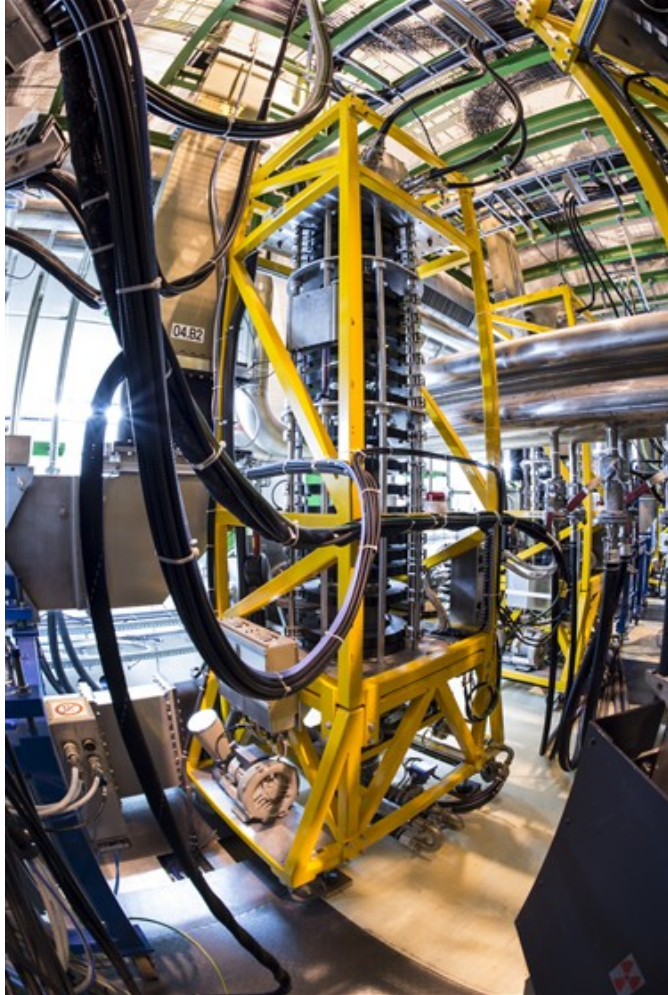


Figure 3.16: One of sixteen 300 kW, 400 MHz klystrons that power the superconducting RF cavities that accelerate the proton beam.

811 At the LHC, 16 400 MHz, 300 kW kylstrons, work together to provide 4800 kW of power
 812 to the superconducting RF cavities [54]. They are also located at Point 4, in the UX45 service
 813 cavern adjacent to the RF cavities, about 6 m below the beamline. An average of 22 m of
 814 waveguide is used to transport the power generated by the kylstrons to the RF cavities. Figure
 815 3.16 shows a kylstron installed at the LHC, and like most modern kylstrons, it also utilizes a
 816 multi-bunching chamber design.

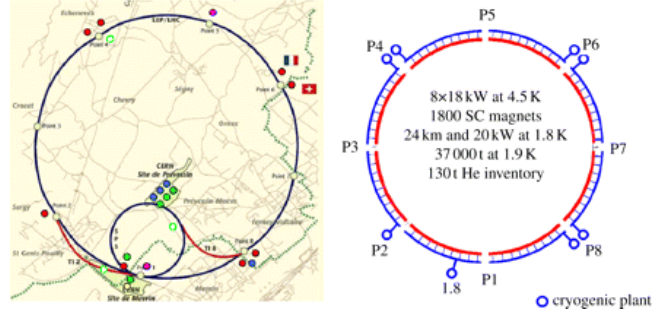


Figure 3.17: Layout of the five cryogenic islands, which are home to the eight facilities that provide liquid helium to the LHC



(a) The compressor station for the 4.5 K refrigeration system

(b) The 4.5 K refrigeration system cold box, containing heat exchanging fins and turbines to cool the He

Figure 3.18: Features of the 4.5 K refrigeration system

3.4 The LHC Cryogen System

The LHC is the largest cryogenic system in the world [66], as its operating temperature is 1.8 K, in order to produce the high-magnetic fields needed by the dipole magnets. Additionally, the acceleration mechanism, the RF cavities, are also superconducting, and must be cooled to 4.5 K. Over 120 tons of Helium are used as the cryogenic medium, since once it is cooled below 2.17 K, it becomes a superfluid, a phase of matter with a high thermal conductivity, making it ideal for refrigeration. Cryogenic and auxiliary equipment are concentrated into 5 cryogenic islands at Points 1, 2, 4, 6, and 8 [54]. As shown in figure 3.17, Point 4, 6, and 8 house two facilities each, making a total of eight, one for each octant of the LHC arc.

At each cryogenic plant, He is cooled to 80 K by circulating it through refrigeration equipment with liquid nitrogen in the heat exchangers [66]. Next, the He is brought to 4.5 K with refrigerators recovered from the LEP experiment [67]. The He gas is first compressed and allowed to expand, where it is cooled by losing energy through mechanical turbo-expanders that run at up to 140,000 rpm on helium-gas bearings. Figure 3.18(a). The He is then liquified after passing through a vacuum sealed box containing heat exchangers and more turbo-expanders [68].

832 The compressor for this system is pictured in figure 3.18(b). Finally, the liquified He is brought
 833 to 1.8 K with a refrigeration unit that uses a cold compression train to decrease the saturation
 834 pressure, and thus temperature as well.

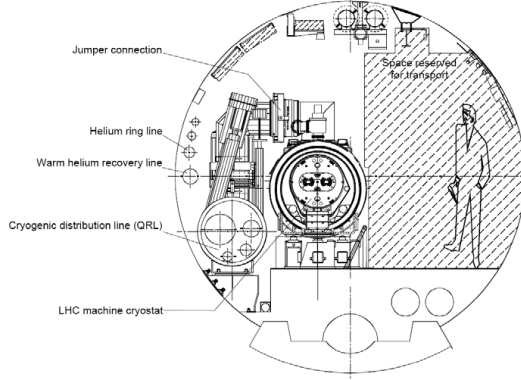


Figure 3.19: Cross section schematic of the cryogenic distribution system in the LHC tunnel

835 In the LHC tunnel, a cryogenic distribution line runs parallel to the machine [67]. It consists
 836 of eight 3.2 km long cryostats, that contain the equipment to supply and recover helium with
 837 temperatures ranging from 4 K to 75 K. A total of 310 service modules, are used to control the
 838 system and provide safety mechanisms against pressure buildup and magnet quenching. Figure
 839 shows a cross section of the cryogen distribution system in the tunnel.

840 3.5 The LHC Vacuum System

841 The LHC is also the largest operational vacuum system in the world and is capable of achieving
 842 pressures lower than outer space [69]. Three different types of vacuum systems are used: one for
 843 insulating the helium distribution lines, another for insulating the dipole magnets, and a final
 844 ultra-high vacuum system for the beam pipe [54].

845 The vacuum systems for insulating the helium distribution and dipoles involves some 104 km
 846 of piping an over 250,000 welding joints [69]. Pressure here is required to be kept at 10^{-1} mbar,
 847 but at cryogenic temperatures, pressures tend to equalize at a much lower level, to 10^{-6} mbar
 848 ($\sim 10^{-9}$ atm) [54].

849 The most stringent requirements come on the vacuum of the beam-pipe. The beam must
 850 minimize the number of interactions it has with any particles outside of the interaction region.
 851 A pressure of 10^{-10} to 10^{-11} mbar are maintained in the 54 km of beampipe [69]. Weeks of
 852 cryogenic pumping, eventually condenses gas trapped in the beampipe into a liquid that can be
 853 absorbed by the walls of the beampipe. The inside beampipe is also coated with a thin layer



Figure 3.20: Beam screen for the LHC, with slits to allow for easy pumping of residual gas molecules in the beampipe.

of a special substance developed at CERN, a titanium-zirconium-vanadium alloy, which absorbs residual particles when heated. 780 ion pumps are used to remove the noble gases and methane, which do not interact with the substance, which acts as its own distributed pumping system. Room-temperature sections of the beampipe are also heated to 300^{deg} to be baked-out from the outside. This is done to periodically remove any material which may have settled and become trapped. Additionally, the beam-pipe is designed with a racetrack shape, which optimises the available aperture while leaving space for the cooling tubes, as shown in figure 3.20. Slits also allow for gas molecules to be easily pumped out from inside its volume.

862 **Chapter 4**

863 **The Compact Muon Solenoid**

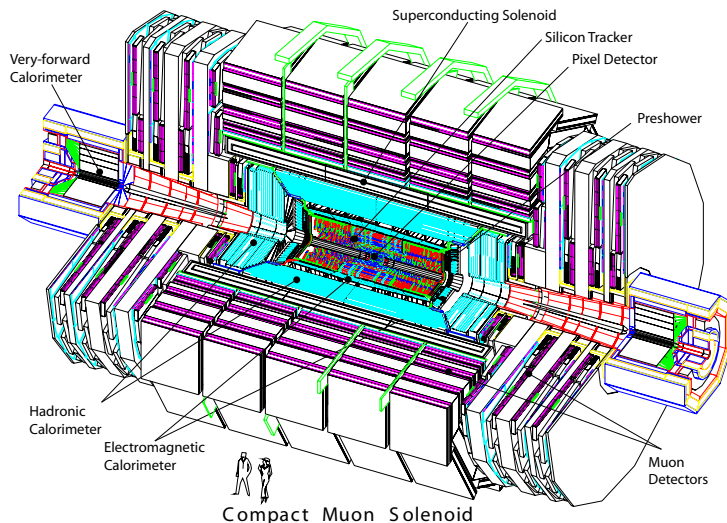


Figure 4.1: A cutaway diagram of the CMS detector. Two humans are present at the bottom of the image to provide scale.

864 The Compact Muon Solenoid (CMS) experiment is a general-purpose particle detector ca-
865 pable of performing a wide range of physics measurements at the TeV energy scale. It provides
866 hermetic, 4π , coverage surrounding the interaction region on Point 5 of the LHC octant, and
867 is capable of identifying and reconstructing charged and neutral hadrons, photons, electrons,
868 and muons directly. Tau leptons, are measured indirectly through a careful reconstruction of
869 its decay products. The hermetic coverage allows the detection of neutrinos by measuring a
870 momentum imbalance in a given collision. The detector is assembled in five sections and weights
871 over 14,000 tons. The "Compact" part of the experiment's name comes from its relativley small
872 volume for a modern particle detector, with length of 28.7 m and a diameter of 15.0 m. Ironi-
873 cally, this is as tall as most 4-5 story buildings and weights as much as \sim 7000 cars. Figure 4.1
874 shows a cutaway drawing of the CMS detector.

A right-handed coordinate system is used to measure particle positions within the detector. The origin is centered at the nominal interaction point with the \hat{x} direction pointed towards the center of the LHC ring, the \hat{y} direction towards the sky, and the \hat{z} direction pointed counter-clockwise along the LHC ring towards Point 2 and the ALICE experiment. In the much more natural polar coordinates, \hat{r} , points radially outward from the interaction point, the azimuthal angle $\hat{\phi}$ is measured as the angle relative to the \hat{x} axis, and the polar angle, $\hat{\theta}$, is measured as the angle relative to the \hat{z} axis. An important lorentz invariant position variable is the rapidity, y , and its approximation in terms of the polar angle, the pseudorapidity, η :

$$\begin{aligned} y &= \frac{1}{2} \ln \left(\frac{E + p_z c}{E - p_z c} \right) \\ \eta &= -\ln \left(\tan \frac{\theta}{2} \right) \end{aligned} \quad (4.1)$$

The psuedorapidity is useful since it is an approximately lorentz invariant version of polar angle, which allows for a more intuitive understanding of the distribution of particles when boosting into different measurement reference frames. The component of the momentum transverse to the beamline, p_T is the most common form of measuring the momentum, and is defined as $p_T = |p| \cos \phi$.

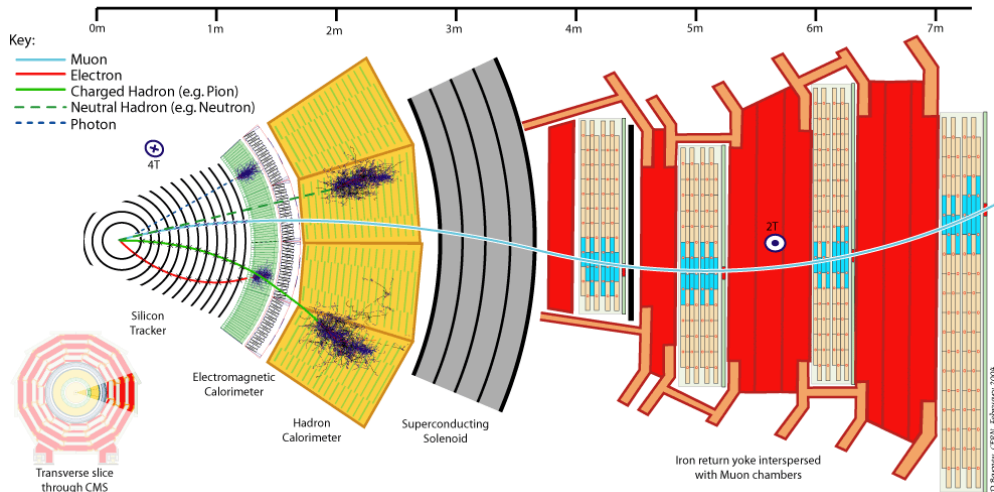


Figure 4.2: A slice of the CMS detector showing how various particles interact and deposit energy. The trajectory of charged particles is measured in the tracker; electrons and photons deposit most of their energy in the ECAL; charged and neutral hadrons deposit most of their energy in the HCAL; the muon chambers measures the trajectory of muons or long-lived charged particles

CMS is composed of a system of sub-detectors, each specialized in measuring a certain type or characteristic of a particle. They are arranged approximately as concentric cylinders of increasing radius, wrapped around the interaction region of the pp collisions and an analogy is often made between the layers of subdetectors being similar to the layers of an onion. The closest sub-

detector to the interaction region is the tracker system. It is an all silicon pixel and strip detector, with a high precision position resolution, which is used to identify the trajectory of charged particles close to the primary vertex of a collision. The Electromagnetic Calorimeter (ECAL) is the next layer, and is used to absorb energy of electromagnetically interacting particles. It uses lead-tungstate (PbWO_4) crystals which act as both the absorbing and scintilating medium for energy deposited by charged particles and photons as they pass through this sub-detector. The Hadronic Calorimeter (HCAL) uses brass and steel tiles to absorb energy and induce hadronic interactions, while a plastic scintillator material layered between the absorber tiles samples the energy of hadrons. The tracker, ECAL, and HCAL systems are all contained in the bore of the 3.8 T solenoid from the CMS namesake. This device bends the trajectory of charged particles as they traverse the detector, and the curvature of this bend is used to obtain information on the charge and momentum of the measured particle. The muon system sits outside of the solenoid structure, and uses three types of detection systems: drift tubes (DTs), resistive strip chambers (RPCs) and cathode strip chambers (CSCs), which provide excellent timing and position resolution. The return yoke structure of the magnet also provides the mechanical support for the muon chambers. Figure 4.2 shows a slice of the CMS experiment showing how various particles interact and traverse the different sub-detector regions, as described above.

At center-of-mass energy of $\sqrt{s} = 14 \text{ TeV}$, the expected event rate is approximately 10^9 events/second. This is too much information to store and analyze, and is mainly dominated by Standard Model QCD multi-jet production, a background for searches for new particles or physics. An online event selection, or trigger, must be used to reduce this rate to a manageable 100 events/second. This is achieved through a combination of hardware, firmware, and software that provides a rough reconstruction of events in near real-time, and makes a decision about whether it meets a minimum set of criteria to be used in an analysis.

4.1 The Tracker

The innermost sub-detector is an all silicon pixel and strip tracker designed to provide precise and efficient measurement of the trajectories of charged particles and reconstruction secondary vertices necessary for identification of b -jets and τ leptons.

At peak LHC design luminosity of $10^{34} \text{ cm}^{-2} \text{ s}^{-1}$, and bunch spacing of 25 ns, there will be ~ 1000 particles from 20 overlapping pp collisions for each bunch crossing. This corresponds to a hit rate density of 1 MHz/mm^2 at a radius of 4 cm, 60 kHz/mm^2 at 22 cm, and 3 kHz/mm^2 at 115 cm from the beam line. This large particle flux will also cause intense radiation damage to detector components. These conditions necessitate the use of radiation-hard silicon, with a high-

925 granularity to create a low occupancy for each detector element, which are read out by fast
 926 electronics. Additional mitigation of the effects of radiation damage is taken by cooling and
 927 operating the entire detector to -10° C in order to maintain a signal to noise ratio of 10:1 for
 928 the sensors. After 10 years of running, it is anticipated that this will need to decrease to -27° in
 929 order to compensate for the accumulated damage.

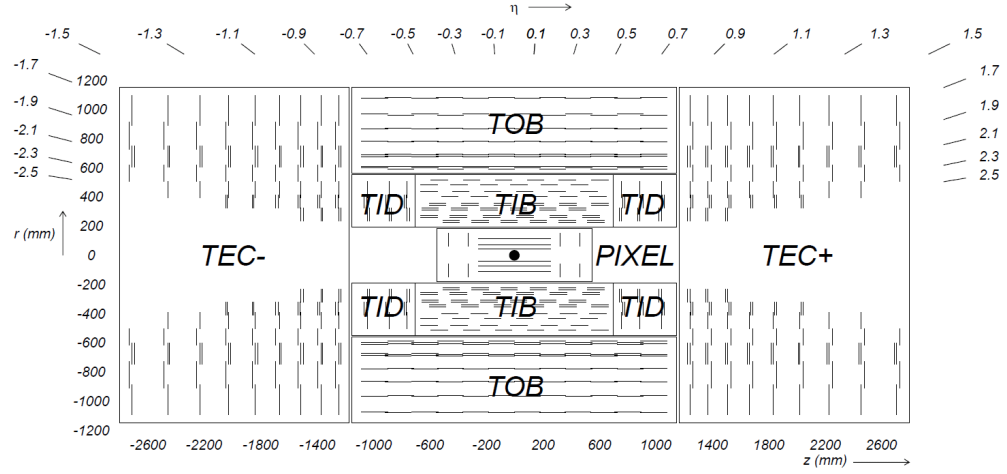


Figure 4.3: A side view of the tracker. The pixel detector is the innermost sub-system, with three concentric rings of detectors in the barrel, and two in the endcap. The tracker inner barrel (TIB) is a silicon strip detector, with four concentric rings. The tracker inner disks (TID) are three layers deep. The tracker outer barrel (TOB) is six concentric rings and the tracker end caps (TEC) are nine layers deep.

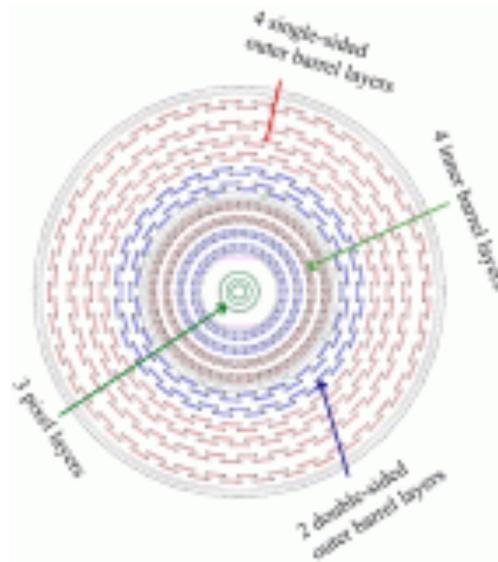


Figure 4.4: A head-on view of the beamline and barrel components of the tracker.

930 The tracker has a cylindrical shape that surrounds the interaction region, with a length of
 931 5.8 m and a diameter of 2.5 m. The large particle flux close to the beamline requires the use
 932 of a pixel detector sub-system in the innermost region, from radius 4.4 cm to 10.2 cm from
 933 the beamline. The particle flux drops off sufficiently at larger radii to use silicon strip detectors,

arranged into four different sub-systems: the tracker inner barrel (TIB), tracker inner disks (TID), tracker outer barrel (TOB) and tracker end caps (TEC), which extend to a radius of 1.2 m from the beamline. Figure 4.3 shows a side view of the tracker layout and figure 4.4 shows a view down the beamline of the barrel sections. The tracker has a total acceptance of $|\eta| < 2.5$.

There are competing factors for the radial length of the tracker. More layers allow for more samples of a particle's trajectory, giving a higher spatial precision, but more material means photons and hadrons are more likely to decay, and create a shower of particles that would better measured through the absorption of energy via calorimeters. The depth of the tracker varies from 0.4 to 1.8 radiation lengths, resulting in small degradation of the ECAL performance, since approximately half the photons will be converted to e^+e^- pairs.

4.1.1 The Silicon Pixel Detector

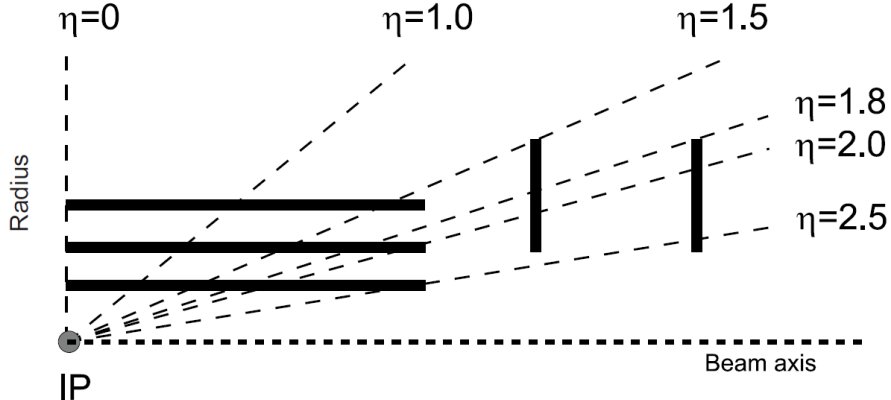


Figure 4.5: The three barrel and two disk layers of the silicon pixel tracker provide coverage of $|\eta| < 2.5$

The pixel detector consists of 66 million $100 \times 150 \mu\text{m}$ pixels, arranged in three concentric cylindrical layers of radius of 4.4, 7.3, and 10.2 cm from the beam line and two disc layers on either side of the barrel detectors. Figure 4.5 shows the eta coverage of the detector out to $|\eta| < 2.5$.

The sensor technology uses a n -on- n concept, where a high-dose n -implant is introduced onto a n -substrate with large resistance. A $p - n$ junction is made by the placement of a p -type semiconductor on the back side of the substrate. When a charged particle passes through the face of the substrate, between the $p - n$ junction, it liberates electrons from the silicon atoms, creating electron-hole pairs. The p -side has a voltage bias of 150 V in the barrel, and 300 V in the disks, that sweeps the pair apart, creating a current. Pixels are isolated from one another using a moderated p -spray in the barrel region, and open p -stops in the disks in order to create an additional $p - n$ structure that acts like a diode to limit current flow between pixels. The 3.7 T

957 magnetic field of the CMS solenoid also induces a Lorentz drift of the current in the $\hat{\phi}$ direction.
 958 This results in the current produced in one pixel being shared among multiple neighboring pixels.
 959 The charge collected by each of the multiple pixels are read-out, using an interpolation between
 960 pixels, resulting in a $15\text{-}20 \mu\text{m}$ spatial resolution on the trajectory of the charged particle - much
 961 smaller than the size of an individual pixel. In order to induce this effect in the disks (where the
 962 pixels are orientated perpendicular to the barrel), the pixels are angled 20° in the \hat{y} direction.

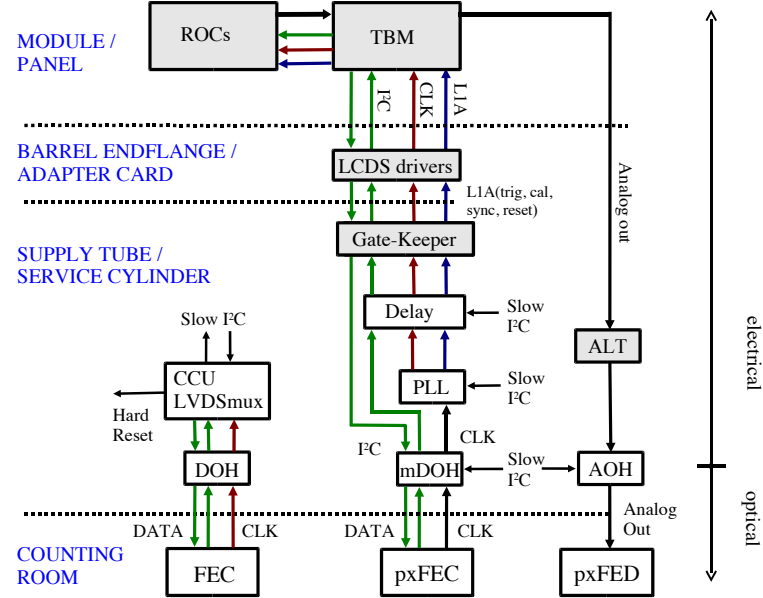


Figure 4.6: The readout electronics chain for the pixel detector

963 The current created by the charged particle is collected by a readout chip (ROC) that is
 964 soldered with a bump bond type connection to the pixel. The ROC is a custom ASIC chip,
 965 that processes the signals for a grid of 52×80 pixels. It provides amplification, buffering, and
 966 zero suppression (threshold) of the charge from each pixel. Depending on the layer, 8-16 ROCs
 967 in the barrel, and 21-24 ROCs in the disks are connected and read-out by a single token bit
 968 manager (TBM) chip. This chip communicates information from the sensors to the trigger
 969 system, which is used to determine whether a given event is stored as data for analysis later.
 970 The pixel front end controller (pxFEC) interfaces with the ROC and TBM and provides central
 971 clocking and communicates to the CMS data acquisition system. The pixel front end digitizer
 972 (pxFED) converts the analog signals from the ROC and TBMs. A total of 40 pxFED (32 in the
 973 barrel and 8 in the disks) modules are used to read-out the entire pixel detector, and figure 4.6
 974 shows a schematic of the pixel read-out chain.

975 The resolution of the pixel detector was measured in 2012 with $\sqrt{s} = 8 \text{ TeV}$ pp collision. The
 976 residual distance between the hit position recorded by a pixel, and an interpolated track that

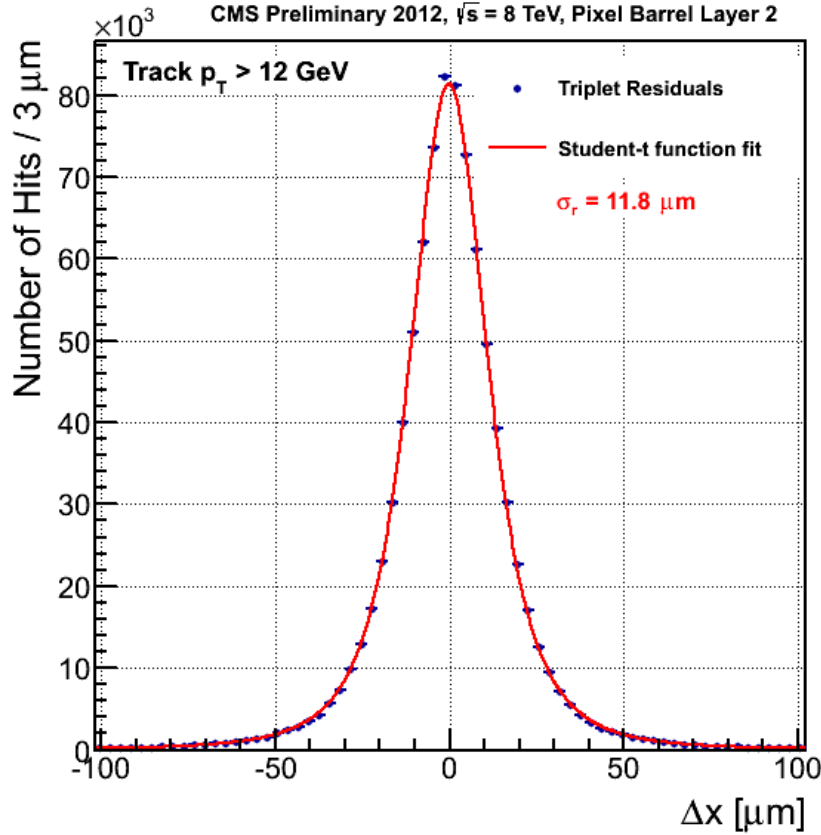


Figure 4.7: In 2012 pp collisions at $\sqrt{s} = 8$ TeV, the pixel detector performed with a resolution of $11.8 \mu\text{m}$. The above is a plot of the residual difference between a pixel and the results of a fit to a particle track.

977 uses that hit is plotted and fit with a student-t function in figure 4.7. For tracks with $p_T > 12$
 978 GeV, the pixel detector was found to have a spatial resolution of $11.8 \mu\text{m}$.

979 4.1.2 The Silicon Strip Detector

980 As shown in figure 4.3, the silicon strip tracking system has four components: the tracker inner
 981 barrel (TIB), tracker inner disks (TID), tracker outer barrel (TOB) and tracker end caps (TEC).
 982 A total of 15,148 detector modules are distributed among these systems, each with either one
 983 $320 \mu\text{m}$ thick sensor, or two $500 \mu\text{m}$ thick sensors, making 24,244 sensors with an active area of
 984 198 m^2 of silicon. A model with two sensors is shown in figure 4.8. Each sensor has either 512
 985 or 768 strips since they are read out by two multiplexed 128-channel front end chips, making it
 986 possible to only read out sensors in groups of 256. Each strip has a pitch that varies between 80
 987 and $200 \mu\text{m}$ and lengths that vary between 10 and 25 cm. All in all, 9.3 million strips are used
 988 in the silicon tracker.

989 The TIB and TID provide radial coverage from 20 to 55 cm. The TIB has four barrel layers,
 990 with $80 \mu\text{m}$ pitch strips on the first two layers, and $120 \mu\text{m}$ strips on the outer two, giving a single

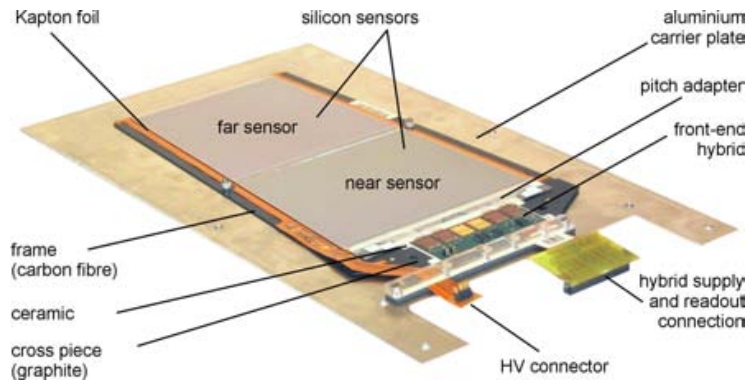


Figure 4.8: A silicon strip module, with two $500 \mu\text{m}$ thick sensors.

point resolution of 23 and $35 \mu\text{m}$ respectively. The strip pitch varies between 100 and $141 \mu\text{m}$ in the three discs of the TID. The TOB surrounds the TIB/TID and is composed of six barrel layers that extend the tracker radius to 116 cm. It is composed of $500 \mu\text{m}$ thick strip sensors, with pitches of $183 \mu\text{m}$ in the first four layers and $122 \mu\text{m}$ in the outer two layers. It provides 6 measurement points of the particle trajectory with a single point resolution of 53 (35) μm in the first four (last two) layers. Each TEC is made of 9 discs, each with 7 rings of strip detectors. The inner four rings of each disk use the single, $320 \mu\text{m}$ thick strip modules, while the outer three rings use the double, $520 \mu\text{m}$ thick strip modules. The average pitch varies between 97 to $184 \mu\text{m}$ in each of the rings. In the first two layers of the TIB, the first two rings of the TID, the first two layers of the TOB, and rings 1, 2, and 5 in each disk of the TEC contain modules mounted back-to-back, with an angle of 100 mrad between them to provide a two-dimensional measurement of a particle's trajectory.

Each of the strips is a single sided p -on- n type silicon sensor manufactured on 6 inch wafers, with a base material of n doped silicon. The front side of the wafer is implanted with a p^+ type semiconductor. A uniform n^+ implantation on the back forms the ohmic contact to 500 V. This forms a pn junction and when a charged particle passes through the face of the wafer, atoms in the junction are ionized and the 500 V potential difference creates a current out of the resulting electron/hole pairs. This current is collected and processed through the read-out system.

A custom integrated circuit, the APV25, is used to amplify, shape, and buffer the signals produced from the silicon strips. It has 128 read-out channels, and samples the detector signals at the 40 MHz, suitable for the 25 ns collisions. It is able to store data for up to 4 μs to account for trigger latency. Two APV25 chips are linked with fiber optics to the Front End Driver

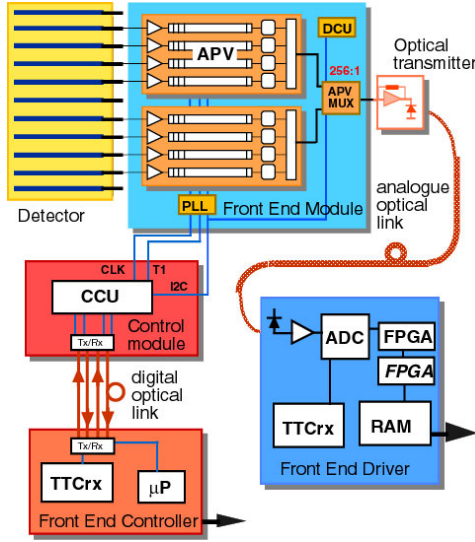


Figure 4.9: Schematic of the readout sequence of the silicon strip detector.

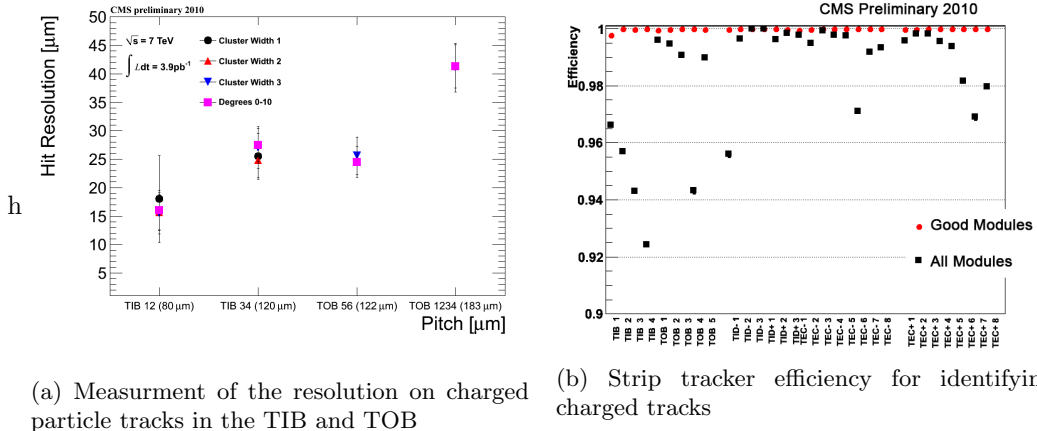


Figure 4.10: Measurements of the performance of the silicon strip track using pp collisions from 2011 at $\sqrt{s} = 7 \text{ TeV}$

1013 (FED) system. Each FED receives data from 94 optical fibers, and digitizes them in parallel.

1014 The Front End Controller (FEC) transmits clock, trigger, and control data to the APV25s. The
1015 entire readout chain is shown in figure 4.9.

1016 In 2011, the strip efficiency and resolution were measured from data in center-of-mass energy,
1017 $\sqrt{s} = 7 \text{ TeV}$ pp collisions. Figure 4.10(a) shows the resolution varying between $15\text{--}40 \mu\text{m}$ for the
1018 TIB and TOB detectors. Figure 4.10(b) shows the efficiency for reconstructing tracks with the
1019 strip tracker, which is well above 99% when only considering operational modules.

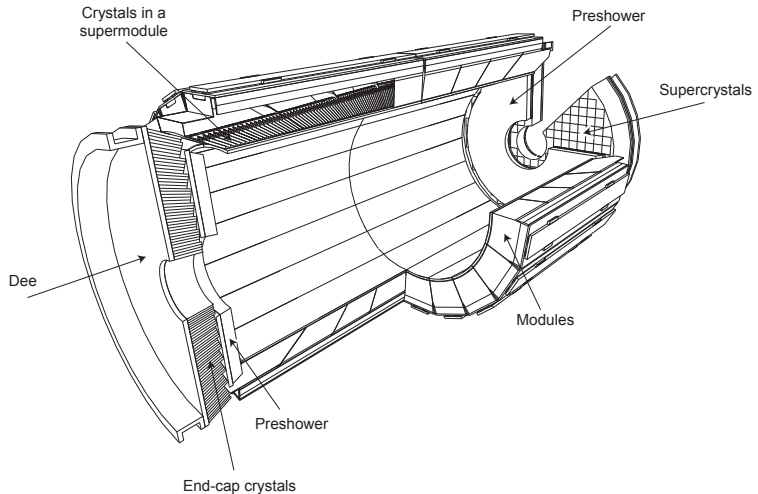


Figure 4.11: Layout of the ECAL sub-detector

1020 4.2 The Electromagnetic Calorimeter

1021 The Electromagnetic Calorimeter (ECAL) surrounds the inner tracker with 61,200 high density
 1022 lead tungstate (PbWO_4) crystals in the central barrel section, and 7,324 crystals in each of
 1023 the two endcaps. The crystals have a fast response, provide fine granularity, and are radiation
 1024 resistant, making them ideal for the LHC environment and the physics goal of observing the
 1025 Standard Model Higgs boson decay to two high energy photons. The primary background for
 1026 this process comes from neutral pions decaying to two photons, which is especially difficult when
 1027 the photons are close together and can potentially be reconstructed as a single high-energy
 1028 photon. This occurs most frequently in the endcaps, so an additional detector, the preshower,
 1029 provides additional spatial resolution with silicon microstrip detectors, similar to those in the
 1030 tracker. Figure 4.11 shows the layout of the ECAL.

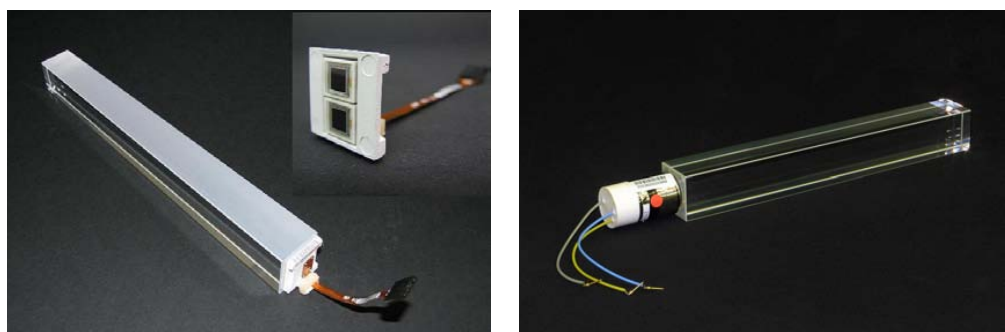


Figure 4.12: Typical Lead Tungstate crystal, with APD attached to the rear face in the left frame, and a VPT attached in the right frame.

1031 Lead tungstate is an ideal material for electromagnetic calorimetry. Figure 4.12 shows a
 1032 typical crystal, with photomultipliers attached to the rear faces, which will be discussed later.

1033 The material has a high density, 8.28 g/cm^3 , giving it a large electromagnetic cross-section,
 1034 making it much more likely for a particle traversing the crystal to interact with one of the atoms
 1035 in its structure. When a particle interacts with the crystal, it does so by depositing energy into
 1036 its atoms, which excite the electrons that are bound to it. The atoms then relax by emitting
 1037 photons, in a process known as scintillation and the PbWO_4 crystals release 80% of their light
 1038 in the 25 ns LHC bunch crossing time. This light is collected by photomultipliers attached to
 1039 the rear face of the crystal and converted into an electrical signal. Read-out electronics amplify,
 1040 digitize, and buffer the signal until it can be stored as data or discarded.

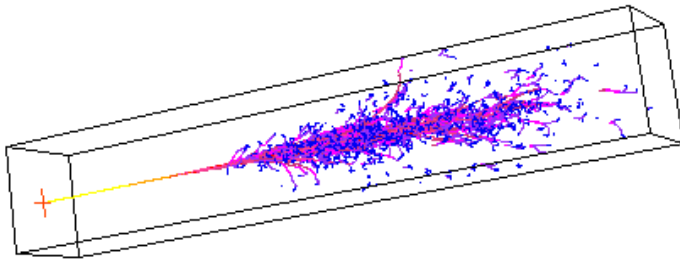


Figure 4.13: A simulation of the evolution of a electromagnetic shower being initiated by an electron entering the center of the front face.

1041 As a charged particle or photon begins to deposit energy, it begins a decay chain into many
 1042 lower energy photons and electrons, known as an electromagnetic shower. Electrons, being
 1043 bent by the CMS magnetic field, and multiple scattering off of the PbWO_4 crystals, create
 1044 bremsstrahlung photon radiation. Since the intensity of bremsstrahlung is inversely proportional
 1045 to the mass of the particle squared, particles heavier than electrons such as muons and hadrons
 1046 do not leave a large signature in the ECAL. Photons convert to e^+e^- pairs, which in turn create
 1047 additional bremsstrahlung. The crystals have a short radiation length, $X_0=0.89\text{cm}$, which is the
 1048 distance it takes an electron to deposit $1/e$ of its energy through bremsstrahlung, and $7/9$ of
 1049 the mean free path of a high energy photon before it converts to an e^+e^- pair. A corollary
 1050 of the crystal's short radiation length is its small Moliere radius, 2.2cm , which is the radius of
 1051 a cylinder that encloses 90% of the electromagnetic shower's energy deposition. A typical
 1052 crystal has a front face that is $22\times 22 \text{ mm}^2$, a rear face of $26\times 26 \text{ mm}^2$, and a length of 230 mm ,
 1053 or $25.8 X_0$ radiation lengths. This means that a relatively small grid of crystals can be used to
 1054 fully collect the energy deposited by a high energy electron or photon. As previously mentioned,
 1055 heavier charged particles will not bremsstrahlung as much as electrons, and will travel through
 1056 the entire ECAL, depositing only a moderate fraction of their energy in the crystals. Figure 4.13
 1057 shows a simulation of an electromagnetic shower produced by an electron entering the front face
 1058 of a crystal.

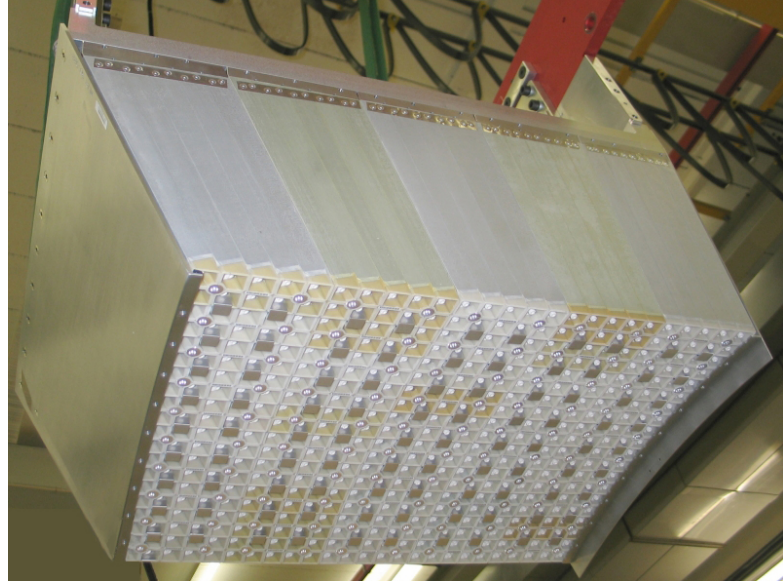


Figure 4.14: A module of 500 crystals (25 crystals wide by 20 crystal tall).

1059 The barrel of ECAL (EB) covers a pseudorapidity range of $|\eta| < 1.479$ with 61,200 crystals
 1060 at a radius 1.29 m from the beam-line. The crystals are positioned in a quasi-projective geometry,
 1061 such that their axes make a 3° angle with respect to the vector pointing to the nominal interaction
 1062 point. This ensures that particles will not pass through the cracks and spaces between crystals,
 1063 and are forced to interact with a portion of the ECAL. Crystals are assembled in groups of
 1064 400 or 500 into modules, as shown in figure 4.14 . Four of these modules are assembled into a
 1065 supermodule contain 1700 crystals, and 36 supermodules make up the barrel region.

1066 The crystals in the EB are read out by Avalanche Photo-Diode (APD) photomultipliers,
 1067 shown in the left frame of figure 4.12. The APDs were manufactured by Hamamatsu and are a
 1068 bulk *n*-type silicon material, with a *p*-type implanted on its surface to form a *pn*-junction. The
 1069 operation principle is similar to that of tracker. When scintillation light from the lead tungstate
 1070 crystals enters the face of the APD, it creates electron-hole pairs in the intrinsic region between
 1071 the *p* implantation and the *n* bulk material. The APD is biased with 45 V, which creates a
 1072 current from the electron-hole pairs and is the signal that a particle has created scintillation in
 1073 the crystal. The APD provides a gain of 50 and has a quantum efficiency of 75%. Both the
 1074 APDs and the PbWO₄ exhibit a strong temperature dependence, so the entire system is kept at
 1075 18° C with a water-based cooling system distributed throughout the barrel and end-caps.

1076 The ECAL readout electronics are designed to read-out a 5×5 array of crystals, known as a
 1077 trigger tower, in the EB, and a single supercrystal in the EE. Each trigger or tower or supercrystal
 1078 consists of 5 Very Front End (VFE) boards, each connected to 5 APDs (VPTs), one Front End
 1079 (FE) board, two (EB) or six (EE) Gigabit Optical Hybrids (GOHs), one Low Voltage Regulator
 1080 (LVR) and a motherboard. Once triggered, the APD (or VPT in the EE) is sampled 10 times, at

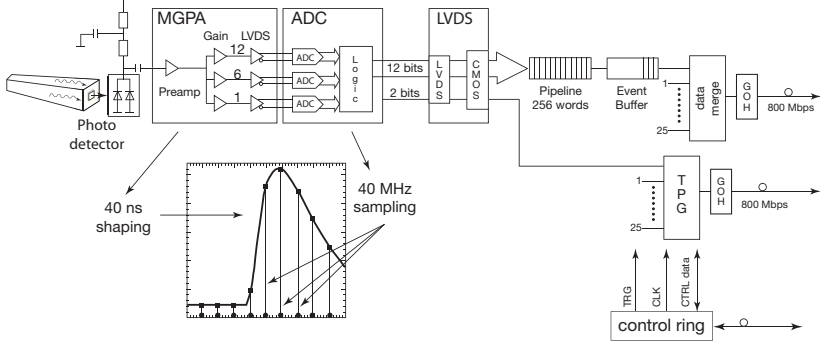


Figure 4.15: Schematic of the On-Detector Readout for the ECAL

1081 a 40 MHz sampling rate, and amplified by a multi-gain amplifier (MGPA), with nominal gains
 1082 of 1, 6, and 12 contained on the VFE. These digitized samples are sent to the FE, where they
 1083 are buffered until receiving a Level-1 trigger, where they are sent to the off-detector elcectronics
 1084 Data Concentrator Card (DCC) via the GOHs. Figure 4.15 shows a schematic of the on-detector
 1085 read-out.

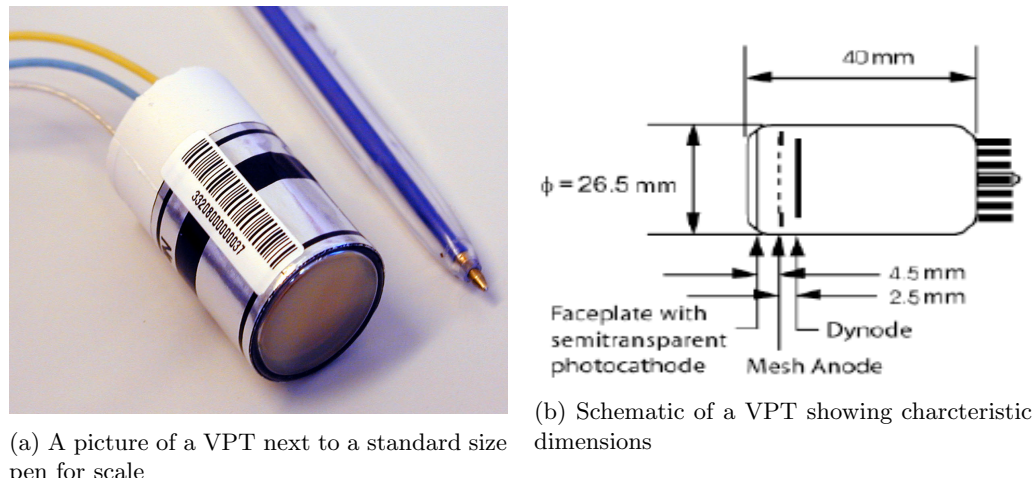
1086 In the barrel, the 5×5 trigger towers are divided in the 5 strips in the $\hat{\phi}$ direction. The energy
 1087 deposits in these strips is summed by the FE cards and define the transvere energy of the tower.
 1088 In the endcaps, supercrystals are divided into groups of five contiguous crystals of variable shape,
 1089 known as psuedo-strips. The energy of these strips is performed by the FE, and the off-detector
 1090 electronics use these to compute the transvere energy deposition.

1091 The preshower detector sits in front of the ECAL end-caps and provides coverage from
 1092 $1.653 < |\eta| < 2.6$. It is a two-layer sampling calorimeter. Lead radiators initiate electromagnetic
 1093 showers from electrons and photons, and silicon strips are placed behind them to measure trajec-
 1094 tories and deposited energy of passing particles. The total thickness is 20cm, which corresponds
 1095 to a 2 raidation lengths in the first layer, and another radiation length in the second layer. 95%
 1096 of photons are converted to e^+e^- pairs after the first layer. Each silicon sensor is composed of
 1097 31 strips, with thickness of $320 \mu\text{m}$ and are 1.9 mm in pitch. A front-end ASIC performs pre-
 1098 amplification, shaping, voltage sampling, and communicates informaiton to the trigger system
 1099 to determine if data is stored or discarded. The structure is formed into Dees, and two Dees
 1100 form a disk with a hole for the beam-line to pass through.

1101 Behind the preshower is the ECAL end-cap (EE). It covers the psuedorapidity range of
 1102 $1.479 < |\eta| < 3.0$, and sits a longitudinal distance of 315.4 cm from the nominal interaction point.
 1103 Crystals are grouped into 5×5 modules known as supercrystals (SCs). Like the preshower, each
 1104 endcap is divided into two sections, Dees, which form a disk with an inner bore for the beam
 1105 line to pass through, as shown in figure 4.16. Each Dee holds 3,662 crystals, which are divided



Figure 4.16: A section of the ECAL end-cap, a Dee. Two Dees form a disk with an inner bore for the beam-line to pass through. 5x5 modules, or supercrystals, are mounted in preparation for installation at CMS



(a) A picture of a VPT next to a standard size pen for scale

(b) Schematic of a VPT showing characteristic dimensions

Figure 4.17: Vacuum Photo-Triode devices used in the ECAL end-caps (EE)

₁₁₀₆ into 138 supercrysals, and 18 special partial-supercrystals for the inner and outer sections of the
₁₁₀₇ Dee.

₁₁₀₈ 4.2.1 Vacuum Photo-Triodes

₁₁₀₉ The photomultier used to readout the lead tungstate crystals in the EE is the Vaccum Photo-
₁₁₁₀ Triode (VPT), shown in the right frame of figure 4.17(a). Each device is 26.5mm in diameter
₁₁₁₁ and 40mm in lenth as shown in figure 4.17(b). It is a gain stage device. Photons from the
₁₁₁₂ lead tungstate scintilation light enter the front face of the VPT and liberate electrons from the
₁₁₁₃ grounded bialkali photocathode (SbKCs) via the photoelectron effect. The cathode material
₁₁₁₄ has a quantum efficiency of $\sim 20 - 25\%$. The photo-electrons are accelerated towards the mesh

1115 anode grid, which is held at 800 V. Approximately half the photo-electrons pass through the
 1116 mesh and encounter a dynode plate held at 600 V. Electrons either collide with the dynode,
 1117 liberating secondary electrons from the collision, or are turned around by the 200 V differenc
 1118 between anode and dynode. Electrons are thus constantly accelerated towards the anode, and
 1119 create secondary electrons as they collide with the anode. The process repeats with the secondary
 1120 electrons, creating an avalanche of charge near the anode. As these charges eventually recombine
 1121 with the anode over the course of a few nanoseconds, the voltage of anode drops, signaling the
 1122 device has detected a photon from the PbWO₄ crystals.

1123 The performance of the VPT is degraded over time by two effects associated with exposure
 1124 to the scintillation light from the crystals. The first is loss of the vacuum inside the tube.
 1125 Molecules from the air become ionized by the large voltages and the positive ions are accelerated
 1126 towards the photo-cathode, which is damaged through the resulting collision. The second effect
 1127 is the gradual depletion of photo-electrons from the bialkali cathode material. The result is a
 1128 decrease in the current, and thus signal, produced by the anode. Both of these effects can be
 1129 effectively modeled as the sum of two falling exponential functions. The University of Virginia
 1130 has studied the performance of VPTs with respect to their light exposure rates over the course
 1131 of several years in order to characterize the device's response and long-term behavior.

1132 4.2.2 Test Rig at UVa

1133 The University of Virginia (UVa) has continuously monitored four production VPTs operated
 1134 at 800 V anode and 600 V dynode, in a 3.8 T field, at 15° to the tube axis, with photocath-
 1135 ode currents of approximately 10 nA. This was done to simulate light exposure from the lead
 1136 tungstate crystals in the forward regions of the ECAL end-caps, as well as provide an accelerated
 1137 simulation of photocurrents that would be experienced in the larger eta regions. As described
 1138 above, the light exposure is theorized to be the most significant cause of the loss of response
 1139 in the VPT, known as burn-in. The amount of light that the device has been exposed to is
 1140 measured in terms of the total number amount of charge liberated from the cathode, measured
 1141 from the cathode current draw, and is known as the integrated charge. By operating at such
 1142 high photocurrents, UVa is able to probe this burn-in effect in an attempt to understand the
 1143 long term behaviour of the VPT response to light.

1144 The University of Virginia is well suited to test these devices, since it operates a 3.8 T
 1145 solenoid magnet, with a sufficiently large inner bore to accommodate a rig containing five (5)
 1146 VPTs, LEDs, LED driving hardware, and amplifying equipment. The magnet itself was built
 1147 by Oxford instruments and has an inner bore diameter of 0.4 m and an outer bore diameter of
 1148 1.5 m. The inner bore is 0.13 m in height from the ground, and the magnet has a length of 1.5m

1149 along its z-axis, which is perpendicular to the normal of the floor.

1150 The VPTs were supplied with high voltage (800 V anode, 600 V cathode) from a CAEN
1151 High Voltage supply. This manufacturer also provides high voltage supplies for the VPTs used
1152 in CMS. They are preferable due to their stability, programmable user interface, and capacity
1153 to drive multiple VPTs simultaneously. A voltage separation between anode and cathode much
1154 larger than this is not recommended due to its potential do damage the device.

1155 The VPTs were pulsed with blue and orange LEDs at rates of 10 kHz, and 20 kHz, to capture
1156 the same features (frequency and rate) that light from the lead tungstate crystals would produce
1157 while collisions were occurring in the detector. The driving circuits are the same as those used in
1158 the LED system in the end-caps at point 5 (the location of CMS at CERN), with the exception
1159 that the current limiting resistors are larger. They are Dallas Semiconductor DS1040Z-D70
1160 Programmable One-Shot Pulse Generators. The TTL signals from the FPGA serve as a trigger
1161 for a Dallas Semiconductor pulse generator chip on the board that generates a 30 nSec pulse, so
1162 there is no overlap in pulses generated by the VPT. The pulsing was also run in an on/off cycle
1163 of 16 hrs on, 8 hrs off to be consistent with the LHC beam fill cycle.

1164 The LED pulsing and data acquisition was automated via a PXI unit manufactured by Na-
1165 tional Instruments, which contains a FPGA card, a digital oscilloscope, and computer running
1166 Windows XP. The FPGA card was programmed with LabVIEW software which controlled LED
1167 pulse rate, low voltage power, and measurements of VPT signals. The data acquisition was
1168 triggered by means of a PIN diode placed next to the VPT. This served the dual purpose of in-
1169 dependent data triggering and also provided the means to correct fluctuations in the illumination
1170 provided by the LEDs.

1171 The current from the VPTs anode and cathode are ultimately routed to the PXI Crates
1172 switches, and then on to the crates DMM or oscilloscope via a preliminary amplification stage.
1173 The VPTs anode is connected directly to a Stephenson amplifier, which connects to a high-
1174 frequency switch. The PIN diode signal passes unmodified to that same high-frequency switch.
1175 The cathode signal cables connect to a distribution box near the PXI Crate. The distribution
1176 box then routes their signals to the terminal block on a low-frequency switch. All of these signals
1177 leave the rig over BNC cables before terminating at or adjacent to the PXI Crate. Figure 4.18
1178 highlights different components of the test stand at UVa.

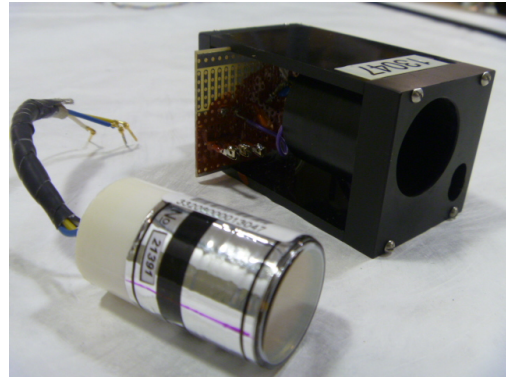
1179 4.2.3 Results of UVa Tests

1180 The University of Virginia rig ran three sets of 5 VPTs for approximately 30 wks each in a
1181 3.8 T magnetic field under high light conditions from blue and orange frequencies to simulate
1182 a large light yield found in large eta regions of the end-cap. The large photocurrents allowed

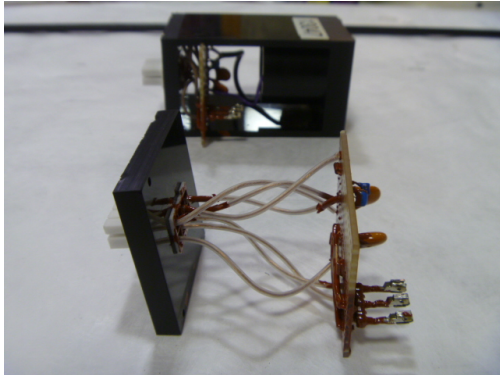


h

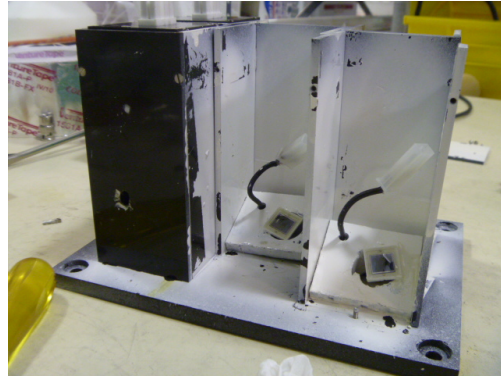
(a) The 3.8 T superconducting solenoid magnet used at UVa to study VPT performance



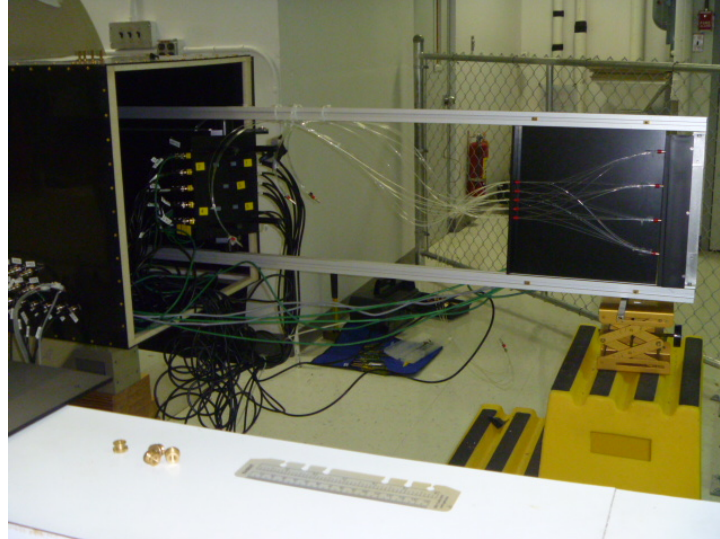
(b) A VPT before being installed in the rig and the housing that provides mechanical support and high voltage connections



(c) The housing for the VPT also provides simple HV filtering to provide stable power to the device



(d) The structure which holds 5 vpts in their housing. A PIN diode is used to measure the LED light and make corrections for fluctuations in brightness



(e) The VPT rig in maintenance position outside of the bore of magnet (during operation the rail is inserted into the bore such that the vpt housing is at the center). Fiber optics feed from the left into the VPT and amplifier housing.

Figure 4.18: Features of the UVa VPT test stand

the collection of an integrated charge of ~ 48 mC for the largest gain VPT, and ~ 16 mC for the other three. All VPTs were characterized by an initial steep decline followed by a plateau region, which was fit with a double exponential function of the form

$$f(x) = A + B \exp(Cx) + D \exp(Ex) \quad (4.2)$$

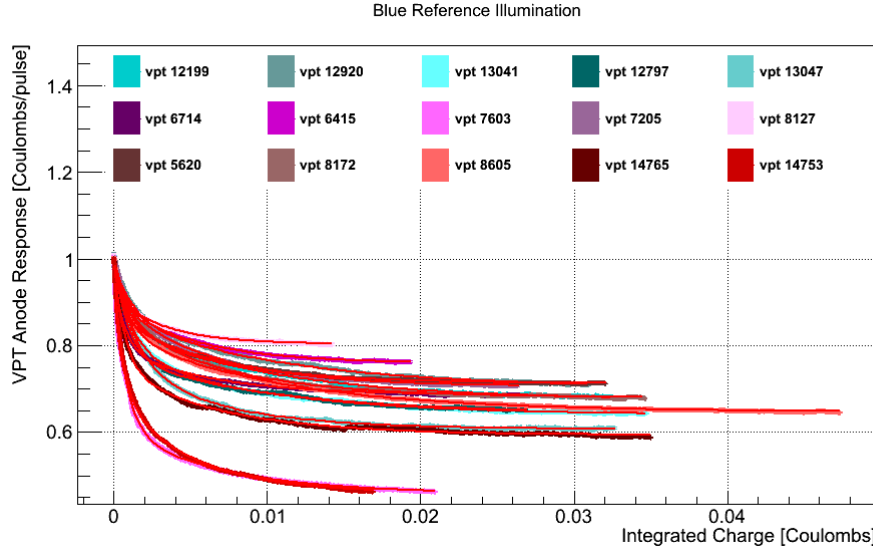


Figure 4.19: 3 runs of 5 VPTs, exposed to blue LED light, and fit to a sum of two exponentials.

Table 4.1: Fit Results for VPT Conditioning Studies at U.Va. and Brunel, Blue Reference LED

RIE Number	% Drop	χ^2/NDF	Pedestal	Fast exp Amplitude	Fast exp τ	Slow exp Amplitude	Slow exp τ
12199	30.1	1.20e+00	1.51e-09	3.42e-10	-8.84e-04	3.85e-10	-1.00e-02
12920	27.0	7.27e-01	1.72e-09	3.16e-10	-1.16e-03	4.03e-10	-1.05e-02
13041	33.5	8.46e-01	1.09e-09	3.43e-10	-1.20e-03	2.46e-10	-9.31e-03
12797	33.6	1.07e+00	6.39e-10	2.18e-10	-9.72e-04	1.31e-10	-9.87e-03
13047	38.1	1.06e+00	5.48e-10	1.98e-10	-1.40e-03	1.49e-10	-6.19e-03
6714	29.3	8.37e-01	1.55e-09	4.10e-10	-6.66e-04	2.48e-10	-6.11e-03
6415	23.6	1.28e-01	1.19e-09	1.54e-10	-6.55e-04	2.20e-10	-5.16e-03
7603	50.3	3.25e+00	1.44e-09	1.02e-09	-8.22e-04	4.87e-10	-6.72e-03
7205	29.4	4.53e-01	1.41e-09	2.14e-10	-5.68e-04	3.94e-10	-5.96e-03
8127	19.6	1.97e-01	1.71e-09	1.82e-10	-3.12e-04	2.35e-10	-3.30e-03
5620	27.4	4.57e+00	1.68e-09	2.85e-10	-5.20e-04	3.68e-10	-6.19e-03
8172	30.3	8.75e+00	8.32e-10	1.52e-10	-1.06e-03	2.27e-10	-6.87e-03
8605	32.1	6.94e+00	1.36e-09	3.33e-10	-8.97e-04	3.94e-10	-1.03e-02
14765	38.9	2.78e+01	3.47e-10	1.37e-10	-7.46e-04	9.24e-11	-6.77e-03
14753	52.9	2.53e+01	1.19e-09	7.45e-10	-5.86e-04	6.10e-10	-4.77e-03
Average	31.0	4.62e+00	1.17e-09	2.94e-10	-1.09e-03	1.66e-10	-3.07e-01

where A is a pedestal parameter, B is the amplitude of the fastest dropping exponential, C is the time constant of the fast dropping exponential, D is the amplitude of the slow dropping exponential, and E is the time constant of the fast exponential. The summary of the fit parameters for blue LED light is shown in table 4.1 and the summary of fit parameters for the orange LED light is shown in table 4.2. Plots of the VPT anode response versus integrated charge, and

the associated fit for each of the devices is shown in figure 4.19 for blue LED exposure and in figure 4.20 for orange LED exposure. Based on these findings, it can be concluded that the VPT "burn-in" eventually reaches a plateau at about $\sim 70\%$ for blue LED exposure and $\sim 50\%$ for orange LED exposure.

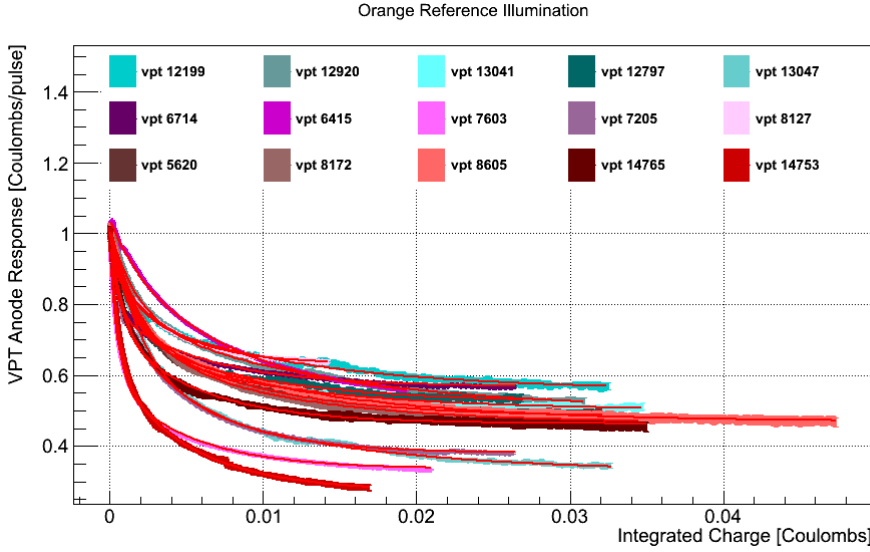


Figure 4.20: 3 runs of 5 VPTs, exposed to orange LED light, and fit to a sum of two exponentials.

Table 4.2: Fit Results for VPT Conditioning Studies at U.Va., Orange LED

RIE Number	% Drop	χ^2/NDF	Pedestal	Fast exp Amplitude	Fast exp τ	Slow exp Amplitude	Slow exp τ
12199	41.9	6.23e-01	4.23e-10	1.79e-10	-1.10e-03	1.76e-10	-1.10e-02
12920	45.3	1.84e-01	6.73e-10	3.24e-10	-1.67e-03	3.72e-10	-1.26e-02
13041	48.3	7.42e-01	2.75e-10	1.81e-10	-1.63e-03	1.04e-10	-1.02e-02
12797	46.4	5.05e-01	2.05e-10	1.14e-10	-1.23e-03	7.87e-11	-8.77e-03
13047	63.0	1.09e+00	1.34e-10	1.73e-10	-2.18e-03	1.07e-10	-1.16e-02
6714	43.4	1.43e+01	7.73e-10	3.29e-10	-4.49e-04	2.84e-10	-6.11e-03
6415	46.5	2.34e+01	4.41e-10	8.75e-11	-1.80e-03	3.47e-10	-7.95e-03
7603	64.8	3.20e+01	3.01e-10	3.42e-10	-5.42e-04	2.24e-10	-5.04e-03
7205	63.2	6.52e+01	1.94e-10	1.29e-10	-4.49e-04	2.16e-10	-5.13e-03
8127	39.4	2.24e+01	7.09e-10	1.54e-10	-2.08e-04	3.10e-10	-3.75e-03
5620	50.3	2.30e-01	4.07e-10	2.13e-10	-1.16e-03	2.37e-10	-7.79e-03
8172	51.7	1.56e-01	4.01e-10	2.73e-10	-1.91e-03	2.08e-10	-9.48e-03
8605	49.6	1.83e-01	2.39e-10	1.46e-10	-1.45e-03	1.33e-10	-1.12e-02
14765	53.3	3.08e-01	2.07e-10	1.27e-10	-8.55e-04	1.17e-10	-5.66e-03
14753	72.2	2.22e-01	1.94e-10	2.76e-10	-6.01e-04	2.47e-10	-5.06e-03
Average	52.0	1.08e+01	3.72e-10	2.03e-10	-1.15e-03	2.11e-10	-8.10e-03

4.3 The Hadronic Calorimeter

The Hadronic Calorimeter (HCAL) is divided into four sub-systems: the barrel (HB), the endcap (HE), the outer calorimeter (HO), and the forward calorimeter (HF). It is especially important for measuring hadronic jets and neutrinos by measuring an imbalance in energy trans-

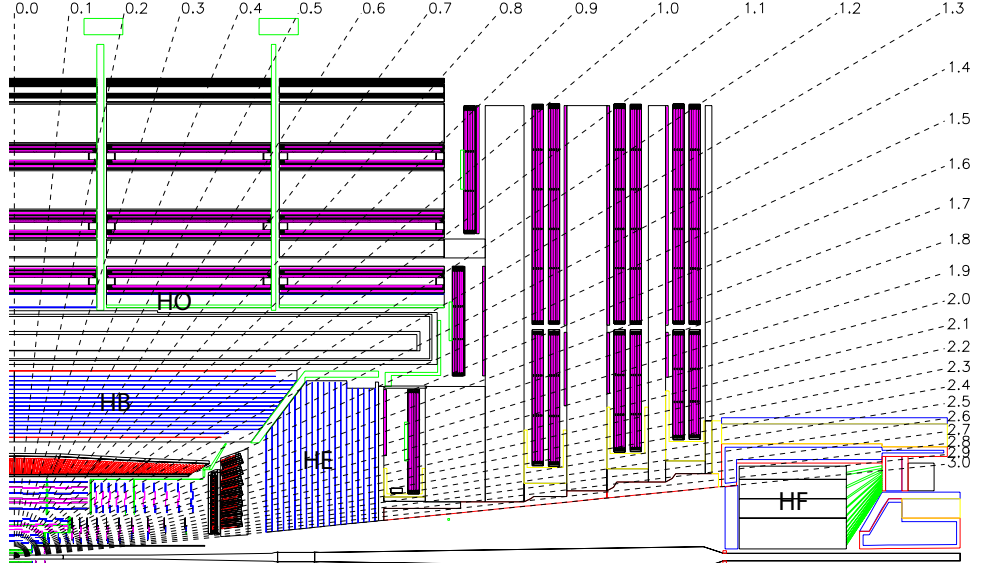


Figure 4.21: Longitudinal cross-section of the HCAL with the four sub-systems labeled

verse to the beamline. It provides coverage from $|\eta| < 3$ from the HB, HE, and HO, and the HF extends the coverage out to $|\eta| < 5.2$. A diagram of the longitudinal cross section is shown in figure 4.21.

The barrel section of the HCAL, the HB, is divided into two sections longitudinally, each with 18 identical azimuthal wedges wrapped around the beamline. Each wedge has four azimuthal sections, with the center two sections aligned and each edge piece angled and staggered in a configuration that creates no projective dead material for the full radial extent of the HCAL. Figure 4.22 shows a closeup photograph of four wedges, where optical fibers are layed out accross the seam that joins the staggered edge layers to the two aligned center layers, and blue lines highlight the four azimuthal divisions for a single wedge.

The HB is a sampling calorimeter, with each azimuthal section composed of 14 alternating layers of brass absorber plates, and layers plastic scintillator tiles, with steel plates on the top and bottom layers for structural support. Each quarter-barrel section of scintillator has 16 η divisions, giving a segmentation of $(\Delta\eta, \Delta\phi) = (0.087, 0.087)$. The brass absorber plates are C26000/Cartridge Brass. The material was chosen since the absorber material could not be distorted or bend under the stress of its own weight for at least 15 years of experimental running. Much of the material was purchased, but over a million Russian WW2 brass shell casings, designed to withstand the stresses of travel aboard 1940s Navy vessels, were melted down and processed into absorber tiles. Figure 4.24 shows members of the Russian Navy posing with some of the shells.

When a hadron passes through a wedge, the brass and steel plates absorb energy and ini-



Figure 4.22: Closeup of the HCAL barrel section. The center section of each of the 18 wedges are labeled, optical cables lay accross the joint of the center and staggered edge sections of each wedge. The blue lines show the apporximate azimuthal division of the wedge.

tiates the decay of the hadron into a number of lighter particles. These particles pass through the scintillator layer, which absorb energy from the interactions or collisions with the passing particles. The electrons of the scintillator become excited and relax by emitting a number of photons in the blue-violet range of the visible spectrum proportional to the amount of energy absorbed by the scintillator. These photons are abosrbed by wavelength shifting fibers (WSFs), which re-emit the light in the green part of the visible spectrum. The WSFs are spliced into four clear fiber optical cables. These fibers transport the light from each of the layers to an optical de-coding unit (ODU), which arranges the fibers into readout towers. A hydrid photodiode (HPD) converts this light into electric signals and is digitized by an ADC contained on the front-end elctronics. The HPD is a photo-cathode, which converts light to electrons via the photoelectric effect, that sits above a silicon diode that amplifies the signal of the cathode. The HPD provides a gain of 2000 to the light signals received from the scintialator trays. The on-detector electronics communicate to the HCAL trigger/readout (HTR) boards, which communicate with the trigger system to decide whether the store the event as data or discard it.

The brass absorbing material has a nuclear interaction length, or the length necesary to reduce the number of charged particles in a hadron shower by $1/e$, of 16.42 cm, and a radiation length of 1.49 cm. This means that te HB will be able to contain a large part of most hadron showers produced at LHC energies, but a portion will still pass through the entire radial distance. The outer barrel layer, HO is designed to measure the remnants of the hadron shower. It sits



Figure 4.23: Over 1 million Russian shells of military artillery were re-processed in the construction of the HCAL

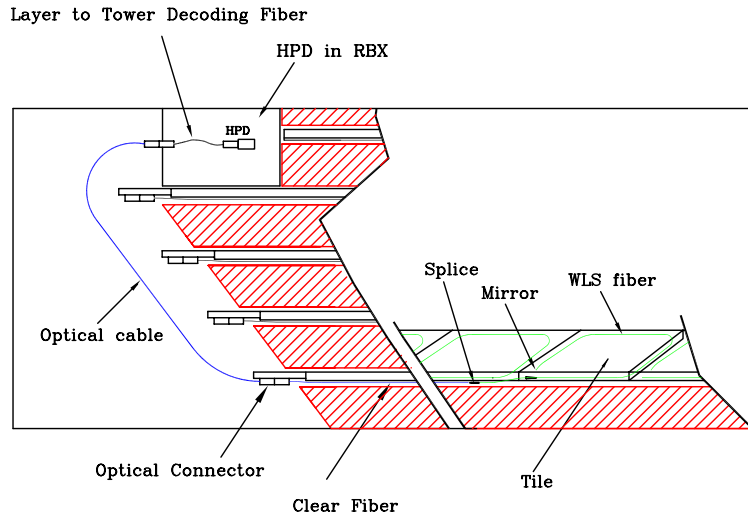


Figure 4.24: Optical readout chain of the HCAL scintilllator tiles

1239 outside of the solenoid magnet, using it as an absorber layer $1.4/\sin \theta$ interaction lengths. It
 1240 consists of 5 sections along the z-axis, which form rings around the beamline. Each ring is a layer
 1241 of scintillator tiles at radial distance of 4.07m, except for the center ring. Since it corresponds
 1242 to the $\eta = 0$ ring, there is a minimum amount of absorber material in front of it. The central
 1243 ring is thus two layers of scintillator at radial distances 3.82 and 4.07 m, which sit on either
 1244 side of a 19.5cm thick piece of iron absorber.

1245 The endcap system, the HE, provide a substantial portion of the total η coverage, from
 1246 $1.3 < |\eta| < 3.0$, and contains $\sim 1/3$ of the final state particles in a collision. Like the HB, it is
 1247 a sampling calorimeter with alternating layers of brass and plastic. The demand for radiation
 1248 hardness, and the need for a non-magnetic material, lead to the same choice of C26000 cartridge

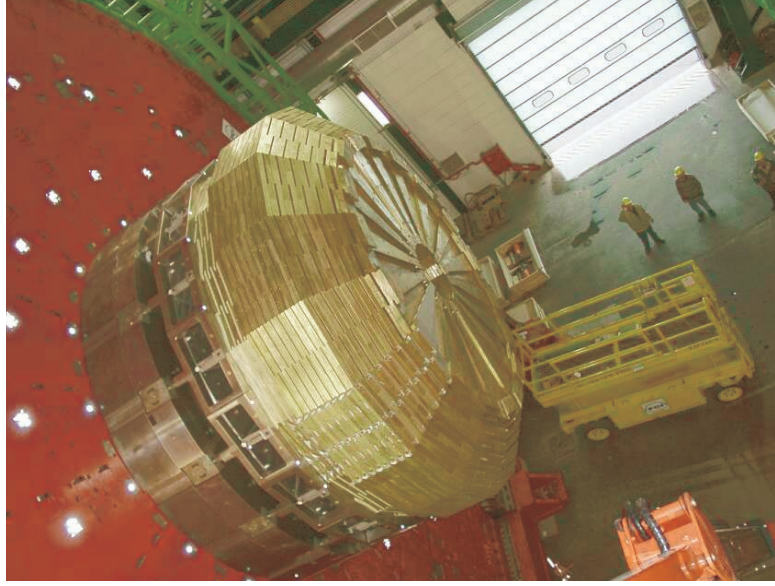


Figure 4.25: HCAL endcap, 18 azimuthal divisions of alternating layers of brass and plastic scintillator.

₁₂₄₉ brass found in the HB. It is also divided into 18 azimuthal wedges, and 16 η divisions, giving
₁₂₅₀ it the same $(\Delta\eta, \Delta\phi) = (0.087, 0.087)$ segmentation. Figure 4.25 shows an image of a partially
₁₂₅₁ assembled endcap before being installed.

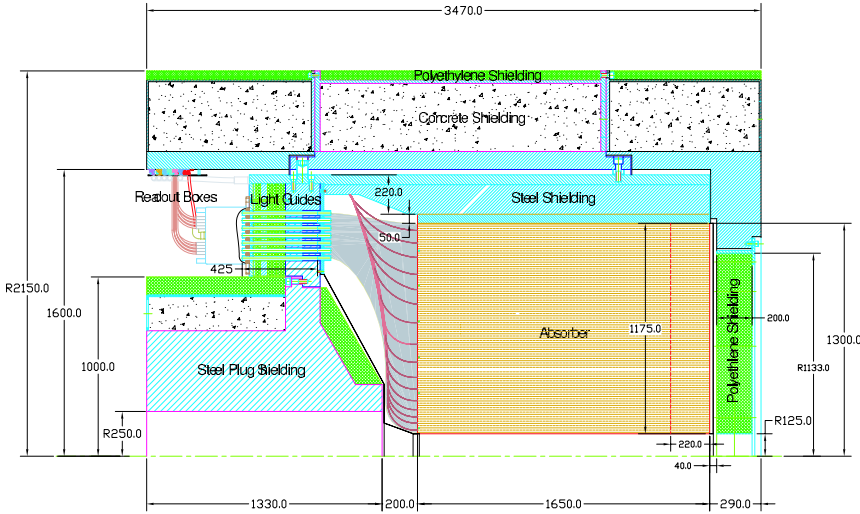


Figure 4.26: Longitudinal cross-section of the HCAL forward calorimetry, the HF

₁₂₅₂ The forward calorimetry, HF, extends the HCAL coverage from $3.0 < |\eta| < 5.0$, and neces-
₁₂₅₃ sarily must sit in the region of the detector with the largest particle fluxes and thus radiation
₁₂₅₄ exposure. The HF is a cylindrical steel structure with an inner bore 12.5 cm from the beam line,
₁₂₅₅ and a outer radius of 130.0 cm. It sits 11.2 m away from the nominal interaction point in the

1256 \hat{z} direction. Like the HE, it has 18 azimuthal divisions on either side of the interaction point.
1257 Relativistic particles that move through the steel generate Cherenkov light, which is collected
1258 by radiation hard quartz fibers, which transport the light to HPDs which are readout in the
1259 manner as described above. Since the detection mechanism is Cherenkov light, this sub-system
1260 is primarily sensitive to the electromagnetic component of the hadronic shower. Figure 4.26 shows
1261 a cross-sectional view of the HF detector.

1262 4.4 Muon Chambers

1263 In pp collisions, muons are only created through electroweak or exotic physics processes, making
1264 the detection of this particle an invaluable tool for reducing the large hadronic backgrounds
1265 produced at the LHC. The muon chambers, positioned furthest from the beamline, sit behind
1266 the ECAL and HCAL detectors, which absorb almost all of the hadronic activity from a collision.
1267 They operate in a relatively low flux environment, allowing for robust measurement of their
1268 kinematics, making it an excellent trigger system. One of the most important discovery channels
1269 for the Higgs boson, involved the decay of the Higgs into two Z bosons, which decay to two pairs
1270 of muons. Only 25 events were needed for a statistically significant observation in that channel,
1271 since the backgrounds had been reduced to only 5 expected events and the muons had provided
1272 high resolution on the invariant mass of the Higgs.

1273 The muon chambers are composed of three types of gaseous detector technology: drift tubes
1274 (DTs), cathode strip chambers (CSCs), and resistive plate chambers (RPCs). In the muon barrel
1275 system (MB), where the magnetic field is uniform DTs provide η coverage, for $|\eta| < 1.4$, and
1276 are supplemented by a system of RPCs that provide an independent trigger source and faster
1277 timing resolution. In the muon endcap system (ME), where the magnetic field would degrade
1278 the performance of DTs, a system of CSCs and RPCs provide η coverage from $1.4 < |\eta| < 2.4$.

1279 The DTs are located in the MB system, which is divided into 5 longitudinal, cylindrical
1280 sections around the beamline, known as wheels. In each wheel there are 4 concentric layers of
1281 drift tube stations, one on either side of the magnet return yoke, and two interspersed inside of
1282 it. Each wheel is divided into two 12 azimuthal sectors, making 48 stations in the barrel, as shown
1283 in figure 4.27. Each station on the first three (fourth) layers contain 3(2) superlayers, where
1284 each superlayer is made of a stack of 4 layers of rectangular drift cells, which are staggered
1285 by half a cell each. Two of the superlayers are oriented such that they are parallel to the
1286 beam, measuring the muon in the $r - \phi$ plane. The first three layers contain a third superlayer,
1287 orientated perpendicular to the beam, measuring a z component of the muon trajectory. Each
1288 drift cell is a hollow 13×42 mm tube, with a relatively thick 1.5mm wall to provide isolation

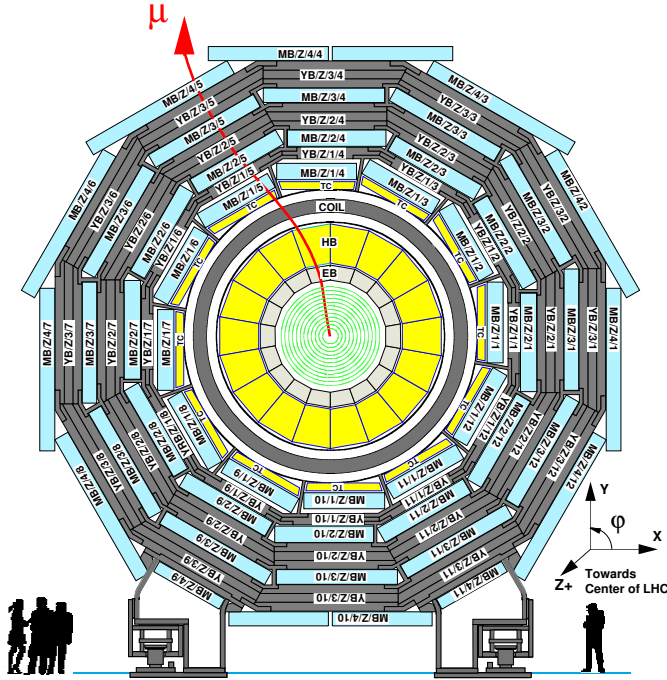


Figure 4.27: Longitudinal cross-section of one of the 5 wheels of the muon system. Drift tubes are placed in 4 concentric layers, with 2 being placed inside the return yoke of the magnet, and 12 azimuthal divisions.

1289 between adjacent cells. Each cell is filled with a mixture of 85% argon + 15% CO₂ gas mixture,
 1290 and contains an anode wire that is held at 3600 V that runs down the axis of the cell. The walls
 1291 of the cell are held at 1800 V or -1200 V depending on the wall. When a muon passes through the
 1292 chamber, it's charge ionizes molecules of the CO₂ gas, causing the electrons to drift towards the
 1293 anode wire, and the CO₂ ions drift towards the wall. As the electrons approach the anode, they
 1294 are accelerated and liberate secondary elctrons from other CO₂ molecules, creating an avalanche
 1295 of electrons near the wire, resulting in a drop in voltage as they are collected. The voltage drop
 1296 is read out by front end electronics as a signal that a muon has passed through the chamber.
 1297 The Argon gas quenches the avalanche reaction, and the maximum drift time for electrons in
 1298 the gas is 380 ns. This long time scale necessitates the use of an addtional, fast-timing system,
 1299 the RPCs. Figure 4.28 shows a cross-section view of a drift cell, including electric field lines
 1300 produced by the potential difference between the anode wire and the walls of the drift cell.

1301 The reisistive place chambers (RPCs) are the fast timing system chosen to supplement the
 1302 DTs in the barrel, and the CSCs in the endcaps. In the barrel, they are adhered to the top and
 1303 bottom of the first two layers of drift stations. In the outer two layers, they are only adhered
 1304 to the bottom of each station. Figure 4.29(a) shows the layout of the barrel RPC system. The
 1305 muon endcap system is composed of three disks on either side of the intreraction point, and is
 1306 shown in figure 4.29(b). RPCs are mounted on the back of the CSC stations of the innermost

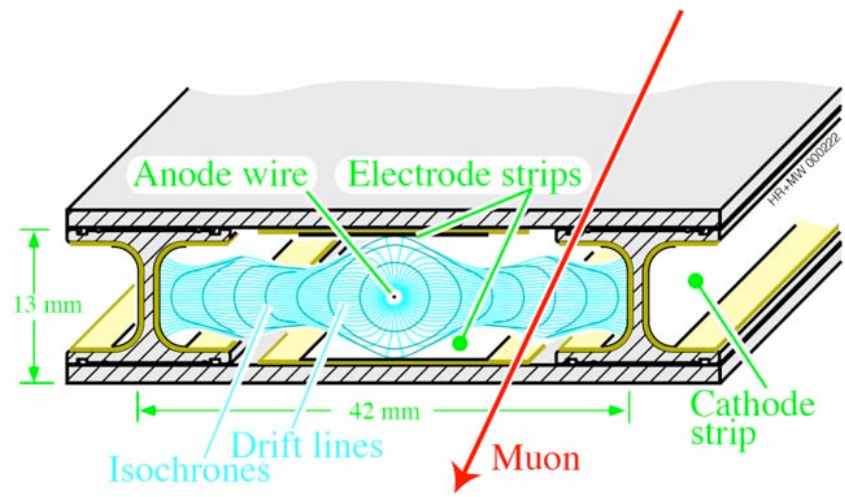
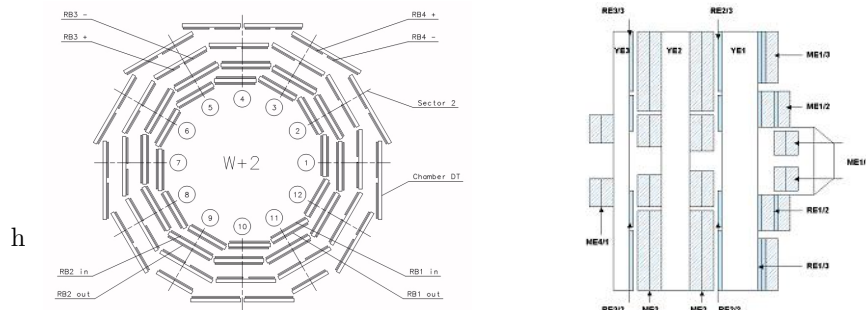


Figure 4.28: A cross-section view of a drift cell. The anode wire is held at 3600 V, creating a potential difference with the walls. Electric field lines are shown in blue.

and outermost disks, and on the front of the CSC for the middle disk. Each RPC consists of two plates of high resistance material, one held at a positive voltage, the anode, and the other held at a negative voltage, the cathode. The volume between the plates is filled with a gas similar to the drift tubes. When a muon passes between the plates, it ionizes the gas molecules, and the electrons are accelerated towards the positive plate, creating an avalanche of secondary electrons that combine with the positive plate creating a voltage drop that is read out as a signal. The timing resolution achieved from the RPCs is less than the 25 ns LHC bunch crossing, supplementing the spatial resolution provided by the DTs in the barrel, and the CSCs



(a) A longitudinal cross-section of the muon barrel RPC system. RPCs are attached to the top and bottom of the first two layers of drift stations, and to the bottom of the outer two layers

(b) Cross-section of muon endcap system. It is composed of three disks, with RPCs mounted on the back of CSC system on the first and last disks, and on the front of the CSC in the middle disk

Figure 4.29: RPC layout for the barrel and endcaps

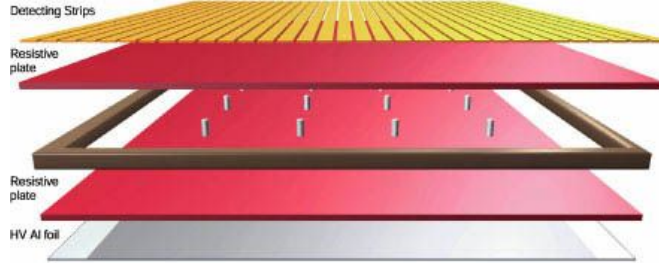


Figure 4.30: Exploded diagram of an RPC

1315 in the endcap.

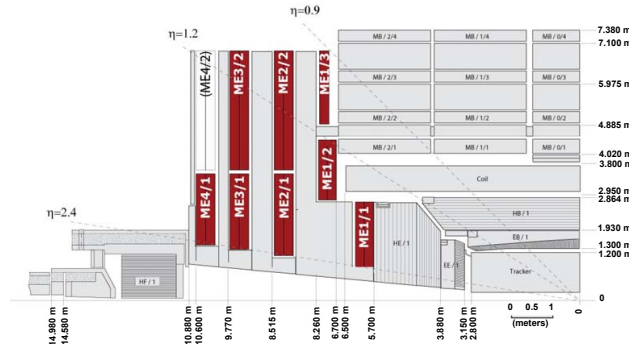


Figure 4.31: Cross-section of one quarter of the muon endcap system, with the 4 disks of CSC systems shown in red

1316 In addition to RPCs, the muon endcap (ME) system, uses cathode strip chambers (CSCs)
1317 to provide additional spatial resolution on muons. Each endcap has 4 layers of CSCs, with a
1318 trapezoidal shape, with 468 cathode strip chambers distributed on each. Three groups of 72
1319 are located on the inner disk, a group of 36 and a group of 72 in the second and third disk, and
1320 a group of 36 in the outer disk. Figure 4.32 shows the layout of a quarter section of the CSC
1321 system in the ME. A CSC station consists of 6 layers of gas chambers, where each chamber is
1322 an array of anode wires, held at a positive voltage, arranged perpendicular to cathode strips,
1323 held at negative voltage. The volume of the chamber is filled with a gas that is 40% Argon,
1324 50% CO₂, and 10% CF₄. When a muon passes through the volume, the gas is ionized, and now,
1325 since the anode and cathode strips are perpendicular, when the electrons and gas ions combine
1326 with the anode and cathode respectively, a 2-D measurement of the muon's position is recorded.
1327 Figure 4.32 shows a diagram of a CSC chamber with 7 layers to create the 6 gas chambers.

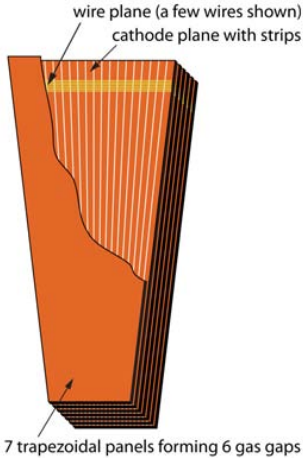


Figure 4.32: A CSC station with 7 layers, making 6 gas chambers. Cathode strips are shown in yellow, perpendicular to the vertical anode wires in orange.

1328 4.5 Data Collection Overview

1329 The LHC is designed to deliver protons at 40 MHz, corresponding to a bunch crossing every 25 ns.
1330 The majority of the interactions will be glancing, low-energy collisions, which do little to reveal
1331 new phenomenon, and would be impossible to store for analysis. A trigger system is designed to
1332 select interesting events with a large potential of revealing new physics. The rate is reduced in
1333 two steps through the Level-1 (L1) trigger, and the High-Level Trigger (HLT). The L1 trigger is
1334 composed of programmable electronics and hardware that buffers the data and perform simple
1335 calculations on tracks and calorimeter energy deposits to determine whether an event should be
1336 kept for analysis. This reduces the event rate from 40 MHz to 10 kHz. The HLT is a computer
1337 farm of \sim 1000 computer processors, that perform a more sophisticated reconstruction of the
1338 tracks and energy deposits, as well as more complicated calculations between reconstructed
1339 objects. This stage reduces the rate to a much more manageable 100 Hz.

1340 The L1 trigger is composed of local, regional, and global components. The process of deter-
1341 mining whether to accept or reject the event begins by calculating Trigger Primitive Generators
1342 (TPGs) based on calorimeter energy deposits, and tracks in the muon chambers. The entire
1343 process has a latency time of $3.2 \mu\text{s}$, which corresponds to the length of the LHC abort gap.
1344 Sufficiently large data buffers allow the storage of all the events processed during a bunch train,
1345 meaning that CMS is capable of running with zero dead time due to detector readout latency.

1346 In the ECAL a trigger tower consists of a 5×5 array of crystals. Front-end electronics on the
1347 crystals receive ADC counts on the amplitudes of the photomultipliers, and uses information
1348 encoded in the electronics to convert this sum to the transverse energy, E_T deposited in the
1349 crystals. The EB TPG also encodes information about the distribution of energy, and thus the

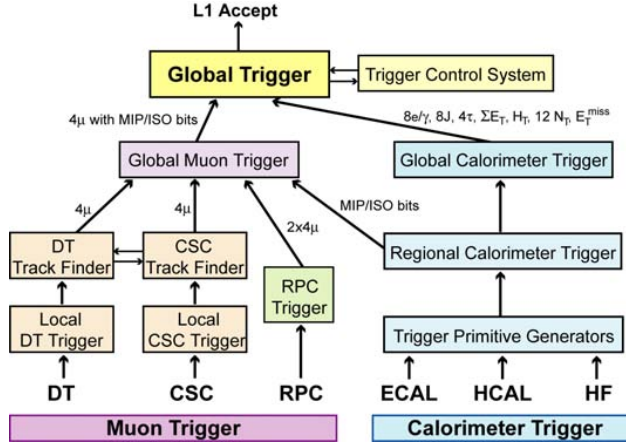
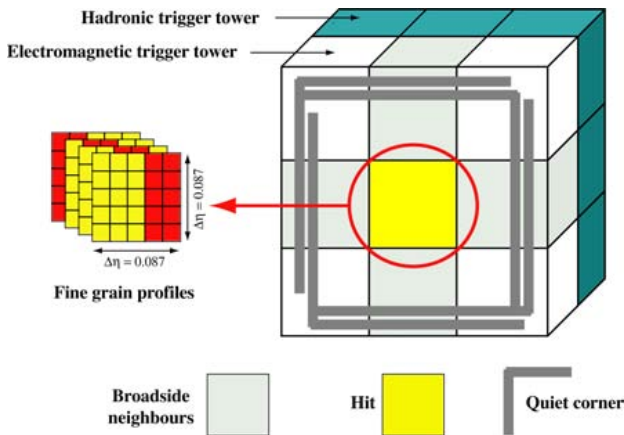


Figure 4.33: A block diagram of the L1 trigger

shower shape in the 5×5 array, which is used to veto anomalous signals. In the HCAL, a trigger tower consists of one of the 16 azimuthal wedges, with segmentation $(\Delta\eta, \Delta\phi) = (0.087, 0.087)$, in the barrel and endcap. Similarly to the ECAL, front-end electronics digitize the signal from the HCAL HPDs, and convert the ADC counts into sums of transverse energy. These calorimeter TPGs are sent to a Regional Calorimeter Trigger (RCT) that is composed of a 4×4 array of trigger towers, with the exception of the HF, which is formed by a single trigger tower.

Figure 4.34: A schematic of the e/γ trigger algorithm

The RCT determines electron and photon candidates from the calorimeter sums. The e/γ trigger searches for the highest energy trigger tower in the ECAL. Within that trigger tower, it checks that the EM shower is contained in a 2×5 array of crystals and that the ratio of ECAL to HCAL energies is less than 5%. It is considered an isolated electron if all eight of its nearest neighbors pass these requirements, and a corner of five neighbors has energy below a threshold requirement. It is considered a non-isolated electron if only the second highest E_T

1362 broadside neighbor trigger tower passes these criteria. Up to four isolated, and four non-isolated
 1363 e/γ candidates per RCT are passed to the Global Calorimeter Trigger (GCT).

1364 The GCT determines jets, total transverse energy, missing transverse energy, jet counts, and
 1365 H_T (scalar sum of transverse momentum), in addition to the highest rank isolated and non-
 1366 isolated *egamma* candidates. Jets are found in a clustering algorithm that looks for large energy
 1367 deposits in 2×12 cells of ϕ or η that span 40° and half the detector in each of coordinates. Up
 1368 to four jets, and four tau jets from the HCAL and four jets from the HF are forwarded to the
 1369 Global Trigger (GT).

1370 The non-calorimeter based triggers are based on measurements of the DTs, CSCs, and RPCs
 1371 in the muon drift chambers. The barrel DTs look for hit patterns among neighboring tubes
 1372 in successive layers, and fits a track segments in the η and ϕ coordinates. The endcap CSCs
 1373 provide 3-dimensional track segments and are combined with the DTs to form tracks that are
 1374 passed to the Global Muon Trigger (GMT). The RPCs provide an independent set of tracks and
 1375 timing hits to the GMT. Each bunch crossing the GMTs receive up to four muon candidates
 1376 in the barrel RPCs, four from the barrel DTs, four from the endcap RPCs, and four from the
 1377 endcap CSCs. The GMT records the candidate's p_T , charge, η , and ϕ position, as well as a
 1378 quality code related to the fit of the track to the hit positions of the detector. The GMT sends
 1379 then sends these muon candidates to the GT.

1380 The Global Trigger can execute up to 128 trigger algorithms in parallel to analyze the p_T ,
 1381 charge, η , and ϕ position, and associated quality codes for muons, electrons, photons, jets, and
 1382 missing transverse energy. Most algorithms compare single object characteristics to thresholds
 1383 to determine if they pass minimally interesting criteria. If any of the algorithms return a passing
 1384 decision, the L1 trigger issues an accept statement that allows the data stored in buffers to be
 1385 readout by the CMS Data Acquisition (DAQ) system.

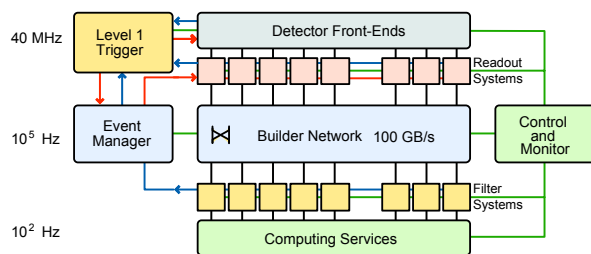


Figure 4.35: Layout of the CMS DAQ

The CMS DAQ collects information from 626 subdetector Front End Drivers (FEDs), which extract the buffered information from the various front-end systems, upon the arrival of a L1 trigger accept. An event builder algorithm assembles the fragments from the various sub-systems into a single coherent event, and transmits the information to the HLT computing farms. Figure 4.35 shows a schematic of the DAQ system.

The HLT computer farm performs the final reduction of data rate, from 100kHz from the L1 to 100Hz. The computer farm performs basic consistency checks to ensure the quality of the data, then performs calculations based on topology of the HLT path. Typically, a more sophisticated reconstruction of an object takes place, and kinematic cuts are applied to the object or in relationship to other objects in the event. Each HLT path forms its own data set, thus creating single muon, single electron, electron+jets, etc. type datasets. The unpacked detector information read by the DAQ is composed of ADC counts for each readout channel, TPGs, and the L1 decision. This is known as the RAW dataset. Reconstructed physics objects are stored RECO data tier, and finally an analysis object data (AOD) tier is created containing only information about the reconstructed objects without having to store detector information. This last format requires the least amount of data per event for storage, and contains the reconstructed physics objects, such as electrons, muons, jets, etc. which are used to search for new physics phenomena.

1404 **Chapter 5**

1405 **Particle Reconstruction at CMS**

1406 Charged and neutral hadrons in the form of jets, missing transverse energy (MET), photons,
1407 electrons, muons, and tau leptons are reconstructed at CMS using the particle flow event-
1408 reconstruction algorithm [70]. The algorithm is based on a three step process of identifying
1409 charged particle tracks using the muon chambers and silicontracker, identifying clusters of energy
1410 in the ECAL and HCAL, and linking the tracks to the calorimeter clusters. The calorimeter
1411 energy deposits were calibrated with test beam sources, data from cosmic rays and beam dumps,
1412 and finally from collision data. The algorithm constructs muons by fitting the tracks formed
1413 between the muon chambers, pixel and silicon trackers. Electrons have tracks from the pixel and
1414 silicon tracker matched to the ECAL, with a minimum energy deposited in the HCAL. Jets are
1415 formed from tracks, ECAL, and HCAL clusters falling with a conical angle. The identification
1416 of one, three, or larger odd number of tracks, and the majoriy of the energy contained in a small
1417 cone size, allows a jet to be tagged as a hadronically decaying tau lepton. Additional algorithms
1418 are also used to identify a jet as coming from the decay of a b-quark, primarily by looking for
1419 secondary vertices in the pixel and silicon tracker.

1420 **5.1 Iterative Tracking**

1421 Since approximately two-thirds of the energy of a jet is carried by charged hadrons, the tracker is
1422 the cornerstone of the particle-flow algorithm [70]. The path of a charged particle in a magnetic
1423 field follows a helical pattern, described by 5 parameters. The extraction of these requires
1424 three 3-dimensional measurements of the particle, or two 3-dimensional measurements and a
1425 constraint on the origin [71]. The pixel detector is ideal for this since each pixel provides a 3-
1426 dimensional measurment of the particle's location. Track reconstruction is the process of using
1427 hits in the pixel and silicon detector elements to estimate the momentum and trajectory of the

1428 charged particle responsible for the hit [71]. The tracking software at CMS is known as the
1429 Combinatorial Track Finder (CTF), which is based on producing tracks over multiple iterations
1430 of the reconstruction sequence, removing the tracks with the largest p_T closest to the interaction
1431 region first, reducing the combinatorial complexity over each iteration.

1432 Each iteration begins by identifying a seed for the particle tracks, which is a minimum
1433 combination of pixel or silicon tracker hits that is used as an initial estimate of the trajectory
1434 of the particle [71]. Then, tracks are found by applying the Kalman filter [72]. This method
1435 is based on applying a small gaussian uncertainty to the location of the seed hits, fitting an
1436 intial track to these hits, then looking for additional hits that fall within the error of the initial
1437 estimate, deeper in the tracker. These hits are added to the fit with their own uncertainties,
1438 and the fit is re-calculated, each time attempting to minimize the mean-square estimation of the
1439 error. The 5 helical trajectory parameters are extracted, and tracks with poor fits are discarded.

1440 A total a six iterations is used, each with a different starting seed or kinematic requirement
1441 on the p_T of the tack, as well as the transverse and longitudinal distance from the reconstructed
1442 vertex [72]. The first iteration is seeded by three hits in the pixel detector. The second, is seeded
1443 by two hits in the pixel detector and a pixel vertex, which is form when at least four pixel tracks
1444 point back to a common origin. The third iteration is seeded once again by three hits in the
1445 pixel detector, except with a looser minimum p_T cut. The fourth iteration uses seeds from any
1446 three hits in the pixel detector or silicon tracker, with at least one hit coming from the pixel
1447 detector. In the fifth iteration seeds are formed from the inner two rings of the TIB, TID, and
1448 TEC. The final iteration begins with seeds from the first two rings of the TOB and the fifth ring
1449 of the TEC.

1450 5.2 Calorimeter Clustering

1451 The clustering algorithm is used to detector the energy and director of stable, neutral particles
1452 such as photons and neutral hadrons [70]. It also seperates the energy contributions from the
1453 netural and charged hadrons, and provides an aditional energy measurement for charged hadrons
1454 with very low or high p_T tracks, both cases that degrade the energy resolution. Finally, the
1455 clustering algorith properly accounts for bremmstrahlung energy losses from electrons. The
1456 algorithm is performed independently for the ECAL barrel, ECAL endcaps, HCAL barrel, and
1457 HCAL endcaps. In the HF, no clustering algorithms are used, as each cell is used as its own
1458 cluster in an event.

1459 The clustering alorithm begins by identifying "cluster seeds", which are the highest p_T cells
1460 above a defined energy threshold [70]. Then, "topological clusters" are formed by grouping

1461 adjacent cells together with energy above 80 MeV in the ECAL barrel, 300 MeV in the ECAL
 1462 endcaps, and 800 MeV in the HCAL. As a new cell is added, the total cluster energy and
 1463 position is updated until no new cells are able to be added. Each cluster seed thus gives rise
 1464 to a "particle-flow cluster". Each of these clusters is used as a candidate to be associated with
 1465 tracks during the third stage of the algorithm, the linking step.

1466 5.3 Calorimeter Energy Calibration

1467 One of the most critical steps in reconstructing particles is the calorimeter energy calibration,
 1468 which is the conversion of calorimeter scintillator light and photodetector current to the energy
 1469 deposited in the calorimeter by the particle traversing it. This is done by exposing the crystals
 1470 to particles of a known energy, using large samples of cosmic ray muons, by measuring minimum-
 1471 bias events assuming a ϕ symmetry, the of π^0 and η^0 meson resonances decaying into photons,
 1472 and W and Z bosons into electrons.

1473 Before installation at P5, the ECAL and HCAL were pre-calibrated using test beam. In
 1474 2006, the ECAL was exposed to an electron beam with energies between 15 and 250 GeV [73]
 1475 at CERN. Additionally, intercalibrations between crystals were performed with 90 and 120 GeV
 1476 beams. Also at CERN in 2006, the HCAL was calibrated, prior to installation using a beam of
 1477 50 GeV pions [74].

1478 Once both calorimeters were installed, the detectors were calibrated with cosmic ray muon
 1479 events in 2007 with the CMS magnet de-energized during the CRUZET (Cosmic RUn at ZErO
 1480 Tesla) data taking campaign, and again with the CMS field on in 2008 during the CRAFT
 1481 (Cosmic Run At Four Tesla) campaign. Shortly after the CRAFT campaign, the LHC delivered
 1482 450 GeV proton beams to collimator targets upstream of the CMS detector, creating accelerator
 1483 muons that are additionally used to calibrate the detector response. The ECAL energy
 1484 resolution was improved from 7.6% to 6.3%, and in the barrel, the intercalibrations from the
 1485 test beam were validated at a 2% level of agreement [75]. The HCAL energy calibration resulted
 1486 in 5% energy resolution in the HB, 10% in the HE, 12% in the HF, and 5% in the HE[76].

1487 After an initial set of data collection three independent calibration methods are combined to
 1488 determine the absolute energy scale and intercalibration coefficients for the crystals [?]. The first
 1489 method uses a large amount of data collected from minimum-bias trigger events, events which
 1490 are dominated by glancing collisions and QCD jet production. The processes that contribute
 1491 to these events have final state particles symmetrically distributed in the ϕ coordinate. By
 1492 grouping the crystals into rings of η , and the response of each crystal can be determined and
 1493 modified such that it matches the average crystal response in that η ring, with the uncertainty on

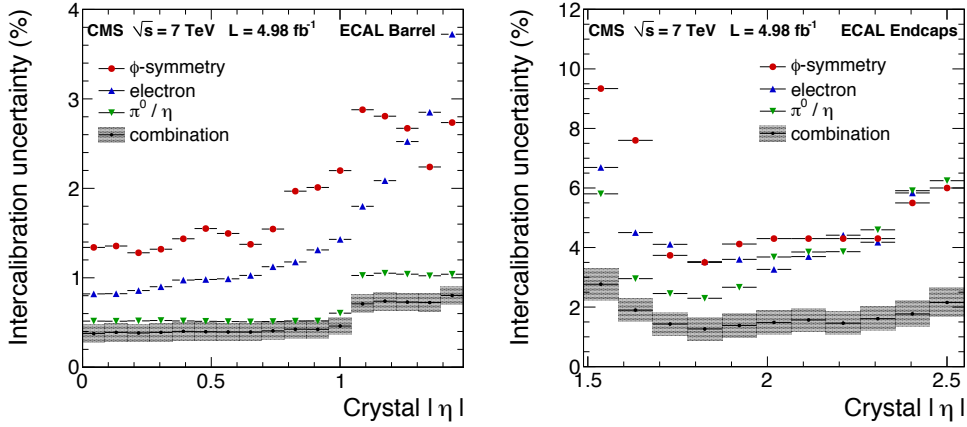


Figure 5.1: Results of the uncertainty on the ECAL intercalibration coefficients for the barrel (left) and endcaps (right)

the average representing the uncertainty on the intercalibration coefficient. The second method involves reconstructing the resonances of the π^0 and η^0 mesons decaying to two photons and relying on the high-precision measurements from other experiments to determine the exact mass of the resonance. Events near the resonance of these two particles are once again divided into rings of η , and averaged over the ϕ coordinate. Decays of the Z boson and electron pair is also used to determine the absolute scale (ADC counts/GeV) of the crystals, once again relying on the higher-precision measurements of previous experiments for the location of the mass peak. Finally, comparisons between the energy measured in the tracker and that measured in the ECAL are made from W and Z boson decays to electrons. Figure 5.1 shows the results of combining all three methods, to determine the uncertainty of the intercalibration coefficients.

The ECAL also has a strong dependence on the rate of instantaneous luminosity that the crystals are exposed to. It is therefore necessary to perform additional crystal calibrations as a function of time during a run of data collection. Blue and orange LED light, and blue laser light is fed through a network of optical fibers to each crystal. A known amount of light is injected and the crystal response is measured. Figure 5.2 shows a plot of the crystal response versus time. Rings of η are formed and crystals within the same η ring are used to calculate an average response, as is done in the intercalibration procedures described above.

The performance of the HCAL calibration to the 50 GeV pion beam is validated by comparing energy measurements in the tracker to energy deposits in the HCAL [77]. Since neutral hadrons contribute approximately 10% of the energy contained in a jet, it is necessary to recalibrate the measured energy in the HCAL using simulated events where the true hadronic energy is known. The equation for the total calorimeter energy is given by:

$$E_{\text{calib}} = a + b(E, \eta)E_{\text{ECAL}} + c(E, \eta)E_{\text{HCAL}} \quad (5.1)$$

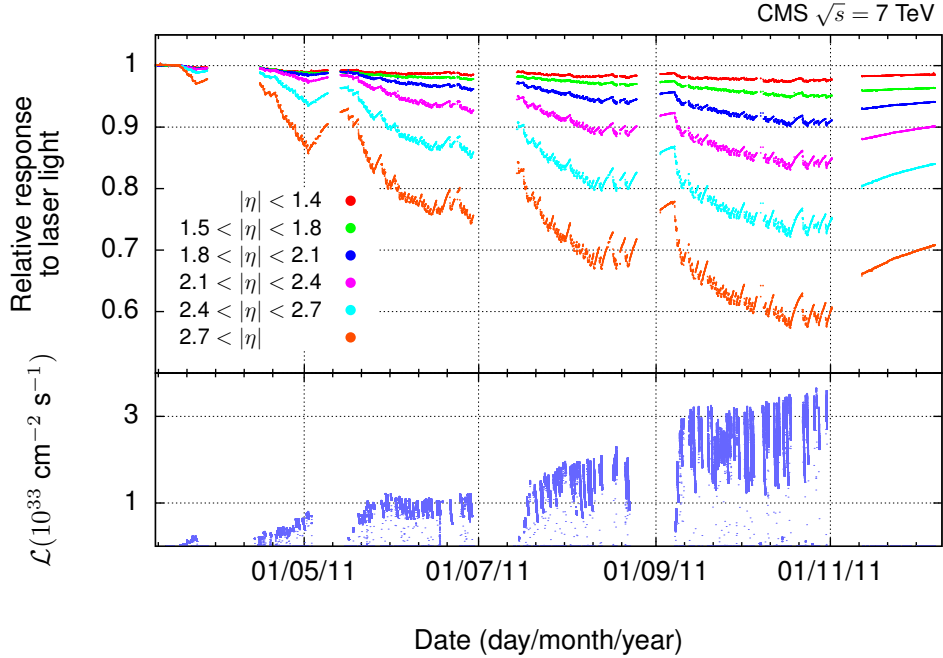


Figure 5.2: Instantaneous luminosity response to the crystals as measured by the laser and LED system. Additional crystal calibration constants are derived to normalize the crystal response over the range of collected data

1516 The coefficients, a, b, and c are determined through a χ^2 minimization procedure over each bin
 1517 of energy, minimizing the difference between the reconstructed and true energies and solving for
 1518 the parameters a, b, and c. Figure 5.3 shows the resulting HCAL energy resolution as a function
 1519 of energy, and the values of the coefficients a, b, and c.

1520 5.4 Linking

1521 Once clusters are formed in the ECAL and HCAL barrels and endcaps, they are associated with
 1522 nearby tracks in the pixel and silicon tracker in the phase of the particle-flow algorithm known
 1523 as linking [70]. Single particles are formed out of the tracks and calorimeter clusters without
 1524 double counting contributions from different detectors, forming "blocks" of linked elements. Due
 1525 to the high granularity of each sub-detector, blocks of two-four elements are typical.

1526 The linking procedure between pixel and silicon strip tracks and the calorimeter deposits
 1527 occurs in three steps: extrapolating the track to the ECAL preshower (PS); then to the ECAL
 1528 to a depth corresponding to the maximum longitudinal shower profile; and finally to the HCAL
 1529 to a depth corresponding to one interaction length. A track is then linked to a cluster if it
 1530 falls within the cluster boundaries. One HCAL cluster may be associated to many tracks, but
 1531 each track can only be associated with a single cluster, determined as the track with the shortest

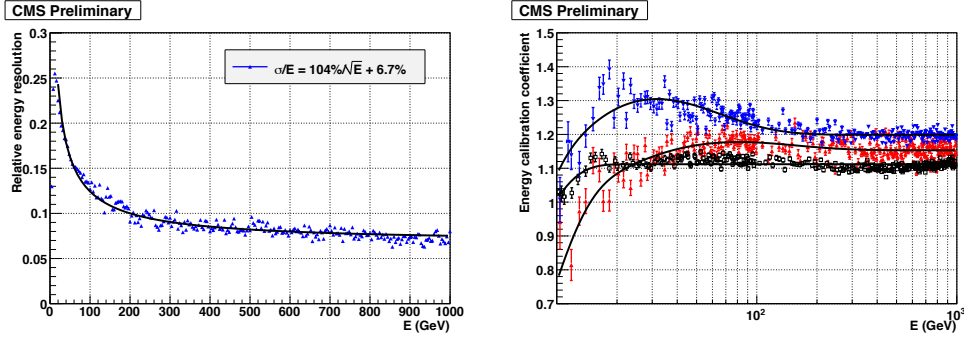


Figure 5.3: Results of using a χ^2 minimization procedure to estimate the neutral hadron energy contribution in the HCAL using simulated events

distance. For the ECAL, one track may be associated with many energy clusters, since they may have originated from hadronic shower fluctuations, so links to tracks should be preserved to avoid double counting the hadron energy. In order to account for the bremmstrahlung energy losses of electrons, tangent lines to the tracks are linked to the ECAL. If this extrapolated, tangent track falls within the ECAL cluster boundaries, it becomes a candidate for a bremmstrahlung photon from an electron. Since the ECAL has a finer granularity than the HCAL, clusters of the ECAL are linked to HCAL clusters if an ECAL cluster falls within the boundary of the HCAL cluster. Finally, linking between the muon chambers and the inner tracker occurs via a χ^2 fit to a muon trajectory that would traverse the entire detector.

5.5 Physics Object Reconstruction

Once tracks have been formed from the muon chambers, pixel, and silicon tracker detectors and linked to clusters in the ECAL and HCAL, particles can be reconstructed. The process begins by reconstructing muons, then electrons and photons, finishing with charged and neutral hadrons. The charged and neutral hadrons are then clustered together to make jets, which can be tagged as τ or b -jets. After each object is formed, the tracks and calorimeter energy depositions associated with it are removed from the collection of blocks that are used to form the particle-flow candidates, ensuring that no double counting of energy contributions is taking place.

5.5.1 Muon Reconstruction

The reconstruction of physics objects in the particle-flow algorithm begins by identifying muons [70]. The algorithm begins by identifying tracks in the pixel and silicon strip detectors that have been linked to tracks in the muon chambers, and fit with a muon trajectory with a minimum χ^2 . Additionally, it is required that muon track that is fit with both muon chambers, pixel,

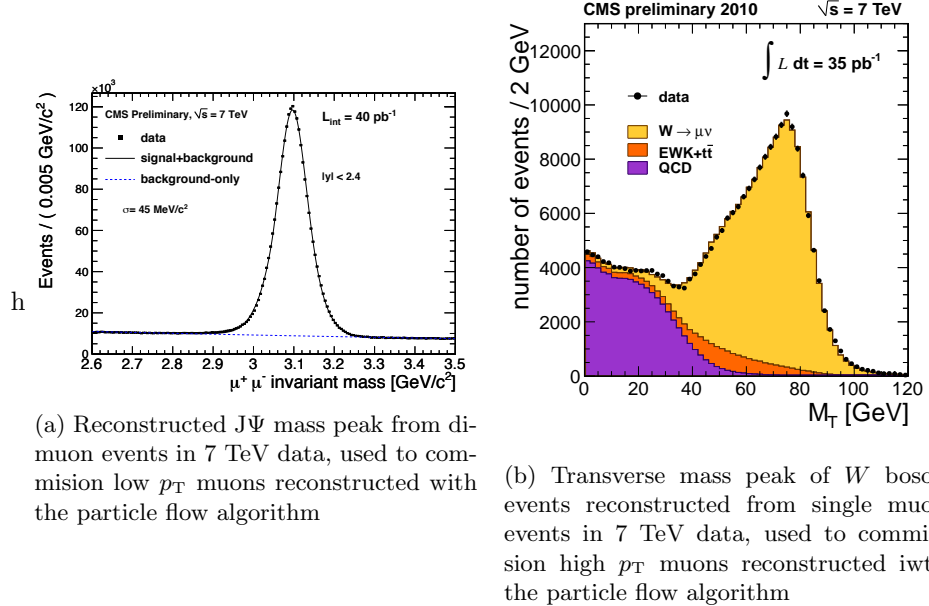


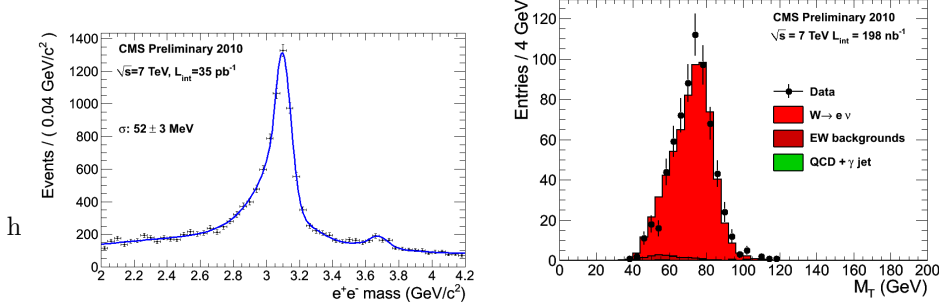
Figure 5.4: Muon validation plots for the particle-flow reconstruction

and silicon tracker information is compatible within 3 sigma, to a track fit with the pixel and silicon tracker information alone. When the "particle-flow" muon is removed from the collection of candidate blocks, the muon tracks, and based on studies from the CRAFT data run, 3 (0.5) $\text{GeV} \pm 100\%$ is removed from the HCAL (ECAL) cells that the muon traverses.

In 2010, 7 TeV data was collected [78] in order to commission the reconstruction of muons. The J/Ψ resonance at 3.1 GeV provides a large number of low p_T di-muon pairs. Figure 5.4(a) shows the reconstructed J/Ψ mass with 40 pb^{-1} of data. High p_T muons are commissioned by reconstructing the W boson mass. Figure 5.4(b) shows the results the first 35 pb^{-1} of 7 TeV data.

5.5.2 Electron Reconstruction

The next stage in particle-reconstruction is the identification of electrons [70]. Electrons leaves hits in the tracker and deposits most of its energy into the ECAL, with the clustering widest in the ϕ direction due to brehmmstralung. Electron tracks tend to be shorter and lose energy in the tracker do to bremsmstrahlung, a highly non-linear process, that the Kalman fitter used in the track identification phase is not optimized for. These tracks are re-fit using the Guassian Sum Filter (GSF) algorithm [79]. This algorithm accounts for the change in trajectory of the electron due to bremmstrahlung, extending the linking to ECAL clusters in the ϕ direction. Blocks that have GSF tracks linked to ECAL clusters, including clusters identified as bremmstrahlung photons, and additionally linked to a HCAL cluster with a much smaller energy deposition than in the ECAL are then identified as a "particle-flow electron".



(a) Reconstructed J/Ψ mass peak from di-electron events in 7 TeV data, used to commission low p_T electrons reconstructed with the particle flow algorithm

(b) Transverse mass peak of W boson events reconstructed from single electron events in 7 TeV data, used to commission high p_T electrons reconstructed with the particle flow algorithm

Figure 5.5: Electron validation plots for the particle-flow reconstruction

Similarly to the muons, the electron identification from the particle-flow algorithm was commissioned using 7 TeV data collected in 2010. Low p_T electrons were commissioned from the J/Ψ mass peak, shown in figure 5.5(a) and high p_T electrons were commissioned from W boson decays, shown in figure 5.5(b).

5.5.3 Charged Hadron Reconstruction

Charged hadrons are reconstructed next in the particle flow algorithm [70]. Tracks linked to both ECAL and HCAL energy deposits give rise to "particle-flow charged hadrons" if calorimeter energy is compatible measured from the curvature of the tracks in the pixel and silicon detector. A fit is then performed between all of the tracks and the HCAL energy clusters to determine an optimally measured momentum. In the case where there is only one track, this fit reduces to a weighted average between the track and HCAL energy clusters.

5.5.4 Photon and Neutral Hadron Reconstruction

The next step in the algorithm is to identify ECAL and HCAL energy clusters that aren't linked to tracks or clusters that are linked to tracks, but have a much larger energy measurement. In the latter case, blocks are kept if the excess energy in the calorimeter clusters is larger than the energy resolution of the calorimeter. In both cases, if the total energy excess in the HCAL is larger than the energy measured in the ECAL, than a "particle-flow photon" is created using the energy in the ECAL and the remaining HCAL energy forms a "particle-flow neutral hadron", with calibrations performed in the manner described in section 5.3. In the case where the ECAL energy is larger than the HCAL energy, both cluster energies form a particle-flow photon. This is justified the observation that, in jets, the neutral component of the hadronic energy only deposits

1595 3% of the total jet energy in the ECAL, compared to 25% of the jet energy from photons.

1596 5.5.5 Jet Reconstruction

1597 After the formation of photons, charged and neutral hadrons, jets can be formed by clustering
 1598 groups of these objects together based on their momentum weighted, spatial separation from one
 1599 another. This clustering procedure is performed with the anti- k_T algorithm [80]. The momentum
 1600 weighted spatial operation function between two particles, i and j , is defined as:

$$d_{ij} = \min\left(\frac{1}{p_{iT}^2}, \frac{1}{p_{jT}^2}\right) \frac{\Delta_{ij}^2}{R^2} \quad (5.2)$$

1601 where $\Delta_{ij}^2 = (y_i - y_j)^2 + (\phi_i - \phi_j)^2$ and $y_{i,j}$ is the rapidity, and ϕ is the azimuthal angle in
 1602 the CMS detector. R is the distance parameter, which is a user-defined quantity for the
 1603 algorithm.

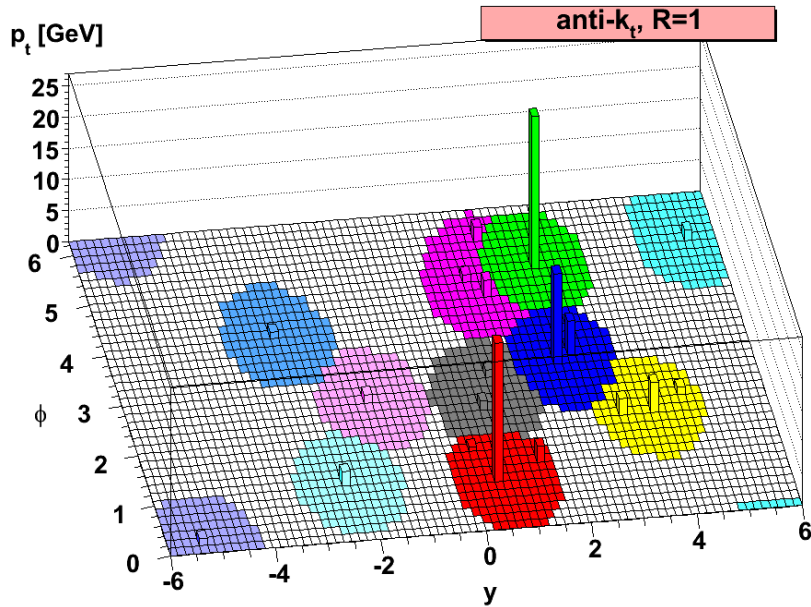


Figure 5.6: The anti- k_T jet clustering algorithm with distance parameter $R=1.0$

1604 The algorithm proceeds by looping over all of the particle-flow candidate objects that have
 1605 been formed and calculates the quantity d_{ij} , and combines the two objects with smallest value,
 1606 into a single object. The process is repeated until the smallest value, d_{ij} has a value $d_{ij} > \frac{1}{p_{Ti}^2}$ for
 1607 all remaining pairs. The parameter, d_{ij} , will be larger for two small p_T objects, when compared
 1608 to a pair of equally separated high p_T objects. Thus, softer particles will cluster around
 1609 harder objects before clustering amongst themselves. No hard particles are present, within the
 1610 distance parameter, then the object will accumulate soft particles in a circle of radius R . The
 1611 tendency is to produce circular jets, but in the case where a soft p_T cluster intersects with a hard

p_T cluster, objects the $1/p_T^2$ weighting will tend to favor clustering around the harder p_T object. Figure 5.6 shows an example of the results of an anti- kt algorithm with distance parameter $R = 1.0$, in the azimuthal-rapidity coordinate system. An example of the preferential grouping around harder p_T objects can be seen at $\phi = 5, y = 2$.

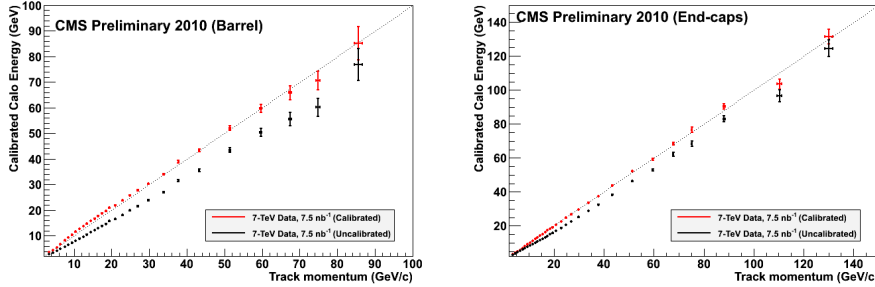


Figure 5.7: Commissioning of the particle-flow algorithm on jets, involved comparing the energy measured from charged hadron tracks, to energy measured in calorimeter clusters linked to the tracks

In 2010, the particle-flow algorithm for jet reconstruction was commissioned with 7 TeV data [81]. The calibration procedure involved selecting charged hadrons from tracks in the pixel and silicon strip detector, and comparing the energy measured there to the energy measured in the calorimeter. After calibration, the measurements between tracker and calorimeter agree within error bars up to 100 GeV, as shown in figure 5.7.

Hadronic Tau Reconstruction

Tau leptons are unstable particles which decay via a weak interaction to lighter particles. If it decays hadronically via a W boson to two quarks, the tau lepton can be reconstructed analyzing the resulting jets that are clustered by the anti- kt algorithm. Tau jets are characterized by the number of charged hadrons produced in the decay. Since charge must be conserved, this results in one charged hadron being produced $\sim 85\%$ of the time, known as a "one-pronged" decay, and three charged hadrons being produced $\sim 15\%$ of the time, known as a "three-pronged" decay. Thus, a tau jet is identified as a jet with only 1 or 3 tracks associated with the calorimeter cluster. Additionally, the jets from hadronic tau decays tend to have their energy more collimated than jets produced from quarks or gluons. Jets are clustered twice, using two different distance-parameters. The ratio of energies of the smaller to the larger of the distance parameters jets is used to determine how collimated a jet is. If the ratio is within a given threshold, determined by the analyst in terms of the reconstruction efficiency and fake rate, the jet is tagged as a hadronic tau jet.

1635 **b-Tagging**

1636 Jet that originate from b -quarks have unique characteristics that allow them to be distinguished
1637 from jets originating from other quarks or gluons. This identification process is known as b -tagging.
1638 Several algorithms exist to identify b -jets, since there are many kinematic variables
1639 that distinguish them from other jets. Due to the heavier nature of the b -quark, b -jets have a
1640 larger transverse momentum compared to lighter-flavour quarks. Since it belongs to the third
1641 quark generation, it is much more likely to find a non-prompt lepton embedded in the jet. Muons
1642 are especially useful to tag b -jets since the information they leave in the tracker can be used to easily
1643 identify if it came from prompt decay or not.

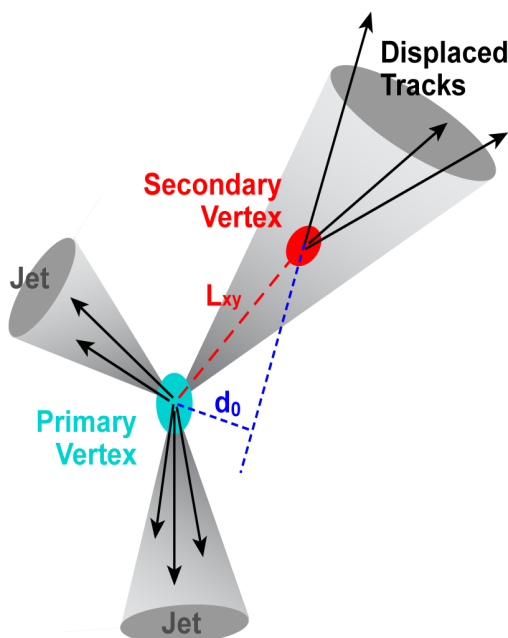


Figure 5.8: A b -meson will travel a distance L_{xy} before decaying and creating a secondary vertex. The impact parameter, d_0 measures the longitudinal displacement of the two vertices

1644 The most important characteristic of the b -quark is its relatively long lifetime compared to
1645 lighter-flavour quarks. The consequence is that a b -meson will travel a very small, but observable
1646 distance within the tracker before it decays, forming a secondary vertex. The distance and
1647 uncertainty measured on the distance between the primary and secondary vertex is then used as
1648 discriminating variables to tag b -jets. Figure 5.8 shows a cartoon of a b -jet creating a secondary
1649 vertex after traveling some distance from the primary vertex.

1650 **5.5.6 Missing Transverse Energy Reconstruction**

1651 CMS has a hermetic design to ensure that all particles produced in a collision would pass through
1652 the detector. Only long-lived, neutral particles avoid detection, such as neutrinos in the standard

¹⁶⁵³ model. Many BSM theories, such as SUSY, are also characterized by stable, neutral particles.
¹⁶⁵⁴ These particles can only be detected by measuring a momentum imbalance after measuring all
¹⁶⁵⁵ of the particles in the event.

¹⁶⁵⁶ The missing transverse energy (MET), \cancel{E}_T , is the vector sum of all of particle-flow candidates
¹⁶⁵⁷ reconstructed in the event. It is defined as

$$\cancel{E}_T = \left| - \sum_{i=1}^{nPF} \vec{p}_{Ti} \right| \quad (5.3)$$

¹⁶⁵⁸ where nPF is the number of particle-flow candidates in the event, and \vec{p}_{Ti} is the vector sum of
¹⁶⁵⁹ their transverse momentum.

¹⁶⁶⁰ The particle-flow algorithm for reconstructing MET was commissioned in 2010 with 7 TeV data
¹⁶⁶¹ [81]. Minimum-bias collisions and QCD multi-jet production are processes that produce no real
¹⁶⁶² MET. Therefore, a sample of these events were collected, allowing for the algorithm to be tuned
¹⁶⁶³ and calibrated.

1664 Chapter 6

1665 Analysis I: The first 5 fb⁻¹ of 8

1666 TeV data

1667 The search for $t\bar{t}H$ production begins by identifying pp collisions consistent with the production
1668 of a top quark pair with additional b jets. Top quarks decay $\sim 100\%$ of the time to a bottom
1669 quark and a W boson, and the W boson can decay either into a charged lepton and a neutrino
1670 or into a pair of quarks. Since there are two W bosons in the event, the decays of the W
1671 bosons determine the specific top pair signatures recorded in the detector. The decay of the two
1672 W bosons define the categorizations of $t\bar{t}$ -like events as either all-hadronic, in the case of zero
1673 charged leptons; semi-leptonic, in the case of one charged lepton; and di-leptonic in the case of
1674 two charged leptons. the detector. This analysis describes the Lepton+Jets (LJ) channel, where
1675 one of the W bosons has decayed to an electron or a muon and the corresponding neutrino,
1676 while the other W boson decays into two quarks. To compensate for the low production rate,
1677 the analysis is optimized to search for the Higgs boson decaying to a b -quark pair. The final
1678 state is then $l\nu qqbbbb$, where l refers to either an electron or a muon. In the case of an ideal
1679 reconstruction of the event, the LJ signal events contains six jets, four of which are b -tagged.
1680 However, to accommodate jets lost to detector acceptance and merging between separate partons,
1681 and the b -tagging efficiency, events with four or more jets and two or more b -tags are included
1682 in the signal region.

1683 The largest background contribution is $t\bar{t}$ +jets production. This process can be decomposed
1684 in terms of the flavour of the extra jets produced in the event. For this analysis, the inclusive
1685 $t\bar{t}$ jets process is broken into three sub-processes: $t\bar{t}$ + light flavor jets where one or more of the
1686 jets is mistagged, $t\bar{t} + c\bar{c}$ and $t\bar{t} + b\bar{b}$. Smaller background contributions come from W +jets,
1687 Z +jets, single top quark, diboson, and $t\bar{t} + W/Z$ production.

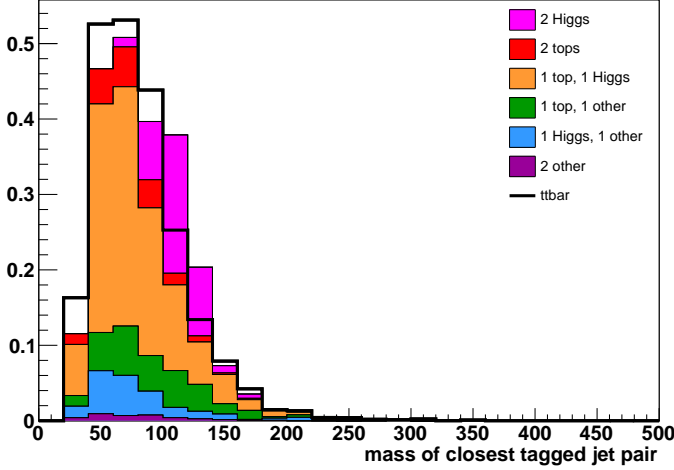


Figure 6.1: This figure shows the breakdown of jet-to-parton assignments for the two jets with the minimum ΔR separation in the event for events with greater or equal 4 b -tagged jets.

In other Higgs searches involving the decay to two b -quarks, the most powerful discriminating variable is the invariant mass of the $b\bar{b}$ pair, which has a peak at the mass of the Higgs. However, for $t\bar{t}H$ production, with a final state of four b -quarks, the combinatorics of selecting the quarks coming from the Higgs, instead of the $t\bar{t}$ system, prevents the reconstruction of a clear resonant peak, as shown in figure 6.1. This results in an additional loss of mass resolution, or smearing, on the $b\bar{b}$ invariant mass spectrum.

Although there is poor resolution on the Higgs boson resonance in the b -quark dijet mass spectrum, there are a number of kinematic variables that can be used to discriminate between the $t\bar{t}+j$ background and the $t\bar{t}H$ signal. For example, the recoil of the Higgs off of the $t\bar{t}$ system, the decay products of the top quarks from the $t\bar{t}H$ signal will have, on average, a slightly larger component of momentum transverse to the beam-line. Additionally, the larger number of authentic b -jets in $t\bar{t}H$ events can be exploited through the likelihood value returned by a b -tagging algorithm for all of the jets in the event. By themselves, none of these variables provide a large degree of discriminating power to separate the $t\bar{t}H$ signal from the large, and kinematically similar background. Therefore, the discriminating power of several variables is combined using a multivariate analysis technique (MVA), which is used to set upper limits on $t\bar{t}H$ production in the data set.

The following sections will describe the analysis that was carried out on the first 5 fb^{-1} of data collected by the CMS detector. This includes definitions of the simulated samples used to estimate the expected backgrounds in data, the event selection used to isolate the $t\bar{t}H$ signal, the application of MVA techniques, evaluation of systematic uncertainties, and upper limit setting on the production rate of $t\bar{t}H$.

6.1 Data and Simulated Samples

pp collision data is collected by the CMS detector, as described in previous chapters. The signal and background signatures are estimated using Monte Carlo simulation techniques. The simulation involves the combination of the most current theoretical and empirical information about the interactions of the known particles. The simulation of an event is decomposed into a sequence of calculations and each signal and background process is calculated separately. Information about Monte Carlo event simulation techniques is taken from reference [82].

The first stage of event simulation for a given signal or background process is to calculate the probability that some set initial state particles with a certain momentum will create a final state of particles with a certain momentum. For example, in the case of the $t\bar{t}H$ signal, this is the probability that two protons travelling towards each other along the z-axis (beam-line), each with a given energy and momentum, will produce a top quark pair and a Higgs boson, each with some momentum vector, \hat{p}_t , $\hat{p}_{\bar{t}}$, \hat{p}_H , which points into the hermetic CMS detector. As discussed in section 2.1, this probability is calculated by examining the lagrangian of the theory describing the process and calculating its scattering amplitude, to some order in perturbation theory, using the Feynman rules derived from the lagrangian. The scattering amplitude is a multi-dimensional probability function, which depends on the initial and final state momentum of the particles in the process. Thus, given some initial state momentum, p_i , it tells you the probability to produce a final state particle with momentum p_f . It is understandable that the scattering amplitude is often referred to as a matrix element, since given a vector of initial state particles with a certain momentum, the scattering amplitude would be a matrix, whose elements would give the probability of creating the vector of final state particles.

Since protons are composite objects, when they collide, it is their quarks or gluons which are actually interacting. The momentum distribution of each of the valence quarks, the gluons, and the sea quarks, which account for quantum fluctuations that temporarily create all other quark flavours inside the proton, is described by a Parton Distribution Function (PDF). The PDF describes what fraction of the proton's momentum is distributed among each of its constituents. Due to the large strength of the QCD interactions that bind the quarks together, the PDF cannot be calculated perturbatively from QCD. It has been measured empirically, and is composed of the results of several experiments over the past decades.

Event generator algorithms are computer programs that, given a lagrangian of particle theory, will calculate the matrix element for a given process. Then, the generator is provided with values of the momentum of the initial state particles. For protons, this would be the beam energy of the LHC. To assign momentum values to the constituent quarks or gluons that actually participate in the interaction, random values are sampled from the probability distributions described by

1745 a PDF that is provided to the algorithm. Given a choice of momentum for the input particles,
 1746 a value and direction of the momentum for each of the final state particles is sampled from
 1747 the probability function provided by the calculated the matrix element (ME). The process of
 1748 randomly sampling a probability function, in order to conduct a calculation, is known as a Monte
 1749 Carlo sampling technique.

1750 In the case where final state particles are quarks or gluons, also known as partons, an ad-
 1751 ditional calculation is necessary to create the physical hadron states. First, the decay sequence
 1752 of each parton is calculated until the decay products reach a user defined value, known as the
 1753 hadronization scale. This decay sequence is referred to as the parton shower (PS), since each
 1754 parton creates a multitude, or a shower, of additional partons. Once the parton shower is cal-
 1755 culated, each of the colored partons are transformed into color-singlet primary hadrons, which
 1756 themselves decay, and form secondary hadrons. This process, known as hadronization, results in
 1757 a collimated spray of hadrons, each with a component of momentum along the original parton's
 1758 direction. These hadrons are clustered together and referred to as a hadron jet.

1759 Once the hadronization is completed, the next stage of the event generation is to simulate the
 1760 response of the CMS detector when this process occurs at the interaction point where the LHC
 1761 beams are made to collide. The Geant 4 detector simulation framework is used to create a model
 1762 of each and every detector element, electronic readout, and mechanical support structures that
 1763 make compose CMS. Geant 4 is also about to describe how energy is deposited into the different
 1764 types of material as a particle passes through each detector element, simulating the response
 1765 each element to presence of a particle in the detector. The digitization and signal acquisition of
 1766 the electronics that read-out the detector elements is also simulated.

1767 The final stage the generation of an event is the reconstruction of the simulated detector
 1768 signals into physics objects. This process is described in detail in the previous chapter. It
 1769 proceeds with simulated, instead of real detector signals.

1770 The entire event simulation, reconstruction, and subsequent analysis is implemented in a
 1771 software framework that is known as CMS Software (CMSSW).

1772 6.1.1 Data Samples

1773 The results presented here are based on the first $5.08 fb^{-1}$ of the 2012 CMS dataset. Data-sets
 1774 are collected through HLT triggers and stored offline for analysis. Table 6.1 lists the datasets
 1775 used for this analysis, which is composed of two runs of data collection triggered on the presence
 1776 of one muon or electron in an event. The luminosities are quoted from a calculation performed
 1777 with minimum-bias events measured with the HF detector and have been determined to have a
 1778 2.2% uncertainty.

Dataset	Run Range	Integrated Luminosity
/SingleMu/Run2012A-PromptReco-v1/AOD	190645–193621	0.87 fb ⁻¹
/SingleMu/Run2012B-PromptReco-v1/AOD	193834–196531	4.21 fb ⁻¹
Total SingleMu	190645–196531	5.08 fb⁻¹
/SingleElectron/Run2012A-PromptReco-v1/AOD	190645–193621	0.87 pb ⁻¹
/SingleElectron/Run2012B-PromptReco-v1/AOD	193834–196531	4.21 pb ⁻¹
Total SingleElectron	190645–196531	5.08 fb⁻¹

Table 6.1: The datasets analyzed for this analysis.

1779 6.1.2 Signal Samples

1780 The $t\bar{t}H$ signal is modeled using the Pythia Monte Carlo generator. Signal events were generated
 1781 privately using the same conditions and configuration as the "Summer" MC campaign, which
 1782 generated the background samples used in this analysis and is a central effort by a dedicated
 1783 team of collaborators within the CMS experiment. The samples and associated cross sections
 1784 used are listed in Table 6.2.

Mass	Dataset	Cross Sect.
110 GeV/c ²	/TTH_HToAll_M_110_8TeV_FastSim_pythia6/lannon-TTH_HToAll_M_110_8TeV _FastSim_pythia6-dff75535147f54d9d70123289019ff88/USER	0.1887 pb
115 GeV/c ²	/TTH_HToAll_M_115_8TeV_FastSim_pythia6/lannonTTH_HToAll_M_115_8TeV _FastSim_pythia6f8fb6149649333009ec8462da200312d/USER	0.1663 pb
120 GeV/c ²	/TTH_HToAll_M_120_8TeV_FastSim_pythia6/puighTTH_HToAll_M_120_8TeV _FastSim_pythia695111b4e2be5b1aa536a508d15d97f92/USER	0.1470 pb
122.5 GeV/c ²	/TTH_HToAll_M_122p5_8TeV_FastSim_pythia6/slaunwhj- TTH_HToAll_M_122p5_8TeV_FastSim_pythia61e2fdcc9a937df208692b27cb39e0444/USER	0.1383 pb
125 GeV/c ²	/TTH_HToAll_M_125_8TeV_FastSim_pythia6/lwmingTTH_HToAll_M_125_8TeV _FastSim_pythia6191b19832235558f2b51f7486e9bfa14/USER	0.1302 pb
127.5 GeV/c ²	/TTH_HToAll_M_127p5_8TeV_FastSim_pythia6_crabv2/jgwoodTTH_HToAll _M_127p5_8TeV_FastSim_pythia6_crabv28cc2ab68d00e069563cff89a5be0e271/USER	0.1227 pb
130 GeV/c ²	/TTH_HToAll_M_130_8TeV_FastSim_pythia6/neuTTH_HToAll_M_130_8TeV _FastSim_pythia65052c957a6363e9b1d5c2be444ffc86d/USER	0.1157 pb
135 GeV/c ²	/TTH_HToAll_M_135_8TeV_FastSim_pythia6/lwmingTTH_HToAll_M_135_8TeV _FastSim_pythia6c8734ad98f674743d713309ea4b6ad34/USER	0.1031 pb
140 GeV/c ²	/TTH_HToAll_M_140_8TeV_FastSim_pythia6/lwmingTTH_HToAll_M_140_8TeV _FastSim_pythia6cf0b11a8bdd755ec1ec3d7a35c9a88be/USER	0.09207 pb

Table 6.2: List of signal MC datasets and cross sections used to determine the SM expectation.

1785 6.1.3 Background Samples

1786 In order to estimate the rate and kinematic behavior of the backgrounds, this analysis primarily
 1787 uses Monte Carlo (MC) samples from the "Summer12" MC campaign. Most of the samples are
 1788 generated either with the Madgraph tree-level matrix element generator matched to Pythia for
 1789 the parton shower, or with the NLO generator Powheg combined with Pythia. These samples
 1790 are reconstructed with the same CMSSW version as the data samples listed above. Table 6.3
 1791 lists the background MC samples and associated cross sections.

Sample	Dataset	Cross Sect.
$t\bar{t}$ +jets	/TTJets_MassiveBinDECAY_TuneZ2star_8TeVmadgraph-tauola/Summer12PU_S6_START52_V9v1/AODSIM	225.197 pb
$t\bar{t} + W$	/TTWJets_8TeVmadgraph/Summer12PU_S7_START52_V9v1/AODSIM	0.249 pb
$t\bar{t} + Z$	/TTZJets_8TeVmadgraph_v2/Summer12PU_S7_START52_V9-v1/AODSIM	0.208 pb
W +jets	/WJetsToLNu_TuneZ2Star_8TeVmadgraphtarball/Summer12-PU_S7_START52_V9v1/AODSIM	36257.2 pb
Z/γ^* + jets $M_{\ell\ell} > 50 \text{ GeV}/c^2$	/DYJetsToLL_M50_TuneZ2Star_8TeVmadgraphtarball/Summer12-PU_S7_START52_V9v2/AODSIM	3503.17 pb
$10 \text{ GeV}/c^2 < M_{\ell\ell} < 50 \text{ GeV}/c^2$	/DYJetsToLL_M10To50filter_8TeVmadgraph/Summer12-PU_S7_START52_V9v1/AODSIM	860 pb
Single t schannel	/T_schannel_TuneZ2star_8TeVpowhegtauola/Summer12-PU_S7_START52_V9v1/AODSIM	3.79 pb
t channel	/T_tchannel_TuneZ2star_8TeVpowhegtauola/Summer12-PU_S7_START52_V9v1/AODSIM	56.4 pb
tW	/T_tWchannelDR_TuneZ2star_8TeVpowhegtauola/Summer12-PU_S7_START52_V9v1/AODSIM	11.1 pb
Single \bar{t} schannel	/Tbar_schannel_TuneZ2star_8TeVpowhegtauola/Summer12-PU_S7_START52_V9v1/AODSIM	1.76 pb
t channel	/Tbar_tchannel_TuneZ2star_8TeVpowhegtauola/Summer12-PU_S7_START52_V9v1/AODSIM	30.7 pb
tW	/Tbar_tWchannelDR_TuneZ2star_8TeVpowhegtauola/Summer12-PU_S7_START52_V9v1/AODSIM	11.1 pb
WW	/WW_TuneZ2star_8TeV_pythia6_tauola/Summer12-PU_S7_START52_V9v1/AODSIM	54.8 pb
WZ	/WZ_TuneZ2star_8TeV_pythia6_tauola/Summer12PU_S7_START52_V9-v1/AODSIM	32.3 pb
ZZ	/ZZ_TuneZ2star_8TeV_pythia6_tauola/Summer12PU_S7_START52_V9-v1/AODSIM	7.7 pb

Table 6.3: List of background MC datasets and cross sections used for normalization.

6.1.4 MC pileup reweighting

During 2012 data collection, the LHC provided increasingly large instantaneous luminosities to the CMS experiment. Consequently, the average number of overlapping events reconstructed in single detector readout window has also increased. When these overlapping events, known as pileup events, occur within the same bunch crossing, which as referred to as "in-time" pileout. Alternatively, "out-of-time" pileup, comes from energy deposits in the detector from previous bunch crossings and from very early arrivals of particles from the forthcoming bunch crossing. Pileup events can affect many aspects of the reconstruction of a more interesting event, such as the degradation of lepton isolation and jet energy resolution. The simulated samples used in the analysis must also have the same distribution of pileup events as what was measured in the data.

During the generation of the simulated samples used in the analysis, the average amount of expected pileup was unknown. Events were thus simulated with a conservatively large estimate of the pileup distribution, so that if the measured data revealed a smaller average value, the simulation could be reweighted to match the data. For the simulation, number of interactions is a user defined value added to every generated event. For the data, the number of pileup interactions for each unit of time depends on the instantaneous luminosity for each bunch pair

and the total inelastic cross section, $\sigma_{inelastic}$, of the proton. The value of $\sigma_{inelastic} = 69.4$ mb was found to describe the data well. To estimate the effect of the systematic uncertainty of this choice, the value was varied by $\pm 7\%$.

To gauge the accuracy of the calibration of the pileup distribution used in the simulated samples, a comparison of the number of reconstructed vertices between data and the simulated $t\bar{t}$ MC sample is shown in figure 6.2. The unweighted MC distribution is shown in blue, the reweighted distribution in red, and the measured data in black points. After reweighting, there is a good level of agreement between the data and MC distributions.

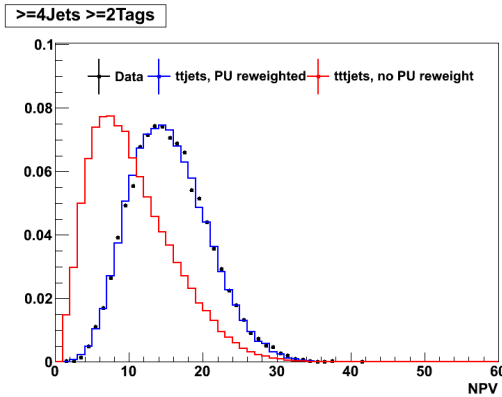


Figure 6.2: Comparison of number of reconstructed vertices for data (black) and the $t\bar{t}$ MC sample before (blue) and after (red) pileup reweighting. After pileup reweighting, the MC matches the data well.

6.1.5 Additional Pileup Corrections

Studies comparing the Monte Carlo simulations to observed data revealed that the jet p_T spectra was not well modeled. Many sources of this discrepancy were investigated, but the clearest correlations arises when the 8 TeV data events are divided into three categories according to their amount of pileup:

• Low PU, number of primary vertices ≤ 10

• Medium PU, number of primary vertices from 11 to 15

• High PU, number of primary vertices ≥ 16

The modeling of jet p_T was worse for events with a larger number of pileup events overlapping in the detector. The same effect was present for the majority of the jets in the event, evidenced by the discrepancy in the H_T distribution, shown in figure 6.3, where H_T is defined as the scalar sum of the transverse momentum for reconstructed jets in the event:

$$H_T = \sum_i^{jets} p_T^i \quad (6.1)$$

The effect makes the data have a softer p_T spectrum than the simulations. The same effect was observed in 7 TeV data as well. It was present, even after employing several sophisticated reconstruction techniques designed to mitigate pileup effects. These techniques included the removal of charged hadrons in the particle-flow algorithm, not associated with the primary vertex and re-weighting the simulated samples to match the pileup distribution measured in the data.

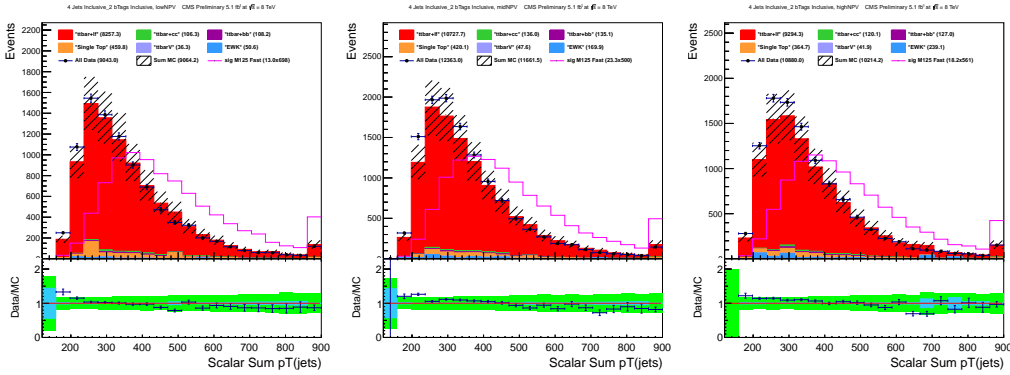


Figure 6.3: H_T distribution for 8 TeV lepton plus jet events with $\geq 4 jets$ and $\geq 2 tags$ shown for different amounts of pileup. The left-hand plot shows low pileup, the middle plot shows medium pileup, and the right-hand plot shows high pileup.

Although the exact underlying cause of the jet mis-modelling effect was not able to be identified, the magnitude of the effect seemed to be related to the number of pileup events. As such, an additional correction factor is needed to account for the remaining difference in pileup effects between data and Monte Carlo. The correction factor was calculated from data that was dominated by background events, with a single lepton, ≥ 4 jets, and ≥ 2 tags. The expected signal-to-background ratio in this sample is 0.002, which is low enough that the correction factor will not be biased by signal events. The correction factor is based on the H_T distribution for data and Monte Carlo for Low pileup (PU), Medium PU, and High PU events. The correction factor is the bin-by-bin ratio of the data and the Monte Carlo H_T distributions in each PU category. By preparing a separate correction factor for each PU category smaller adjustments were made to well-modeled Low PU events and larger adjustments to the poorly modeled High PU events. H_T shows the same mis-modelling as each of the jet p_T s and it effects all of the jet p_T s. This makes it a natural choice for a correction factor.

In order to evaluate the systematic shape uncertainty introduced by the correction factor, the uncorrected simulated distributions are used as -1σ systematic uncertainty and the $+1\sigma$ uncertainty is determined by doubling the correction factor. The factor of two for the $+1\sigma$ variation is motivated by the desire to provide a large enough systematic uncertainty to cover

any possible over-correction of the simulations. This is a reasonable choice because it creates a deviation that is the same size as the original observed difference between data and simulations.

The correction factor and uncertainty improved the agreement between data and Monte Carlo. Figure 6.4 compares the H_T distributions before and after reweighting. The data-to-MC ratio plots are the clearest indicators of the improvement from the correction factor. Before the correction, the H_T ratio plot forms a line with a slope. After the correction the slope is gone.

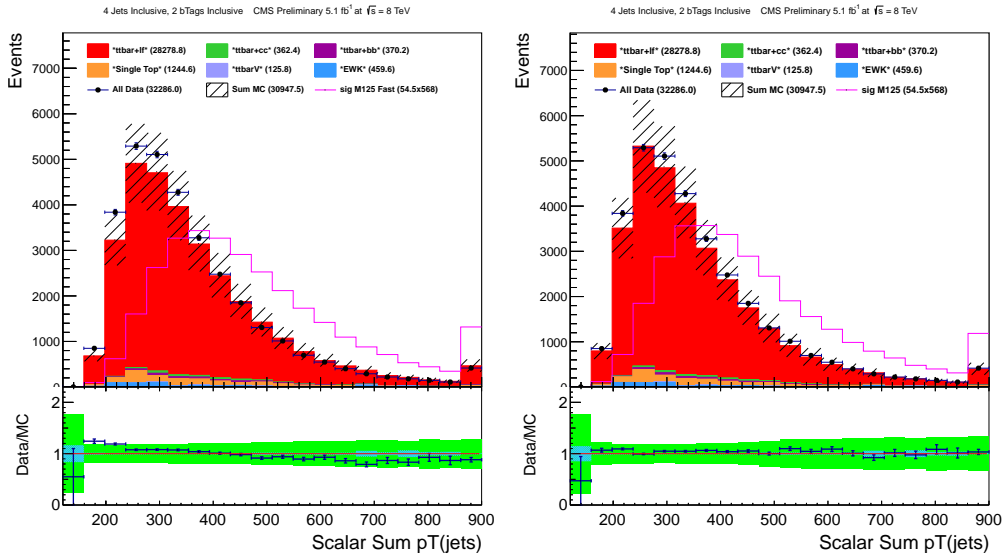


Figure 6.4: H_T distribution for 8 TeV lepton plus jet events with ≥ 4 jets and ≥ 2 tags. The left-hand plot shows the distribution before correction. The right-hand plot shows the distribution after correction. Note that the ratio in the right-hand plot is flatter than the left-hand plot.

6.2 Event Selection

This section defines the common physics objects and event selection requirements. Leptons are classified into two categories, tight and loose, defined for muons in section 6.2.3 and for electrons in 6.2.4. For this analysis, exactly one tight muon or exactly one tight electron is required and events with any additional loose leptons are rejected.

6.2.1 Event cleaning

For data and MC events, certain cuts are applied to remove events that are either non-physical or that come from non-collision events, such as instrumental noise or beam backgrounds. In the data, every event is required to pass the following filters:

- CSC tight beam halo filter - Secondary particles are produced in showers which are initiated by collisions of the beam with residual gas inside the LHC vacuum chamber or by interactions of the particles with a large transverse emmitance with limiting apertures.

- HBHE noise filter with isolated noise rejection - this filters spurious signals from the HCAL barrel and endcap subdetectors which are not associated with particles measured in a collision event.
- HCAL laser filter - ensures that data is not taken simultaneous with the laser calibration system
- ECAL dead cell trigger primitive (TP) filter - removes dead or noisy ECAL cells from being used in the reconstruction, these compose < 1% of the total crystals in the ECAL
- Tracking failure - designed to catch events with too few tracks
- Noisy SCs in EE - new filter from the ECAL Detector Performance Group (PDG), and validated by the MET Physics Object Group (POG)

which are described in [83].

Additionally, beam scraping events are filtered based on the fraction of good tracks. We require that at least 25% of tracks are of high purity. Finally, every data event must contain at least one primary vertex (PV) that passes the following selection:

- The number of degrees of freedom used to find the PV must be larger than 4,
- The absolute value of the z -coordinate of the PV must be smaller than 24 cm,
- The absolute value of the ρ -coordinate of the PV must be smaller than 2 cm,
- The PV must not be identified as fake.

6.2.2 Trigger

Each data and MC event is required to pass one of the triggers in Table 6.4, which are a subset of the total number of SingleMu and SingleEle HLT triggers available. Muon+jet events must pass the SingleMu trigger, while electron+jet events must pass the SingleEle trigger.

Dataset	Trigger Name
SingleMu	HLT_IsoMu24_eta2p1_v*
SingleEle	HLT_Ele27_WP80_v*

Table 6.4: List of lepton+jets triggers

6.2.3 Muon Selection

In this analysis, muons are selected from the set of "particle-flow" muon objects that have been reconstructed in the event. Muons are classified into two categories: tight and loose, according

1893 to the quality of their reconstruction. This is ensured by applying the selection cuts shown in
1894 Table 6.5. The cuts are defined as follows:

- 1895 • p_T - the component of the momentum transverse to the beam-line.
- 1896 • PFRelIso - this is the quantity known as relative isolation, computed by the particle flow
1897 algorithm. It is a ratio of the energy deposits remaining in the calorimeter and tracker,
1898 after the contribution from the muon has been removed, in a cone size $\Delta R = 0.3$, around
1899 the muon track.
- 1900 • $|\eta|$ - the absolute value of the pseudorapidity of the muon
- 1901 • ID - This refers to whether the muon was reconstructed with a χ^2 fit to the tracks from
1902 the tracker only (tracker muon), the tracker and the muon chambers (global muon), or if
1903 the particle was reconstructed from the particle-flow algorithm (PFmuon)
- 1904 • $N_{layers}(\text{tracker})$ - the number of layers in the tracker with hits used in the muon track
1905 reconstruction
- 1906 • X^2 of track fit - the reduced χ^2 (raw χ^2 /Number of Degrees of Freedom in the fit), typically
1907 a value of 1 indicates the fit describes the data well
- 1908 • $N_{layers}(\text{pixel})$ - the number of layers in the inner pixel detector with hits used in the muon
1909 track reconstruction
- 1910 • $N_{segments}(\mu)$ - the number of segments in the muon chambers used to reconstruct the
1911 muon tracks
- 1912 • $|d0(\text{BS})|$ - the absolute value of the transverse distance of the extrapolated muon track to
1913 the primary vertex, as calculated from the beam spot (BS)
- 1914 • $|dZ(\text{BS})|$ - the absolute value of the longitudinal distance of the extrapolated muon track
1915 to the primary vertex

1916 6.2.4 Electron Selection

1917 Electrons are selected from the set of "particle-flow electron" objects reconstructed in the event.
1918 Similarly to muons, electrons are classified into two categories: tight and loose, according to the
1919 quality of their reconstruction. The selection cuts are shown in Table 6.6. The definitions
1920 are identical to the ones provided in section 6.2.3. Additional variables not described are:

- 1921 • E_T - the transverse energy of the electron, which due to its relatively light mass, is approx-
1922 imately equal to its p_T

Cuts	Tight μ	Loose μ
p_T	$>30 \text{ GeV}/c$	$>10 \text{ GeV}/c$
PFRelIso(0.4)	0.12	<0.2
$ \eta $	<2.1	<2.5
ID	Global Muon	Global Muon or Tracker Muon
ID	PFMuon	PFmuon
$N_{\text{layers}}(\text{tracker})$	>5	
X^2 of track fit	<10	
$N_{\text{layers}}(\text{pixel})$	>0	
$N_{\text{segments}}(\mu)$	>1	
$ d0(\text{BS}) $	<0.2 cm	
$ dZ(\text{BS}) $	<0.5 cm	

Table 6.5: Tight and loose muon definition

- ID - electron ID is passed on a multivariate analysis (MVA) technique, which provides a discriminant value to separate fake from real electrons, and is trained with events that are required to pass a HLT trigger (mvaTrigV0), or not (mvaNonTrigV0). The "passConversionVeto" ID ensures that the electron has not been reconstructed from a photon which has converted to an electron positron pair

Cuts	Tight e	Loose e
E_T	$>30 \text{ GeV}/c^2$	$>15 \text{ GeV}/c^2$
PFRelIso(0.3)	<0.1	<0.2
$ \eta $	<2.5	<2.5
ID	MVA ID("mvaTrigV0") >0.0	MVA ID("mvaNonTrigV0") >0.0
ID	passConversionVeto	passConversionVeto
$ d0(BS) $	<0.02 cm	
$ dZ(PV) $	<1 cm	

Table 6.6: Tight and loose muon definition

6.2.5 Lepton selection and trigger efficiencies

The cumulative reconstruction efficiency of id+isolation+trigger has been calculated from data, as a function of pT and eta, as shown in figure 6.5 for electrons and muons. In order to reproduce the same response in the simulations as found in data, an event-by-event scale factor is applied to correct for this difference in efficiency.

The efficiency in data was measured by selected events with two tight muons, or two tight electrons with an invariant mass in a range between 70 and 130 GeV. This is centered on the Z boson resonance, and ensures that the selected leptons are authentic. The two leptons are additionally required to have opposite charge, which is measured by the direction of the curvature of their tracks in the magnetic field. A "tag" lepton is selected if has $p_T > 30 \text{ GeV}$, and passes the appropriate muon or electron trigger. The second lepton, the "probe" lepton, since selected as a pair coming from a Z boson, should be identical to the tag lepton, and thus should be identically reconstructed. The efficiency is then the ratio of the number events where both tag and probe leptons pass the p_T and trigger requirements over the number of events where only

1942 the tag lepton passes the p_T and trigger requirements. This study is repeated in bins of p_T and
 1943 η to remove any kinematic dependence on lepton efficiency.

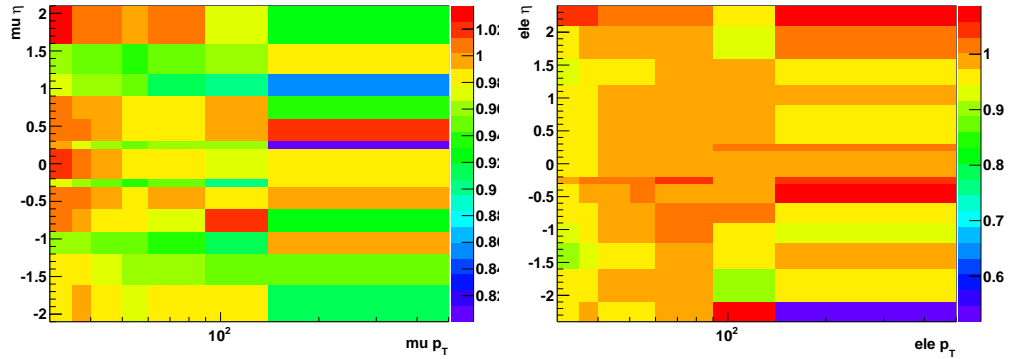


Figure 6.5: Muon and electron ID, isolation selection and trigger efficiency scale factors in bins of p_T and η .

1944 The combined ID, isolation, and trigger scale factor uncertainty is evaluated by looking at the
 1945 variation of the scale factor as a function of parameters besides p_T and η , such as pileup and b -tag
 1946 scale factor reweighting. A flat uncertainty of 4% covers the variations that are observed, and is
 1947 thus adopted as a conservative estimate of the uncertainty on the combined lepton reconstruction
 1948 efficiency.

1949 6.2.6 Jet selection

1950 As described in the previous chapter, jets are reconstructed with the anti-KT clustering algo-
 1951 rithm [80], with a distance parameter of 0.5, starting from the set of objects reconstructed
 1952 by the particle flow algorithm [70]. Non-isolated leptons, not associated with the decay of a
 1953 W boson, are allowed to be clustered into the jets. The selection cuts defining our jets can be
 1954 found in Table 6.7. The cuts use the following variables to ensure the reconstruction of authentic
 1955 hadronic jets:

- 1956 • p_T - component of the momentum transverse to the beam-line
- 1957 • η - the pseudorapidity of the reconstructed jet
- 1958 • CEF - Charged Electromagnetic Fraction: the ratio of charged particles to the total number
 1959 of particles in the jet
- 1960 • NHF - Neutral Hadron Fraction: the ratio of neutral particles to the total number of
 1961 particles in the jet
- 1962 • NEF - Neutral Electromagnetic Fraction: the ratio of photons to the total number of
 1963 particles in the jet

- CHF - Charged Hadron Fraction: the ratio of charged hadrons to the total number of particles in the jet
- NCH - Number of Charged Hadrons: raw charged hadron multiplicity
- $N_{\text{constituents}}$ - Number of constituents, which can be charged and neutral hadrons, as well as non-prompt photons and leptons.

Cuts	Jet
p_T	$>30 \text{ GeV}/c$
$ \eta $	<2.4
CEF, NHF, NEF	<0.99
CHF, NCH	>0
$N_{\text{constituents}}$	>1

Table 6.7: Jet definition

Additional correction factors are required such that the measured energy of the jet correctly reproduces the energy of the initial parton. This is done in four stages. The L1 Charged Hadron Subtraction (CHS) correction, is implemented in the particle-flow algorithm, and involves subtracting the energy contributions from charged hadrons that are not associated with the jet from the energy cluster. The next stage, L2 correction is a relative correction to make the measured jet response flat in η . The third stage, L3, is an absolute correction to the measured p_T of a jet in order to match the simulated jet p_T created using generator level input and a similar jet clustering algorithm. The L2 and L3 corrections are calculated using Monte Carlo, and thus an fourth correction factor, the L2L3 residual correction is applied that fixes the discrepancies between Monte Carlo and data. The correction factors are described in reference [84], and are derived from 2011 7 TeV data, with a selection of dijet events near the Z -boson mass peak. A "tag-and-probe" procedure similar to the lepton scale factors is applied to jets to determine the kinematic dependence (p_T and η) of the detector in both simulations and data. Additionally, a scale factor is needed to adjust for the difference in jet energy resolution as measured in data and predicted in simulation. Table 6.8 gives the scale factors, and uncertainties, as derived from dijet events [84] as a function of η only, since no significant p_T dependence was observed.

$ \eta $	Data/MC Ratio (factor +stat. +syst.- syst.)
0.00-0.5	$1.052 \pm 0.012 + 0.062 - 0.061$
0.51-1.1	$1.057 \pm 0.012 + 0.056 - 0.055$
1.11-1.7	$1.096 \pm 0.017 + 0.063 - 0.062$
1.72-2.3	$1.134 \pm 0.035 + 0.087 - 0.085$
2.35-3.0	$1.288 \pm 0.127 + 0.155 - 0.153$

Table 6.8: Jet Energy Resolution (JER) scale factors

1985 **6.2.7 *b*-tagging selection**

1986 The algorithm used to perform *b*-tagging in this analysis is the combined secondary vertex (CSV)
 1987 algorithm [85]. It relies on the superior ability of the inner tracker to reconstruct secondary
 1988 vertices, which are the characteristic signature of *b*-quark decays. Tracks are selected if they
 1989 meet the following requirements:

- 1990 • At least 8 hits in the pixel and silicon tracker, with at least 2 hits in the pixel detector
 1991 • tracks must have $p_T > 1$ GeV
 1992 • χ^2/NDF of the fitted track < 10
 1993 • $|d_0|$ - transverse impact parameter $< 2\text{mm}$, since *b*-quarks will on average travel 0.45 mm
 1994 in the detector before decaying

1995 Additionally, the following cuts are required:

- 1996 • The transverse distance between the primary and secondary vertices, L_T , is between 100
 1997 μm and 2.5 cm
 1998 • The ratio of L_T and the uncertainty on its measurement, $L_T/\sigma_{L_T} < 3$
 1999 • The invariant mass formed by adding the four-vectors of all the tracks forming the sec-
 2000 ondary vertex < 6.5 GeV
 2001 • The invariant mass falls outside a window near 50 MeV, corresponding to the K_S^0 resonance

2002 Secondary vertices are decomposed into three categories. If a secondary vertex is found meeting
 2003 the above criteria, it is a "reco vertex". If no secondary vertex is found meeting all the above
 2004 criteria, the event can be classified as a "psuedo vertex" if more than two tracks have a signed
 2005 transverse impact parameter significance, relative to the primary vertex, greater than 2. "No
 2006 vertex" is found if neither of the prior two classification criteria can be met.

2007 For each of the vertex categories, a set of variables is used to create a single discriminating
 2008 variable, using a likelihood ratio technique. The following input variables are used:

- 2009 • The invariant mass of the charged particles associated with the secondary vertex
 2010 • The multiplicity of charged tracks associated with the primary vertex
 2011 • The distance between the primary and secondary vertex in the transverse plane, divided
 2012 by its error (only used in reco vertex category)
 2013 • The psuedorapidities of the charged particle tracks associated with the secondary vertices

- The track impact parameter significance of the highest p_T track with invariant mass larger than the charm quark threshold, 1.5 GeV.

The likelihood function is split to separate between the charm and light-flavour backgrounds and is defined as:

$$\mathcal{L}^{b,c,q} = f^{b,c,q}(\alpha) \times \prod_i f_{\alpha}^{b,c,q}(x_i) \quad (6.2)$$

where $\alpha = 1,2,3$, denotes the different vertex categories, x_i are the individual variables, q stands for the light flavour quarks, while b and c stand for the bottom and charm quarks respectively. $f^{b,c,q}(\alpha)$ is the probability for a quark flavour b, c , or q , to fall into category α . $f_{\alpha}^{b,c,q}(x_i)$ is the probability density function of the variable x_i in category α for quark flavour b, c , or q . The combined discriminant is defined as

$$d = f_{BG}(c) \times \frac{\mathcal{L}^b}{\mathcal{L}^c + \mathcal{L}^b} + f_{BG}(q) \times \frac{\mathcal{L}^b}{\mathcal{L}^q + \mathcal{L}^b} \quad (6.3)$$

where $f_{BG}(c)$, and $f_{BG}(q)$ are the a-priori probabilities for the content of charm and light flavour quarks in non-b jets.

A jet is considered b -tagged if the CSV discriminant is greater than 0.679, which is the medium working point defined by the BTAG Physics Object Group (POG) [86], defined in order to produce a light-flavour mistag rate at $\sim 1\%$, with the reconstruction efficiency for real b-jets at $\sim 70\%$.

Additionally, it is necessary to account for differences in the measured efficiency for b -tagging jets between data and simulation [87]. An event weight scale factor is used to correct the MC b -tagging efficiency ($SF_{tag} = \epsilon_{tag}^{data} / \epsilon_{tag}^{MC}$). The scale factor is measured for three different cuts, or working points, on the CSV discriminant value, and it is binned in terms of the p_T and η and flavour of the jet.

In addition to providing jet flavour identification for event classification, the discriminant value of the algorithm will be used to separate between $t\bar{t}H$ signal and $t\bar{t} + jets$ background. Therefore, a correction value for the efficiency difference between data and MC over the whole range of discriminator values is needed, not just for three working points. This procedure was developed in the context of the search for the standard model Higgs boson produced in association with a W or Z boson, with the Higgs decaying to bottom quarks [88].

For each of the three operating points and for each of the data/MC SFs, an equivalent cut on the CSV value is determined, CSV_{equiv} , such that

$$\epsilon_{CSV>CSV_{orig}}^{data} = SF_{CSV>CSV_{orig}} \cdot \epsilon_{CSV>CSV_{orig}}^{MC} = \epsilon_{CSV>CSV_{equiv}}^{MC} \quad (6.4)$$

2042 where the SFs are measured in data and the MC efficiency measurements are calculated for each
 2043 sample.

2044 In order to correct or "reshape" the CSV discriminator output values, a function is applied to
 2045 the MC to produce a corrected CSV value: $CSV_{\text{corr}} = f(CSV_{\text{orig}})$. Given that there are three b -
 2046 tag efficiency measurements, there are three pairs of $(CSV_{\text{orig}}, CSV_{\text{equiv}})$. The reshaping function
 2047 must satisfy $f(CSV_{\text{equiv}}) = CSV_{\text{orig}}$ for each of the operating points and for the upper and lower
 2048 values of the CSV discriminant to make sure those values do not change (e.g., $CSV = 0.0$ and
 2049 $CSV = 1.0$). The whole range of CSV discriminant values is found by linearly interpolating
 2050 between these five points (the three working points, and upper and lower limit of the discriminant
 2051 range).

2052 6.2.8 Lepton + Jets Selection

2053 The final Lepton+Jets (LJ) selection is finally carried out by requiring that events have exactly
 2054 one tight lepton (e or μ), and at least four jets. Events with any additional loose or tight leptons
 2055 are vetoed so this analysis can later be combined with a diLepton final state, without double
 2056 counting events. Additionally, each event must have at least three jets with $p_T > 40 \text{ GeV}/c$.

2057 Events are further categorized by the reconstructed jet, and b -tagged jet multiplicities as
 2058 follows:

2059 • ≥ 6 jets, $==2$ b -tags: At least 6 jets, 2 of which are b -tagged

2060 • $==4$ jets, $==3$ b -tags: Exactly 4 jets, 3 of which are b -tagged

2061 • $==5$ jets, $==3$ b -tags: Exactly 5 jets, 3 of which are b -tagged

2062 • ≥ 6 jets, $==3$ b -tags: At least 6 jets, 3 of which are b -tagged

2063 • $==4$ jets, $==4$ b -tags: Exactly 4 jets, 4 of which are b -tagged

2064 • $==5$ jets, $==4$ b -tags: Exactly 5 jets, 4 of which are b -tagged

2065 • ≥ 6 jets, ≥ 4 b -tags: At least 6 jets, with at least 4 of which are b -tagged

2066 Events with either 4 or 5 jets, where 2 of those jets are b -tagged, make up two categories,
 2067 which are used only as a control region to validate comparisons between collected data and
 2068 simulations. The number of $t\bar{t}H$ events increases with the number of jets and tags because the
 2069 largest branching fraction is H to $b\bar{b}$. Data to monte carlo comparisons of the jet and b -tag
 2070 multiplicities are shown in figure 6.6. The event yields for the μ +jets and e +jets channels are
 2071 shown in tables 6.9 and 6.10 respectively.

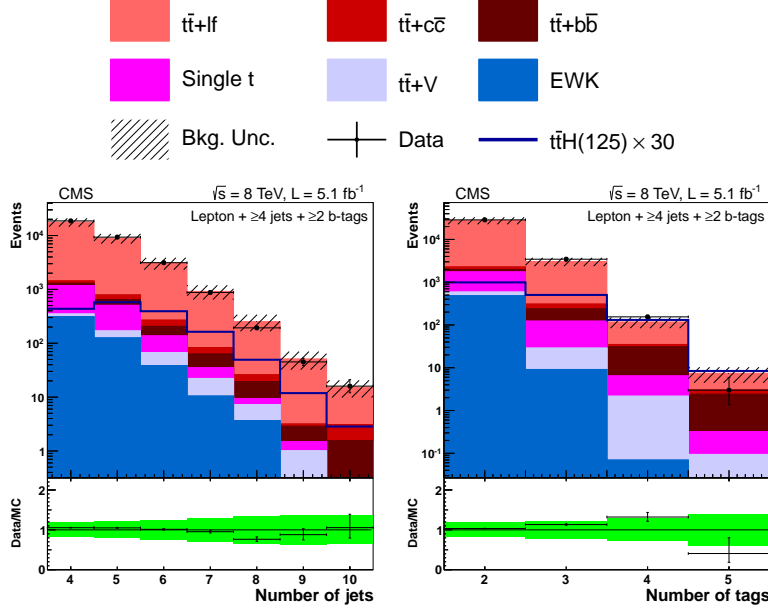


Figure 6.6: Number of jets (left) and number of b-tagged jets (right) in data and simulation for events with ≥ 4 jets + ≥ 2 b-tags in the lepton+jets channel at 8 TeV. The background is normalized to the SM expectation; the uncertainty band (shown as a hatched band in the stack plot and a green band in the ratio plot) includes statistical and systematic uncertainties that affect both the rate and shape of the background distributions. The $t\bar{t}H$ signal ($m_H = 125 \text{ GeV}/c^2$) is normalized to $30 \times$ SM expectation.

2072 6.3 Multivariate Analysis

2073 As discussed in the chapter introduction, no single variable offers sufficient discriminating power,
 2074 to separate the $t\bar{t}H$ signal from the $t\bar{t} + \text{jets}$ background. Instead, the combined power of several
 2075 input variables is utilized through a multivariate analysis (MVA) technique. For this analysis, the
 2076 MVA algorithm chosen from the sub-class of artificial neural network (ANN) algorithms, known
 2077 as multi-layer perceptrons (MLPs). The specific algorithm is the Clermont-Ferrand Multi-Layer
 2078 Perceptron Artificial Neural Network (CFMlpANN). It was first developed at the Universite
 2079 Blaise Pascal in Clermont-Ferrand, for the ALEPH experiment at the LEP collider to search for
 2080 the Standard Model Higgs and has also been utilized by the BABAR experiment to search for
 2081 rare B meson decays [89]. It has been implemented in the ROOT TMVA framework, available
 2082 in all CMSSW releases. A CFMlpANN is trained for each jet-tag category listed in section 6.2.8.
 2083 A total of 10 input variables is used in each category, with the exception of the ≥ 6 jets, ≥ 4
 2084 b -tags category, where the full reconstruction of the $t\bar{t}H$ system is possible, features an additional
 2085 variable that is the invariant mass of the di-jet system of b -jets selected by a χ^2 minimization
 2086 algorithm.

2087 **6.3.1 Artificial Neural Network Overview**

2088 An artificial neural network (ANN), most generally speaking, is any collection of interconnected,
 2089 simulated "neurons" which produce a certain response to a set of input variables [89]. A sim-
 2090 ulated neuron, is some independent function, which takes several input variables, performs a
 2091 mathematical operation, and passes the result to one or more other neurons. In the most gen-
 2092 eral case, a set of n input variables, connected to a single output, will produce on the order
 2093 n^2 connections. For case of using the network to discriminate between signal from background
 2094 (a yes or no answer on whether an event is signal-like), the ANN is mapping an n -dimensional
 2095 space onto a one-dimensional space.

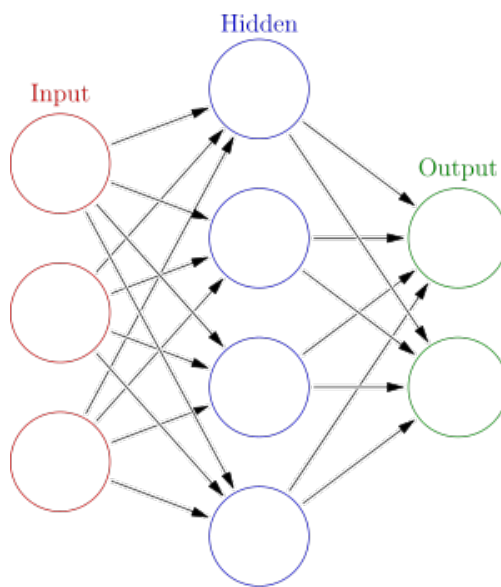


Figure 6.7: A simple example of a MLP type ANN, with one layer of input neurons that make connections to a hidden layer, which is connected to the output layer

2096 The multi-layer perceptron (MLP) is a specific type of arrangement of neurons. Any number
 2097 of neurons are arranged into a single layer, and connections to other neurons are only made if
 2098 they are arranged in a successive layer [89]. This is known as feed-forward network, and a simple
 2099 example with one input layer, one hidden layer, and one output layer is shown in figure 6.7.
 2100 This limits the complexity of the connections formed by the neurons and allows for simplified
 2101 calculations.

2102 This analysis uses an architecture that consists of two hidden layers, with N and $N - 1$
 2103 variables respectively, where N is the number of input variables for the given jet/tag category.
 2104 An example diagram is shown in figure 6.8. The output of the CFMlpANN algorithm is one-
 2105 dimensional discriminant with range from 0 to 1, for background-like and signal-like events.
 2106 Each neuron response is based on an activation function $A(\alpha)$, and a synapse response, α .

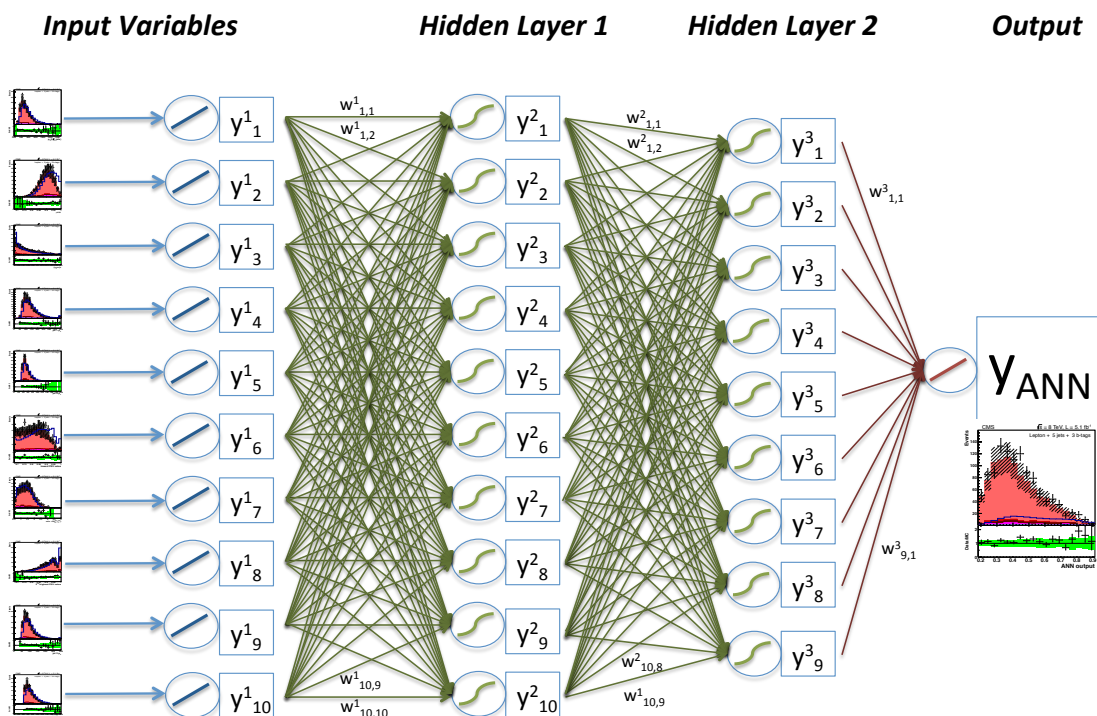


Figure 6.8: The CFMlpANN architecture used in this analysis features two hidden layers, and 10 input variables for each jet/tag category (11 variables for the ≥ 6 jets, ≥ 4 b -tags category)

²¹⁰⁷ In this case, a sigmoid function is used as the activation function:

$$A(\alpha) = \frac{1}{1 + e^{-x}} \quad (6.5)$$

²¹⁰⁸ and the synapse response is a simple weighted sum:

$$\alpha = w_{0j}^{(l)} + \sum_{i=1}^n y_i^{(l)} w_{ij}^{(l)} \quad (6.6)$$

²¹⁰⁹ The entire CFMlpANN response is then

$$y_{ANN} = \sum_{k=1}^{n-1} y_k^{(3)} w_{k1}^{(3)} = \sum_{k=1}^{n-1} A \left(\sum_{j=1}^n y_j^{(2)} w_{jk}^{(2)} \right) w_{k1}^{(3)} = \sum_{k=1}^{n-1} A \left(\sum_{j=1}^n A \left(\sum_{i=1}^n x_i w_{ij}^{(1)} \right) w_{jk}^{(2)} \right) w_{k1}^{(3)} \quad (6.7)$$

²¹¹⁰ where n is the number of input variables for that jet tag category and A is the sigmoid function
²¹¹¹ described in equation 6.5.

²¹¹² The CFMlpANN is trained with $t\bar{t}H$ signal events and inclusive $t\bar{t} + jets$ background events
²¹¹³ in order to optimize the weights $w_{ij}^{(l)}$ that are used for each neuron connection such that the
²¹¹⁴ output, y_{ANN} is closest to 1 for signal-like events, and closest to 0 for background-like events.
²¹¹⁵ This process involves sending the CFMlpANN an event from a known source (either signal or
²¹¹⁶ background), calculating the response, y_{ANN} , and computing an error function associated with
²¹¹⁷ the answer, given by:

$$E(x_1, \dots, x_N | w) = \sum_{a=1}^N E_a(x_a | w) = \sum_{a=1}^N \frac{1}{2} (y_{ANN} - \hat{y}_a) \quad (6.8)$$

²¹¹⁸ where \hat{y}_a is the correct response (either 0 or 1), knowing that the event was either signal or
²¹¹⁹ background, and N is the number of events used to train the CFMlpANN. The optimized set
²¹²⁰ of weights is the set that minimizes this error function. This is done by the method of steepest
²¹²¹ descent, where a random set of weights is moved a small distance in the direction that gives the
²¹²² largest change in minimizing the error function.

$$w^{t+1} = w^t - \eta \nabla_w E \quad (6.9)$$

²¹²³ where ∇_w is the direction that reduces the error function the most, and η is a parameter that
²¹²⁴ determines how large of an adjustment is made. After the weights are adjusted, the CFMlpANN
²¹²⁵ makes another iteration over the training events, re-calculating the CFMlpANN output for each
²¹²⁶ event and the error function. For this analysis a total of 2000 iterations were used to train the
²¹²⁷ CFMlpANN.

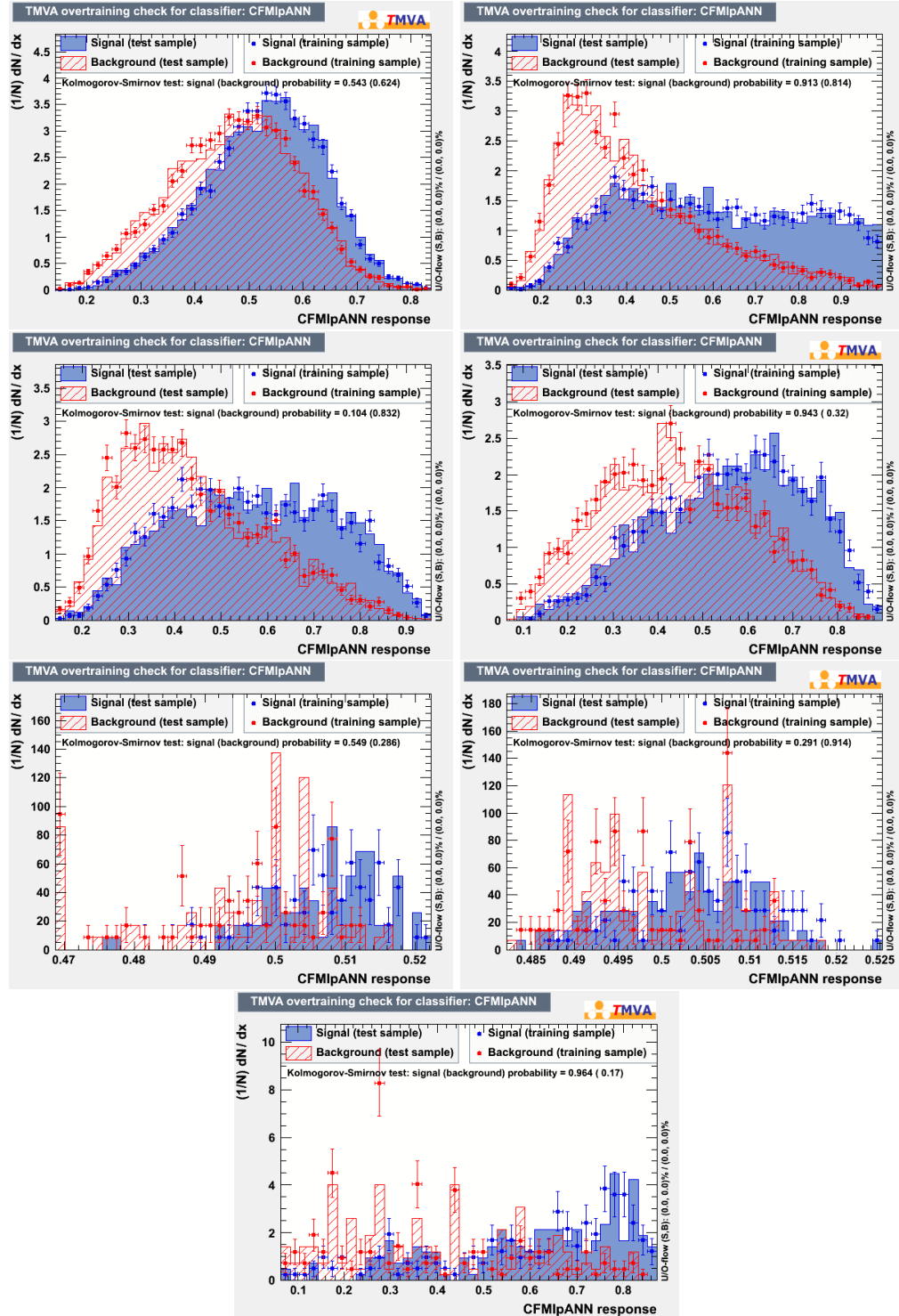


Figure 6.9: Comparisons of the testing and training samples used to optimize the CFMlpANN weights for each jet/tag category

2128 It is possible to bias the CFMlpANN response, by overtraining it. This is the case where the
 2129 weights are over-adjusted to correctly classify events in the training sample. If overtrained, small
 2130 fluctuations in the input variable distributions of authentic signal events can lead to incorrect
 2131 classification of the signal events when the CFMlpANN attempts to classify the data. To avoid
 2132 this, half of the simulated events for $t\bar{t}H$ signal and $t\bar{t} + jets$ background are used during training.
 2133 After training, the other half are used to test the response of the algorithm. If properly trained,
 2134 the testing and training samples should have identical CFMlpANN responses. The figure of
 2135 merit used to assess this is the Kolmogorov-Smirnov test, which computes the probability that
 2136 two distributions have been sampled from the same underlying probability distribution. The
 2137 results of the training and testing for each of the jet/tag categories is shown in figure 6.9. No
 2138 signs of overtraining are observed.

2139 6.3.2 MVA Input Variables, Data to Monte Carlo Comparisons

2140 As mentioned in the previous section, each jet/tag category has been trained with its own
 2141 CFMlpANN. Each category uses ten input variables, except for the $\geq 6j$, $\geq 4t$ category, which
 2142 uses eleven. A total of 24 unique input variables are used in the 7 different jet/tag categories
 2143 and are listed in table 6.11. The most discriminating variable for each category is denoted by
 2144 a \star . The inputs are selected from a ranked list based on initial separation between signal
 2145 and background. The separation of the individual variables is evaluated using a separation
 2146 benchmark $\langle S^2 \rangle$ [89] defined as follows:

$$\langle S^2 \rangle = \frac{1}{2} \int \frac{(\hat{y}_S(y) - \hat{y}_B(y))^2}{\hat{y}_S(y) + \hat{y}_B(y)} dy, \quad (6.10)$$

2147 where y is the input variable, and \hat{y}_S and \hat{y}_B are the signal and background probability density
 2148 functions for that input variable in the signal and background samples, respectively. The maxi-
 2149 mum number of input variables used in each category is limited by the statistics in the simulated
 2150 samples used for the CFMlpANN training. The number of variables per category is determined
 2151 by reducing the number of variables until the minimum number of variables needed to maintain
 2152 roughly the same ANN performance is reached. In this case, 10 input variables yields stable and
 2153 approximately identical performance to using 15, while using 5 variables degraded discrimination
 2154 power significantly.

2155 The input variables used in the CFMlpANN can be broken down into several classes. The
 2156 first is related to jet, and multi-object kinematics. The b -jets produced by the Higgs boson tend
 2157 to have a harder p_T spectrum compared to b -jets produced from gluon radiation. Additionally,
 2158 the recoil of the Higgs off of the top-system produces small differences in the p_T and invariant

2159 mass of the reconstructed $t\bar{t} + jet$ system.

2160 • Jet 1 p_T - the highest value of transverse jet momentum in the event

2161 • Jet 2 p_T - the second highest value of transverse jet momentum in the event

2162 • Jet 3 p_T - the third highest value of transverse jet momentum in the event

2163 • Jet 4 p_T - the fourth highest value of transverse jet momentum in the event

2164 • $p_T(\ell, E_T^{\text{miss}}, \text{jets})$ - the transverse momentum of the four-vector formed by summing the four-vectors of the lepton, MET, and all selected jets in the event

2166 • $M(\ell, E_T^{\text{miss}}, \text{jets})$ - the invariant mass of the four-vector formed by summing the four-vectors of the lepton, MET, and all selected jets in the event

2168 • Average $M((j_m^{\text{untag}}, j_n^{\text{untag}}))$ - the average di-Jet mass formed by all combinations of jets that have not been b -tagged in the event

2170 • $M((j_m^{\text{tag}}, j_n^{\text{tag}})_{\text{closest}})$ - the invariant di-Jet mass of the two b -tagged jets that are closest to one another in the detector

2172 • $M((j_m^{\text{tag}}, j_n^{\text{tag}})_{\text{best}})$ - the invariant mass constructed from the two tagged jets least likely to be a part of the $t\bar{t}$ system as determined by a minimum χ^2 search among all the jet, lepton, and E_T^{miss} combinations in the event, using the W boson and top masses as kinematic constraints.

2176 The next class of input variables describe the angular relationship between reconstructed objects in the event. These are event shape variables. Production of a relatively massive object, in addition to top quarks, such as the Higgs, tends to make $t\bar{t}H$ events more spherically distributed in the detected, while the background events are more collimated. Variables in this class include angular correlations, like the opening angle between the tagged jets

2181 • Average $\Delta R(j_m^{\text{tag}}, j_n^{\text{tag}})$ - the average ΔR spatial separation between all combinations of b -tagged jets in the event

2183 • Minimum $\Delta R(j_m^{\text{tag}}, j_n^{\text{tag}})$ - the smallest value of ΔR measured between a pair of b -tagged jets

2185 • $\Delta R(\ell, j_{\text{closest}})$ - the ΔR spatial separation of the lepton and the closest reconstructed jet

2186 • Sphericity - Event shape variable equal to $\frac{3}{2}(\lambda_2 + \lambda_3)$, where λ_2 and λ_3 are the second and third eigenvalues of the sphericity tensor as described in [90]

2188 • Aplanarity - Event shape variable equal to $\frac{3}{2}(\lambda_3)$, where λ_3 is the third eigenvalue of the
2189 sphericity tensor as described in

2190 • H_0 - the zeroth Fox-Wolfram moment [91]

2191 • H_1 - the first Fox-Wolfram moment

2192 • H_2 - the second Fox-Wolfram moment

2193 • H_3 - the third Fox-Wolfram moment

2194 where $\Delta R = \sqrt{\Delta\eta^2 + \Delta\phi^2}$. The sphericity tensor is given by the equation:

$$S^{a,b} = \frac{\sum_i p_i^a p_i^b}{\sum_i |\hat{p}_i|^2} \quad (6.11)$$

2195 where $a, b = x, y, z$ coordinates. This tensor is diagonalized, and solved for its eigenvalues,
2196 which are used to compute the sphericity and aplanarity variables. The Fox-Wolfram moments
2197 are defined are momentum weighted spherical harmonics, defined as:

$$H_\ell = \sum_{i,j=1}^{N_{Jets}} \frac{|\hat{p}_i||\hat{p}_j|}{|\hat{p}|_{tot}^2} P_\ell(\cos \Omega_{ij}) \quad (6.12)$$

2198 where $P_\ell(\cos \Omega_{ij})$ is the ℓ^{th} spherical harmonic, with polar angle calculated between jets i and j.

2199 The final class of variables is based on the discriminant output from the b-tagging algorithm.

2200 For many of the categories, the average b -tag discriminant of all of the jets in the event tends to
2201 be the most powerful single variable. This is due to the high multiplicity of authentic b -jets in
2202 a $t\bar{t}H$ event.

2203 • μ^{CSV} - the average value of the output of the CSV algorithm for all selected jets in the
2204 event.

2205 • $(\sigma_n^{\text{CSV}})^2$ - the variance of the average value of the output of the CSV algorithm for all
2206 selected jets in the event.

2207 • Highest CSV value - the highest value of the CSV discriminant for any selected jet in the
2208 event

2209 • 2^{nd} -highest CSV value - the second highest value of the CSV discriminant for any selected
2210 jet in the event

2211 • Lowest CSV value - the lowest value of the CSV discriminant for any selected jet in the
2212 event

2213 The modeling of the input variables is compared against data for each of the jet/tag diagrams
2214 in the the following figures:

- 2215 • ≥ 6 jets, ==2 b -tags: Figure 6.10, and Figure 6.11
- 2216 • ==4 jets, ==3 b -tags: Figure 6.12, and Figure 6.13
- 2217 • ==5 jets, ==3 b -tags: Figure 6.14, and Figure 6.15
- 2218 • ≥ 6 jets, ==3 b -tags: Figure 6.16, and Figure 6.17
- 2219 • ==4 jets, ==4 b -tags: Figure 6.18, and Figure 6.19
- 2220 • ==5 jets, ==4 b -tags: Figure 6.20, and Figure 6.21
- 2221 • ≥ 6 jets, ≥ 4 b -tags: Figure 6.22, and Figure 6.23

2222 Below each histogram is a ratio of the yields for data over the simulated sample prediction. The
2223 green band is the total uncertainty estimated for the simulation, and the error bars on the points
2224 are determined by the statistical error on the data collected.

Table 6.9: Expected event yields in 5 fb^{-1} for signal and backgrounds in the $\mu+\text{jets}$ channel.

	≥ 6 jets 2 tags	4 jets 3 tags	5 jets 3 tags	≥ 6 jets 3 tags	≥ 6 jets 4 tags	4 jets 4 tags	5 jets ≥ 4 tags	≥ 6 jets ≥ 4 tags
$t\bar{t}H(125)$	6.1 ± 1.1	2.1 ± 1.9	3.2 ± 2.7	3.6 ± 3.3	0.3 ± 0.3	0.8 ± 0.9	1.3 ± 1.4	
$t\bar{t}+\text{lf}$	1750 ± 480	680 ± 150	460 ± 110	270 ± 84	9.5 ± 3.2	13.0 ± 4.2	20.6 ± 7.8	
$t\bar{t}+b\bar{b}$	34 ± 19	21 ± 12	24 ± 14	17.3 ± 10.0	1.5 ± 1.1	5.1 ± 3.2	8.6 ± 5.6	
$t\bar{t}+c\bar{c}$	29.5 ± 8.7	10.0 ± 2.9	13.2 ± 3.9	11.1 ± 3.5	0.2 ± 0.2	0.2 ± 0.1	1.1 ± 0.8	
$t\bar{t}V$	18.7 ± 3.9	2.3 ± 0.6	3.3 ± 0.8	4.1 ± 1.1	0.1 ± 0.0	0.4 ± 0.2	0.8 ± 0.2	
Single t	42.6 ± 9.8	25.8 ± 6.0	14.3 ± 3.8	4.3 ± 1.3	0.2 ± 0.3	1.6 ± 1.8	0.7 ± 0.5	
V+jets	39 ± 32	1.0 ± 0.9	0.0 ± 0.0	0.0 ± 0.0	0.0 ± 0.0	0.0 ± 0.0	0.0 ± 0.0	
Diboson	0.6 ± 0.2	0.9 ± 0.4	0.3 ± 0.1	0.1 ± 0.1	0.0 ± 0.0	0.0 ± 0.0	0.0 ± 0.0	
Total bkg	1910 ± 500	740 ± 160	520 ± 120	307 ± 90	11.4 ± 3.8	20.3 ± 6.1	32 ± 11	
Data	1780	861	585	362	15	32	37	

Table 6.10: Expected event yields in 5 fb^{-1} for signal and backgrounds in the $e+\text{jets}$ channel.

	≥ 6 jets 2 tags	4 jets 3 tags	5 jets 3 tags	≥ 6 jets 3 tags	≥ 6 jets 4 tags	4 jets 4 tags	5 jets ≥ 4 tags	≥ 6 jets ≥ 4 tags
$t\bar{t}H(125)$	5.6 ± 1.0	1.8 ± 1.2	2.9 ± 1.8	3.2 ± 2.1	0.3 ± 0.2	0.7 ± 0.6	1.2 ± 1.0	
$t\bar{t}+\text{lf}$	1720 ± 470	640 ± 140	410 ± 94	293 ± 85	8.6 ± 2.9	14.5 ± 5.2	20.7 ± 7.8	
$t\bar{t}+b\bar{b}$	27 ± 15	14.3 ± 7.9	19 ± 11	18 ± 10	1.0 ± 1.0	3.3 ± 2.6	6.7 ± 4.3	
$t\bar{t}+c\bar{c}$	32.8 ± 9.4	9.6 ± 2.9	11.8 ± 3.5	14.8 ± 4.8	0.4 ± 0.3	0.6 ± 0.6	2.6 ± 1.4	
$t\bar{t}V$	17.0 ± 3.6	2.1 ± 0.6	2.8 ± 0.7	4.5 ± 1.1	0.0 ± 0.0	0.3 ± 0.1	0.6 ± 0.2	
Single t	35.9 ± 8.9	30.5 ± 6.4	11.3 ± 3.4	6.0 ± 2.0	0.1 ± 0.3	1.4 ± 1.2	0.4 ± 0.4	
V+jets	14 ± 14	4.8 ± 5.8	0.8 ± 0.9	0.0 ± 0.0	0.0 ± 0.0	0.0 ± 0.0	0.0 ± 0.0	
Diboson	0.7 ± 0.3	1.0 ± 0.3	0.2 ± 0.1	0.1 ± 0.0	0.0 ± 0.0	0.0 ± 0.0	0.0 ± 0.0	
Total bkg	1850 ± 490	700 ± 150	460 ± 110	336 ± 93	10.1 ± 3.2	20.2 ± 6.6	31 ± 11	
Data	1723	785	531	324	13	24	37	

Table 6.11: The ANN inputs for the nine jet-tag categories in the 8 TeV $t\bar{t}H$ analysis in the lepton+jets and dilepton channels. The choice of inputs is optimized for each category. Definitions of the variables are given in the text. The best input variable for each jet-tag category is denoted by \star .

Jets Tags	Lepton+Jets						
	≥ 6 2	4 3	5 3	≥ 6 3	4 4	5 ≥ 4	≥ 6 ≥ 4
Jet 1 p_T		✓	✓		✓		
Jet 2 p_T		✓	✓				
Jet 3 p_T	✓	✓	✓			✓	
Jet 4 p_T	✓	✓	✓			✓	
$p_T(\ell, E_T^{\text{miss}}, \text{jets})$		★	✓		✓	✓	
$M(\ell, E_T^{\text{miss}}, \text{jets})$	✓	✓		✓	✓		✓
Average $M((j_m^{\text{untag}}, j_n^{\text{untag}}))$	✓			✓			
$M((j_m^{\text{tag}}, j_n^{\text{tag}})_{\text{closest}})$				✓			✓
$M((j_m^{\text{tag}}, j_n^{\text{tag}})_{\text{best}})$				✓			✓
Average $\Delta R(j_m^{\text{tag}}, j_n^{\text{tag}})$				✓	✓	✓	✓
Minimum $\Delta R(j_m^{\text{tag}}, j_n^{\text{tag}})$			✓				
$\Delta R(\ell, j_{\text{closest}})$						✓	✓
Sphericity	✓			✓			✓
Aplanarity	✓				✓		
H_0	✓						
H_1	✓				✓		
H_2				✓			✓
H_3	★			✓			✓
μ^{CSV}	✓	✓	★	★	★	★	★
$(\sigma_n^{\text{CSV}})^2$		✓	✓	✓	✓	✓	
Highest CSV value						✓	
2^{nd} -highest CSV value	✓	✓	✓	✓	✓	✓	✓
Lowest CSV value	✓	✓	✓	✓	✓	✓	✓

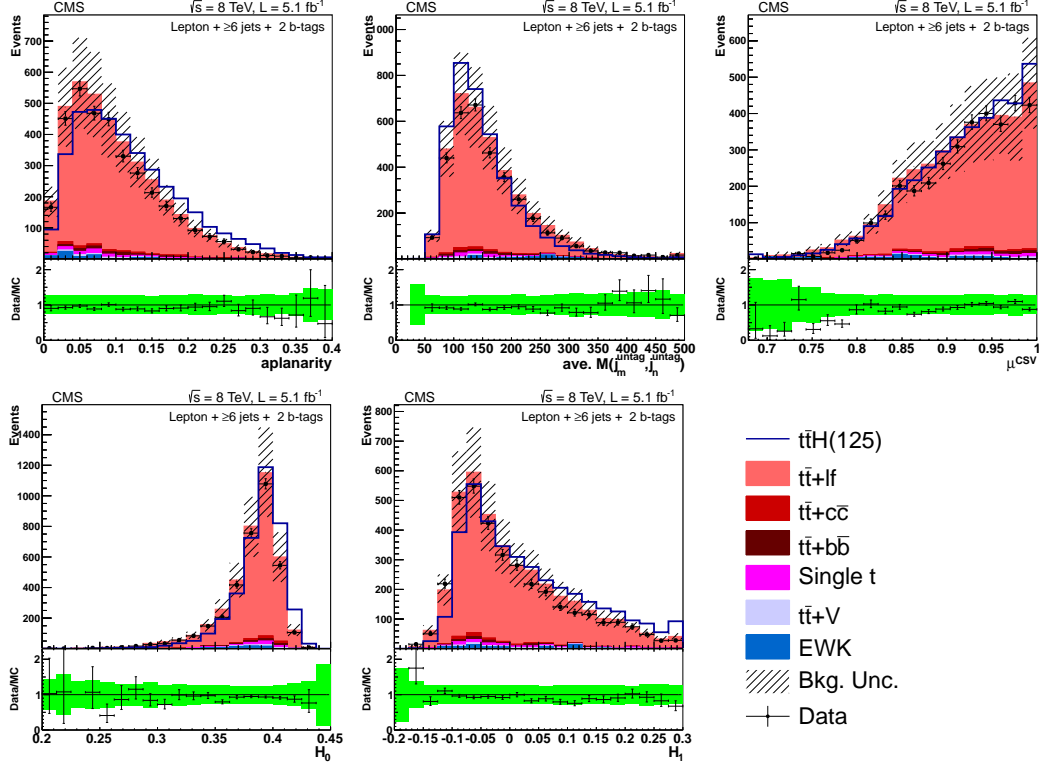


Figure 6.10: Lepton + jets data/MC comparison for the ≥ 6 jets + 2 tag category. The uncertainty band includes statistical and systematic uncertainties that affect both the rate and shape of the background distributions.

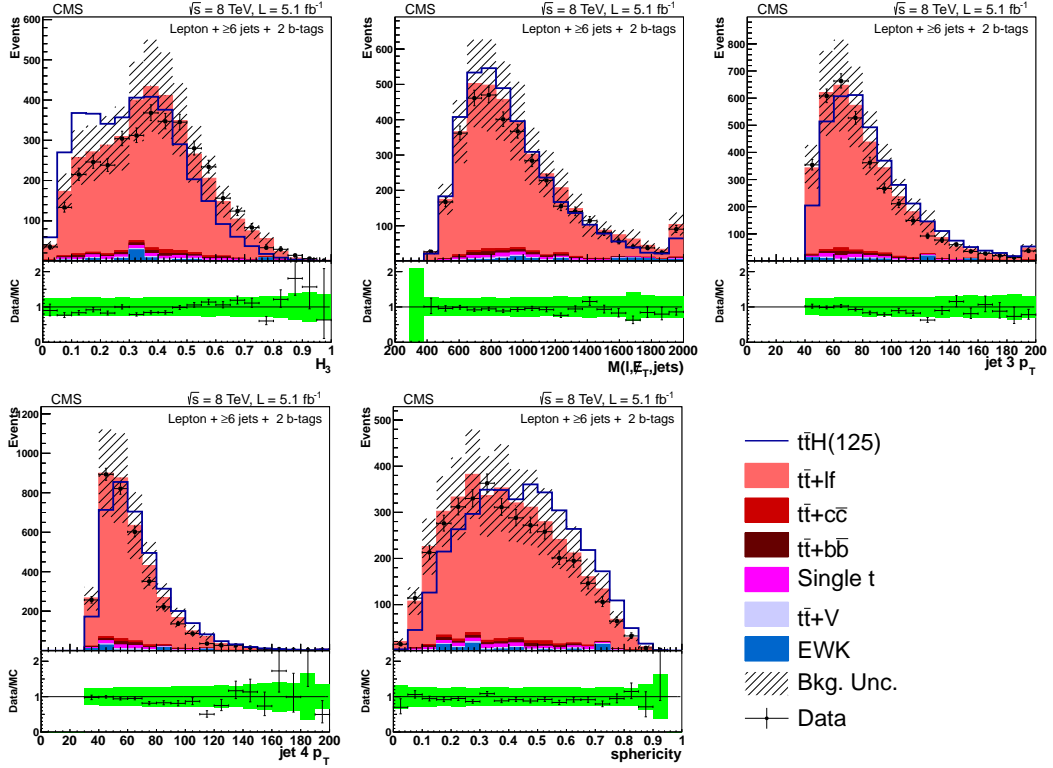


Figure 6.11: Lepton + jets data/MC comparison for the ≥ 6 jets + 2 tag category. The uncertainty band includes statistical and systematic uncertainties that affect both the rate and shape of the background distributions.

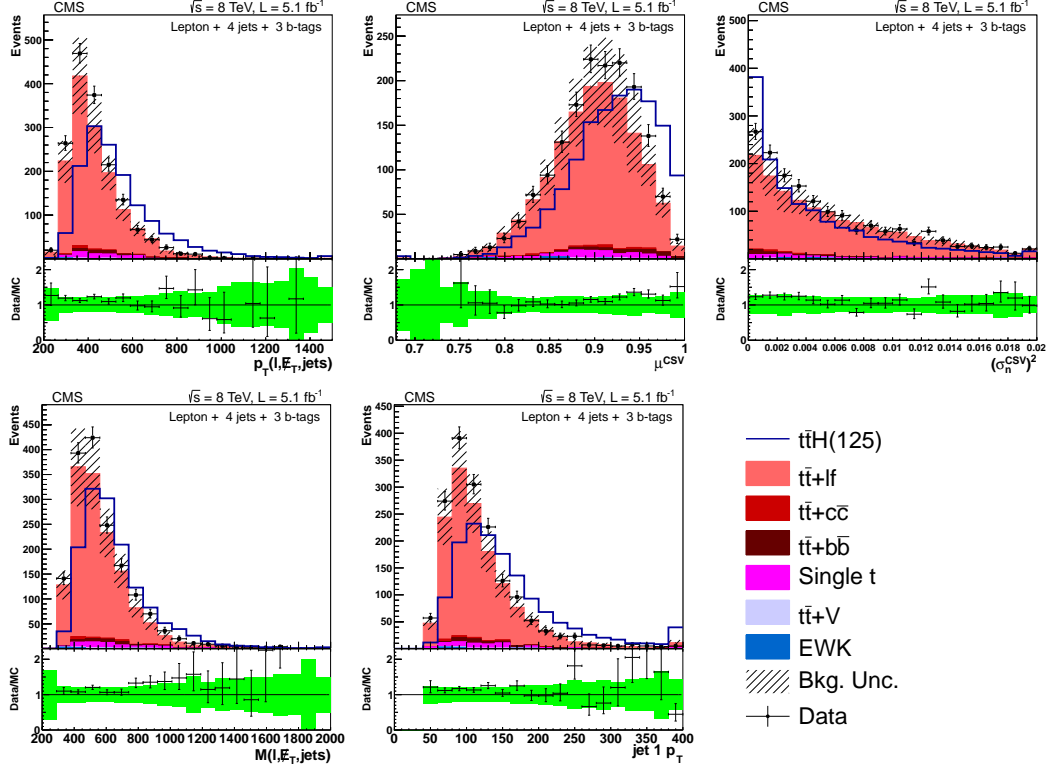


Figure 6.12: Lepton + jets data/MC comparison for the 4 jets + 3 tag category. The uncertainty band includes statistical and systematic uncertainties that affect both the rate and shape of the background distributions.

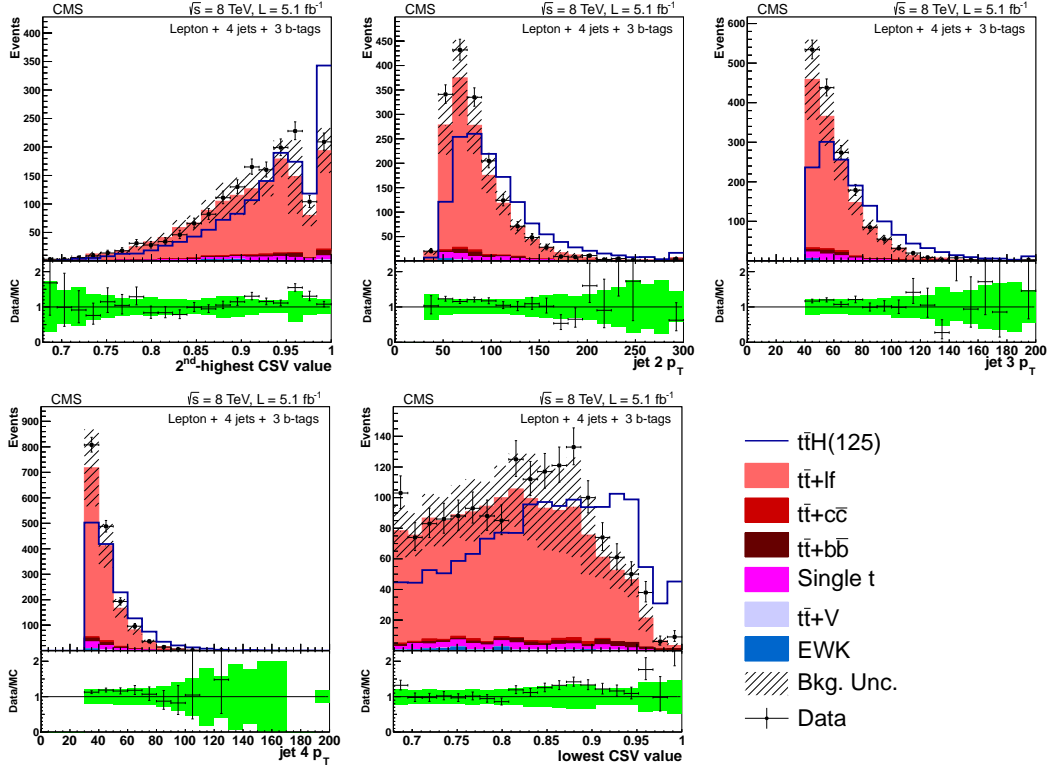


Figure 6.13: Lepton + jets data/MC comparison for the 4 jets + 3 tag category. The uncertainty band includes statistical and systematic uncertainties that affect both the rate and shape of the background distributions.

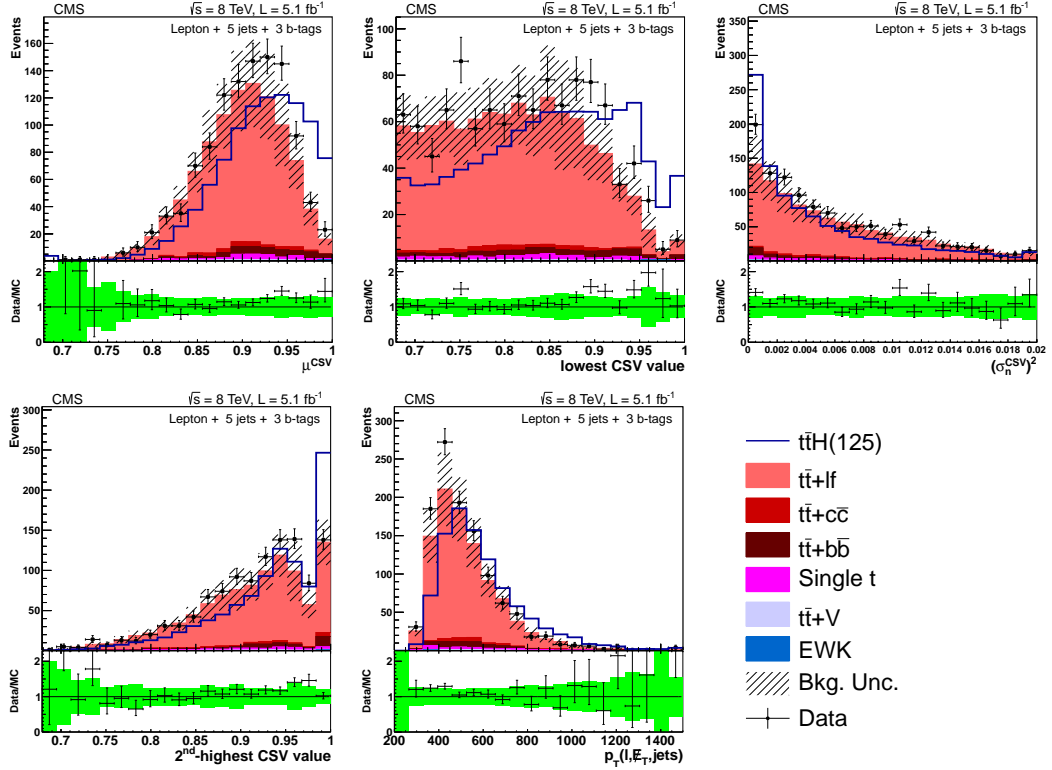


Figure 6.14: Distributions of the five ANN input variables with rankings 1 through 5, in terms of separation, for the 5 jets + 3 b-tags category of the lepton+jets channel at 8 TeV. Definitions of the variables are given in the text. The background is normalized to the SM expectation; the uncertainty band (shown as a hatched band in the stack plot and a green band in the ratio plot) includes statistical and systematic uncertainties that affect both the rate and shape of the background distributions. The $t\bar{t}H$ signal ($m_H = 125 \text{ GeV}/c^2$) is normalized to the total background yield, for easier comparison of the shapes.

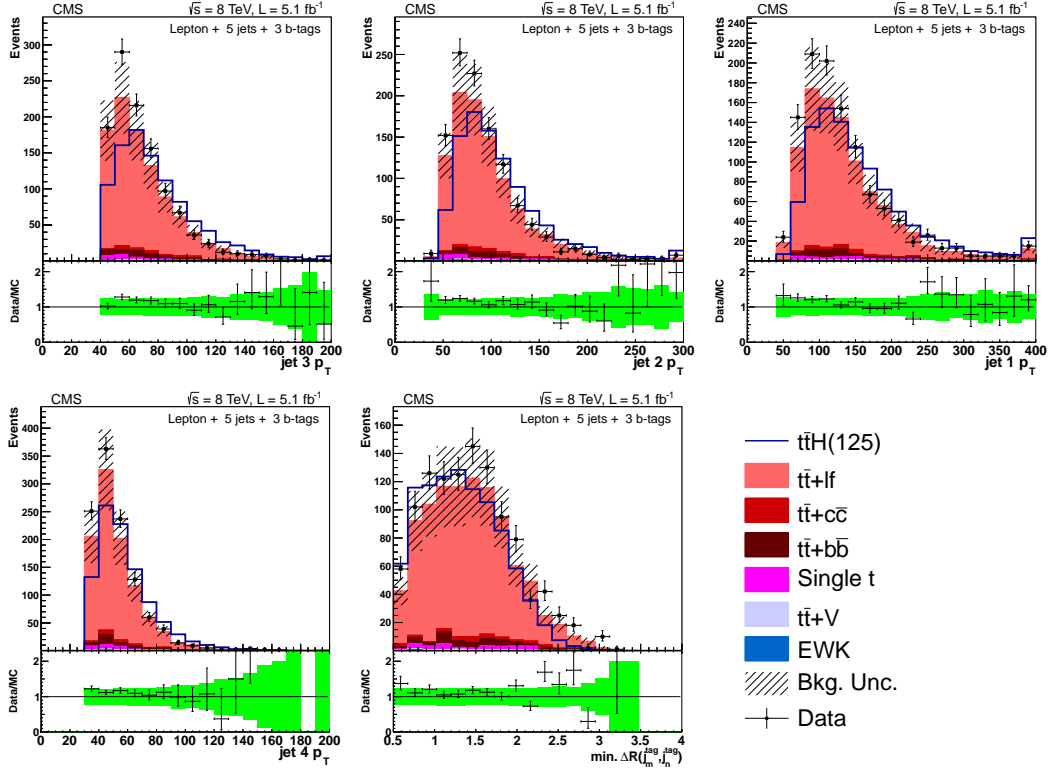


Figure 6.15: Distributions of the five ANN input variables with rankings 6 through 10, in terms of separation, for the 5 jets + 3 b-tags category of the lepton+jets channel at 8 TeV. Definitions of the variables are given in the text. The background is normalized to the SM expectation; the uncertainty band (shown as a hatched band in the stack plot and a green band in the ratio plot) includes statistical and systematic uncertainties that affect both the rate and shape of the background distributions. The $t\bar{t}H$ signal ($m_H = 125 \text{ GeV}/c^2$) is normalized to the total background yield, for easier comparison of the shapes.

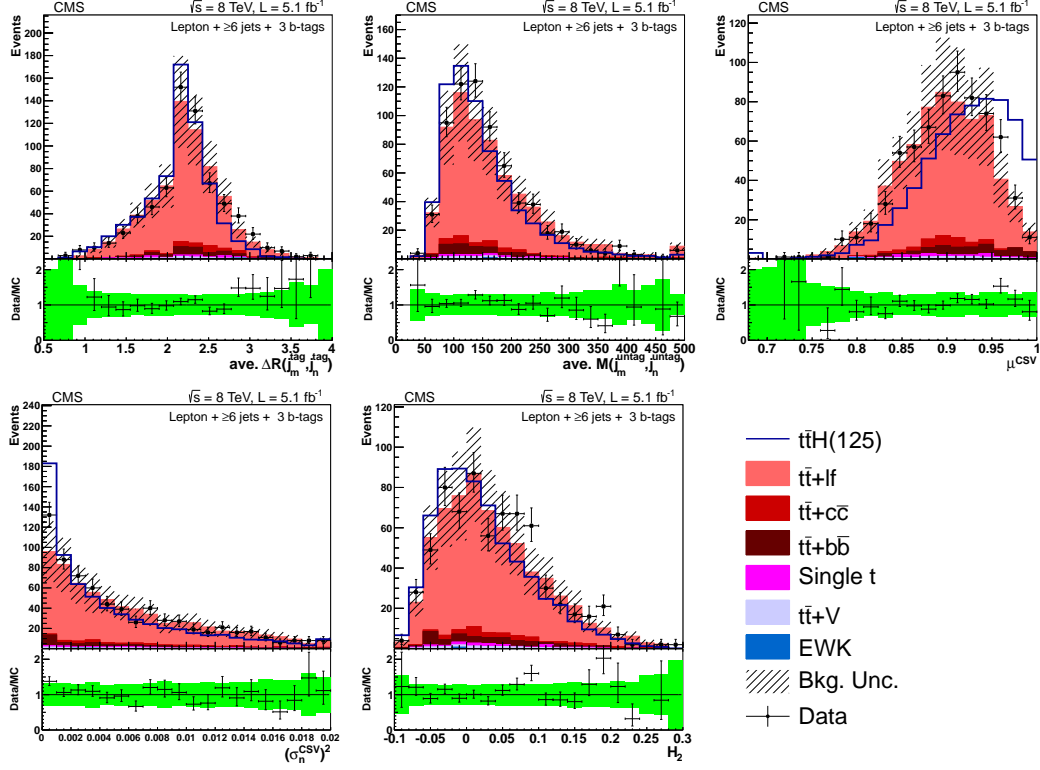


Figure 6.16: Lepton + jets data/MC comparison for the ≥ 6 jets + 3 tag category. The uncertainty band includes statistical and systematic uncertainties that affect both the rate and shape of the background distributions.

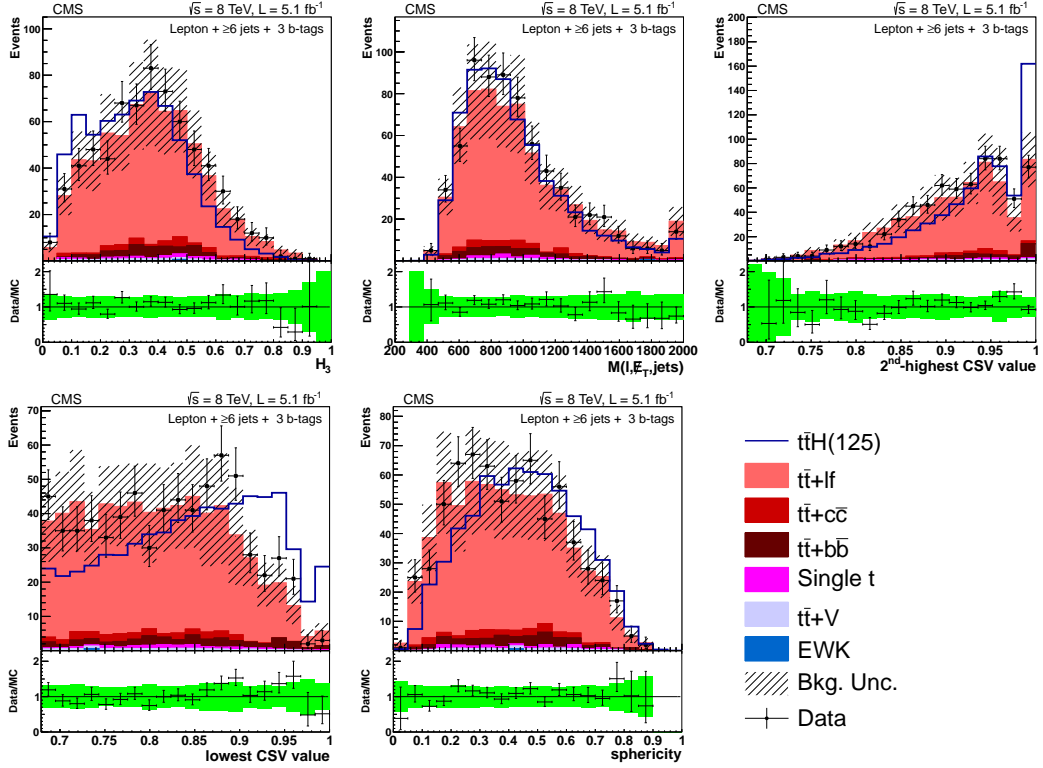


Figure 6.17: Lepton + jets data/MC comparison for the ≥ 6 jets + 3 tag category. The uncertainty band includes statistical and systematic uncertainties that affect both the rate and shape of the background distributions.

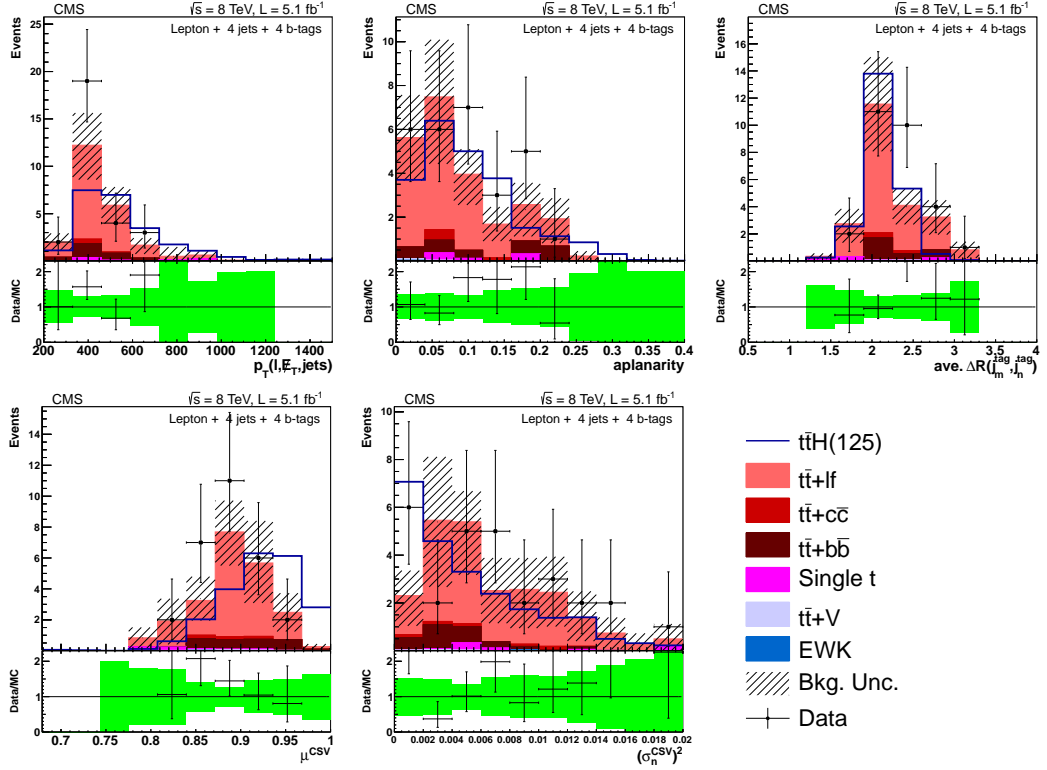


Figure 6.18: Lepton + jets data/MC comparison for the 4 jets + 4 tag category. The uncertainty band includes statistical and systematic uncertainties that affect both the rate and shape of the background distributions.

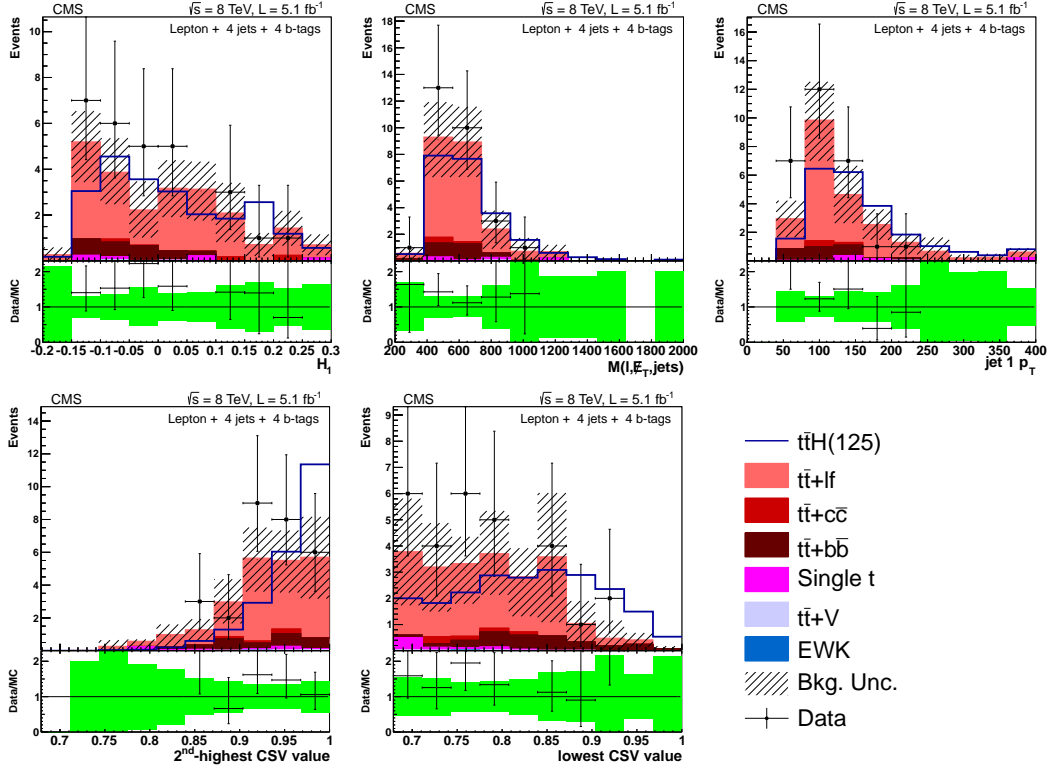


Figure 6.19: Lepton + jets data/MC comparison for the 4 jets + 4 tag category. The uncertainty band includes statistical and systematic uncertainties that affect both the rate and shape of the background distributions.

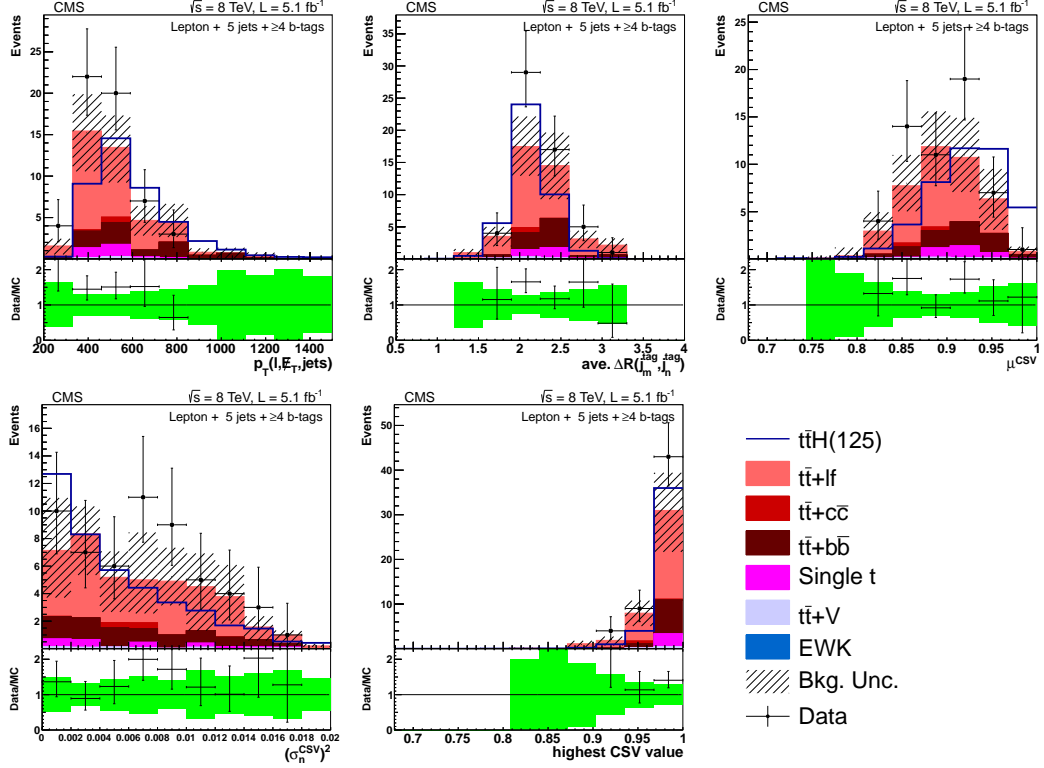


Figure 6.20: Lepton + jets data/MC comparison for the 5 jets + 4 tag category. The uncertainty band includes statistical and systematic uncertainties that affect both the rate and shape of the background distributions.

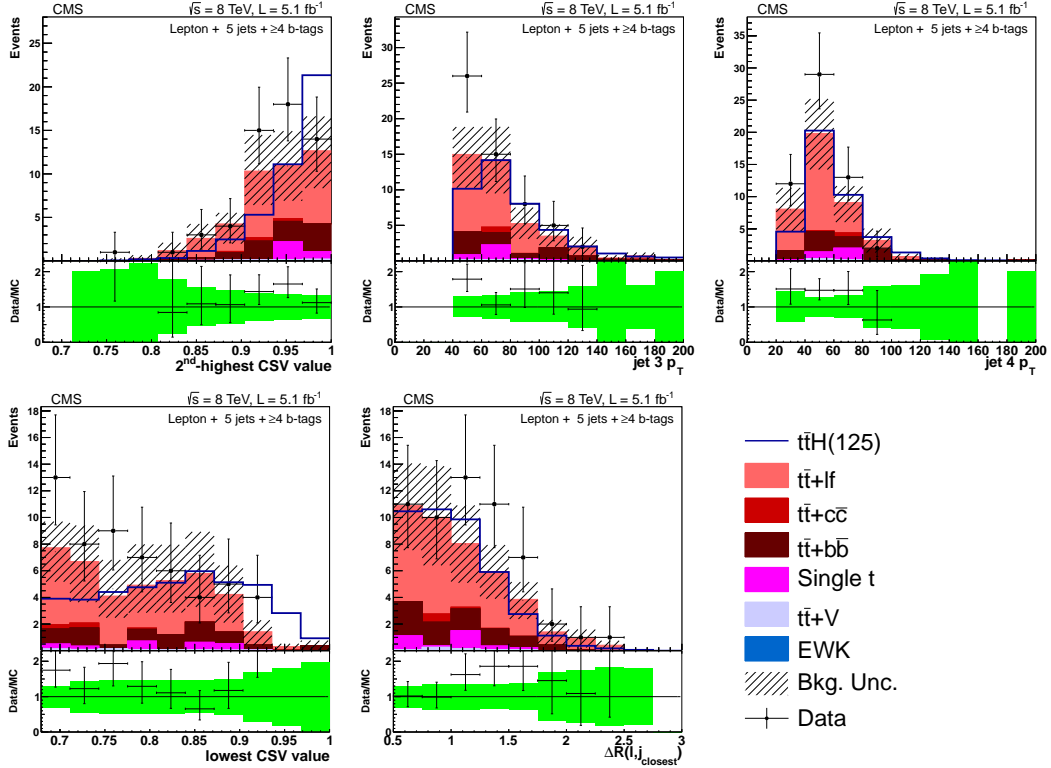


Figure 6.21: Lepton + jets data/MC comparison for the 5 jets + 4 tag category. The uncertainty band includes statistical and systematic uncertainties that affect both the rate and shape of the background distributions.

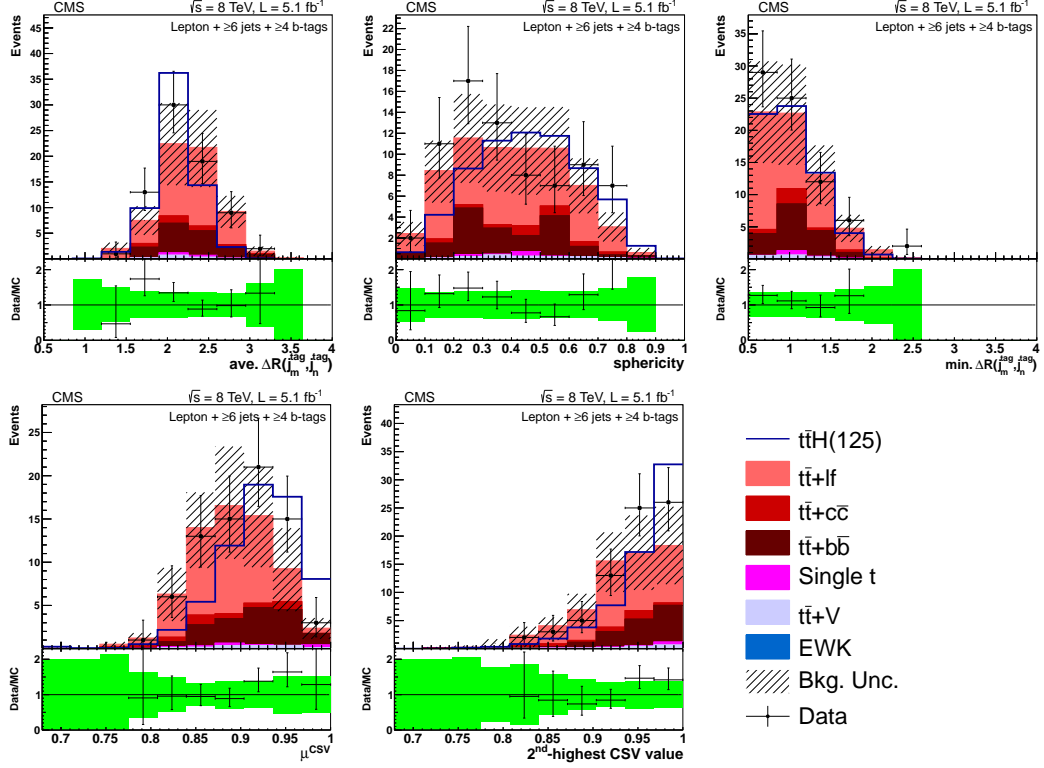


Figure 6.22: Lepton + jets data/MC comparison for the ≥ 6 jets + ≥ 4 tag category. The uncertainty band includes statistical and systematic uncertainties that affect both the rate and shape of the background distributions.

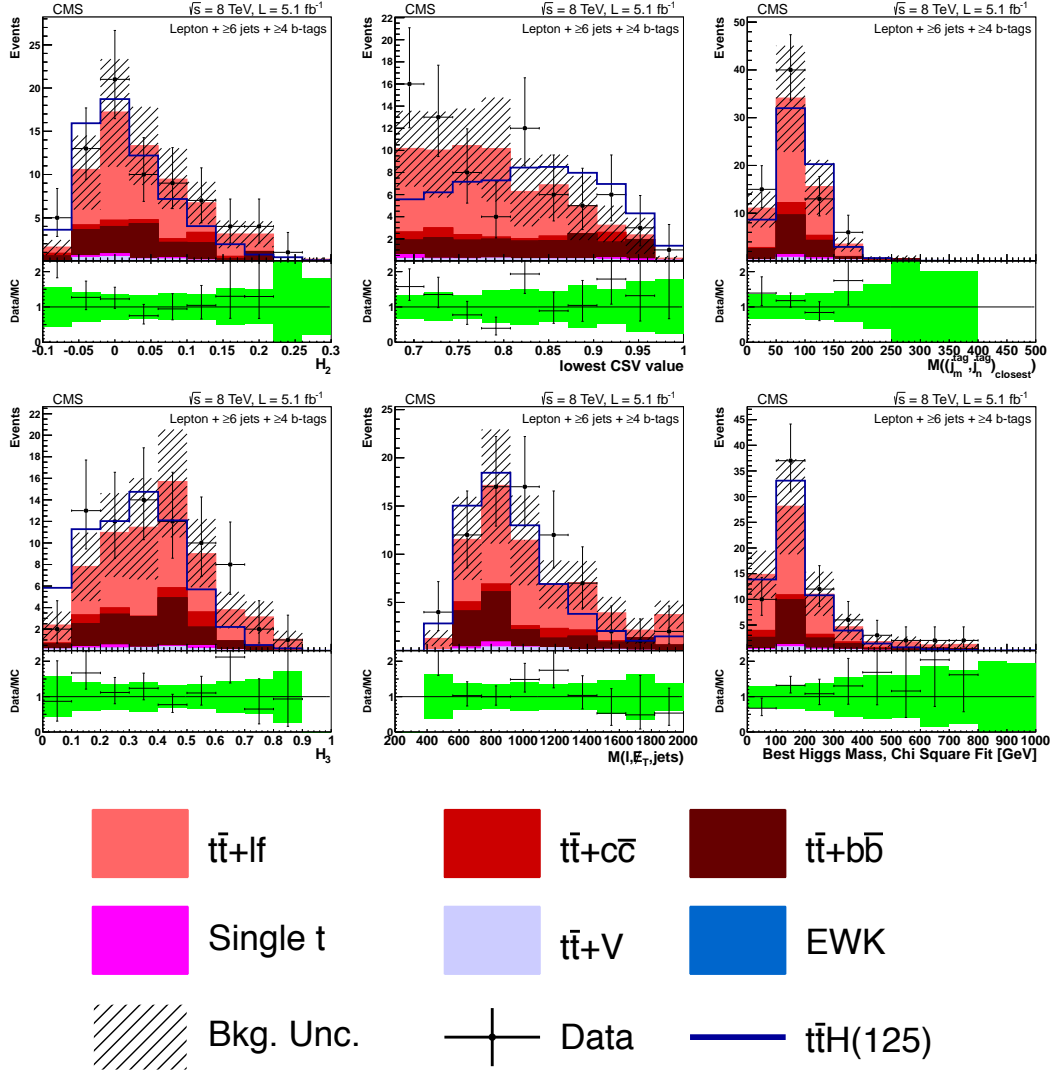


Figure 6.23: Lepton + jets data/MC comparison for the ≥ 6 jets + 4 tag category. The uncertainty band includes statistical and systematic uncertainties that affect both the rate and shape of the background distributions.

6.3.3 MVA Output, Data to Monte Carlo Comparisons

Data to Monte Carlo comparisons for the CFMlpANN output can be seen on figure 6.24. In the plots, the signal shape has been multiplied by a factor of 30 in order to make its shape visible, and in order to gauge a scale of the expected size of signal to background in each jet/tag category.²²²⁶

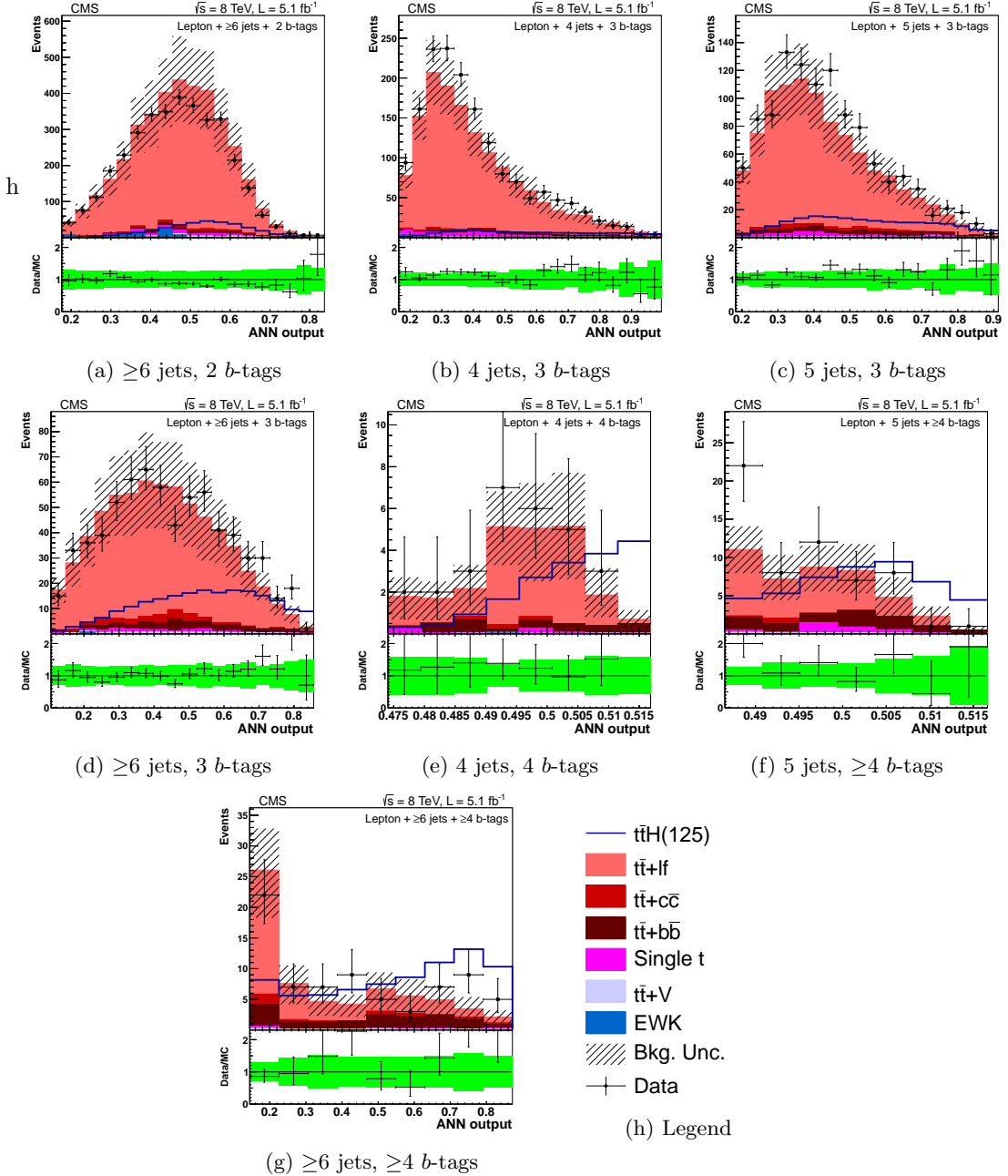


Figure 6.24: The distributions of the CFMlpANN output for lepton+jets events at 8 TeV in the various analysis categories. Background-like events have a low CFMlpANN output value. Signal-like events have a high CFMlpANN output value. The background is normalized to the SM expectation; the uncertainty (shown as a hatched band in the stack plot and a green band in the ratio plot) includes statistical and systematic uncertainties that affect both the rate and shape of the background distributions. The $t\bar{t}H$ signal ($m_H = 125 \text{ GeV}/c^2$) is normalized to $30 \times$ SM expectation.

2230 6.4 Systematic Uncertainties

2231 There are three types of systematic effects considered in this analysis: those that affect only the
 2232 rates of signal or background processes, those that affect only the shapes of the CFMlpANN
 2233 discriminants for signal or background processes, and those that affect both the rate and the
 2234 shape. In the last case, the rate and shape effects are treated simultaneously so that they are
 2235 considered completely correlated. Unless otherwise noted, all of the uncertainties listed here
 2236 apply equally to signal and background and are treated as 100% correlated between the two.
 2237 Below is a list of systematic effects considered for this analysis:

Table 6.12: Summary of the systematic uncertainties considered on the inputs to the limit calculation. Except where noted, each row in this table will be treated as a single, independent nuisance parameter.

Source	Rate Uncertainty	Shape	Remarks
Luminosity (8 TeV)	2.2%	No	All signal and backgrounds
Lepton ID/Trig	4%	No	All signal and backgrounds
Pileup	1%	No	All signal and backgrounds
Additional Pileup Corr.	–	Yes	All signal and backgrounds
Jet Energy Resolution	1.5%	No	All signal and backgrounds
Jet Energy Scale	0-60%	Yes	All signal and backgrounds
b-Tag SF (b/c)	0-33.6%	Yes	All signal and backgrounds
b-Tag SF (mistag)	0-23.5%	Yes	All signal and backgrounds
MC Statistics	–	Yes	All backgrounds
PDF (gg)	9%	No	For gg initiated processes ($t\bar{t}$, $t\bar{t}Z$, $t\bar{t}H$)
PDF ($q\bar{q}$)	4.2-7%	No	For $q\bar{q}$ initiated processes ($t\bar{t}W$, W , Z).
PDF (qg)	4.6%	No	For qg initiated processes (single top)
QCD Scale ($t\bar{t}H$)	15%	No	For NLO $t\bar{t}H$ prediction
QCD Scale ($t\bar{t}$)	2-12%	No	For NLO $t\bar{t}$ and single top predictions
QCD Scale (V)	1.2-1.3%	No	For NNLO W and Z prediction
QCD Scale (VV)	3.5%	No	For NLO diboson prediction
Madgraph Scale ($t\bar{t}$)	0-20%	Yes	$t\bar{t}+jets/b\bar{b}/c\bar{c}$ uncorrelated. Varies by jet bin.
Madgraph Scale (V)	20-60%	No	Varies by jet bin.
$t\bar{t} + bb$	50%	No	Only $t\bar{t} + bb$.

2238 **Jet Energy Scale (JES):** The Jet Energy Scale systematic is based on the uncertainty on the
 2239 L1, L2, L3, and L2L3 residual corrections to the reconstructed jet energy, as described
 2240 in section 6.2.6. To evaluate the effect on the CFMlpANN output, the jet energy scale is
 2241 shifted by one standard deviation up and down using the standard JetMET procedure [92].
 2242 For each variation, the jet energies are recalculated, allowing for new jets to pass the selection
 2243 where once they failed, or fail the selection where once they passed, resulting in a migration
 2244 of events across jet/tag categories. Finally, the CFMlpANN response is recalculated, and
 2245 the effect for signal and the $t\bar{t} + jets$ background is shown in figure 6.25.

Jet Energy Resolution (JER): The jet p_T resolution in MC differs from that observed in
 data by approximately 10% in a η dependent way, as described in table ??, as per the
 recommendations of the JetMET group [93]. The value of the jet p_T is adjusted according

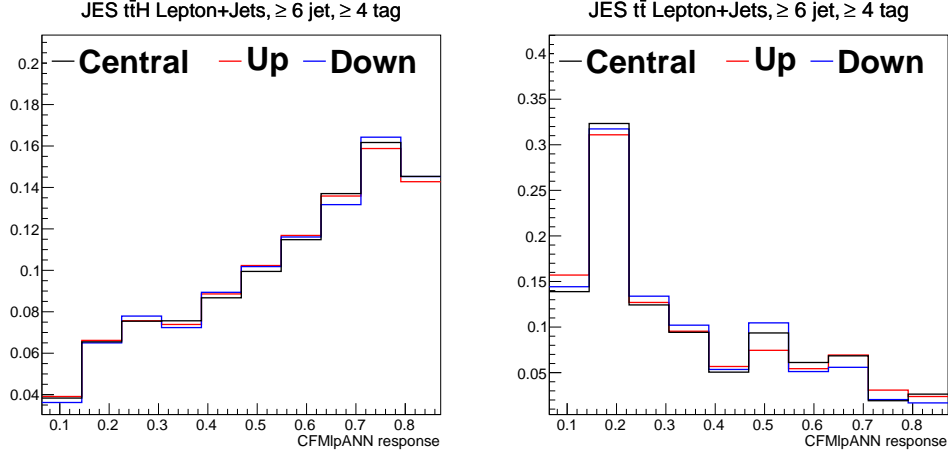


Figure 6.25: Comparison of the MVA discriminator for JES shift upwards (red) and downwards (blue) relative to the nominal (black) shape for the $t\bar{t}H(120)$ signal (left) and the main background sample $t\bar{t}$ + light flavor (right). The plots shown are from the ≥ 6 jet ≥ 4 tag category in the lepton+jets channel. All plots are normalized to unit area.

JES systematic yield change			
sys	shift	lepton+jets	
		$t\bar{t}H(120)$	$t\bar{t}$
JES	up	+8.6%	+12.1%
	down	-8.4%	-7.3%

Table 6.13: Relative yield change due to JES shift up/down for the ≥ 6 jets + ≥ 4 tags category in the lepton+jets channel.

to the formula:

$$p'_T = \max [0, p_T^{gen} + c(p_T^{reco} - p_T^{gen})] \quad (6.13)$$

2246 The correction factor c is taken from table ???. To assess the effect of the systematic
 2247 uncertainty on the JER, the value of c is shifted up and down by standard deviation, the
 2248 JER correction is applied to the jets using this new c value, and the event rates and ANN
 2249 shapes are recalculated. The effect of the JER on the shape variation is negligible, so it is
 2250 treated as a rate-only effect in limit setting.

2251 **b-tag Scale Factor:** The uncertainty in the b -tagging scale factor is assessed according to the
 2252 prescriptions developed by the BTag POG [94]. Each per-jet b -tag scale factor is shifted
 2253 up or down by its uncertainty, and the new CSV output value corresponding to that
 2254 uncertainty is recalculated. This new CSV value is used to determine both the number of
 2255 tags associated with that systematic and the new shape of variables that use the CSV
 2256 output, such as the average CSV value for b -tagged jets. This uncertainty effects both rate
 2257 and shape estimates. The effects of the b -tag scale factors on the ANN shape and event
 2258 yields are summarized in Fig. 6.26 and Table 6.14 respectively.

2259 **Lepton ID and Trigger Scale Factors:** As discussed previously, an uncertainty of 4% covers

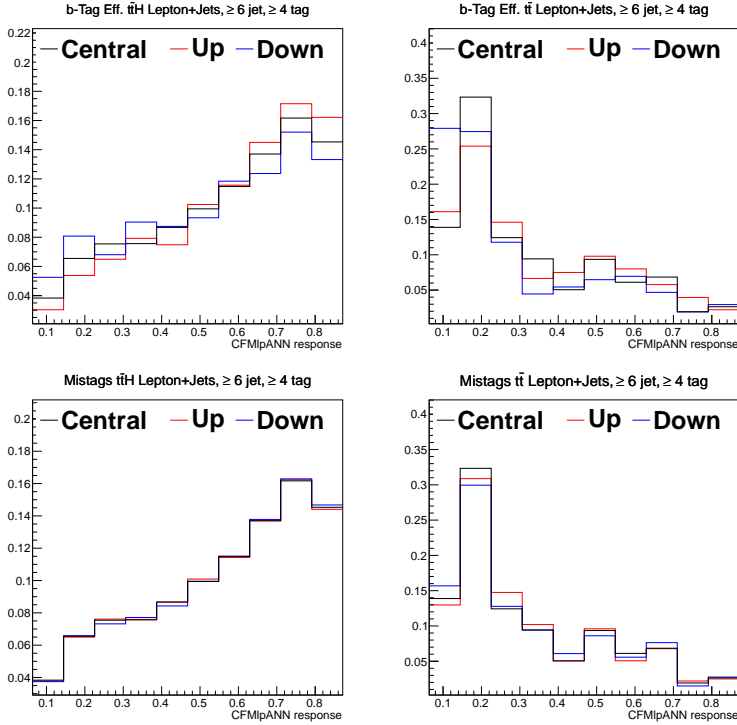


Figure 6.26: Comparison of the MVA discriminator for b -tag scale factor shift upwards (red) and downwards (blue) relative to the nominal (black) shape for the $t\bar{t}H(120)$ signal (left) and the main background sample $t\bar{t} + \text{light flavor}$ (right). The plots are from the ≥ 6 jets + ≥ 4 tags category in the lepton+jets channel. All plots are normalized to unit area.

b -tag systematic yield change			
		lepton+jets	
sys	shift	$t\bar{t}H(120)$	$t\bar{t}$
heavy flavor SF	up	+14.9%	+23.7%
	down	-15.3%	-16.0%
light flavor SF	up	+0.7%	+5.7%
	down	-1.1%	-4.2%

Table 6.14: Relative yield change due to b -tag scale factor shift up/down for the ≥ 6 jets + ≥ 4 tags category in the lepton+jets channel.

variations of the combined trigger, ID, and isolation scale factor.

Pileup Reweighting: The uncertainty on the pileup reweighting comes from changing the minimum bias cross section used to calculate the pileup reweighting by $\pm 7\%$ from the default value of 69.4 mb. The pileup reweighting is calculated using the shifted cross sections and the new weights are applied to determine the uncertainty on both the rate and shapes. Since the effect of the pileup on the shape variation is negligible, the effects of pileup are accounted through a rate-only uncertainty for the limit calculations.

Additional Pileup Correction The uncertainty associated with the additional pileup correction, described in section 6.1.5, is applied as a pure shape uncertainty to all processes. Fig. 6.27 shows the effects of the additional pileup correct uncertainty on the CFMlpANN shape.

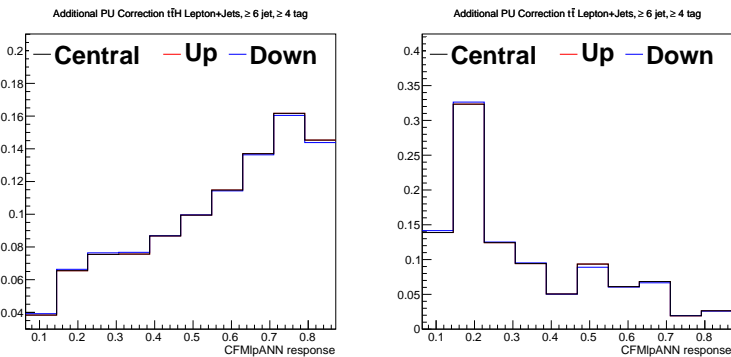


Figure 6.27: Comparison of the MVA discriminator for additional PU correction systematic upwards (red) and downwards (blue) relative to the nominal (black) shape for the $t\bar{t}H(120)$ signal (left) and the main background sample $t\bar{t} + \text{light flavor}$ (right). The plots are from the ≥ 6 jets + ≥ 4 tags category in the lepton+jets channel. All plots are normalized to unit area.

Cross Sections: The expectation for signal and background yields are derived from theoretical predictions of at least NLO accuracy. Uncertainties affecting these normalizations are summarized in table 6.15. Where appropriate, factors contributing to these uncertainties that are common to multiple processes are treated as 100% correlated. Note that for the $t\bar{t}+\text{jets}$ (including $t\bar{t} + b\bar{b}$ and $t\bar{t} + c\bar{c}$ processes, as well as the $V+\text{jets}$ processes, there is an additional uncertainty coming from the scale choice in Madgraph that effects these channels in a jet-bin specific way. This uncertainty is not included in the table 6.15, but is detailed in the next point.

Luminosity: The uncertainty on the luminosity estimate is 2.2%. This affects all rates.

Madgraph Q^2 Uncertainty: Although that backgrounds are normalized using NLO accurate theoretical caluclations, these are only applicable to inclusive distributions. To extrapolate

Process	pdf			QCD Scale			
	gg	qb	qg	$t\bar{t}$	V	VV	$t\bar{t}H$
$t\bar{t}H$	9%						12.5%
$t\bar{t}+jets$	9%			12%			
$t\bar{t} + W$		7%		15%			
$t\bar{t} + Z$	9%			15%			
Single top			4.6%	2%			
$W+jets$		4.8%			1.3%		
$Z+jets$		4.2%			1.2%		
Dibosons						3.5%	

Table 6.15: Cross section uncertainties used for the limit settings. Each column in the table is an independent source of uncertainty, except for the last column which represents uncertainties uncorrelated with any others. Uncertainties in the same column for two different processes (different rows) are completely correlated.

late these inclusive predictions to exclusive rates in particular jet bins requires the use of a Monte Carlo sample. The MADGRAPH generator is used at the matrix element level and includes tree-level calculations for processes with multiple additional jets, matched to the PYTHIA parton shower to model additional soft and collinear radiation. Since the MADGRAPH + PYTHIA is tree-level, the choice of the renormalizations and factorizations scales in this calculation has a significant impact. To include the effects of this uncertainty, the factorization and renormalization scales are varied by a factor of two. The ideal way to study this effect would be to generate dedicated samples with the varied scale choice, however the required statistics to get a precise determination of the systematic effect is computationally prohibitive. Therefore, as an alternative, we reweight the amplitudes, dividing by the appropriate power of α_s and the *pdf* values at the original scale, and multiplying by the values at the new scale choice. This reweighting procedure is supported by the CMS Monte Carlo Generators group, and has been validated against dedicated scale-varied samples and has been shown to produce consistent results [95]. This reweighting procedure provides both a rate and a shape uncertainty, separately for $t\bar{t}$ +light flavor, $t\bar{t} + c\bar{c}$, and $t\bar{t} + b\bar{b}$ components of the $t\bar{t}$ sample. Figure 6.28 shows the shape and rate variations for selected event categories. To prevent the strength of the $t\bar{t}+jets$ constraint from overconstraining the $t\bar{t} + b\bar{b}$ and $t\bar{t} + c\bar{c}$ components, we allow the Madgraph scale to vary independently for these three components.

MC Statistics Uncertainty: To account for the effect of limited MC statistics in the analysis, a method described by Barlow and Beeston, is used to select regions of the CFMlpANN output that should have additional nuisance parameters applied [?, ?]. For the CFMlpANN shapes of every MC process in all different categories, each bin is allowed to float within statistic uncertainty and a corresponding nuisance parameter is added. To make the limit

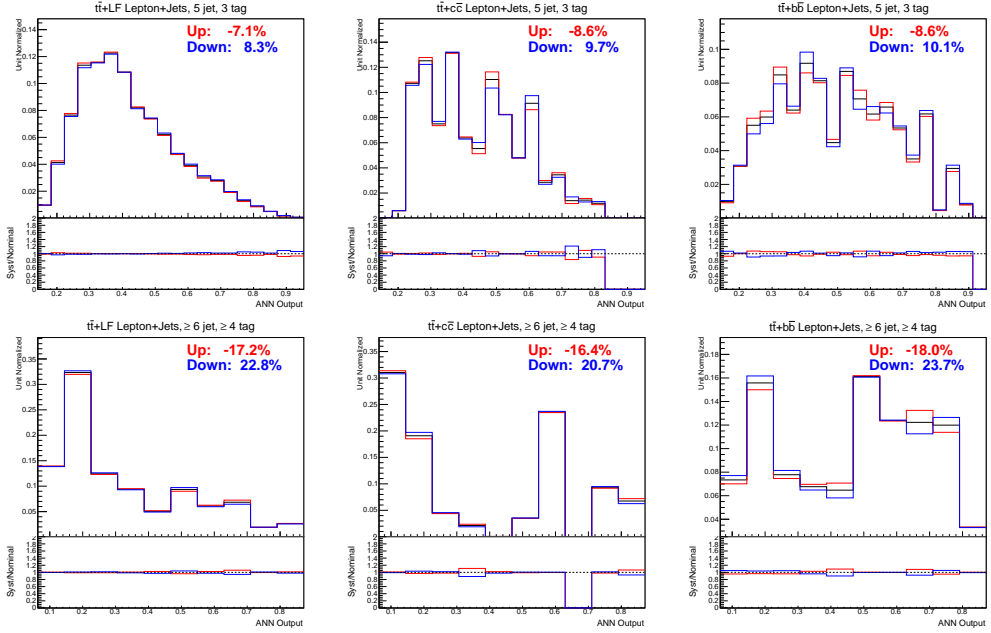


Figure 6.28: The rate and shape variations for selected categories due to the Q^2 uncertainty.

computation more efficient and stable, bins are removed as nuisance parameters if the MC statistics uncertainty is negligible compared to the data statistics uncertainty or where there is no appreciable contribution from signal. In total, there are 60 nuisance parameters used to describe the MC statistics for this analysis. Tests show that the effect of neglecting bins as described above is smaller than 5%.

Additional $t\bar{t} + b\bar{b}$ Rate Uncertainty: $t\bar{t} + b\bar{b}$ background is very similar to our signal, the uncertainty on its rate and shape will have a big impact on our search. Due to the lack of more accurate next leading order(NLO) theoretical prediction for this process, we obtained this background and assessed its uncertainty based on the inclusive 8 TeV $t\bar{t}$ sample. Since the inclusive $t\bar{t}$ sample is generated with Madgraph + Pythia, we need to apply a K-factor to the Madgraph cross section. According to calculations done in [96], the K-factor from leading order(LO) to NLO ranges between 1.2 and 1.8, depending on the scale choice. To be conservative, an extra 50% rate uncertainty is assigned to $t\bar{t} + b\bar{b}$ which corresponds to a K-factor of 1.7 for $\sigma_{NLO}/\sigma_{Madgraph}$. Studies also showed consistently that $t\bar{t} + b\bar{b}$ rate is correct to within factor of 2 in control regions dominated by $t\bar{t}$ +light flavor statistics. The extra 50% rate uncertainty should possibly include additional uncertainty beyond the 20% from Q^2 scale to account for the differences between NLO and Madgraph.

In order to validate this assessment further, a dedicated CFMlpANN was trained to separate $t\bar{t} + b\bar{b}$ from the $t\bar{t} + jets$ background. In order to have sufficient statistics, two jet/tag categories are used: 5jets, $\geq 3b$ -tags, and ≥ 6 jets, $\geq 3b$ -tags. The nominal $t\bar{t} + b\bar{b}$ cross section

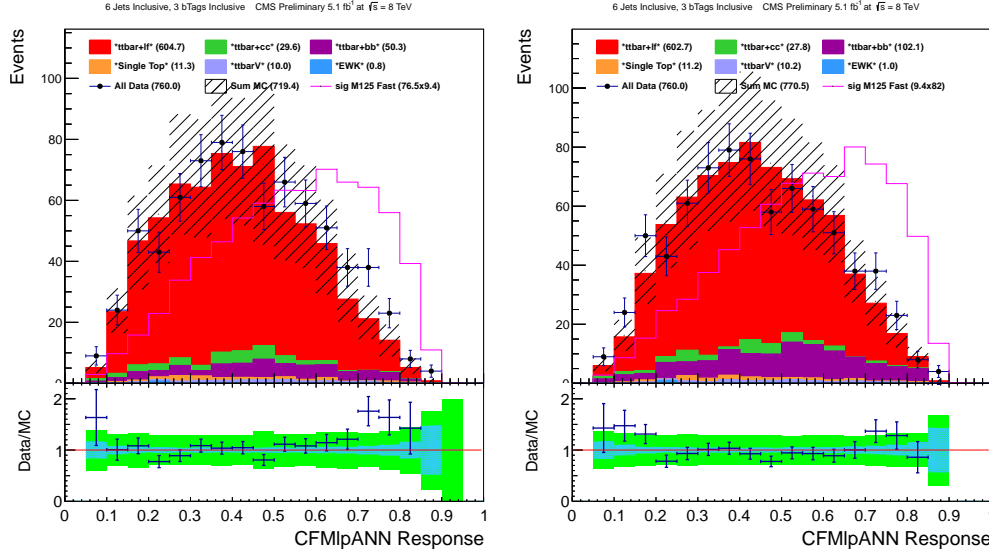


Figure 6.29: A dedicated CFMlpANN trained to isolate $t\bar{t} + b\bar{b}$ from $t\bar{t} + jets$. The left plot shows is for the case of nominal $t\bar{t} + b\bar{b}$ cross-section, the right plot shows the case for $x2 t\bar{t} + b\bar{b}$ cross-section. The left-most region of both plots is the most sensitive to the $t\bar{t} + b\bar{b}$ normalization, and shows no significant improvement in data to MC agreement, justifying the reasoning that an uncertainty larger than 50% is needed.

2326 was doubled, in an attempt to observe an improvement in the range of the discriminant
 2327 that was enriched in $t\bar{t} + b\bar{b}$. However, as figure 6.29 shows, no significant improvement
 2328 was seen, justifying the reasoning that an uncertainty much larger than 50% is needed.

2329 6.5 Statistical Methods

2330 In the lack of an observation of any deviation from SM predictions, upper limits are set on the
 2331 Higgs boson production cross section, with respect to the SM expectation, $\sigma^{95\%}/\sigma^{SM}$. Although
 2332 the analysis has been optimized for Higgs decays to b -quarks, there is still acceptance from WW
 2333 and ZZ decays. As such, limits on the inclusive decay of the Higgs boson are set. The statistical
 2334 method used to report results is the modified frequentist approach, also known as CL_s .

2335 For the CL_s method, the likelihood function $\mathcal{L}(\text{data}|\mu, \theta)$ is defined as

$$\mathcal{L}(\text{data}|\mu, \theta) = \text{Poisson}(\text{data}|\mu \cdot s(\theta) + b(\theta)) \cdot p(\tilde{\theta}|\theta) \quad (6.14)$$

$$= \prod_i \frac{(\mu s_i + b_i)^{n_i}}{n_i!} e^{-(\mu s_i + b_i)} \cdot p(\tilde{\theta}|\theta) \quad (6.15)$$

2336 where μ is the signal strength modifier which is often reported in the upper limit results as the
 2337 ratio of the cross-section upper limit over the standard model cross-section and θ represents
 2338 a full set of nuisance parameters that are used to incorporate systematic uncertainties. The

2339 Probability Distribution Function (*pdf*) of the nuisance parameter $p(\tilde{\theta}|\theta)$, where $\tilde{\theta}$ is the default
 2340 value, reflects the degree of confidence in what the true value of θ is.

2341 To compare the compatibility of the data with the *background-only* and *signal+background*
 2342 hypotheses, where the signal is allowed to be scaled by some factor μ , the test statistic \tilde{q}_μ is
 2343 constructed based on the profile likelihood ratio:

$$\tilde{q}_\mu = -2 \ln \frac{\mathcal{L}(\text{data}|\mu, \hat{\theta}_\mu)}{\mathcal{L}(\text{data}|\hat{\mu}, \hat{\theta})} \quad , 0 \leq \hat{\mu} \leq \mu \quad (6.16)$$

2344 where $\hat{\theta}_\mu$ refers to the conditional maximum likelihood estimator of θ , given the signal strength
 2345 parameter μ and data. The pair of parameter estimators $\hat{\mu}$ and $\hat{\theta}$ correspond to the global
 2346 maximum of the likelihood.

2347 To perform the computation of the limits, RooStats-based statistical analysis tools recom-
 2348 mended by Higgs PAG have been used. The corresponding software is the "Higgs Combination"
 2349 package. There are two versions of the limit calculation technique that we use. The frequen-
 2350 tist CL_s approach uses a large number of pseudo-experiments to extract the limit results. The
 2351 "asymptotic" approach makes an analytic approximation of the full CL_s technique and there-
 2352 fore avoids throwing pseudo-experiments. The asymptotic approach is used for optimizing the
 2353 analysis, for the results of this analysis. However, for the limits set from the combined Lep-
 2354 ton+Jets and di-Lepton channels, using both 7 and 8 TeV data, the results are calculated using
 2355 the full CL_s treatment. Comparisons have shown that limits obtained with the two techniques
 2356 agree at the 10% level.

2357 In the limit calculation, the backgrounds are decomposed into the following distinct cate-
 2358 gories: $t\bar{t}$ +jets, $t\bar{t} + b\bar{b}$, $t\bar{t} + c\bar{c}$, single top (s -channel, t -channel, and tW -channel combined),
 2359 W +jets, Z +jets, $t\bar{t} + W$, $t\bar{t} + Z$, and dibosons (WW , WZ , and ZZ combined). The rates and
 2360 shapes of these background processes, as well as the signal are allowed to vary according to a set
 2361 of nuisance parameters, and the values of these nuisance parameters are constrained according
 2362 to the uncertainties summarized in Table ???. Except where noted below, each row in that table
 2363 represents a single nuisance parameter, completely correlated across all categories and processes
 2364 to which it applies. The exceptions to this approach are as follows:

- 2365 • In the case of the Madgraph Q^2 uncertainty, there are separate nuisance parameters for
 2366 each of the three components of the $t\bar{t}$ background (+jets, + $b\bar{b}$, and + $c\bar{c}$). Furthermore, for
 2367 the $t\bar{t}$ +jets component, the uncertainty is actually broken into three nuisance parameters
 2368 for the contributions coming from diagrams with zero extra partons, one extra parton, or
 2369 at least two extra partons.

- For the b -tagging efficiency and mistag rate uncertainties, the rate and shape components are described by separate, independent nuisance parameters. Furthermore, each event selection category has its own, independent nuisance parameter. This is to prevent the high statistics background rich regions from overconstraining the shape uncertainties in the lower statistics, more signal rich regions.

For systematic effects such as the jet energy scale or the rate component of the b -tagging scale factor that may cause migration between event categories, care has been taken to correlate properly the different categories so that, for example, increasing the jet energy scale will cause the appropriate increases and decreases in the yields in various categories. The binning of the CFMlpANN output is chosen to minimize the impact of MC statistics and, as described in section 6.4 the MC statistics for bins where the MC statistical uncertainty causes a significant impact are accounted for.

6.6 Results and Conclusions

The variable used for signal extraction is the shape of the MVA output discriminator distribution. The fit of the simulated samples to the measured data will test for the presence of signal and, in its absence, it will set upper limits on the Higgs boson cross section. Besides the MVA discriminator shapes for data, background and signal, inputs to the "Higgs Combination" package also include the number of events passing our selection for each of the above processes. Various systematic uncertainties described in section 6.4 have all been taken into account in our limit calculation. The Higgs mass points we set limits for are: 110, 115, 120, 125, 130, 135 and 140 GeV/c^2 . The upper limits are shown in Tab. 6.16 and Fig. 6.30.

Higgs Mass	Observed	Median	Expected 68% C.L. Range	Expected 95% C.L. Range
110 GeV/c^2	5.9	3.1	[2.1,4.6]	[1.6,6.8]
115 GeV/c^2	7.2	3.9	[2.7,5.7]	[2.0,8.1]
120 GeV/c^2	8.8	4.8	[3.4,6.9]	[2.5,9.7]
125 GeV/c^2	9.5	5.4	[3.8,7.9]	[2.8,11.1]
130 GeV/c^2	11.4	6.6	[4.6,9.6]	[3.4,13.7]
135 GeV/c^2	15.0	8.9	[6.3,12.8]	[4.7,18.1]
140 GeV/c^2	17.0	11.0	[7.7,15.9]	[5.7,22.5]

Table 6.16: Expected and observed upper limits for SM Higgs for lepton + jets channel using the first 5.1 fb^{-1} of the 2012 dataset. These limits were extracted using the asymptotic method.

For this first 5.1 fb^{-1} of data collected by the CMS detector, the first search for the Standard Model Higgs boson produced in association with top-quark pairs. Although there have been no observed sign of Higgs production in association with top quarks, upper limits are set on the production cross-section, using the statistical methods described above. If this data set was

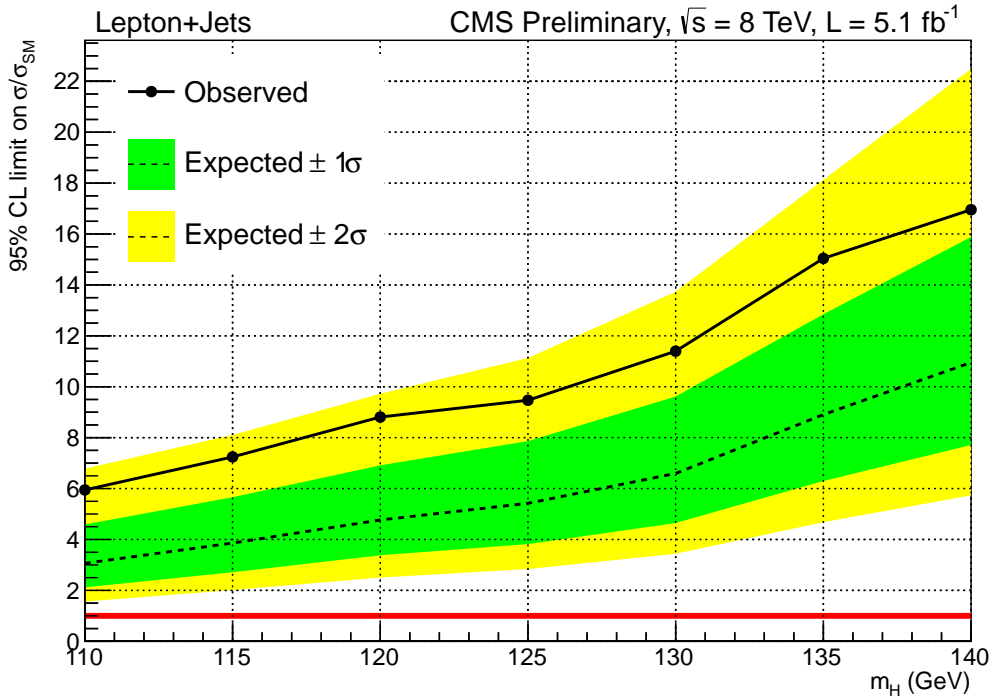


Figure 6.30: The expected and observed 95% CL upper limits on the signal strength parameter $\mu = \sigma/\sigma_{SM}$ for the lepton+jets channel using the 2012 dataset. These limits were extracted using the asymptotic method.

2395 repeatedly collected, allowing for statistical fluctuations, it should be expected that 95% of the
 2396 results would fail to observe the signal unless its cross-section was modified by a factor of 9.5.
 2397 From simulations alone, this expected factor is 5.4, a difference of less than 2 σ from the
 2398 observed data.

²³⁹⁹ Bibliography

- ²⁴⁰⁰ [1] “LHC Aerial View”.
²⁴⁰¹ URL <http://www.coepp.org.au/files/coepp/images/cern-aerial2.jpg>.
- ²⁴⁰² [2] CMS Collaboration, “Observation of a new boson at a mass of 125 GeV with the CMS
²⁴⁰³ experiment at the LHC”, *Phys.Lett.B* (2012) [arXiv:1207.7235](#).
- ²⁴⁰⁴ [3] ATLAS Collaboration, “Observation of a new particle in the search for the Standard
²⁴⁰⁵ Model Higgs boson with the ATLAS detector at the LHC”, *Phys.Lett.B* (2012)
²⁴⁰⁶ [arXiv:1207.7214](#).
- ²⁴⁰⁷ [4] M. E. Peskin and D. V. Schroeder, “An Introduction to Quantum Field Theory”.
²⁴⁰⁸ Westview Press, URL <http://www.westviewpress.com>, 1995.
- ²⁴⁰⁹ [5] K. G. Wilson, “Renormalization Group and Critical Phenomena. I. Renormalization
²⁴¹⁰ Group and the Kadanoff Scaling Picture”, *Phys. Rev. B* **4** (Nov, 1971) 3174–3183,
²⁴¹¹ doi:[10.1103/PhysRevB.4.3174](https://doi.org/10.1103/PhysRevB.4.3174).
- ²⁴¹² [6] K. G. Wilson, “Renormalization Group and Critical Phenomena. II. Phase-Space Cell
²⁴¹³ Analysis of Critical Behavior”, *Phys. Rev. B* **4** (Nov, 1971) 3184–3205,
²⁴¹⁴ doi:[10.1103/PhysRevB.4.3184](https://doi.org/10.1103/PhysRevB.4.3184).
- ²⁴¹⁵ [7] S. Bethke, “The 2009 World Average of alpha(s)”, *Eur.Phys.J. C***64** (2009) 689–703,
²⁴¹⁶ doi:[10.1140/epjc/s10052-009-1173-1](https://doi.org/10.1140/epjc/s10052-009-1173-1), [arXiv:0908.1135](#).
- ²⁴¹⁷ [8] H. Weyl, “The theory of groups and quantum mechanics”. Dover Press,
²⁴¹⁸ URL <https://ia700807.us.archive.org/20/items/ost-chemistry-quantumtheoryofa029235mbp/quantumtheoryofa029235mbp.pdf>, 1930.
- ²⁴²⁰ [9] C. N. Yang and R. L. Mills, “Conservation of Isotopic Spin and Isotopic Gauge
²⁴²¹ Invariance”, *Phys. Rev.* **96** (Oct, 1954) 191–195, doi:[10.1103/PhysRev.96.191](https://doi.org/10.1103/PhysRev.96.191).
- ²⁴²² [10] M. Gell-Mann, “A Schematic Model of Baryons and Mesons”, *Phys.Lett.* **8** (1964)
²⁴²³ 214–215, doi:[10.1016/S0031-9163\(64\)92001-3](https://doi.org/10.1016/S0031-9163(64)92001-3).

- 2424 [11] G. Zweig, “An SU₃ model for strong interaction symmetry and its breaking; Version 1”,
 2425 Technical Report CERN-TH-401, CERN, Geneva, Jan, 1964.
- 2426 [12] G. Zweig, “An SU₃ model for strong interaction symmetry and its breaking; Version 2”,.
- 2427 [13] O. W. Greenberg, “Spin and Unitary-Spin Independence in a Paraquark Model of Baryons
 2428 and Mesons”, *Phys. Rev. Lett.* **13** (Nov, 1964) 598–602,
 2429 doi:10.1103/PhysRevLett.13.598.
- 2430 [14] P. Higgs, “Broken symmetries, massless particles and gauge fields”, *Physics Letters* **12**
 2431 (1964), no. 2, 132 – 133, doi:[http://dx.doi.org/10.1016/0031-9163\(64\)91136-9](http://dx.doi.org/10.1016/0031-9163(64)91136-9).
- 2432 [15] S. Weinberg, “A Model of Leptons”, *Phys. Rev. Lett.* **19** (Nov, 1967) 1264–1266,
 2433 doi:10.1103/PhysRevLett.19.1264.
- 2434 [16] S. L. Glashow, “Partial-symmetries of weak interactions”, *Nuclear Physics* **22** (1961),
 2435 no. 4, 579 – 588, doi:[http://dx.doi.org/10.1016/0029-5582\(61\)90469-2](http://dx.doi.org/10.1016/0029-5582(61)90469-2).
- 2436 [17] A. Salam and J. Ward, “Electromagnetic and weak interactions”, *Physics Letters* **13**
 2437 (1964), no. 2, 168 – 171, doi:[http://dx.doi.org/10.1016/0031-9163\(64\)90711-5](http://dx.doi.org/10.1016/0031-9163(64)90711-5).
- 2438 [18] Nobelprize.org, “The Nobel Prize in Physics 1957”.
 2439 URL http://www.nobelprize.org/nobel_prizes/physics/laureates/1957/.
- 2440 [19] N. Cabibbo, “Unitary Symmetry and Leptonic Decays”, *Phys. Rev. Lett.* **10** (Jun, 1963)
 2441 531–533, doi:10.1103/PhysRevLett.10.531.
- 2442 [20] M. Kobayashi and T. Maskawa, “CP Violation in the Renormalizable Theory of Weak
 2443 Interaction”, *Prog.Theor.Phys.* **49** (1973) 652–657, doi:10.1143/PTP.49.652.
- 2444 [21] G. Arnison et al., “Experimental observation of isolated large transverse energy electrons
 2445 with associated missing energy at s=540 GeV”, *Physics Letters B* **122** (1983), no. 1, 103
 2446 – 116, doi:[http://dx.doi.org/10.1016/0370-2693\(83\)91177-2](http://dx.doi.org/10.1016/0370-2693(83)91177-2).
- 2447 [22] G. Arnison et al., “Experimental observation of lepton pairs of invariant mass around 95
 2448 GeV/c² at the {CERN} {SPS} collider”, *Physics Letters B* **126** (1983), no. 5, 398 – 410,
 2449 doi:[http://dx.doi.org/10.1016/0370-2693\(83\)90188-0](http://dx.doi.org/10.1016/0370-2693(83)90188-0).
- 2450 [23] M. Banner et al., “Observation of single isolated electrons of high transverse momentum
 2451 in events with missing transverse energy at the {CERN} pp collider”, *Physics Letters B*
 2452 **122** (1983), no. 56, 476 – 485,
 2453 doi:[http://dx.doi.org/10.1016/0370-2693\(83\)91605-2](http://dx.doi.org/10.1016/0370-2693(83)91605-2).

- [24] P. Bagnaia et al., “Evidence for Z0e+e at the {CERN} pp collider”, *Physics Letters B* **129** (1983), no. 12, 130 – 140,
`doi:http://dx.doi.org/10.1016/0370-2693\(83\)90744-X`.
- [25] The ALEPH, DELPHI, L3, OPAL, SLD Collaborations, the LEP Electroweak Working Group, the SLD Electroweak and Heavy Flavour Groups, “Precision Electroweak Measurements on the Z Resonance”, *Phys. Rept.* **427** (2006) 257,
`arXiv:hep-ex/0509008`.
- [26] The ALEPH, DELPHI, L3, OPAL Collaborations, the LEP Electroweak Working Group, “Electroweak Measurements in Electron-Positron Collisions at W-Boson-Pair Energies at LEP”, *Phys. Rept.* **532** (2013) 119, `arXiv:1302.3415`.
- [27] F. Abe et al., “Observation of Top Quark Production in $\bar{p}p$ Collisions with the Collider Detector at Fermilab”, *Phys. Rev. Lett.* **74** (Apr, 1995) 2626–2631,
`doi:10.1103/PhysRevLett.74.2626`.
- [28] S. Abachi et al., “Search for High Mass Top Quark Production in $p\bar{p}$ Collisions at $\sqrt{s} = 1.8$ TeV”, *Phys. Rev. Lett.* **74** (Mar, 1995) 2422–2426,
`doi:10.1103/PhysRevLett.74.2422`.
- [29] LHC Higgs Cross Section Working Group Collaboration, “Handbook of LHC Higgs Cross Sections: 3. Higgs Properties”, `doi:10.5170/CERN-2013-004`, `arXiv:1307.1347`.
- [30] W. Beenakker et al., “Higgs radiation off top quarks at the Tevatron and the LHC”, *Phys.Rev.Lett.* **87** (2001) 201805, `doi:10.1103/PhysRevLett.87.201805`,
`arXiv:hep-ph/0107081`.
- [31] W. Beenakker et al., “NLO QCD corrections to t anti-t H production in hadron collisions”, *Nucl.Phys.* **B653** (2003) 151–203, `doi:10.1016/S0550-3213(03)00044-0`,
`arXiv:hep-ph/0211352`.
- [32] R. Frederix et al., “Scalar and pseudoscalar Higgs production in association with a top-antitop pair”, *Phys.Lett.* **B701** (2011) 427–433,
`doi:10.1016/j.physletb.2011.06.012`, `arXiv:1104.5613`.
- [33] M. Garzelli, A. Kardos, C. Papadopoulos, and Z. Trocsanyi, “Standard Model Higgs boson production in association with a top anti-top pair at NLO with parton showering”, *Europhys.Lett.* **96** (2011) 11001, `doi:10.1209/0295-5075/96/11001`, `arXiv:1108.0387`.

- 2484 [34] S. Dawson, L. Orr, L. Reina, and D. Wackerlo, “Associated top quark Higgs boson
 2485 production at the LHC”, *Phys.Rev.* **D67** (2003) 071503,
 2486 [doi:10.1103/PhysRevD.67.071503](https://doi.org/10.1103/PhysRevD.67.071503), [arXiv:hep-ph/0211438](https://arxiv.org/abs/hep-ph/0211438).
- 2487 [35] T. Gleisberg et al., “Event generation with SHERPA 1.1”, *JHEP* **0902** (2009) 007,
 2488 [doi:10.1088/1126-6708/2009/02/007](https://doi.org/10.1088/1126-6708/2009/02/007), [arXiv:0811.4622](https://arxiv.org/abs/0811.4622).
- 2489 [36] P. Artoisenet, R. Frederix, O. Mattelaer, and R. Rietkerk, “Automatic spin-entangled
 2490 decays of heavy resonances in Monte Carlo simulations”, *JHEP* **1303** (2013) 015,
 2491 [doi:10.1007/JHEP03\(2013\)015](https://doi.org/10.1007/JHEP03(2013)015), [arXiv:1212.3460](https://arxiv.org/abs/1212.3460).
- 2492 [37] F. Cascioli, P. Maierhofer, and S. Pozzorini, “Scattering Amplitudes with Open Loops”,
 2493 *Phys.Rev.Lett.* **108** (2012) 111601, [doi:10.1103/PhysRevLett.108.111601](https://doi.org/10.1103/PhysRevLett.108.111601),
 2494 [arXiv:1111.5206](https://arxiv.org/abs/1111.5206).
- 2495 [38] F. Krauss, R. Kuhn, and G. Soff, “AMEGIC++ 1.0: A Matrix element generator in
 2496 C++”, *JHEP* **0202** (2002) 044, [doi:10.1088/1126-6708/2002/02/044](https://doi.org/10.1088/1126-6708/2002/02/044),
 2497 [arXiv:hep-ph/0109036](https://arxiv.org/abs/hep-ph/0109036).
- 2498 [39] T. Gleisberg and F. Krauss, “Automating dipole subtraction for QCD NLO calculations”,
 2499 *Eur.Phys.J.* **C53** (2008) 501–523, [doi:10.1140/epjc/s10052-007-0495-0](https://doi.org/10.1140/epjc/s10052-007-0495-0),
 2500 [arXiv:0709.2881](https://arxiv.org/abs/0709.2881).
- 2501 [40] Planck Collaboration, “Planck 2013 results. I. Overview of products and scientific results”,
 2502 *Astron.Astrophys.* **571** (2014) A1, [doi:10.1051/0004-6361/201321529](https://doi.org/10.1051/0004-6361/201321529),
 2503 [arXiv:1303.5062](https://arxiv.org/abs/1303.5062).
- 2504 [41] V. Rubin, N. Thonnard, and J. Ford, W.K., “Rotational properties of 21 SC galaxies with
 2505 a large range of luminosities and radii, from NGC 4605 /R = 4kpc/ to UGC 2885 /R =
 2506 122 kpc/”, *Astrophys.J.* **238** (1980) 471, [doi:10.1086/158003](https://doi.org/10.1086/158003).
- 2507 [42] Super-Kamiokande Collaboration Collaboration, “Measurements of the solar neutrino flux
 2508 from Super-Kamiokande’s first 300 days”, *Phys.Rev.Lett.* **81** (1998) 1158–1162,
 2509 [doi:10.1103/PhysRevLett.81.1158](https://doi.org/10.1103/PhysRevLett.81.1158), [arXiv:hep-ex/9805021](https://arxiv.org/abs/hep-ex/9805021).
- 2510 [43] KamLAND Collaboration Collaboration, “Measurement of neutrino oscillation with
 2511 KamLAND: Evidence of spectral distortion”, *Phys.Rev.Lett.* **94** (2005) 081801,
 2512 [doi:10.1103/PhysRevLett.94.081801](https://doi.org/10.1103/PhysRevLett.94.081801), [arXiv:hep-ex/0406035](https://arxiv.org/abs/hep-ex/0406035).
- 2513 [44] MINOS Collaboration Collaboration, “Observation of muon neutrino disappearance with
 2514 the MINOS detectors and the NuMI neutrino beam”, *Phys.Rev.Lett.* **97** (2006) 191801,
 2515 [doi:10.1103/PhysRevLett.97.191801](https://doi.org/10.1103/PhysRevLett.97.191801), [arXiv:hep-ex/0607088](https://arxiv.org/abs/hep-ex/0607088).

- [45] S. P. Martin, “A Supersymmetry primer”, *Adv.Ser.Direct.High Energy Phys.* **21** (2010) 1–153, doi:10.1142/9789814307505_0001, arXiv:hep-ph/9709356.
- [46] J. Aguilar-Saavedra, R. Benbrik, S. Heinemeyer, and M. Prez-Victoria, “Handbook of vectorlike quarks: Mixing and single production”, *Phys.Rev.* **D88** (2013), no. 9, 094010, doi:10.1103/PhysRevD.88.094010, arXiv:1306.0572.
- [47] G. Burdman, M. Perelstein, and A. Pierce, “Large Hadron Collider tests of a little Higgs model”, *Phys.Rev.Lett.* **90** (2003) 241802, doi:10.1103/PhysRevLett.90.241802, arXiv:hep-ph/0212228.
- [48] M. Perelstein, M. E. Peskin, and A. Pierce, “Top quarks and electroweak symmetry breaking in little Higgs models”, *Phys.Rev.* **D69** (2004) 075002, doi:10.1103/PhysRevD.69.075002, arXiv:hep-ph/0310039.
- [49] H.-C. Cheng, I. Low, and L.-T. Wang, “Top partners in little Higgs theories with T parity”, *Phys. Rev. D* **74** (Sep, 2006) 055001, doi:10.1103/PhysRevD.74.055001.
- [50] H.-C. Cheng, B. A. Dobrescu, and C. T. Hill, “Electroweak symmetry breaking and extra dimensions”, *Nucl.Phys.* **B589** (2000) 249–268, doi:10.1016/S0550-3213(00)00401-6, arXiv:hep-ph/9912343.
- [51] M. S. Carena, E. Ponton, J. Santiago, and C. E. Wagner, “Light Kaluza Klein States in Randall-Sundrum Models with Custodial SU(2)”, *Nucl.Phys.* **B759** (2006) 202–227, doi:10.1016/j.nuclphysb.2006.10.012, arXiv:hep-ph/0607106.
- [52] C. T. Hill, “Topcolor: Top quark condensation in a gauge extension of the standard model”, *Phys.Lett.* **B266** (1991) 419–424, doi:10.1016/0370-2693(91)91061-Y.
- [53] R. Contino, L. Da Rold, and A. Pomarol, “Light custodians in natural composite Higgs models”, *Phys.Rev.* **D75** (2007) 055014, doi:10.1103/PhysRevD.75.055014, arXiv:hep-ph/0612048.
- [54] L. Evans and P. Bryant, “LHC Machine”, *JINST* **3** (2008) S08001, doi:10.1088/1748-0221/3/08/S08001.
- [55] M. Benedikt et al., “LHC Design Report Vol3 - The Injection Chain”. CERN, Geneva, 2004.
- [56] C. Hill et al., “Tests of the CERN proton linac performance for LHC - type beams”, *eConf* **C000821** (2000) TUD17, arXiv:physics/0008102.
- [57] K. S. Klaus Hanke, and Michel Chanel.

- 2547 [58] “Image, CERN PSbooster Layout”.
2548 URL <http://psb-machine.web.cern.ch/psb-machine/>.
- 2549 [59] S. Baird, “Accelerators for pedestrians; rev. version”, Technical Report AB-Note-2007-014.
2550 CERN-AB-Note-2007-014. PS-OP-Note-95-17-Rev-2. CERN-PS-OP-Note-95-17-Rev-2,
2551 CERN, Geneva, Feb, 2007.
- 2552 [60] “CERN Website, Super Proton Synchrotron”.
2553 URL <http://home.web.cern.ch/about/accelerators/super-proton-synchrotron>.
- 2554 [61] G. Dme, “The SPS acceleration system travelling wave drift-tube structure for the CERN
2555 SPS”, .
- 2556 [62] O. S. Brning et al., “LHC Design Report Vol1 - The Main Ring”. CERN, Geneva, 2004.
- 2557 [63] “CERN, List of All LHC Magnets”. URL http://lhc-machine-outreach.web.cern.ch/lhc-machine-outreach/components/magnets/types_of_magnets.htm.
- 2559 [64] M. Barnes, J. Borburgh, B. Goddard, and M. Hourican, “Injection and extraction
2560 magnets: septa”, [arXiv:1103.1062](https://arxiv.org/abs/1103.1062).
- 2561 [65] M. Barnes et al., “Injection and extraction magnets: Kicker magnets”, [arXiv:1103.1583](https://arxiv.org/abs/1103.1583).
- 2562 [66] “Outreach, CERN LHC, Cryogenic System”. URL <http://home.web.cern.ch/about/engineering/cryogenics-low-temperatures-high-performance>.
- 2564 [67] “The challenge of keeping cool”, .
- 2565 [68] P. Lebrun, “Large Cryogenic Helium Refrigeration System for the LHC”, Technical
2566 Report LHC-Project-Report-629. CERN-LHC-Project-Report-629, CERN, Geneva, Feb,
2567 2003. revised version number 1 submitted on 2003-02-19 11:44:11.
- 2568 [69] “Outreach, CERN LHC, Vacuum System”. URL <http://home.web.cern.ch/about/engineering/vacuum-empty-interplanetary-space>.
- 2570 [70] CMS Collaboration Collaboration, “Particle-Flow Event Reconstruction in CMS and
2571 Performance for Jets, Taus, and MET”, Technical Report CMS-PAS-PFT-09-001, CERN,
2572 2009. Geneva, Apr, 2009.
- 2573 [71] CMS Collaboration, “Description and performance of track and primary-vertex
2574 reconstruction with the CMS tracker”, *JINST* **9** (2014), no. 10, P10009,
2575 [doi:10.1088/1748-0221/9/10/P10009](https://doi.org/10.1088/1748-0221/9/10/P10009), [arXiv:1405.6569](https://arxiv.org/abs/1405.6569).

- 2576 [72] R. Frhwirth, “Application of Kalman filtering to track and vertex fitting”,
 2577 *Nucl.Instrum.Meth.* **A262** (1987) 444–450, doi:10.1016/0168-9002(87)90887-4.
- 2578 [73] CMS Electromagnetic Calorimeter Group Collaboration, “Intercalibration of the barrel
 2579 electromagnetic calorimeter of the CMS experiment at start-up”, *JINST* **3** (2008)
 2580 P10007, doi:10.1088/1748-0221/3/10/P10007.
- 2581 [74] K. Cankocak, Y. Onel, P. de Barbaro, and D. Vishnevskiy, “CMS HCAL Installation and
 2582 Commissioning”, Technical Report CMS-CR-2008-047, CERN, Geneva, Jul, 2008.
- 2583 [75] CMS Collaboration Collaboration, “Commissioning of the CMS ECAL calibration with
 2584 muons from cosmic rays and beam dumps”, Technical Report CMS-CR-2009-339, CERN,
 2585 Geneva, Nov, 2009.
- 2586 [76] CMS Collaboration Collaboration, “Performance of the CMS Hadron Calorimeter with
 2587 Cosmic Ray Muons and LHC Beam Data”, *J. Instrum.* **5** (Nov, 2009) T03012 . 35 p.
- 2588 [77] CMS Collaboration Collaboration, “HCAL performance from first collisions data”,.
- 2589 [78] CMS Collaboration Collaboration, “Particle-flow commissioning with muons and electrons
 2590 from J/Psi and W events at 7 TeV”, Technical Report CMS-PAS-PFT-10-003, CERN,
 2591 2010. Geneva, 2010.
- 2592 [79] W. Adam, R. Frhwirth, A. Strandlie, and T. Todor, “Reconstruction of Electrons with the
 2593 Gaussian-Sum Filter in the CMS Tracker at the LHC”,.
- 2594 [80] M. Cacciari, G. P. Salam, and G. Soyez, “The Anti-k(t) jet clustering algorithm”, *JHEP*
 2595 **0804** (2008) 063, doi:10.1088/1126-6708/2008/04/063, arXiv:0802.1189.
- 2596 [81] CMS Collaboration Collaboration, “Commissioning of the Particle-Flow reconstruction in
 2597 Minimum-Bias and Jet Events from pp Collisions at 7 TeV”, Technical Report
 2598 CMS-PAS-PFT-10-002, CERN, Geneva, 2010.
- 2599 [82] Particle Data Group Collaboration, “Review of Particle Physics”, *Chin.Phys.* **C38**
 2600 (2014) 090001, doi:10.1088/1674-1137/38/9/090001.
- 2601 [83] “MET Optional Filters”.
 2602 <https://twiki.cern.ch/twiki/bin/view/CMS/MissingETOptionalFilters>.
- 2603 [84] CMS Collaboration, “Jet Energy Resolution in CMS at sqrt(s)=7 TeV”,.
- 2604 [85] C. Weiser, “A Combined Secondary Vertex Based B-Tagging Algorithm in CMS”,
 2605 Technical Report CMS-NOTE-2006-014, CERN, Geneva, Jan, 2006.

- 2606 [86] “Operating Points for b -Tag Algorithms”.
2607 <https://twiki.cern.ch/twiki/bin/viewauth/CMS/BTagPerformanceOP>.
- 2608 [87] “ b -Jet Identification in the CMS Experiment”,
- 2609 [88] VHbb Team, “Search for the SM Higgs Boson Produced in Association with W or Z and
2610 Decaying to Bottom Quarks (ICHEP 2012)”, CMS Note 2012/181, 2012.
- 2611 [89] A. Hocker et al., “TMVA - Toolkit for Multivariate Data Analysis”, *PoS ACAT* (2007)
2612 040, [arXiv:physics/0703039](https://arxiv.org/abs/physics/0703039).
- 2613 [90] J. D. Bjorken and S. J. Brodsky, “Statistical Model for Electron-Positron Annihilation
2614 into Hadrons”, *Phys. Rev. D* **1** (1970) 1416, doi:10.1103/PhysRevD.1.1416.
- 2615 [91] G. C. Fox and S. Wolfram, “Event Shapes in e^+e^- Annihilation”, *Nucl. Phys. B* **149**
2616 (1979) 413, doi:10.1016/0550-3213(79)90003-8.
- 2617 [92] “Jet Energy Scale Uncertainties”. <https://twiki.cern.ch/twiki/bin/view/CMSPublic/WorkBookJetEnergyCorrections>.
- 2618 [93] “Jet Energy Resolution Uncertainties”.
2619 <https://twiki.cern.ch/twiki/bin/view/CMS/JetResolution>.
- 2620 [94] “ b -Tag Scale Factor Uncertainties”.
2621 <https://twiki.cern.ch/twiki/bin/viewauth/CMS/BtagPOG>.
- 2622 [95] T. Peiffer., “ Q^2 Systematic MC Samples re-weighting”. <https://indico.cern.ch/getFile.py/access?contribId=5&resId=0&materialId=slides&confId=177717>, 2012.
- 2623 [96] A. Bredenstein, A. Denner, S. Dittmaier, and S. Pozzorini, “NLO QCD corrections to top
2624 anti-top bottom anti-bottom production at the LHC: 2. full hadronic results”, (2010).
2625 [arXiv:1001.4006](https://arxiv.org/abs/1001.4006).
2626

²⁶²⁸ List of Acronyms

²⁶²⁹ **ATLAS** A Toroidal LHC Apparatus

²⁶³⁰ **BSM** Beyond the Standard Model

²⁶³¹ **CERN** European Center for Nuclear Research

²⁶³² **CMS** Compact Muon Solenoid

²⁶³³ **ECAL** Electromagnetic Calorimeter

²⁶³⁴ **FSR** Final State Radiation

²⁶³⁵ **HCAL** Hadronic Calorimeter

²⁶³⁶ **ISR** Initial State Radiation

²⁶³⁷ **JHEP** Journal of High Energy Physics

²⁶³⁸ **LHC** Large Hadron Collider

²⁶³⁹ **LO** Leading Order

²⁶⁴⁰ **MVA** Multi-Variate Analysis

²⁶⁴¹ **NLO** Next to Leading Order

²⁶⁴² **QCD** Quantum Chromodynamics

²⁶⁴³ **QED** Quantum Electrodynamics

²⁶⁴⁴ **QFT** Quantum Field Theory

²⁶⁴⁵ **SM** Standard Model